Structure and Persistence of Surface Ship Wakes

John Ryan Somero

Dissertation submitted to the Faculty of the
Virginia Polytechnic Institute and State University
in partial fulfillment of the requirements for the degree of

Doctor of Philosophy
in
Aerospace Engineering

Eric G. Paterson, Chair
Joseph A. Schetz
Stefano Brizzolara
Scott L. England

November 17, 2020
Blacksburg, Virginia

Keywords: ship wake, Langmuir-type circulations, wave-action balance, surface-roughness modification, synthetic-aperture radar (SAR) imagery

Structure and Persistence of Surface Ship Wakes

John Ryan Somero

(ABSTRACT)

It has long been known that ship wakes are observable by synthetic aperture radar. However, incomplete physical understanding has prevented the development of simulation tools that can predict both the structure and persistence of wakes in the ocean environment. It is the focus of this work to develop an end-to-end multi-scale modeling-and-simulation methodology that captures the known physics between the source of disturbance and the sensor. This includes turbulent hydrodynamics, free-surface effects, environmental forcing through Langmuir-type circulations, generation of surface currents and redistribution of surface-active substances, surface-roughness modification, and simulation of the signature generated by reflection and scattering of electromagnetic waves from the ocean surface. The end-to-end methodology is based upon several customized computational fluid dynamics solvers and empirical models which are linked together. The unsteady Reynolds-averaged Navier-Stokes equations, including models for the Craik-Leibovich vortex force and near-surface Reynolds-stress anisotropy, are solved at full-scale Reynolds and Froude numbers on domains that extend tens of kilometers behind the ship. A parametric study is undertaken to explore the effects of ship heading, ship propulsion, ocean-wave amplitude and wavelength, and the relative importance of Langmuir-type circulations vs. near-surface Reynolds-stress anisotropy on the generation of surface currents that are transverse to the wake centerline. Due to the vortex force, the structure of the persistent wake is shown to be a function of the relative angle between the ambient long-wavelength swell and the ship heading. Ships operating in head seas observe 1-3 streaks, while ships operating in following seas observe 2 symmetric streaks. Ships operating in calm seas generate similar wakes to those in following seas, but with reduced wake width and persistence. In addition to the structure of the persistent wake, the far wake is shown to be dominated by ship-induced turbulence and surface-current gradients generating a wide center wake. The redistribution of surface-active substances by surface currents is simulated using a scalar-transport model on the ocean surface. Simulation of surface-roughness modification is accomplished by solving a wave-action-balance model which accounts for the relative change in the ambient wave-spectrum by the surface currents and the damping-effects of surface-active substances and turbulence. Simulated returns from synthetic aperture radar are generated with two methods implemented. The first method generates a perfect SAR image where the instrument and platform based errors are neglected, but the impact of a randomized ocean field on the radar cross section is considered. The second method simulates the full SAR process including signal detection and processing. Comparisons are made to full-scale field experiments with good agreement between the structure of the persistent wake and observed SAR imagery.

Structure and Persistence of Surface Ship Wakes

John Ryan Somero

(GENERAL AUDIENCE ABSTRACT)

It has long been known that ship wakes are observable by synthetic aperture radar. However, incomplete physical understanding has prevented the development of simulation tools that can predict both the structure and persistence of wakes in the ocean environment, which is critical to understanding both the design and operation of maritime remote sensors as well as providing tactically relevant operational guidance and awareness of the maritime domain. It is the focus of this work to develop an end-to-end multi-scale modeling-and-simulation methodology that captures the known physics between the source of disturbance and the sensor. This includes turbulent hydrodynamics, free-surface effects, environmental forcing, generation of surface currents and redistribution of surface-active substances, surface-roughness modification, and simulation of the signature from the ocean surface. The end-to-end methodology is based upon several customized computational fluid dynamics solvers and empirical models. The unsteady Reynolds-averaged Navier-Stokes equations, including models to account for environmental effects and near-surface turbulence, are solved at full-scale on domains that extend tens of kilometers behind the ship. A parametric study is undertaken to explore the effects of ship heading, ship propulsion, ocean-wave amplitude and wavelength, and the relative importance of environmental forcing vs. near-surface turbulence on the generation of surface currents that are transverse to the wake centerline. Due to the environmental forcing, the structure of the persistent wake is shown to be a function of the relative angle between the ambient long-wavelength swell and the ship heading. Ships operating in head seas observe 1-3 streaks, while ships operating in following seas observe 2 symmetric streaks. Ships operating in calm seas generate similar wakes to those in following seas, but with reduced wake width and persistence. In addition to the structure of the persistent wake, the far wake is shown to be dominated by ship-induced turbulence and surface-current gradients generating a wide center wake. The redistribution of surface films by surface currents is simulated using a scalar-transport model on the ocean surface. Simulation of surface-roughness modification is accomplished by solving a wave-action-balance model which accounts for the relative change in the ambient surface profile by the surface currents and the damping-effects of surface-active substances and turbulence. Simulated returns from synthetic aperture radar are generated with two methods implemented. The first method generates a perfect SAR image where the instrument and platform based errors are neglected, but the impact of a randomized ocean field on the radar cross section is considered. The second method simulates the full SAR process including signal detection and processing. Comparisons are made to full-scale field experiments with good agreement between the structure of the persistent wake and observed SAR imagery.

Dedication

This work is dedicated to my Lord and Savior, Jesus Christ, for only by His grace has this work been accomplished; and to my incredible wife, Audrey, for her years of patience and loving support that have enabled this work to be completed.

Acknowledgments

This work has been supported by Newport News Shipbuilding through internal research and development funding. This work was also supported in part by high-performance computer time and resources from the DoD High Performance Computing Modernization Program as well as Advanced Research Computing at Virginia Tech.

Contents

List of Figures

List of Tables

List of Abbreviations

ADCP Acoustic Doppler Current Profiler

ALOS-2 Advanced Land Observation Satellite-2

CFD Computational Fluid Dynamics

EOM ERIM Ocean Model

ERIM Environmental Institute of Michigan

ERS-1/2 European Remote Sensing Satellites 1/2

ESA European Space Agency

IDP Initial Data Plane

LTC Langmuir Type Circulations

ONR Office of Naval Research

RANS Reynolds Averaged Navier Stokes

RCS Radar Cross Section

SAR Synthetic Aperture radar

SARSEX Synthetic Aperture Radar Internal Wave Signature Experiment

SAS Surface Active Substances

TKE Turbulent Kinetic Energy

USS United States Ship

Chapter 1

Introduction

Remote sensing of surface ship wakes has gained significant interest in the technical community since it first became practical on a global scale with the introduction of synthetic aperture radar (SAR) on the NASA satellite SEASAT in 1978.Prior to the introduction of SAR on SEASAT, remote sensing of the Earth's surface was conducted either via aircraft or by optical methods on satellites. Aircraft based systems naturally were limited on range and only truly practical for monitoring high value areas or investigating already identified areas of interest. Satellite based optical instruments could provide resolution sufficient for maritime surveillance (O(10 m)), but wavelengths in the visible and infrared spectrum are subject to significant levels of absorption through clouds and are dependent on reflected sunlight, requiring day-time only operation. Use of the microwave spectrum would allow for operation regardless of weather and time of day as the longer wavelengths are less attenuated by clouds and do not rely on reflected sunlight, but equal resolution to optical sensors (10m) would require an aperture of O(10 km).

Application of a synthetic aperture though, inverts the relationship between antenna size and resolution. Here, pulses are emitted that are sufficiently wide to cover a location on the surface over a range of pulses. The phase and Doppler shift of the return from that location between pulses is recorded and processed to generate a synthetic aperture that covers the full distance over which the location is observable. This method allows for resolutions similar to optical sensors to be achieved at microwave frequencies with relatively small physical antennas. The use of SAR on SEASAT allowed for the study of a previously unachievable number of ship wakes in addition to other oceanographic features such as internal waves and bathymetry [19, 41, 125, 153].

Research on these original images focused heavily on the Kelvin wake and the formation of internal waves in the near field as these were readily observable. Discussion on the narrow V-wake also drew attention as traditional Kelvin wake theory did not predict the formation of such features where wake half angles ranged from 1° to the classically predicted 19.5°. In addition, features that were previously attributed to internal waves were observed in regions with deep mixed layers where internal waves were not expected to be generated. These observations led to follow on experiments such as the Georgia Straight and Gulf of Alaska experiments [19], 1984 SARSEX Experiment [75], WAKEX 86 [73], the 1989 Office of Naval Research (ONR) Field Experiment [118], the 1994 Loch Linnhe radar ocean imaging trials [105], in addition to numerous target of opportunity studies.

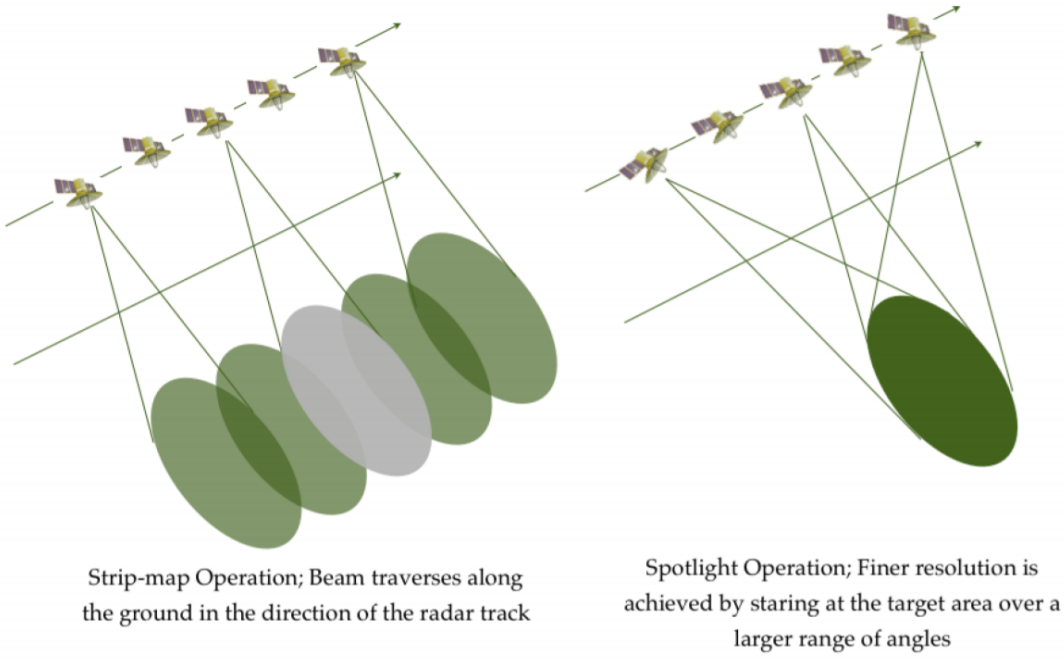

Figure 1.1: SAR imaging modes. Used with permission of Muff [104].

Advances in SAR technology have made the monitoring of the maritime environment possible from space based systems. The European space agency utilizes the Copernicus program, through its system of Sentinel satellites, for maritime surveillance [53]. The Canadian space agency uses RADARSAT-2 [85] for the same as does the German space agency with TerraSAR-X [152] and the Italian space agency with COSMO-SkyMed [18]. A brief survey of current space based SAR systems is provided in Table 1.1 with resolutions in both spotlight and strip map modes, Figure 1.1. Spotlight modes are used for the finest of resolutions on a single fixed location. Strip map modes are more used for scanning or surveillance.

In general, these systems are capable of directly observing the presence of surface ships as available resolution has improved, though the direct detection of ships, especially those traveling at high speed, can be challenging. This has led to research of remote detection via the ship's wake [50, 52, 74, 164]. In addition, operational information such as ship speed and heading can be estimated from wake parameters [49, 51, 163].

Table 1.1: Modern satellite based SAR systems. [1, 2, 64, 79, 109]

Satellite	Country	Launched	Band	Spotlight Resolution (m)	Strip Mode Resolution (m)
RADARSAT-2	Canada	2007	C	1x3	25
TeraSAR-X	Germany	2007	X	1	16
Cosmo-SkyMed	Italy	2007	X	1	15
SAR-Lupe	Germany	2007	X	0.5	1
HJ1C	China	2012	S	5	20
KOMPSAT-5	Korea	2013	X	1	3
ALOS-2	Japan	2014	L	1x3	3
Sentinel-1	Europe	2015	C	-	5
NovaSAR	UK	2018	S	6	30
Paz	Spain	2018	X	1	6
ICEYE	Finland	2018	X	0.25	0.5x3
RISAT-2B	India	2019	X	1	3
Capella	USA	2019	X	0.3	1

There are several distinct processes generated by a self–propelled ship: surface waves generated by the ship hull (Kelvin wake); propeller and hull–induced near–surface flow and turbulence; and bubbles produced by the propellers and breaking bow waves [114]. These features are well documented in field [115] and towing–tank [116, 143] experiments. Most of these features decay several ship lengths behind the vessel [143], which is also shown by simulations presented in this work. Nevertheless, it is well known that some features of ship wakes can be observed well after the passage of the ship, in some cases tens of kilometers behind the vessel, Figure 1.2. This dissertation addresses the physical mechanisms for the formation and resulting structure of such long–lasting ship wakes, and describes their qualitative and some quantitative features.

A distinction should be made between different stages in the development of a ship wake. Commonly, a near and far wake are described [42, 113, 124]. The near wake consists of perturbations generated in the vicinity of the ship by propellers, appendages, and the hull. The far wake is the region of the wake where these perturbations evolve and decay behind the ship. The physical mechanism of persistence of the ship wake beyond this far-field region is not currently explained. Here, the part of the wake that exists long after the initial perturbations generated by the ship dissipate is called *the persistent wake*.

In SAR images of the sea surface, ship wakes produce one or several streaks along the trajectory of the ship. The brightness of the streaks, in comparison to the background, depends on the amplitude of the short surface waves, which are responsible for reflection of the radar waves. Dark and bright streaks correspond to lower and higher amplitude short surface waves, respectively. The amplitude of the short surface waves is affected mainly by surface currents, near–surface turbulence, and films of surface–active substance (SAS) which

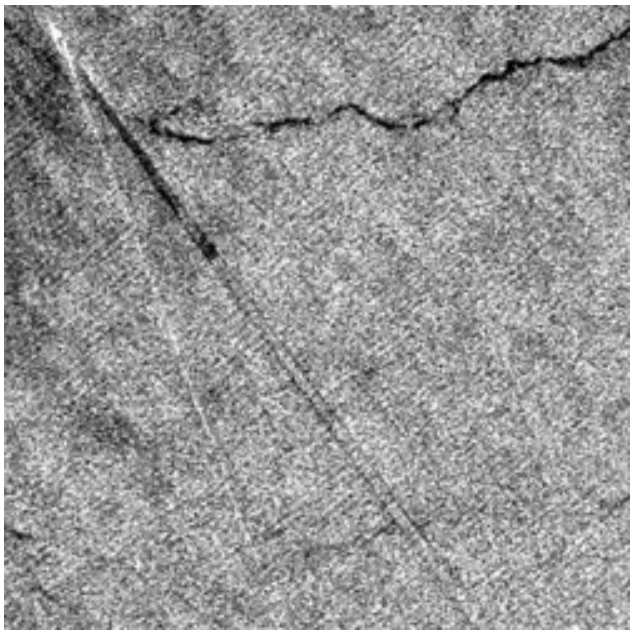

Figure 1.2: SAR image of ship wake from ERS-1 in the Straight of Malacca, 1996. Photo:ESA.

alter the elasticity of the ocean surface. Surface-active substances are chloroform-soluble material that primarily consist of fatty esters, fatty acids, fatty alcohols, and hydrocarbons that form thin films at the surface [44]. Surface currents can produce some effect on the wave amplitude in the near– and far–wake regions [42]. However, since the velocity of surface currents generated in the ship wake is relatively low, the turbulence and SAS play more important roles in the formation of surface images. In general, the far wake, where initial turbulent perturbations still exist, is normally seen in the image as a dark streak called the centerline wake, which is formed due to damping of the short surface waves by turbulence.

Further away from the ship, and depending on environmental conditions, there are two major types of persistent wakes that could be observed: a "centerline" wake or a "railroad–track" wake. Examples of such ship wakes are presented in figures 1.3 and 1.4, which are SAR images from Milgram et al. [97]. The centerline persistent wake appears as a dark streak, while the railroad–track persistent wake appears as a bright streak along the centerline with two dark streaks around it ("the railroad tracks"). Under conditions of following seas, it can be seen in the SAR image presented in Figure 1.4, that in the far wake, the centerline wake transforms into the railroad–track type of persistent wake.

Considerable efforts have been placed towards the understanding and prediction of wakes observed in SAR with several mechanisms suggested that do not have published predictions of persistence for actual surface ship conditions. Two primary mechanisms whose persistence had not previously been quantified are the transverse surface currents induced by Langmuir-

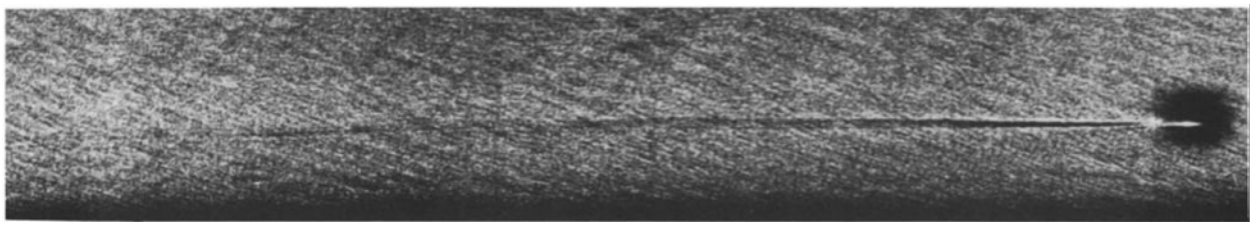

Figure 1.3: SAR image of USS Chandler (DDG-996) in head seas with a persistent centerline wake [97]

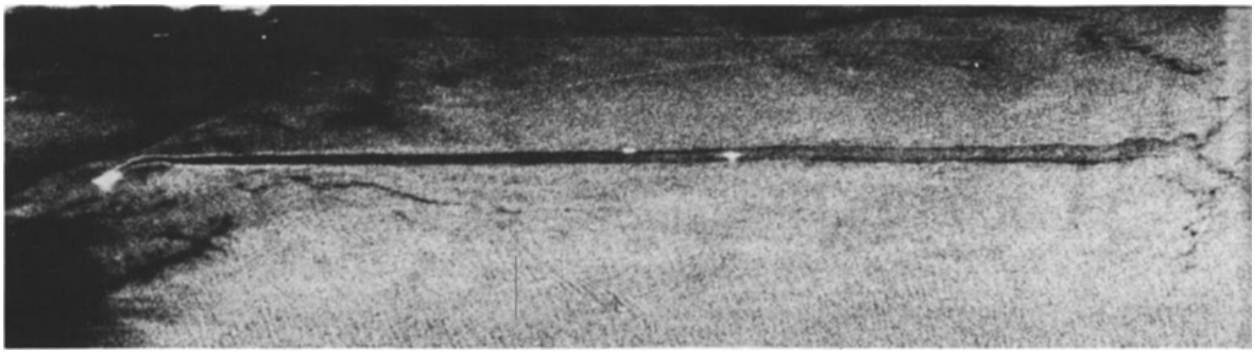

Figure 1.4: SAR image of USS Chandler (DDG-996) in following seas with a "railroad–track" persistent wake [97].

type circulations [13] and near–surface Reynolds stress anisotropy [156]. In this work we first study the impact of Langmuir-type circulations (LTC) generated by a surface ship and demonstrate the long lasting persistence of such circulations and their impact on the formation and structure of surface currents in the far and persistent wake. Then the effects of near-surface Reynolds stress anisotropy are included and it is shown that the two mechanisms have complementary roles in defining the structure of the persistent wake. It is also shown that the wake is dependent not only on the physical and operational characteristics of the ship, but also on the ambient environmental conditions in which it operates. The surface currents that are generated by LTC and turbulence anisotropy are then shown to redistribute ambient SAS into the observed centerline or rail-road track streaks that define the persistent wake in SAR imagery. Whether the wake forms a centerline or rail-road track persistent wake is shown to be a function of the relative angle between the ship heading and the ambient wave field vector and the strength of induced LTC. The short wave damping due to the compacting of SAS is taken with the effects of ship induced turbulence and surface currents to model the modification of ocean surface roughness, which is measured by SAR as the backscattering coefficient. It is demonstrated that SAS plays the primary role in the formation of the persistent wake, with turbulence and surface currents contributing to the structure in the near and far wake.

This dissertation is outlined as follows. First a review of previous research into the formation

and modeling of the persistent wake is provided. Discussions on the physical mechanisms responsible for the damping of short wind waves is provided along with experimental results that support the development of mathematical models to describe the damping. Descriptions of previously developed wave action balance models are discussed along with their applicability for use with remote sensing applications. Second, the effect on the persistent wake by Langmuir-type circulations is explored. The formation and evolution of the vortex force is discussed and shown to be responsible for the formation of LTC and in turn persistent surface currents. Third, the redistribution of surface active substances are modeled based on the LTC induced surface currents and the resulting damping of short wind waves is discussed. Fourth, a model that incorporates surface currents due to near surface Reynolds stress anisotropy is discussed and implemented along with LTC. Relative comparisons are made between the two mechanisms on their impact on ocean surface roughness. The effects of turbulence and surface currents are also incorporated into the surface roughness modification model to study the relative importance of each mechanism in the far and persistent wake. Finally, the model is exercised within a SAR prediction algorithm that incorporates a randomized ocean realization and comparison to available full scale experimental data is made. A discussion on the limitations of the model as well as future efforts that would improve the prediction of ship wakes is provided in conclusion.

Chapter 2

Review of Literature

2.1 Wave Action

SAR instruments are capable of detecting the presence of a ship wake by the modification of the surface roughness, which is measured as the radar back scatter. Dark areas show regions of low surface roughness where as bright areas show regions of high surface roughness. The roughness of the surface is a function of the distribution of wave energy through the wave number spectrum and the frequency of the radar being used. Higher frequency radar will be Bragg resonant with shorter wavelength waves and lower frequency radar will be resonant with relatively longer wavelengths such that the water wave number (k_w) that is Bragg resonant with a given electromagnetic wave number (k_r) is given by

$$k_w = 2k_r \sin(\phi) \tag{2.1}$$

where ϕ is the incident angle of the incoming radar beam. SAR instruments in general operate at frequencies ranging from $f_r = 1 - 10$ GHz which corresponds to water wave numbers and frequencies (f_w) for gravity-capillary waves as given in Table 2.1 for a 50 degree incidence angle.

Radar Band	f_r (GHz)	k_r	f_w (Hz)	k_w
L Band	1.25	2.62	3.18	40.1
S Band	3.1	6.49	5.15	99.5
C Band	5.3	11.1	7.16	170
X Band	9.6	20.1	11.4	308

Table 2.1: Water wave numbers that are Bragg resonant with SAR relevant electromagnetic frequencies and wave numbers.

In addition to the wave frequency, the direction of energy propagation is also important. In general, SAR will receive the strongest variation in returns from energy traveling either towards or away from the incident beam. Just as variations in global and local wind conditions drive a range of wave frequencies and directions, Figure 2.1, the hydrodynamic phenomena that act in the wake of a ship along with variable currents and wind directions generate a spectrum of wave energy that is termed as the energy density spectrum $E(f, \theta)$.

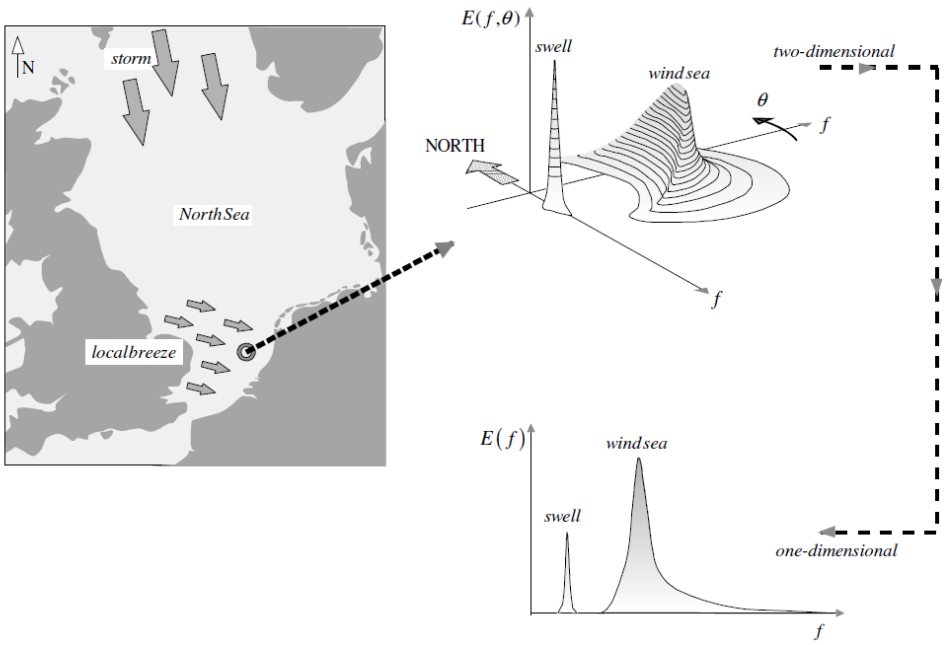

Figure 2.1: Illustration of spectral wave energy density (Holthuijsen [61]) Used permission of Cambridge University Press through PLSclear

The energy density though, is not conserved during propagation with ambient currents. The action spectral density (E/ω), where ω is the water wave intrinsic frequency, however is and can be written as given by Hasselmann [55], Hughes [62] as

$$\frac{\partial N}{\partial t} + (C_{gi} + U_i)\frac{\partial N}{\partial x_i} - k_i \frac{\partial U_i}{\partial x_j}\frac{\partial N}{\partial x_j} = (\beta - \gamma)N - \alpha N^2 \tag{2.2}$$

where N is the action spectral density of wave action, k_m denotes a wave vector of wind waves, C_{gi} is the wind–wave group velocity, and U_i is the velocity of the surface currents. The right–hand side follows the formulation of Hughes [62] where β is the wind–wave growth rate, γ accounts for the damping of the waves due to surface films and turbulence, and α is a phenomenological coefficient to account for the nonlinear effects that limit the wave growth such as wave breaking.

The wind-wave growth rate, β, is traditionally modeled using the formulation of Plant [120] as

$$\beta = 0.04\omega\left(\frac{u_\star}{c}\right)^2 \tag{2.3}$$

where $u_\star$ is the wind friction velocity, c is the phase velocity ($c = \omega/k$), and k is the wavenumber. This relationship has been shown to well correlate with experiment [151].

An alternate expression has been suggested by Donelan and Pierson Jr [33] given as

$$\beta = K\frac{\rho_a}{\rho_w}\left[U\left(\frac{\lambda}{2}\right)c - 1\right]^2 \omega. \tag{2.4}$$

Here K is an empirical constant originally given as $K = 0.194$, but later improved agreement with experiment was found for $K = 0.17$ [34]. The terms ρ_a and ρ_w designate the density of air and water and $U\left(\frac{\lambda}{2}\right)$ is a function of $U(z)$ and $u_\star$ as

$$U\left(\frac{\lambda}{2}\right) = U(z) + \frac{u_\star}{\kappa}\ln\left(\frac{\lambda}{2z}\right) \tag{2.5}$$

where κ is von Karman's constant, $\kappa = 0.4$, and z is the vertical height above the water. These two formulations have been shown to provide good correlation with data and almost identical predictions of wave growth for wavelengths relevant to remote sensing by SAR in the gravity-capillary regime [34]. Discussion on damping terms will be provided in the next sections.

Several codes have been developed to solve for the wave action balance with various primary purposes. Most modern general wave action balance solvers are referred to as third generation wave models, as they have built upon several generations of predecessors. These types of models include SWAN [15], developed and maintained by Delft University of Technology, WAVEWATCH III [162], developed and maintained by the National Oceanic and Atmospheric Administration (NOAA), and WAM [54], developed by the WAMDI Group and maintained by the National Oceanography Centre (UK). These models are in general used for oceanic scale modeling for weather prediction and analysis. As such, only gravity waves are currently supported and the impact of higher wavenumbers are suppressed through a damping function

$$\Delta N = \gamma\frac{\alpha_{PM}}{2\sigma k^3 c_g} \tag{2.6}$$

where γ is a limitation factor, usually taken as $\gamma = 0.1$, $\alpha_{PM} = 8.1 \times 10^{-3}$ is the Phillips constant for a Pierson-Moskowitz spectrum, σ is the wave frequency, k is the wave number, and c_g is the wave group velocity. While this is required for numerical stability, it limits the applicability of such codes for remote sensing applications where wavenumbers of order O(100) are relevant.

The Environmental Research Institute of Michigan (ERIM) developed an ocean model commonly referred to as EOM (ERIM Ocean Model) to solve the wave action balance with interest in remote sensing applications. This requires the solver be suitable for wave numbers that are applicable for SAR. The code uses a modified upwind finite difference method for the advective and wave-current interaction terms. Here the action spectral density is solved at fixed wave number and spatial coordinates and designated as (A), to permit use of a sweeping algorithm where each grid point is solved each iteration only if it had not

reached a converged state the previous iteration. Solutions are considered converged once residuals are reduced to less than 10^{-6}. In order to account for the need to resolve high wavenumbers, $\partial A/\partial K$ is solved as a perturbation function where $A = A_{eq} + \Delta A$, where A_{eq} is the equilibrium value and ΔA is the difference from equilibrium. This modification is required as the action spectrum falls off as $K^{-4.5}$ at high wavenumbers, which are of utmost interest to SAR. Various versions of this model have been used by a range of authors to study multiple oceanographic processes and scales, Ainsworth et al. [3], Allan et al. [4], Fischer and Shuchman [39], Fischer et al. [40], Jansen et al. [66], Johannessen et al. [67, 68, 69], Lyden et al. [88, 89], Lyzenga [91, 92], Lyzenga and Bennett [93], RA et al. [122].

Additional models developed for the purpose of remote sensing applications are detailed in Romeiser et al. [126], Kudryavtsev et al. [80], Apel [10], Holliday et al. [60], and Jansen et al. [66]. The NRL (Naval Research Laboratory) Time Dependent Ocean Wave (NTOW) model [66] was compared to EOM with good agreement between the models. In particular, the NTOW model and EOM compared well when comparing the modulation of the action spectral density due to a stationary soliton-like current. Allan et al. [4] also compared the results from NTOW and EOM and found similar results when analyzing wave-current interaction off Cape Hatteras, NC. While results between the models were comparable, they both under predicted the RCS modulation due to an under prediction of the scattering due to wave breaking. In a similar study, the model of Romeiser et al. [126] (M4S) was also compared with a NRL model based on Lyzenga and Bennett [93], a formulation similar to EOM, for predicting SAR modulation in the gulf stream with comparisons made to SAR images from the space shuttle [21]. Comparisons to the data show variations less than 0.5 dB with the majority of the field producing variations less than 0.2 dB. Johannessen et al. [67] conducted a study of a range of models that included EOM and the model of [126] (M4S). It was found that similar results were achieved in SAR backscatter due to current shear and convergence/divergence zones as well as the modeling of internal waves. True [148] conducted the most complete model validation of EOM with comparisons made to exact theoretical solutions where linear solutions could be solved when the assumption of small shear is made, code-to-code testing conducted against the SAIC and DTI-SAR models, and finally to experimental data. The results for the theoretical comparison showed some level of numerical diffusion for generally coarser meshes, but this was resolved with increased mesh density. The code-to-code comparisons and comparisons to data showed similar results across codes with good agreement to the experimental data for most cases. Comparisons between codes were made using the perfect SAR mode, where effects due to speckle and instrumentation limitations are neglected as the comparison codes did not include the functionality to predict the full SAR process and simply impose a speckle distribution on the final RCS image.

In the following sections, mechanisms for the damping of surface roughness will be discussed. As the primarily interest here is in the persistent wake, focus is placed on previous research into the long lasting effects of the wake. Research into the hydrodynamics of the persistent centerline wake focus primarily on the effects of surface active substances (SAS) and turbu-

lence. Milgram [96] found that the short wave decay rate due to the presence of both SAS and turbulence was equal to the sum of the decay rates of SAS and turbulence alone, at least for turbulence levels that could be generated in the laboratory. As such, the effects of each are studied in turn. Relevant experimental studies at both laboratory and full scale are discussed along with theory and model formulations.

2.2 Short Wave Dampening by Surface Active Substances

2.2.1 Full Scale Experiments

A significant full scale field study was conducted by the Office of Naval Research to quantify the effect of SAS films on the persistent wake([118]). A range of vessels were used in the experiment with the majority of published data focusing on the USS Chandler (DDG-996), a US Navy destroyer. Ship speeds from 12 knots to 25 knots were used, corresponding to Froude numbers of 0.156 to 0.324. Measurements were taken of surface tension across the wake to identify the location of SAS streaks while overhead SAR data was also collected by aircraft. In situ measurements at the sea surface demonstrated that the streaks in the persistent wake observed in SAR imagery are caused by the redistribution of SAS films, which dampen the short surface waves, reducing their amplitude and thereby locally changing the brightness of the surface imagery. Additionally, the width of the wake was found to be a function of the Froude number as wider wakes were observed with increasing Froude number. Further analysis into the data by Golbraikh et al. [47] found an improved relationship for the downstream wake width by incorporating a Fr^2 term into the self similarity profile. Some level of variability through remained in the analysis. Golbraikh et al. [47] commented that the scatter is most likely due to varying environmental conditions.

An additional full scale field study was conducted by the Naval Research Laboratory, Kaiser et al. [73], where the surface tension in the wake of large commercial shipping vessels were measured as well as axial and transverse surface currents. Similar to the results of Peltzer et al. [118], SAS were found to be compacted along the edges of the wake with regions of reduced surface tension on the order of several meters wide. Surface tension was measured using spreading oils on toothpicks that were dropped into the wake off a trailing vessel. In addition, surface currents were measured by placing floaters in the wake and recording their motion via aircraft. It was found that cross-wake transverse currents were measured that occurred for large ship types and which decayed at a slower rate than the axial velocity ($x^{-5/4}$ vs x^{-2}). The same transverse currents were not easily detected for the smaller research vessels, but significant uncertainty existed for these measurements.

Small scale experiments have also been conducted by Ermakov and Kapustin [35] and Ermakov et al. [36]. Ermakov and Kapustin [35] and Ermakov et al. [36] measured velocity

profiles in the wake of ships using an Acoustic Doppler Current Profiler (ADCP) as well as collected surface samples in the regions of the SAS bands. Ermakov and Kapustin [35] found that slicks did not form directly behind the vessels of interest, but appeared several ship lengths after passage. It was also found that the persistence of the wake was a function of the near-surface wind speeds. As wind speeds increased from 1 – 6 m/s, both the persistence and the width of the wake increased. The rate of growth was found to be consistent across wind speeds, but the duration of the expansion stage was a function of the near-surface wind speed.

2.2.2 Dampening of SAS

The damping effect of SAS is caused by increased viscous damping in the interface boundary layer ([5]). As a wave passes through an area with a surface film, local areas of contraction and expansion form, which generate gradients in surface tension. The elastic stress that is induced by the gradients in surface tension are balanced by shear stresses in the interface boundary layer. This effect occurs over a very thin layer at the surface (O(1mm)) that exists within the viscous sublayer of the free surface boundary layer. Comparing the velocity gradients at the surface with a film layer to a clean surface, Alpers and Hühnerfuss [5] showed an increase of almost two orders of magnitude. This effect is often referred to in the literature as the Marangoni wave damping theory.

The relative damping ratio between a surface with a film and a clean surface is given by

$$\gamma_s = \frac{1 + X\,(cos\theta - sin\theta) + XY - Y sin\theta}{1 - 2X\,(cos\theta - sin\theta) + 2X^2} \tag{2.7}$$

where

$$X = \frac{|E|k^2}{\sqrt{2\omega^3\nu}} \tag{2.8}$$

and

$$Y = \frac{|E|k}{4\omega\nu\rho} \tag{2.9}$$

Here, θ is the phase angle for the complex dilational modulus, $E = |E|exp(-i\theta)$. Alpers and Hühnerfuss [5] studied five different monomolecular slicks and found values of θ between 175-177 degrees. Assuming the phase angle to be approximately 180 degrees, equation 2.7 simplifies to

$$\gamma_s = \frac{1 - X + XY}{1 - 2X + 2X^2} \tag{2.10}$$

This form the equation is used by Da Silva et al. [29] in the study of internal waves passing through ambient slicks. This form of the equation is also reflected, with a modest simplification of the form presented, by Cini and Lombardini [22] under the assumption that the diffusional relaxation time is small.

Milgram et al. [100] offers a variation to equation 2.10, using

$$\gamma_s = \frac{X + XY + 2X^2}{1 - 2X + 2X^2}. \tag{2.11}$$

The film elasticity, E, is related to the film pressure, Π, by

$$E = -A\frac{d\Pi}{dA} = -\frac{d\Pi}{d(ln(A))}. \tag{2.12}$$

Peltzer et al. [118] provides a simplified relationship that is used here based on samples taken from a range of sources from Barger and Klusty [11] as

$$E = \frac{26.3\Pi}{\Pi + 2.4}. \tag{2.13}$$

The relative damping due to SAS for a range of film data for S-Band Brag-resonant waves is shown in Figure 2.2. Data from two days of the ONR Field Experiment [115], January 28 and 29, are shown along with data from Da Silva et al. [29]. The data from the ONR Field experiment is shown using both equations 2.12 and 2.13, while Da Silva et al. [29] uses only equation 2.12. Equation 2.13 returns similar results using data from either January 28 or 29, but differ significantly from those using the theoretical formulation. Equation 2.13 tends to find a smoothed average between the theoretical values from the two data sets. The values from January 29 using equation 2.12 compare reasonably well with those from Da Silva et al. [29] up to SAS concentration ratios around 2 and follow similar trends till concentration ratios of 3. Here, equation 2.13 is primarily used, but comparison is made to the properties from Da Silva et al. [29].

Experimental studies on the short wave dampening of SAS were also conducted by Mass and Milgram [94] and Milgram [96]. Mass and Milgram [94] studied the dynamic behavior of SAS as it was well known that the elasticity of SAS played a critical role in its dampening characteristics, but the impact of wave frequency on the elasticity was not well understood. Studying a range wave frequencies and SAS types, it was found that both the surface viscosity as well as the elasticity's dependency on wave frequency did not significantly impact the dampening characteristics. Application of the Marangoni wave damping theory provided the best agreement with the experimental results when quasi-static values of the elasticity were used along with zero surface viscosity. Milgram [96] applied these findings to compare experimentally measured spatial decay rates with theory. Excellent results were achieved across a frequency range of 3-7 Hz using a range of surface films, providing verification of theory. It should also be noted here the relationship between wave number, elasticity,

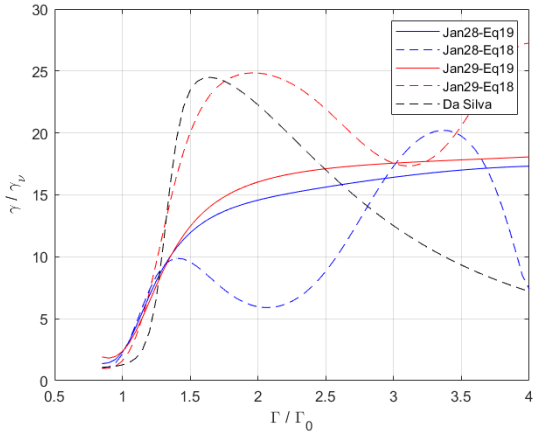

Figure 2.2: SAS damping relative to clean water viscous damping using film elasticity data from [118] and Da Silva et al. [29] at S-Band.

and energy damping. Mass and Milgram [94] showed a variation in the surface elasticity associated with the peak decay rate for water wave frequencies ranging from 0-25 Hz, figure 2.3. Primary interest here is focused on frequencies between 3-11 Hz. At higher frequencies (11 Hz), an inverse relationship between elasticity and decay rate is observed, whereas for lower frequencies (3 Hz), a direct relationship is observed. The curve for an elasticity of $20\,{}^{mN}/_{\mathrm{m}}$ crosses the higher elasticises at a frequency corresponding to S-Band and the curve for an elasticity of $10\,{}^{mN}/_{\mathrm{m}}$ crosses at a frequency corresponding to C-Band. This results in the situation where an elasticity of $10\,{}^{mN}/_{\mathrm{m}}$ at C-Band produces similar damping to $40\,{}^{mN}/_{\mathrm{m}}$ at X-Band. The impact of elasticity and frequency will be further discussed in chapters 5 and 6.

Several sources for the formation and persistence of the observed SAS streaks have been offered. Initial redistribution of ambient SAS in ship wakes has been shown to be caused by hull induced currents and breaking waves from the bow and stern. Peltzer et al. [117] compared overhead imagery of the near wake of DDG-996 along with a model scale destroyer, DD model 5359, and found close agreement between the visible near wake of the ship driving through an ambient SAS field and the model moving through a seeded tow tank. Skop et al. [132] demonstrates that rising bubbles generated in the near wake by the propellers and breaking waves scavenge subsurface SAS and deposits it on the surface with lesser scavenging also possible by upwelling currents. Ship induced bubble clouds have been shown to persist for up to an hour after passage of the vessel, providing a consistent source of SAS to the surface. Peltzer et al. [117], based on the observations of Kaiser et al. [73], suggests that cross-wake surface currents transport the scavenged SAS to the wake edges, reinforcing the already formed initial streaks and widening the width of the wake.

Croot et al. [28] and Wurl et al. [161] have found significant levels of below surface SAS concentrated above the pycnocline where in some cases concentrations were greater within

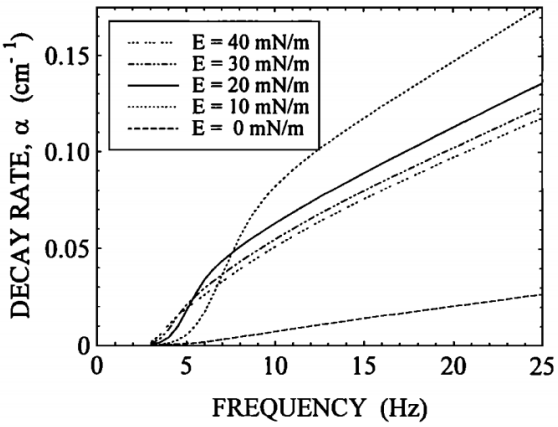

Figure 2.3: Impact of water wave frequency and surface elasticty on wave energy damping. Mass and Milgram [94]

the water column than on the surface, Figure 2.4. Peak values of SAS around 60m depth were observed on most days in the study of Croot et al. [28], but with variations in the magnitude and distribution throughout the remaining water column. Wurl et al. [161] observed similar variation in the location of maximum subsurface SAS with depths ranging from 20-150 m.

These surface active substances are found to be comprised of amino acids, proteins, fatty acids, lipids, phenol, and additional organic compounds that are usually monomolecular with hydrophilic heads and hydrophobic tails. This orientation stands SAS molecules on end once deposited on the free surface and resists desorption back into the bulk fluid. The largest source of these organic materials are from phytoplankton as part of their metabolic process and decay [87, 94, 161, 165]. The distribution of phytoplankton within the water column therefore directly influences the distribution of subsurface SAS. The level of phytoplantkon production tends to be seasonal and is highly dependent on location,(Gašparović and Ćosović [45], Weston et al. [158]), leading to a seasonal variation in the levels of ambient SAS within the water column.

2.2.3 Surface Currents

Several authors have offered explanations for the mechanism responsible for the formation of SAS redistributing surface currents. The most prominate theories are swirl generated by propellers [42, 150]; hull–induced transverse currents; and flow generated by rising bubbles [36, 115]. Lyden et al. [88] suggested that the surface currents are generated by twin bilge vorticies that shed off the hull based on studies by Swanson [142]. In the case of a displacement vessel, a down force is generated by flow acceleration under the hull. The formation of this down force, or negative lift, is accompanied by generation of circulation which must be shed as a vortex pair. This vortex pair is predicted to generate outboard surface currents

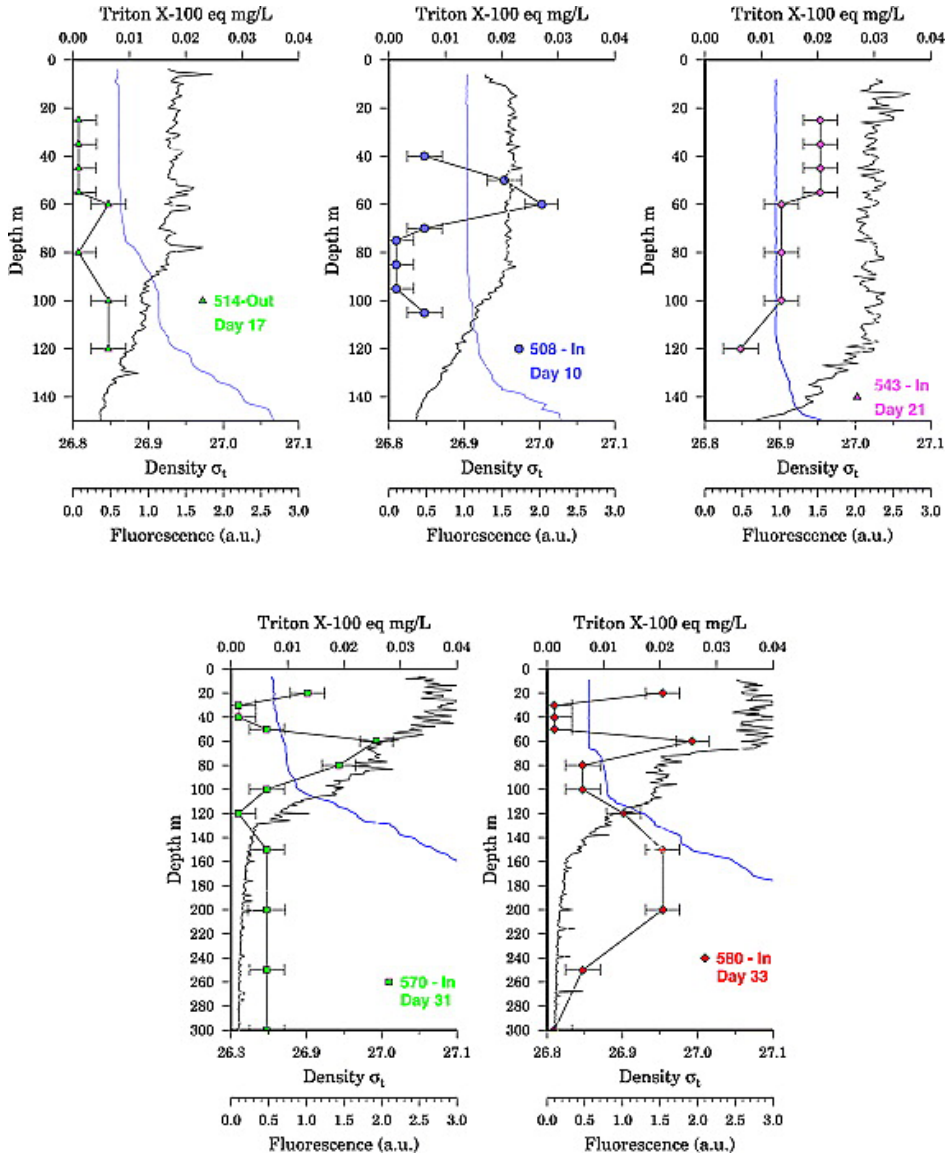

Figure 2.4: Distribution of SAS, density, and florescence within the water column over a 2 week period. SAS-symbols, density-blue line, florescence-black line. (Croot et al. [28])

on the order of O(1 cm/s) 1km aft of a 5000 ton ship and 10km aft of a 500,000 ton vessel. The presence of such features in the near wake, however, has been found to be highly ship dependent. Johnston and Walker [71] studied the near wake of a 1/12 scale model of the U.S. Navy fleet tug Quapaw, which has been used extensively in full scale ship wake research. While a consistent transverse surface current was observed, no evidence was found of hull induced vorticies that would impact the surface. Hoekstra and Aalbers [59] performed an experimental study with 9 ships: 3 tankers, 3 container ships, and 3 frigates, and found the ability to detect hull induced vorticies in the near wake to be dependent on stern shape and propulsion type. Not all towed hulls were found to generate hull vorticies, and of those that did, the inclusion of propellers and rudders often complicated the flow field sufficiently to render the presence of a structured hull induced vortex in-perceivable. Towing–tank experiments reported by Swean [143] show the formation of a pair of secondary inward rotating vortices with outward rotating propellers that are speculated to be shed from the hull or induced by the propeller swirl, but the same secondary vortex pair is not observed with inward rotating propellers. Computational simulations of the U.S. Navy ship model 5415 with outward rotating propellers, relative to surface centerline, by Hyman [63] and Stern et al. [139] also show the formation of secondary induced circulatory motions that rotate inward in agreement with the experimental findings of Swean [143]. The circulations that can be attributed to the redistribution of SAS to the wake's outer edges, however, must be outward rotating. Kaiser et al. [73] also found that smaller planning vessels, which generate positive lift, did not generate circulations opposite to those of the larger displacement hulls as was expected based on Swanson [142].

Anthony and Willmarth [8] and Walker et al. [156] experimentally studied the formation of surface currents due to near surface free shear flows over a range of Reynolds numbers (Re=UD/ν) and Froude numbers (Fr=U/$\sqrt{gD}$). It was found that a surface current transverse to the direction of a near surface turbulent jet formed due to the Reynolds stress anisotropy induced by the free surface. In low Froude number conditions ($Fr = {}^{U}/_{\sqrt{gD}} = 1$), i.e. flat free surface, the vertical stresses are damped at the surface with their energy redistributed to the horizontal normal components. This effect is limited to a thin surface layer, approximately equal to the diameter of the jet, Figure 2.5. In the case of low Froude number, the free surface fluctuations (η') are much smaller than the vertical length scale (δ) such that the flat free surface boundary condition requires ${}^{\partial\overline{U}}/_{\partial z} = {}^{\partial\overline{V}}/_{\partial z} = 0$ (ie. no shear) at the surface. Based on an order of magnitude analysis by Walker et al. [156], to the first order, the y-momentum Reynolds Averaged Navier Stokes (RANS) equation reduces to:

$$\overline{U}\frac{\partial V}{\partial x} + \overline{V}\frac{\partial V}{\partial y} = \frac{\partial}{\partial y}\left(\overline{w^2} - \overline{v^2}\right). \tag{2.14}$$

Walker [155] demonstrates that it is the departure from isotropy that drives the surface currents as a function of $\left(\overline{w'^2} - \overline{v'^2}\right)$, where w' and v' are the vertical and transverse velocity fluctuations. This work also provided a slightly simpler explanation for the formation of the transverse surface currents compared to Launder and Rodi [83]. There it was suggested that

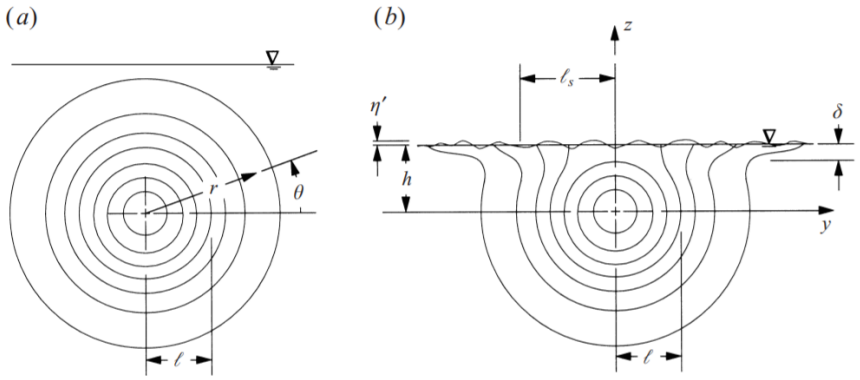

Figure 2.5: Schematic of the streamwise velocity of a deep turbulent jet (a) and a turbulent jet near the free surface (b). (Walker [155])

the currents were due to the production of streamwise vorticity. This process would require the presence of both horizontal and vertical Reynolds stress gradients. Walker [155] suggests that the only requirement for the formation of surface currents is the lateral Reynolds stress gradient.

Ramberg et al. [123] and Swean Jr et al. [144] studied the case of a turbulent plane jet issued directly beneath the free surface where the vertical Reynolds stresses were redistributed to the horizontal components with increasing anisotropy with increasing downstream distance. Miner et al. [101] performed numerical studies of the same experiments using a modified algebraic turbulence model and achieved reasonable correlation with the experimental data through the use of a Reynolds stress redistribution model, supporting the hypothesis of Walker [155] that the surface currents can be reproduced simply through the redistribution of the Reynolds stresses.

The previously discussed experiments all used conditions where the surface of the water was free of contaminants. In a real ocean environment, the surface can be covered with films as discussed in the previous section. Anthony et al. [9] experimentally studied the influence of a surface film on a near surface turbulent jet at Fr=5.7 and found that in the case with a surface film, the significant lateral spreading and transverse currents were reduced compared to the clean surface condition. It was hypothesized that the presence of the surface films induces the production of secondary vorticity parallel to the surface just beneath the film layer which allows for turbulent mixing normal to the surface. In the case of a clean surface, vortex filaments connect to the free surface as observed in medium/high Froude number cases, which aligns these filaments normal to the surface and prevents effective turbulent mixing normal to the surface.

Shen et al. [127] used DNS to study the impact of surface films on a turbulent shear flow and found the redistribution of the Reynolds stresses to be primarily reduced due to the elasticity of the surface film. As the elasticity of the surface film is able to support shear stresses, the

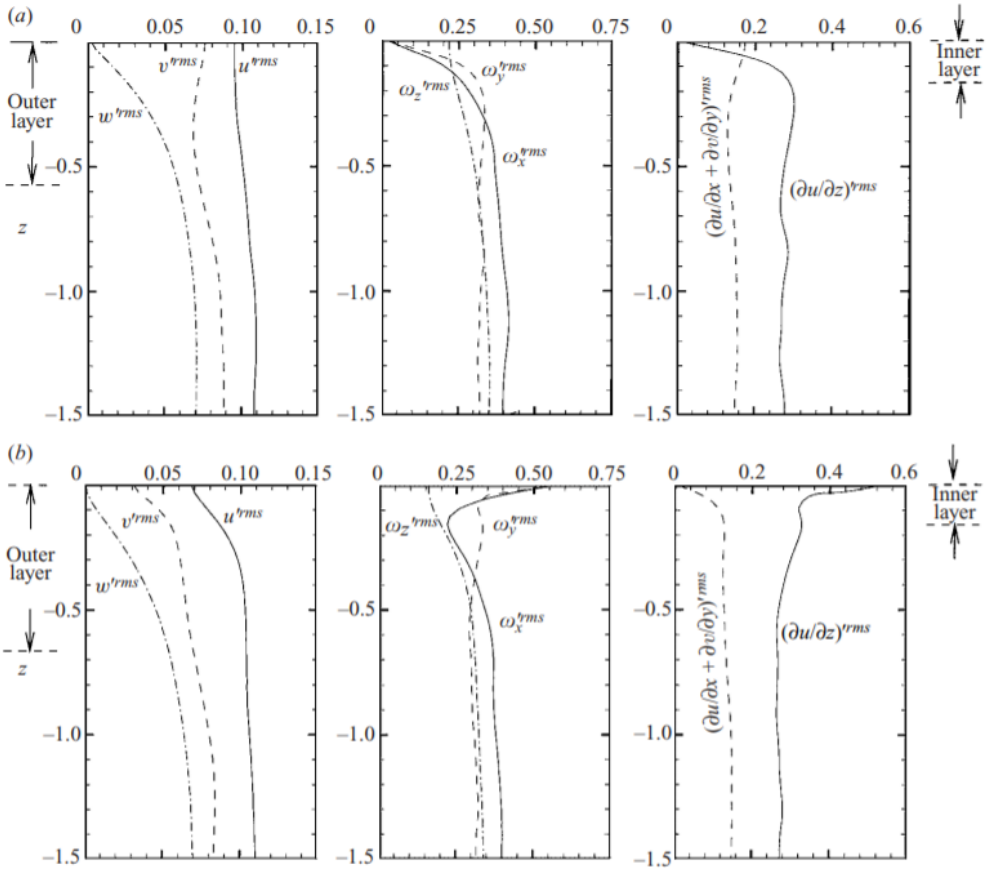

Figure 2.6: Vertical profiles of velocity fluctuations, vorticity components, and vertical velocity gradients for shear flow issuing under a clean free surface (a) and a contaminated free surface (b). (Shen et al. [127])

shear-free boundary condition in the case of a clean surface no longer applies. Turbulent kinetic energy (TKE) at the surface is partially absorbed by the elasticity of the surface film with reductions observed in both u and v velocity fluctuations. McKenna [95] found that the TKE at the surface in the presence of surface films was half that of a clean surface. Shen et al. [127] showed that the presence of surface films also significantly increases streamwise and tangential vorticity at the surface, both of which go to zero for a clean surface due to the surface boundary conditions, Figure 2.6. As the surface film can support shear stresses, $\partial u/\partial z$ and $\partial v/\partial z$ significantly increase approaching the surface, giving rise to the horizontal vorticity components. This result supports the conjecture of Anthony et al. [9] of the formation of surface parallel vorticity. The mechanism reducing near surface fluctuations can further be observed through the impact on the TKE budget. It was observed that as the contaminated surface is approached the terms in the pressure strain correlation, which are responsible for the transfer of turbulent energy from the streamwise component to the vertical and tangential, are reduced as the velocity fluctuations are all reduced. The elasticity of the surface film increases turbulent dissipation and viscous diffusion while reducing turbulent production and transport. The turbulent dissipation rate, ε, though is substantially increased due to the increased surface tangential stresses. The impacts of a surface film were observed to occur for even low concentrations, but with increasing effect as the concentration increases.

Basovich [13] also described a mechanism for the generation of large scale circulations in a ship wake. It was shown that such circulations are produced by the interaction of a near–surface current with ambient surface waves as displayed in Figure 2.7. The current induces near surface vorticity which interacts with the ambient surface waves and generates a form of the Craik-Leibovich (CL) vortex force. A full derivation of the CL vortex force is provided in Appendix A. These circulations are similar in nature to Langmuir circulations, which are generated by the interaction of wind induced vorticity with ambient surface waves [14, 26, 43, 81, 140]. Langmuir circulations (LC) are formed near the sea surface as a result of an instability of the wind–driven surface current interacting with the surface waves. The non–uniform structure of the current in that case is due to the instability of the developing current. In contrast, the circulations described by Basovich [13] are generated around a non–uniform current introduced by an external source, such circulations are referred to as Langmuir–type circulations (LTC). The characteristic scales of the resulting circulations are larger than the transverse scale of the current itself. Basovich [13] found the distance from the center of a surface jet to the point where the horizontal velocity reduced by an order of magnitude from its peak, to be approximately three times the horizontal characteristic length scale of the initial current after only 60 seconds. The size of the circulations were found to be relatively independent of the ambient wave field's wavelength, while the maximum horizontal surface velocity was a function of both the wavelength and current characteristic length scale as $v_m \propto \frac{\sqrt{\lambda}}{a}$, where λ is the wavelength and a is the horizontal characteristic length scale. Using a characteristic horizontal length scale of 20m, which would be a reasonable ship beam, and an ambient wavelength of 10m, maximum surface currents over 1 cm/s were predicted after 60 seconds and grew linearly with time. Generation and development of LTC were

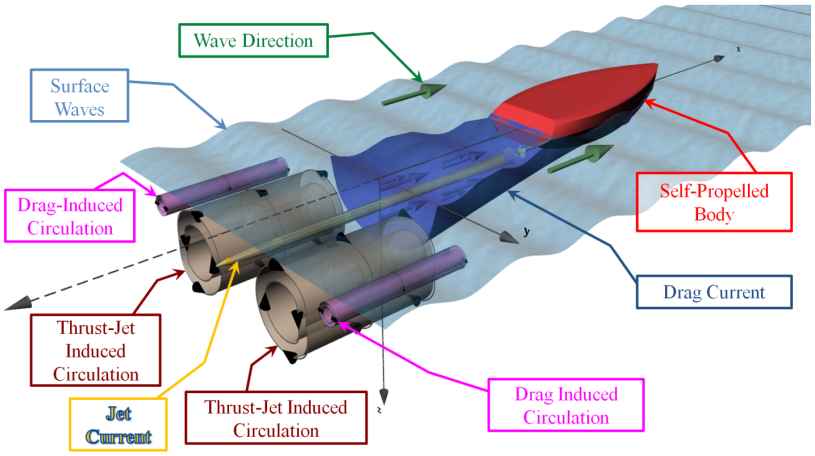

Figure 2.7: Schematic of the formation of Langmuir-type circulations. Used with permission of [25].

studied using an idealized model of low eddy viscosity, and the effect of viscosity on both the initial current and LTC was neglected. Three types of currents were considered: a near–surface jet, a near–surface shear current and an underwater jet. It was demonstrated that the intensity of LTC can be significant under realistic assumptions regarding the magnitude of the initial current and amplitude and wavelength of the ambient surface waves. In the case of the near–surface jet, Basovich [13] predicted the formation of twin counter-rotating circulations near the surface and symmetric about the jet centerline. The magnitude and sign of the vortex force depends on the cosine of the angle between the directions of the current velocity and the propagation of the surface waves Craik and Leibovich [26]. In the case when the current and ambient wave field propagate in the same direction, the LTC induce an outboard current at the surface. As expected, in the case when the current and ambient wave field propagate opposite one another, an inboard current is generated with a convergence zone along centerline.

2.3 Short Wave Damping by Turbulence

Short wave dampening by turbulence has been studied both experimentally and theoretically by several authors with a variety of models resulting. A theoretical framework established by Boyev [16] suggested that surface wave energy is convected downward and dissipated into the bulk fluid below by vertical velocity fluctuations. Kitaigorodskii and Lumley [76] and Kitaigorodskii et al. [77] further refined the mathematical description of this process by deriving a system of equations for the below surface turbulent boundary layer and a

wave-turbulence interaction term that appears in the turbulent energy equations as

$$\frac{1}{2}\langle\left(u^w\right)^2 u_3'\rangle \tag{2.15}$$

where u^w is the wave velocity and u_3' is the vertical velocity fluctuation.

Ölmez and Milgram [111] experimentally studied the damping of short periodic waves by grid generated turbulence in waves generated by an axisymmetric plunging wave maker considering the arguments of Boyev [16] and Kitaigorodskii and Lumley [76]. In addition to surface elevation, horizontal velocity fluctuations were measured to establish the turbulence spectra for various grid oscillation heights and frequencies. Kitaigorodskii and Lumley [76] outlines that the damping effect of turbulence is due to the vertical velocity fluctuations, u_3'. Ölmez and Milgram [111] approximate the vertical velocity fluctuations as a function of the horizontal fluctuations, the integral length scale, and the depth to derive an expression for the turbulent decay rate, γ_t, as a function of the horizontal velocity fluctuations, u_1', the integral length scale, L_1 , and wavelength of the short waves, λ

$$\gamma_t = 0.103\frac{u'}{L_1^{\frac{1}{3}}\lambda^{\frac{2}{3}}} \tag{2.16}$$

There is significant scatter in the data. Data presented by Skoda [131] is also included in the data analysis, but only adds to the scatter. The data of Ölmez and Milgram [111] shows a general trend in line with equation 2.16. These findings generally supported the argument that the dominate mechanism for turbulence induced wave decay is vertical mixing as the wave amplitude was not observed to be a key contributor.

Milgram [96] conducted an additional experiment using grid generated turbulence with waves induced by an oscillated vertical wedge. In this experiment, the horizontal and vertical velocity fluctuations and integral length scales were measured. General trends in the data are clear, but again significant scatter exists in both the measurements for the velocity fluctuations and the integral length scales. Applying equation 2.16 to the averaged data provided good agreement with the measured wave spatial decay rates. Milgram [96] notes that equation 2.16 is approximate to the extent that $u_1'/L_1^{\frac{1}{3}}$ is approximate, but the agreement with the data supports its validity. In addition, the combined damping due to turbulence and SAS was experimentally tested by Milgram [96]. The increase in damping due to turbulence was small compared to SAS, but agreed well with measured data, figure 2.8.

Teixeira and Belcher [146] developed a model based on Rapid Distortion Theory where kinetic energy is transferred from the wave to turbulence by the tilting of vertical vorticity by Stokes drift. This tilting leads to stretching and the formation of elongated streamwise vorticies. The tilting of the vertical vorticity also generates a shear stress, which acts as an energy sink for the wave. A model describing the energy transferred from the wave to turbulence was established based on an order of magnitude scaling analysis as

$$\gamma_t = a\left(\frac{u'}{c_w}\right)^2\sigma_w \tag{2.17}$$

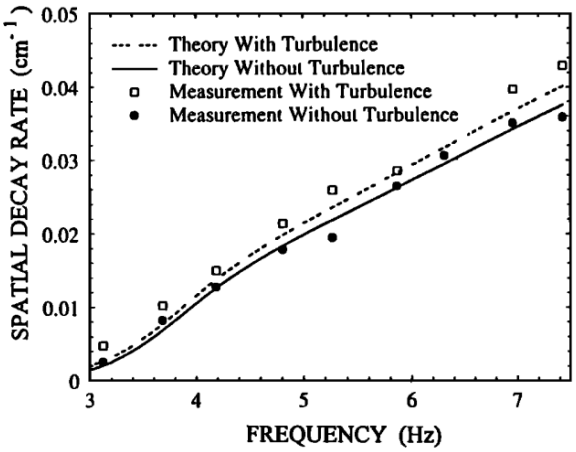

Figure 2.8: Comparison of wave decay rates due to SAS on seawater with and without induced turbulence. SAS collected from Hampton, NH. Milgram [96]

where u' is the velocity fluctuation, c_w is the phase velocity of the wave, σ_w is the frequency of the gravity–capillary wave, and a is a non-dimensional constant taken as a=0.6 based on a best fit to the data of Ölmez and Milgram [111]. Comparisons are made against the data of Ölmez and Milgram [111] and Skoda [131] where the author claims similar levels of agreement as the model of Ölmez and Milgram [111], equation 2.16. Lower values of $(u/c_w)^2 \sigma_w$ show reasonable correlation with equation 2.17, but higher values are significantly over predicted, while equation 2.16 maintains correlation throughout the data set. It is interesting to note that Teixeira and Belcher [146] also shows that the effect on near surface Reynolds stresses and turbulent length scales due to the vorticity distortion by Stokes drift are similar to those of Langmuir turbulence. This suggests another potential source for the formation of Langmuir circulations in addition to the well studied shear-current instability of Craik and Leibovich [26].

Ermakov et al. [37] performed an additional experiment using a tank on a vibrotable with a stationary perforated plate to generate both surface waves and turbulence. Unlike previous experiments, waves generated here were not periodic, but random in nature. The table was oscillated using a two-frequency operation. Small amplitude, relatively high frequency oscillations generated gravity-capillary waves while larger amplitude, low frequency oscillations excited turbulence. A correlation was made based on short wave damping due to molecular viscosity, $\gamma = 2\nu k^2 + \sqrt{\frac{\nu\omega}{2}}\frac{2}{a}$. The damping due to turbulence in the tank was described as

$$\gamma_t = 2\nu_T k^2 + \sqrt{\frac{\nu_T \omega}{2}}\frac{2}{a} \tag{2.18}$$

where the first term describes the damping of waves on the surface and the second term describes damping by the tank walls. Here k is the wave number of the surface waves, ω is the wave frequency, and a is the width of the tank. The damping coefficient was directly measured, allowing for the calculation of ν_T from the experimental data, assuming equation

2.18 to be valid. Comparison of equation 2.18 to the data of course had good agreement as the values of the eddy viscosity, ν_T, were calculated from the data. Comparison of equations 2.16 and 2.17 were shown to under predict the data. Of the two models, Equation 2.17 showed better agreement with Ermakov et al. [37].

DTI developed a model on the dissipation rate due to turbulence using similar assumptions as Ermakov et al. [37] where a direct analogy is made between molecular viscosity and turbulent viscosity and Kolmogorov's law is invoked. A formulation similar to equation 2.16 was derived, but with a damping rate constant about 100 times greater. The primary source for the discrepancy comes from the use of Kolmogorov's law, which assumes turbulence is isotropic. Ölmez and Milgram [111] found the turbulence to be anisotropic, which is also supported by Anthony and Willmarth [8] and Walker et al. [156].

In addition to experimental studies, George [46] studied the impact of turbulence in the wake of a submerged half-sphere using direct numerical simulation (DNS). This study used a Reynolds number of 1000 as the application of DNS to full scale Reynolds numbers (10^9) is not computationally achievable. Only surface velocity profiles were used from the DNS experiment, limiting the resolvable scale to 0.25 m. Sub-scale models such as those previously described were not implemented, limiting the full impact of turbulence on the model. Despite this assumption, it was found that S-Band radar (3.1 GHz) produced the greatest modulation to the normalized radar cross section (NRCS) relative to the ambient environment. L-Band radar (1.2 GHz) demonstrated higher sensitivity to surface currents in line with the radar look direction and higher frequencies (C & X-Band) demonstrated high sensitivity to current gradients. It was also found that peak modulation occurred for lower wind speeds O(2 m/s) where the wind was in line with the transverse surface currents.

True et al. [149] evaluated the impact of turbulence on the RCS modulation 1000m behind a simulated surface combatant using the model of Milgram et al. [100], figure 2.9. This simulation also included the effects of surface currents and wind, but did not include dissipation due to SAS. It was observed that a distance of 1000m, turbulence is the primary mechanism for RCS modulation while surface currents added fine structure to the wake.

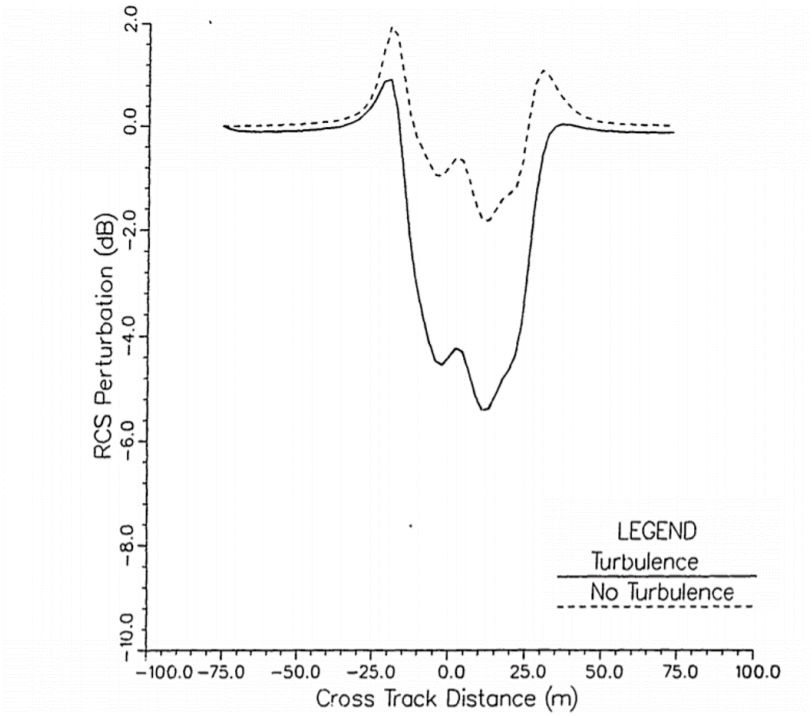

Figure 2.9: Simulated RCS in the wake of a surface combatant 1000m downstream with and without turbulent damping. Used with permission. (True et al. [149])

Chapter 3

Structure and Persistence of Ship Wakes and the Role of Langmuir-Type Circulations

(Work adapted from Somero et al. [135].)

3.1 Introduction

It is well known that some features of ship wakes can be observed well after the passage of the ship, in some cases tens of kilometers behind the vessel. This chapter addresses a physical mechanism for the formation and resulting structure of such long–lasting ship wakes, and describes their qualitative and some quantitative features.

There are several hypotheses considered by different authors regarding the nature of the surface currents in the region of the persistent wake as discussed in chapter 2. The more frequently suggested mechanisms for the generation of these surface currents until now have been: swirl generated by propellers [42]; hull–induced transverse currents; and flow generated by rising bubbles [36, 115]. However, these mechanisms cannot explain the observed persistent–wake features. The swirl produced by the propellers decays relatively quickly as demonstrated in this paper by direct simulations, and thus cannot induce the long–lasting surface currents that can cause the persistent wake. Also as discussed in chapter 2, measurements of the hull–induced transverse currents have not consistently shown persistent circulatory motions that would redistribute SAS to the wake edges. Lastly, flows generated by rising bubbles in the wake of the ship are even less studied, and descriptions of the mechanism of their generation are more the result of speculation than of experimental measurement. The magnitude of bubble–induced fluid velocity, in the case of a reasonable concentration of bubbles, can be expected to be extremely small.

Here, we investigate the impact on the persistent wake by surface currents induced by Langmuir-type circulations, which were first suggested and described by Basovich [13]. The work of Basovich [13] was limited to the initial formation of LTC as persistence could not be well quantified under the assumptions of zero viscosity. In addition, only simple geometric currents were considered in the previous work. In reality, the structure of the current pro-

duced by a self–propelled ship is more complex than a simple jet, and the current evolves and decays due to the presence of the strong ship–generated turbulence. At a minimum, the ship–induced current consists of a propeller–generated thrust current directed away from the ship and a drag current with flow in the direction of the ship motion (e.g., [57, 112]). It is shown in this chapter that, in general, there are four circulations produced due to the interaction of the complex ship–induced currents with surface waves, as shown in Figure 2.7. The resulting system of circulations is unlike the case of a pure jet where only two circulations are generated [13]. The velocity of the initial ship–induced current system decreases with time (and distance from the ship) due to the effect of ship–generated turbulence on the current. Thus, the development of LTC due to interaction of the current with the ambient surface waves takes place only for a limited time interval. During the time that the LTC develops, the turbulence generated by the ship decays and eddy viscosity decreases. Therefore, LTC can persist for a long time (and distance) after the passage of the ship. All these features of the persistent wake are analyzed in the present paper. It is demonstrated that the structure of the persistent ship wake depends not only on the current produced by the ship, but also on the surface–wave amplitude and direction relative to the course of the ship. Under some conditions, the persistent wake may not develop at all. In short, the persistent wake results from the generation of a secondary flow in the form of LTC due to interaction of a ship–generated thrust– and drag–current system with the ambient surface wave field.

This chapter is structured as follows. This section presents the statement of the problem. The next section presents the modeling approach and a description of the numerical algorithms employed in the simulations. Then the structure of the ship–generated flow field, or system of thrust and drag currents, is described for a particular ship configured to model the naval surface combatant used in the at–sea experimental study of Peltzer [115]. This ship–generated current system represents the near wake, which is used as the input for CFD simulations of the development of the wake. Some general features of the current system are also discussed. Simulations of the wake evolution in the absence of an ambient surface wave field are described. Then, simulation results, including LTC, for the two general cases of head and following seas are presented. Existence of the centerline and railroad–track persistent wakes are explained. The effect of LTC on the redistribution of the SAS film at the surface is discussed, and a comparison of theoretical results with available experimental data is provided. Results and further required work are also discussed.

3.2 Model formulation

The formulation of the numerical modeling is based on the goal of simulating wakes that are generated by ships operating in realistic oceanic conditions. This approach stands in contrast to much of the previous work, which has focused on simple towed or self–propelled vehicle geometries at model–scale Reynolds numbers under highly–stratified laboratory conditions [17, 20, 31, 32, 48, 57]. We employ an extensible computational framework that can include

initial conditions specified from geometry–resolving simulations or theoretical models; that can incorporate many types of oceanic forcing; and that is capable of spanning the length and time scales of interest. While our approach is general, we will limit the discussion to the models, methods, and parameters used for the simulations presented herein. To begin, we assume that a ship with length $L = \mathcal{O}(100)\,\mathrm{m}$ is traveling with velocity $U_0 = \mathcal{O}(10)\,\mathrm{m/s}$ in an Earth-fixed frame of reference and generates a persistent wake with length of $\mathcal{L} = \mathcal{O}(10)\,\mathrm{km}$. The Cartesian coordinate system $x_i = (x_1, x_2, x_3) = (x, y, z)$ is aligned such that x is the downstream direction, y is the cross–wake direction, and z is the upward direction with its origin at the ocean surface. For seawater with a kinematic viscosity of $\nu = 10^{-6}\,\mathrm{m^2/s}$, the corresponding Reynolds and Froude numbers are $Re = U_0 L/\nu = \mathcal{O}(10^9)$ and $Fr = U_0/\sqrt{gL} = \mathcal{O}(0.3)$.

3.2.1 Governing equations

The governing equations are described by the conservation of mass and linear momentum for an unsteady incompressible flow. The model is formulated to include oceanic forcing from current–wave interaction through the Craik–Leibovich (CL) vortex force, originally derived based on time averaging the vorticity transport equation [26] and later by applying the Generalized Lagrangian Mean [7] to the conservation of mass and momentum equations, see Appendix A. This time averaging is applied assuming that the characteristic time scales are long relative to the average wave period, but short relative to the time of formation of the ship induced current. This requirement suggests that application of the CL vortex force is only appropriate once the axial velocity gradients of the ship induced current have become small, delaying the time and distance behind the ship for where the influence of the force can be observed. This requirement also suggests that it would not be appropriate to include the vortex force in near field simulations of the ship hydrodynamics where the initial wake field is under formation.

Here we assume that contributions due to Coriolis acceleration and Ekman forcing are small in comparison to the Craik-Leibovich vortex force. Jones and Paterson [72] demonstrated that in low wind conditions, Ekman forcing is negligible and in conditions of moderate sea state, Ekman forcing plays a secondary role to Langmuir–type circulations. Contributions by Coriolis acceleration are considered small here as the characteristic width of the wake is O(100m).

While our simulation toolkit accommodates large–eddy simulation, the length and time scales of interest dictate that unsteady Reynolds averaging be used to model the effects of turbulence. Decomposing the instantaneous velocity field into moving mean U_i and fluctuating u_i' components, i.e., $u_i = U_i + u_i'$, and taking the time–average gives the following mathematical model

$$\frac{\partial U_j}{\partial x_j} = 0, \tag{3.1}$$

$$\frac{\partial U_i}{\partial t} + \frac{\partial (U_i U_j)}{\partial x_j} = -\frac{1}{\rho_0}\frac{\partial \hat{p}}{\partial x_i} + \nu \frac{\partial^2 U_i}{\partial x_j \partial x_j} + \frac{\partial}{\partial x_j}\overline{u_i' u_j'} + \frac{\Delta\rho}{\rho_0} g_j \delta_{ij} + \epsilon_{ijk} U_j^{St} \omega_k, \tag{3.2}$$

where $\hat{p} = \overline{p} - \rho_0 g z$ is the mean piezometric pressure, $\overline{p}$ is the mean total pressure, g_j is the gravitational vector (which is assumed to be pointing downward in the negative z direction), ν is the kinematic viscosity, δ_{ij} is the kronecker delta, $\omega_k = \epsilon_{ijk}\frac{\partial U_i}{\partial x_j}$ is the mean fluid vorticity, ϵ_{ijk} is the permutation tensor for defining the cross–product in tensor notation, and U_j^{St} is vector of the Stokes–drift velocity generated by ocean waves.

In the context of the unsteady Reynolds-averaged Navier-Stokes (URANS) equations, we are forced to assume that the resolved unsteadiness in the simulation is sufficiently removed from the period over which mean variables are averaged. Flows considered here have Reynolds numbers on the order of 10^9, such that there is a considerable variation between viscous scales and integral scales with a time scale ratio(f_L/f_ν) of O(10^4). Characteristic Kolmorgorov length scales are on the order of $10^{-5}m$, while characteristic integral length scales are on the order of $1m$. To compute the Reynolds stresses $\overline{u_i' u_j'}$, we use the standard eddy–viscosity model $-\overline{u_i' u_j'} = 2\nu_t S_{ij} - \frac{2}{3}k\delta_{ij}$, which is a linear closure relating the Reynolds stresses to the mean rate of strain $S_{ij} = \frac{1}{2}\left(\frac{\partial U_i}{\partial x_j} + \frac{\partial U_j}{\partial x_i}\right)$.

The last term in equation (3.2) is the Craik–Leibovich vortex force (normalized by water density) that results from current–wave interaction. It is a function of the Stokes–drift velocity produced by the surface waves. For the work here, we consider monochromatic surface waves in deep water. In this case, a magnitude of the Stokes–drift velocity can be written as

$$U^{St} = \left(2\pi\frac{a_s}{\lambda}\right)^2 \sqrt{\frac{g\lambda}{2\pi}} \exp\left(4\pi\frac{z}{\lambda}\right), \tag{3.3}$$

where a_s is the wave amplitude, λ is the wave length. The Stokes–drift velocity vector is horizontal and has only two components: $U_x^{St} = U^{St}\cos\theta$ and $U_y^{St} = U^{St}\sin\theta$, where θ is the angle between the Stokes–drift velocity and the direction of the ship–produced current (x axis).

In order to better understand generation of LTC in a ship wake and the results of numerical simulations presented in this chapter, it is instructional to look at the components of the vortex force. Here we consider the vortex force for a case of two–dimensional current, which is a basic case for all further analysis, with velocity $U(y,z)$ in x direction that is a function of y and z coordinates. For this case components of the vortex force corresponding to the last term in equation (3.2) are

$$F_x = -\rho_0 U_y^{St}\frac{\partial U}{\partial y}, \quad F_y = \rho_0 U_x^{St}\frac{\partial U}{\partial y}, \quad F_z = \rho_0 U_x^{St}\frac{\partial U}{\partial z}. \tag{3.4}$$

Horizontal and vertical components of the vortex force, F_y and F_z, transverse to the current velocity are responsible for generation of the circulations. The component F_x will affect the velocity of the initial current. The transverse components, F_y and F_z, are proportional to the x component of the Stokes–drift velocity and the gradient of the current velocity in the direction of that component. The presence of a non–uniform gradient in the initial current, e.g., from a practical ship wake, produces a non–uniform vortex force field which in turn will generate the circulations. The value of the angle θ between the ship trajectory and the wave direction is of critical importance. Clearly, the magnitude of F_y and F_z and corresponding rate of growth of the LTC will be maximum when the Stokes–drift velocity is parallel or anti-parallel to the direction of the current; $\theta = 0$ or $\theta = 180°$. In the case of a 180° change in ship course, the vortex force and resultant circulations will change sign and direction of rotation, respectively. For waves orthogonal to the ship track ($\theta = 90°$), the transverse components of the vortex force are zero, and we could therefore expect the current–wave interaction to vanish. At the same time the F_x component of the vortex force disappears for the cases of $\theta = 0$ or $\theta = 180^0$ and its effect on the initial current is negligible. Therefore, in this study we focus on the two cases of head seas and following seas.

3.2.2 Computational approach

While the governing equations are fully unsteady and three dimensional, simulation over both multiple hours of time and sufficiently large domains, while resolving centimeter–scale gradients, is not tractable with current–generation supercomputers. Therefore, we use a "two–dimensions plus time" (2D+t) approach, where the three–dimensional problem is reduced to two spatial dimensions, under the assumptions that the wake is slowly evolving in the axial direction, and that characteristic scale of the change of wake parameters (such as velocity and turbulent kinetic energy) in the direction of the wake is much larger than the characteristic width of the wake. In addition, application of the CL vortex force requires that the time scale for formation of the current is long compared with the period of the surface waves. These conditions are satisfied if the ship speed is much larger than both the axial defect velocity and the transverse velocity perturbations, which is always the case for a fast–moving ship.

The computational mesh is designed and the boundary conditions are selected to force axial gradients to zero, and therefore facilitate 2D+t simulations in an otherwise fully–general CFD solver. This is accomplished by using periodic boundary conditions in the axial x direction, and constructing a mesh which is only one–cell thick in that direction. Wakes therefore evolve in both time and in the (y, z) crossplane directions. Assuming that the ship is traveling at a constant speed U_0, the x–coordinate location in the evolving wake can be reconstructed from the simulation time as $x = U_0 t$.

The computational domain is a rectangular parallelepiped, with dimensions, in meters, of $-500 < y < 500$ and $-500 < z < 0$. Mesh resolution is approximately 0.3 m with mesh

density clustered near the ship and coarsening in the far field, with a total mesh size of 2,200,000 cells. Time-stepping is set to $\Delta t = 1\,\mathrm{s}$ and simulations are conducted over a period of 1 hour. The $x = 0\,\mathrm{m}$ position is set as the initial data plane (IDP) and, so as to not violate the assumptions of the 2D+t approach, is located beyond the rapidly evolving near wake. In a classical shear–flow, this would be at the point where asymptotic behavior begins. For practical reasons, we assume this location to be about one–half of a ship length downstream from the stern.

3.2.3 Numerical scheme

Solution of the governing equations is achieved using the segregated pressure–implicit split–operator (PISO) algorithm [65]. In this approach, the equations are sequentially solved, and the nonlinear advection term is linearized with velocity from the previous time step. In our solver, the order of solution within a time step is as follows: 1) compute density given the temperature, salinity, and pressure fields from the previous time step; 2) solve the momentum equations for the velocity field, but with pressure from the previous time step; 3) iteratively solve the pressure–Poisson equation and velocity–field correction to enforce mass conservation; 4) solve the turbulence–model equations. The process is then repeated for each time step over the simulation.

The governing partial–differential equations are discretized using a cell–centered finite–volume method, which makes use of the Gauss–Green theorem which states that the surface integral of a scalar function is equal to the volume integral of the gradient of the scalar function. Gradients at the cell faces are computed using weighted interpolation between the adjacent cell centers.

To limit numerical dissipation, a second–order energy conserving scheme was used for the divergence operator in the advection term of equation 3.2. Detailed studies were undertaken to properly select parameters that balance accuracy and stability, and to demonstrate over long time integration that the prescribed kinetic energy, in the absence of turbulent eddy viscosity, could be maintained. The scheme blends 2nd-order linear interpolation with a small amount of upwinding, and additionally applies a filter to eliminate high–frequency ringing. All viscous Laplacian terms were discretized with a second–order linear scheme. The time derivatives were discretized with a second–order backward finite difference.

The resultant algebraic system of equations are solved using iterative schemes. The momentum and scalar–transport equations are solved using a pre–conditioned bi–conjugate gradient (PBiCG) scheme, with absolute and relative convergence criterion of 10^{-8} and 10^{-5}, respectively. This means that the solution residuals must be less than 10^{-8} or be reduced 5 orders–of–magnitude over the iteration process. The pressure-Poisson equation is solved with a generalized algebraic multi-grid (GAMG) scheme, with absolute and relative convergence criterion of 10^{-5} and 10^{-3}, respectively. For the pressure–velocity coupling in the PISO algorithm, two iterations are used; and since the mesh is perfectly orthogonal, zero

non–orthogonal correctors are required.

To support our analysis, data is extracted from the simulations. Locations of data extraction include one–dimensional lines on the ocean surface in the y–direction at every time step, where time t can subsequently be converted to x so that (x, y) ocean–surface contour maps can be created. In addition, the entire (y, z) cross plane is saved at various points in time that correspond to locations downstream of the ship. To visualize large–scale circulations (LTC), we present contours of the streamfunction ψ, which is computed from the x–component of the vorticity field ω_x by solving the Poisson equation, $\nabla^2\psi = -\omega_x$. These contour maps serve as a good tool for understanding both the genesis and dynamics of LTC and LTC–induced surface currents, and the structure and longevity of the persistent wake.

3.2.4 Initial and boundary conditions

Initial conditions at t=0 s must be specified at the initial data plane (IDP) for all simulation variables, U, k, ϵ, T, S, and p. The IDP can be prescribed from theory, geometry–resolving CFD simulations, or even experimental data. For the work here, an empirical–analytical representation of the wake one-half ship length downstream, Figure 3.1, is established based on a formulation similar to Miner et al. [102]. This model includes resistance contributions from the ship's hull, wave breaking, and rudders; in addition to the thrust current and swirl from the propellers as detailed in Appendix B.

The axial velocity produced by the ship is presented in Figure 3.1a as a contour plot of its magnitude on the (y, z) plane. The axial velocity is positive in the direction of the thrust current, which is opposite to the direction of ship velocity. The strongest current is produced obviously in the area of the propellers. We call it a thrust current, whereas a negative current in the direction of the ship velocity we call the drag current since it is created by the drag of the ship hull. The velocity is normalized by the ship speed U_0. Of course, for all other factors being equal, the ratio between the velocity magnitudes of thrust and drag currents depends on the ship speed and, correspondingly, on Froude number. At higher speeds, the contribution of wave–making resistance increases and the relative contribution of frictional resistance decreases.

The transverse (rotational) flow produced by the ship propellers is presented in Figure 3.1b as contour lines of the streamfunction on the same (y, z) plane. The contour map of streamfunction in Figure 3.1b should not be confused with the contour lines of the magnitude of axial velocity used in the previous Figure 3.1a. The map of the streamfunction shows the direction of the transverse velocity. Proximity of the streamlines to each other (density) characterizes the magnitude of the rotational velocity. Knowing that every contour in Figure 3.1b corresponds to a change in streamfunction of 0.1 m^2/s, one can estimate the velocity. This representation of the transverse flow as streamlines is employed throughout this chapter to characterize the evolution of circulations in the ship wake in the manner used by Basovich [13]. Since the propellers in this case are rotating outward, the circulatory

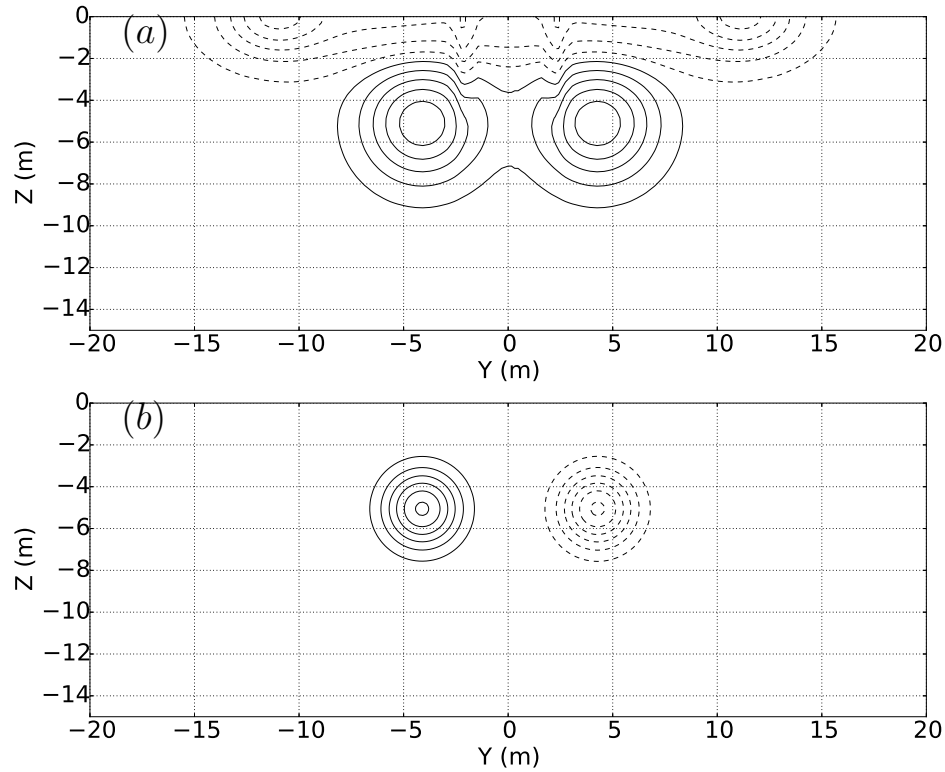

Figure 3.1: Initial data plane at $Fr = 0.35$. a) contour map of axial–component of velocity, where contour spacing is $1\%U_0$, contour range is -4.95%U_0 to 5.4%U_0, and dashed lines represent negative contours. b) contour map of streamfunction, where contour (streamline) spacing is 0.1 m^2/s.

motion represented in Figure 3.1b is also outward rotating. The maximum computed value of transverse velocity of the flow presented in Figure 3.1b is below the surface and has a value of 0.4 m/s.

To perform 2D+t simulations, periodic boundary conditions are used in the axial x–direction for all variables. The ocean surface is treated as a slip boundary (zero gradient for all variables, except for the normal component of velocity which is set to zero) to allow the formation of transverse surface currents; the bottom is also treated as a slip boundary, but is set sufficiently below the area of interest so as to not influence mass conservation and the pressure field; the far–field side boundaries are treated as pressure–outflow boundaries, but are also set sufficiently wide to prevent internal–gravity wave reflections when running stratified simulations.

3.2.5 Fluid properties and flow conditions

The fluid properties are described by the density and the kinematic viscosity. In general, the density in our solver is computed using the TEOS-10 seawater equation–of–state. To isolate the effects of the LTC, and since surface ships often operate in the ocean mixed layer, it is assumed here that the fluid is iso–thermal and iso–haline with $T = 20\,\mathrm{C}$ and $S = 35\,\mathrm{psu}$. Furthermore, to eliminate the generation of weak internal gravity waves we have disabled the influence of pressure on the equation of state, thus creating an isopycnic fluid with a density of $\rho = 1025\,\mathrm{kg/m^3}$. The kinematic viscosity is set to $\nu = 1.0 \times 10^{-6}\,\mathrm{m^2/s}$.

Relative wave–ship heading angles of 0° and 180° are used to simulate head– and following–seas conditions. Full–scale ship parameters are used with $Fr = 0.35$, $Re = 1.85 \times 10^9$, and a ship speed of $U_0 = 13\,\mathrm{m/s}$. Surface wave parameters are set to realistic ocean conditions with wave amplitudes of 0 and 0.25 m and wavelength of 10 m. It should be noted that Figure 1.3 shows the presence of some long regular surface waves with wavelength on the order of tens of meters. It is difficult to estimate their amplitude from the image, but it was reported from the ship that during the experiment the sea surface was dominated by small wind waves [117]. It is understood therefore that the amplitude of the long waves was on the order of or smaller than the shorter wind waves. The impact of these longer wind-waves will be discussed in later chapters.

Simulations are conducted for an IDP that would be generated by a full–scale naval surface combatant, as described by the David Taylor Model Basin (DTMB) Model 5415. The hull geometry includes both a sonar dome and transom stern, and propulsion is provided through twin open–water propellers driven by shafts supported by struts. For the full–scale ship, the key geometric parameters which serve as inputs to our theoretical model, described in Appendix A, are as follows; length $L = 142\,\mathrm{m}$, beam $B = 18.9\,\mathrm{m}$, draft $D = 6.16\,\mathrm{m}$, displacement $\nabla = 8425.4\,\mathrm{m^3}$, wetted surface area $S = 2949.5\,\mathrm{m^2}$, propeller diameter $D_p = 5.29\,\mathrm{m}$, propeller depth $z_p = 5.11\,\mathrm{m}$, propeller horizontal offset $y_p = 4.2\,\mathrm{m}$, rudder depth $z_r = 1.76\,\mathrm{m}$, rudder horizontal offset $y_r = 3.16\,\mathrm{m}$, rudder thickness $t_r = 0.95\,\mathrm{m}$, and rudder planform area $S_r = 12.1\,\mathrm{m^2}$.

3.3 Simulations of wake features under different surface wave conditions

3.3.1 Wake evolution without ambient surface waves (calm seas)

First, we consider the case of wake evolution without ambient surface waves. This case is important since it allows us to evaluate the characteristic lifetime of the wake without interaction of the ship–generated current with the surface waves, and later compare it to the persistent wake caused by such interaction.

The evolution of the IDP (Figure 3.1) is shown in Figure 3.2 through snapshots of the velocity component along the x–axis at four downstream distances (100m, 450m, 850m, and 1250m). The four snapshots illustrate the evolution of the axial current: the two separate thrust currents produced by the propellers (shown in Figure 3.2a) merge relatively soon into one larger jet, in agreement with Hyman [63]. By a distance of 850m behind the ship, the drag current has the appearance of two smaller jet–like currents above and on each side of the thrust current (Figure 3.2c), but with axial velocity in the opposite direction. An awareness and the characterization of the axial flow component is crucial to understanding the generation of LTC, which result from the interaction of this axial flow with the surface wave field, as described later. The evolution of the transverse current and related streamlines is not shown for the case without ambient surface waves, since the diverging circulatory motions shown in Figure 3.1b simply decay as the distance behind the ship increases.

In the present study of the persistent wake, we are primarily interested in the character of the near–surface currents, because they are responsible for the redistribution of SAS films at the surface [116, 145]. Figure 3.3a shows the distribution of the axial component and 3.3b shows the transverse component of the surface velocity as a function of the transverse y–coordinate at three distances (1250m, 3500m, and 7000m) behind the ship. Figure 3.4 shows the distribution of the transverse velocity of the surface current on the (x, y) plane in the frame of reference related to the ship, in which the flow is stationary.

As can be seen from Figure 3.3a, the axial surface velocity at each of the three distances behind the ship has regions with positive or negative values, which correspond to the thrust or drag currents, respectively. The transverse flow, which is shown in Figure 3.3b, has a divergence zone in the middle of the wake (centerline), since the velocity is directed away from the centerline and the two weak convergence zones at the edges. We call these convergence zones weak because the velocity on one side of such a zone is zero. The flow shown in Figure 3.3b will redistribute SAS away from the centerline toward the edges. Both the axial and transverse components of the velocity decrease with distance behind the ship. The transverse component of the surface velocity decays faster than does the axial. Figure 3.4 illustrates that the transverse velocity practically disappears at a distance on the order of 5000m behind the ship, which is about 35 ship lengths.

3.3.2 Wake evolution in presence of ambient surface waves

Two effects generated by the ship, near–surface turbulence and surface flow, are mainly responsible for the ocean–surface manifestations of the ship wake. They each affect the short surface waves that define SAR and optical images of the surface. Turbulence increases dissipation of the short waves directly. Surface currents change the intensity of the short surface waves by changing their propagation velocity and by changing SAS concentration at the surface, which in turn affect short–wave dissipation. The relative contributions of these two mechanisms that alter the short surface waves are further discussed in chapter

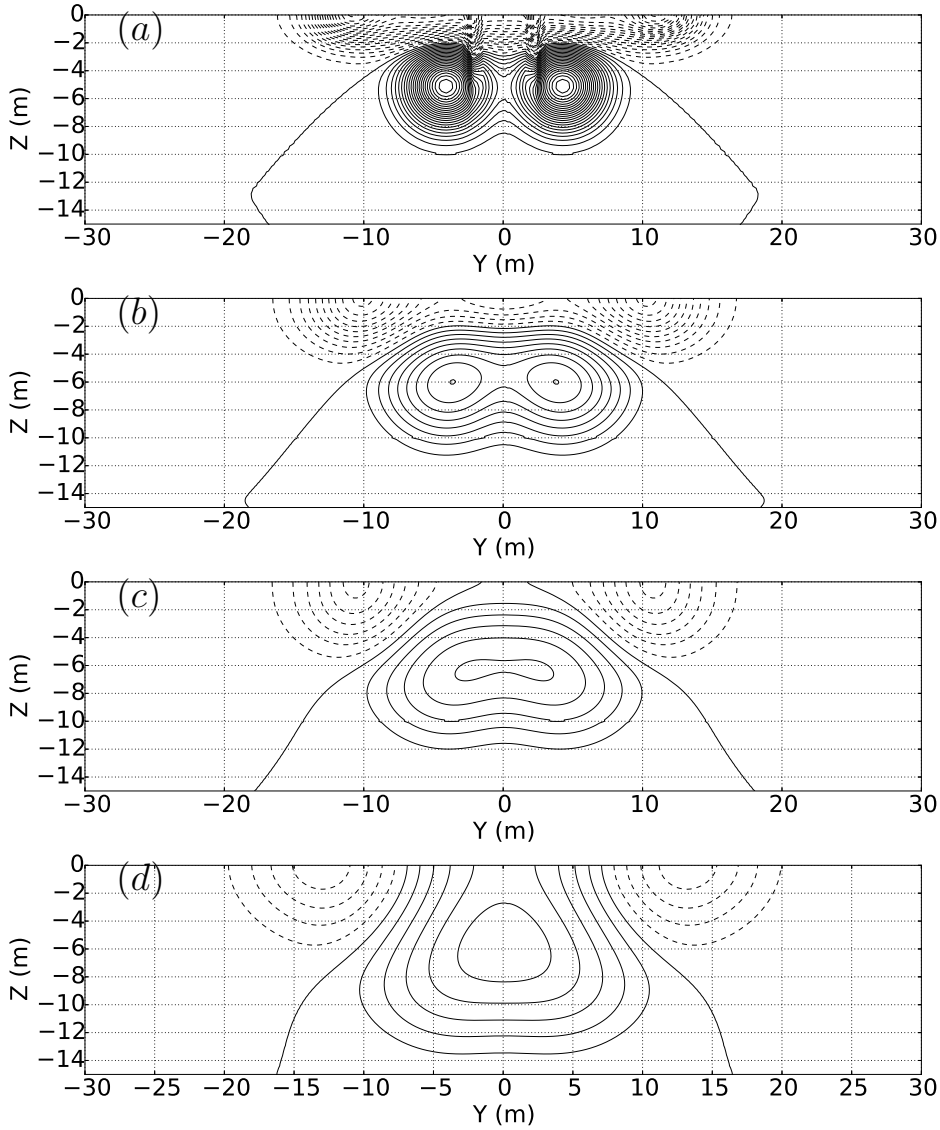

Figure 3.2: Contours of axial velocity at (a) $x = 100\,\mathrm{m}$, (b) $x = 450\,\mathrm{m}$, (c) $x = 850\,\mathrm{m}$, and (d) $x = 1250\,\mathrm{m}$ at $Fr = 0.35$, without ambient surface waves. Contour spacing $= 0.02\,\mathrm{m/s}$. Dashed lines are negative contours.

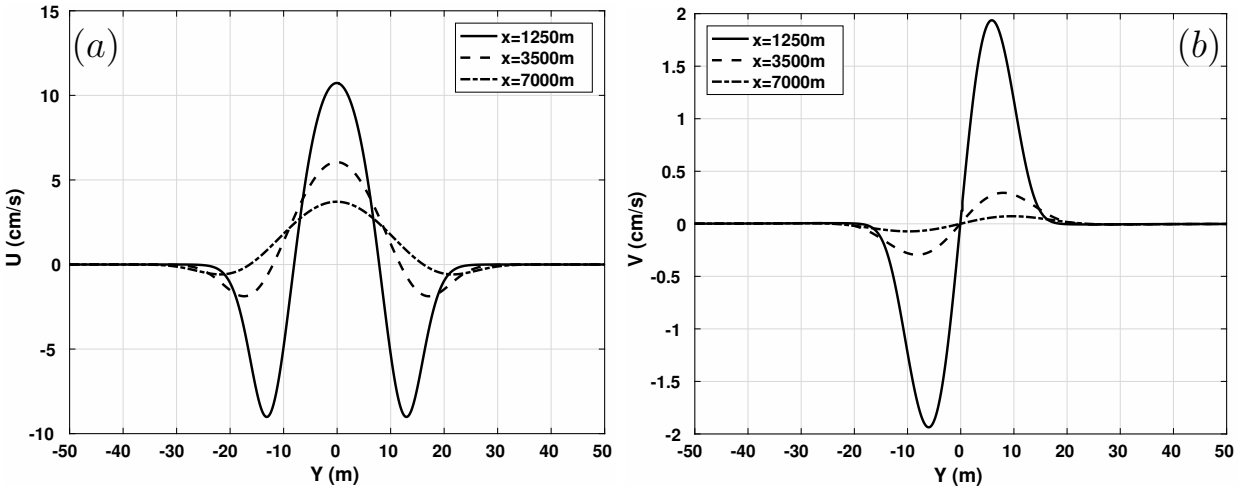

Figure 3.3: Evolution of surface currents at $Fr = 0.35$, without ambient surface waves. a) axial–component of velocity; b) transverse–component of velocity.

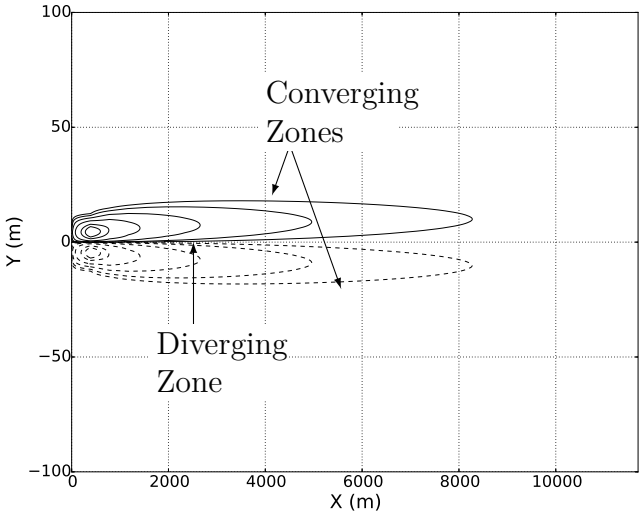

Figure 3.4: Contour map of transverse–component of velocity on ocean surface at $Fr = 0.35$ without ambient surface waves. Contours = +/- 0.05, 0.15, 0.5, 1.5, 3.5, 5 cm/s. Dashed lines are negative contours.

5. Still, some qualitative conclusions about such contributions can be made here. The direct kinematic effect of the surface currents on the short surface waves can be significant in the near– and far–wake regions, where the ship–induced surface current is still relatively strong. If the effect of the surface currents is dominant, the change in the short surface–wave field is asymmetric: the change is more pronounced on one side of the wake [42]. For the weak currents found in the persistent wake, redistribution of SAS at the surface may be more important than the change of kinematics of the surface waves, especially if the initial concentration of SAS is significant. This redistribution is mainly caused by the transverse component of the surface current when the SAS films are collected in convergence zones. When the effect of the SAS films is dominant, then the change in the amplitude of the short waves is expected to be symmetric, as observed in figures 1.3 and 1.4.

The genesis of the persistent wake and its structure are described in the next sections. The ship–induced persistent wake develops in the presence of ambient surface waves that interact with the ship–generated current described above. This interaction can produce large–scale LTC that exist for an extended time and, correspondingly, a long distance behind the ship. The vorticity in LTC and the structure of the persistent wake depend on the relative direction between the surface waves and the ship course [13]. Therefore, we consider two cases: first, the ship is headed into the seas, that is the ship travels in a direction generally opposite to the direction of propagation of the surface waves (head seas) and, second, the ship's course is in the same general direction as the direction of the surface waves (following seas). In the head seas case, the angle between the ship's velocity vector and the wave vector of the surface waves is greater than 90 degrees, while for the following seas case this angle is less than 90 degrees. When this angle is close to 90 degrees, the vortex force imposed on the initial ship-generated current is close to zero. Thus, for the 90 degree case, the LTC are not generated and there is no persistent wake. First the case of head seas is considered, since in this case, the transition from far wake to persistent wake is easier to observe.

3.3.3 Wake evolution for ship in head seas

In this section we consider simulations of the persistent wake for the case of head seas. The amplitude and wavelength of the surface waves have been selected based on the wind speed and fetch described in the paper on full–scale at–sea experiments by Milgram et al. [97]. For simplicity, we consider a sinusoidal wave with amplitude of 0.25 m and wavelength of 10m. It should be noted that an exact characterization of the surface wave spectrum is not crucial to the success of simulations. It is important that the vortex force is present and the direction of propagation of surface waves relative to the ship course, which defines the structure of the persistent wake, is known.

First, the distribution of the vortex force and its change with the distance behind the ship are considered. Figures 3.5 and 3.6 show the evolution of horizontal and vertical components of the vortex force in head seas. The contour lines are used to describe distribution of the vortex

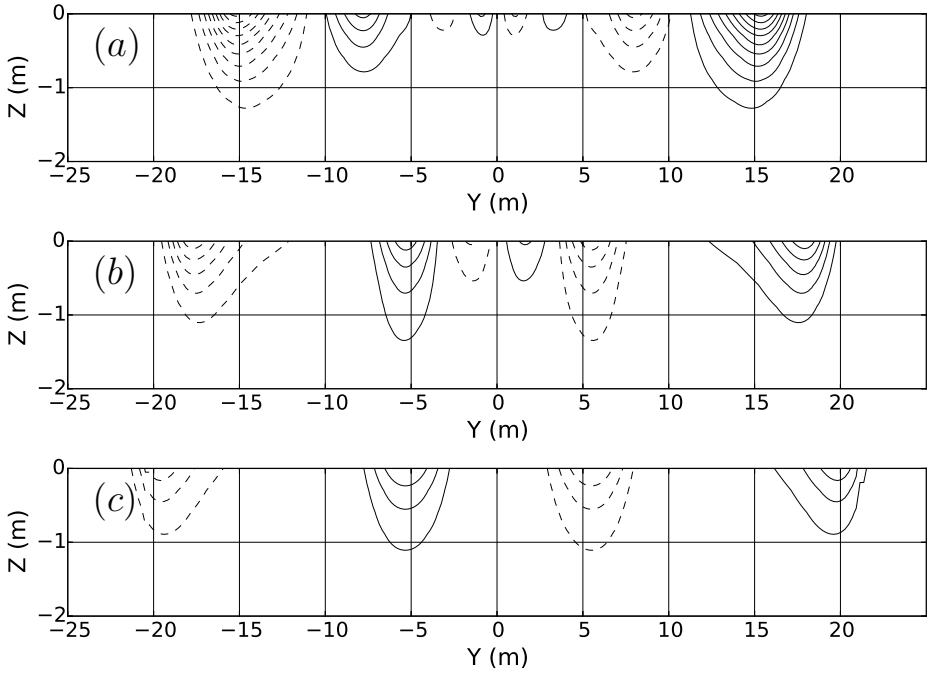

Figure 3.5: Contour maps of the horizontal component of vortex force F_y at (a) $x = 450$m, (b) $x = 850$m, and (c) $x = 1250$m in head seas at Fr $= 0.35$. Surface waves with $\lambda = 10m$ and $a_s = 0.25m$. Contour spacing $= 0.001$ N/kg. Peak Vortex Force at x=450m is 0.0094 N/kg. Dashed lines are negative contours.

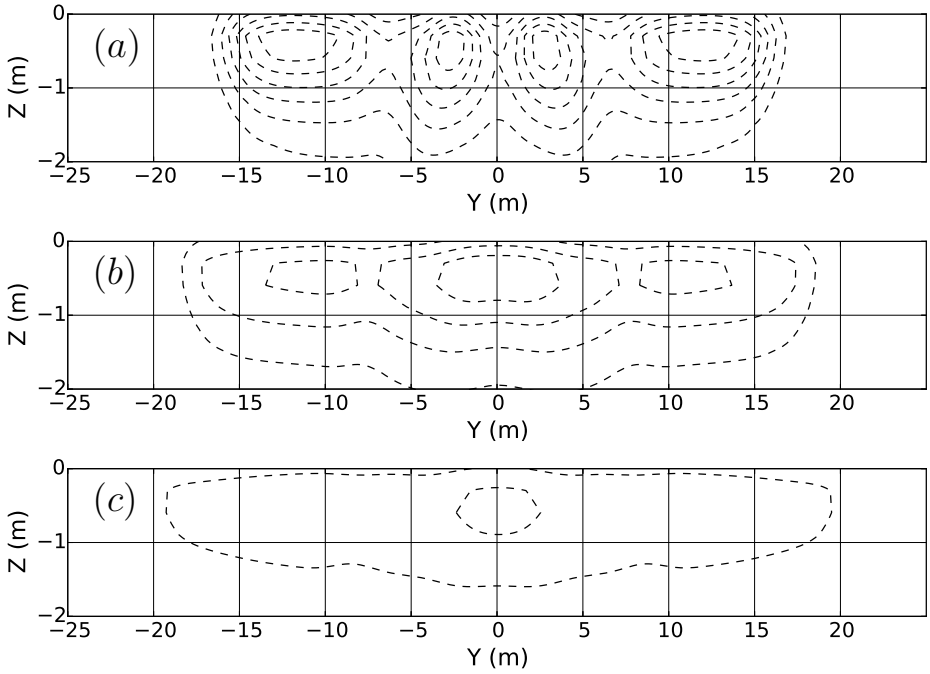

Figure 3.6: Contour maps of the vertical component of vortex force F_z at (a) $x = 450$m, (b) $x = 850$m, and (c) $x = 1250$m in head seas at Fr $= 0.35$. Surface waves with $\lambda = 10m$ and $a_s = 0.25m$. Contour spacing $= 0.001$ N/kg. Dashed lines are negative contours.

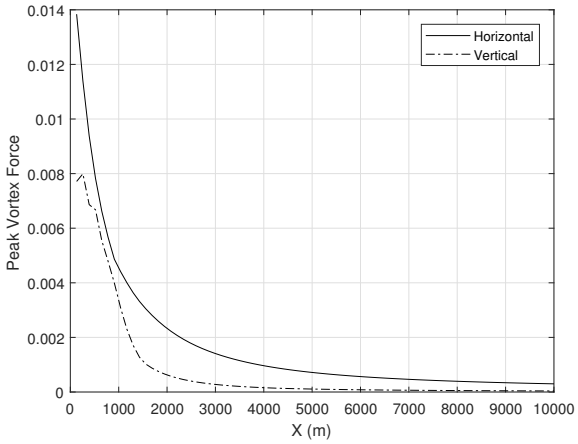

Figure 3.7: Decrease of maximum (peak) values of the components of vortex force (N/kg) in head seas as a function of distance behind the ship at Fr = 0.35. Surface waves with $\lambda = 10m$ and $a_s = 0.25m$.

force components which are shown for three different distances behind the ship. At relatively small distance (Fig.7 a) the structure of the horizontal component of the vortex force is complex with several regions where the force changes sign. This structure reflects complexity of the initial current which is in turn influenced by the ship geometry. As the structure of the ship induced drag current bifurcates, the distribution of the horizontal component of the vortex force simplifies into four symmetric regions with alternating directions and increasing distance between them. The vertical component of the vortex force maintains a primarily negative direction as the vertical velocity gradient is negative nearest the surface. Distribution of the vertical component of the vortex force changes in a similar manner to the horizontal component, but decays faster than the horizontal component. As the ship induced current evolves (see Figure 3.2) the horizontal velocity gradient near the surface becomes greater than the vertical gradient, leading to a stronger and more persistent horizontal component of the vortex force than vertical (see Figure 3.7). The slight shift observed in the peak vertical vortex force around x=500m is due to the peak vortex force moving from just outboard to centerline as the wake evolves.

The horizontal component of the vortex force creates converging and diverging flows along the surface with spacing between them on the order of tens of meters. Converging flows form downwelling regions and diverging flows form upwelling regions due to continuity, which lead to the formation of large scale LTC. These circulations, once formed, can persist for tens of kilometers, as the ship induced turbulence decays as shown in Figure 3.8. Maximum TKE is observed to have reduced by an order of magnitude around the distance of 3000 m.

The development of the transverse flow in the ship wake for the case of head seas is shown in Figure 3.9 for three different distances behind the ship. These distances are chosen purely for illustration purposes and are within the range of values that are shown in Figure 3.3.

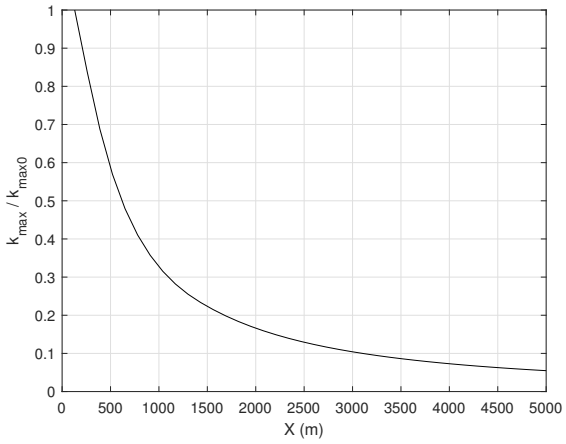

Figure 3.8: Decay of the maximum (peak) value of the turbulent kinetic energy as a function at Fr=0.35. Values are non-dimensionalized by the maximum initial value of the TKE (k_{max0}).

The structure of the current is very different from the case with no surface waves. The initial distribution of the transverse velocity immediately behind the ship is the same as shown in Figure 3.1: two circulatory flows created by the ship propellers rotating outward. These flows caused by propellers are still observed in Figure 3.9 several hundred meters behind the ship (with their intensity reduced). Simultaneously, four new LTC develop as a result of the vortex forcing as is seen in Figure 3.9a. As the distance behind the ship increases, the circulatory motions caused by the propellers dissipate (see Figure 3.9b). Finally they disappear completely by 3500 m (Figure 3.9c) and only four circulations exist in the area far behind the ship creating the persistent wake. Note, that the complex structure of the flow in the center of Figure 3.9a and Figure 3.9b is a result of superposition of flow caused by propellers and the inner set of developing LTC. The developed structure of the LTC in the persistent wake for the head seas case, as presented in Figure 3.9c, is as follows: the inner circulations are inward rotating, relative to the surface centerline, while outer circulations are outward rotating.

The persistence of LTC can be demonstrated by tracking the peak transverse velocity in head seas and calm seas cases. The peak transverse velocity ($\sqrt{v^2 + w^2}$) is tangential to the rotational streamlines generated by the propeller or LTC. Figure 3.10 shows that both cases are dominated by propeller swirl in the near/far field (x <1000m), but that LTC are several orders of magnitude stronger in the persistent wake. In the near field, the propeller swirl decays proportional to $x^{-0.65}$ while the two propeller wakes are distinct, Figure 3.2a. Sirviente and Patel [130] suggest the swirl in an axisymmetric momentumless wake decays as $x^{-0.6}$ for cases with weak swirl and $x^{-0.75}$ for cases with strong swirl. The swirling jets here are not in an axisymmetric momentumless wake, but this condition is considered more appropriate for comparison in the near field than a pure swirling jet. Once the two propeller

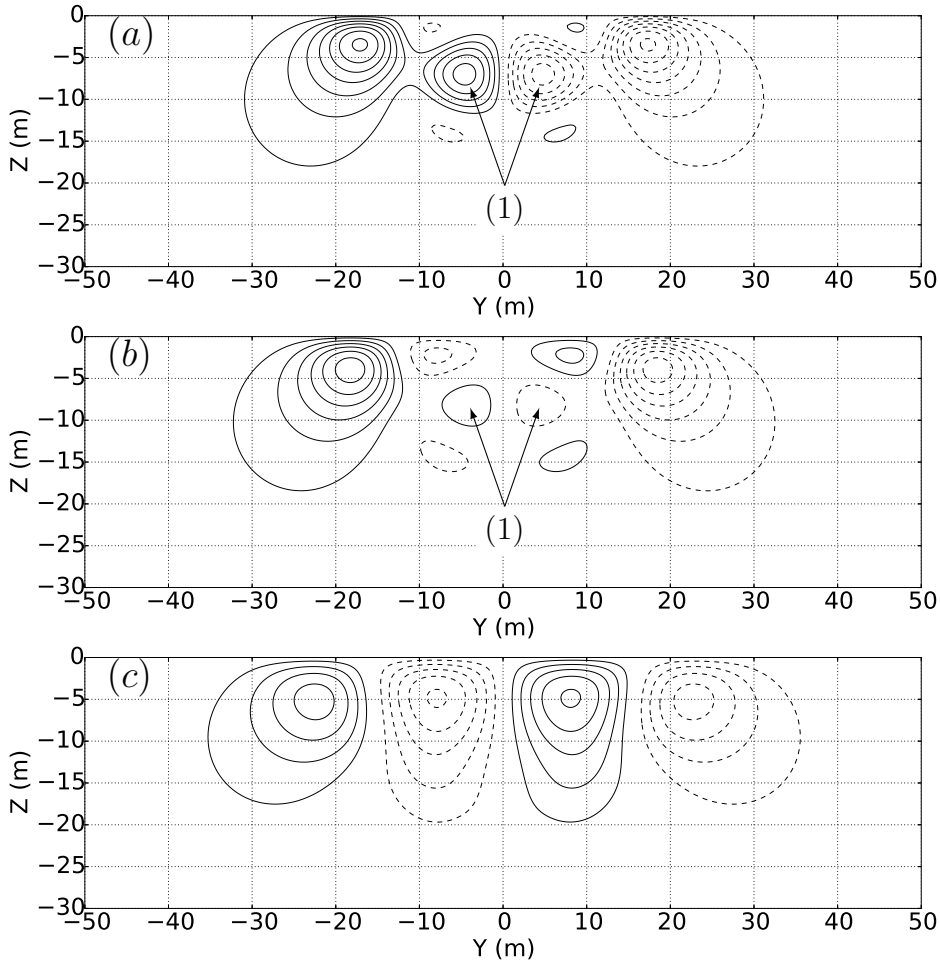

Figure 3.9: Contour maps of streamfunction at (a) $x = 1250\,\mathrm{m}$, (b) $x = 1650\,\mathrm{m}$, and (c) $x = 3500\,\mathrm{m}$ in head seas at $Fr = 0.35$. Surface waves with $\lambda = 10\,\mathrm{m}$ and $a_s = 0.25\,\mathrm{m}$. Contour spacing $= 0.005\,\mathrm{m}^2/\mathrm{s}$. Dashed lines are negative contours. (1) designates twin propeller swirl, which is non-traceable at 3500m. All other circulations are Langmuir-type circulations.

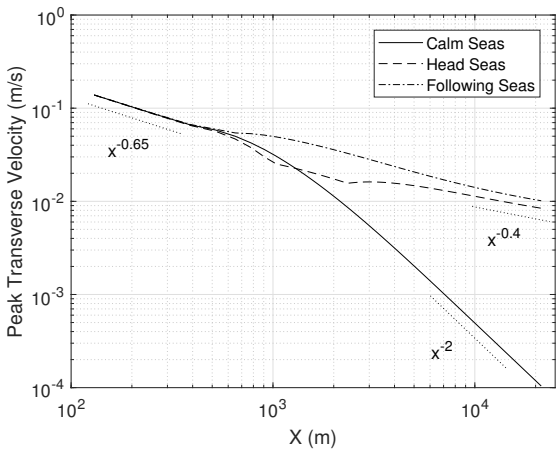

Figure 3.10: Decay of the peak transverse velocity in calm, head, and following seas at Fr=0.35. Surface waves with $\lambda = 10m$ and $a_s = 0.25m$.

jets have merged (x≈1000m) and the drag current has bifurcated, the transverse velocity decays proportional to x^{-2} for the case of calm seas. This condition is more appropriate for comparison to a pure swirling jet and shows good agreement with the studies of Shiri et al. [129] and Ewing [38] based on conservation of angular momentum and equilibrium similarity.

In the head seas case, a complex interaction between the decaying propeller swirl and growing LTC occurs between x=1000m and 2000m. Around x=1000m, the propeller swirl has decayed below the peak transverse velocity of the outer circulations in Figure 3.9a. As the inner circulations continue to grow, the outer circulations decay, until the inner circulations have a greater peak transverse velocity around x=2300m. The inner circulations decay into the persistent wake with the peak transverse velocity proportional to $x^{-0.4}$. Here, we define the beginning of the persistent wake as the point where the peak LTC induced transverse velocity is an order of magnitude greater than the peak propeller induced transverse velocity. In head seas, this is occurs around x=6000m.

Figure 3.11 presents the evolution of axial and transverse components of the surface velocity in head seas as a function of the transverse coordinate y. Plots are presented in Figure 3.11 for the same three distances behind the ship as shown in Figure 3.3. Evolution of axial velocity for the case of head seas shown in Figure 3.11a is similar to the behavior observed in the case without surface waves, as depicted in Figure 3.3. Several kilometers behind the ship only a small residual of the axial velocity remains. However, the evolution of the transverse velocity in the presence of ambient surface waves is totally different than in the absence of a surface wave field. Its structure reflects the four LTC developed due to interaction of the axial current with surface waves. The magnitude of the LTC–related transverse surface current grows during the initial stage of LTC development and then stays relatively unchanged (Figure 3.11b). The magnitude of the flow caused by the pair of inner LTC changes very little as the distance increases from 3500 m to 7000 m. The magnitude

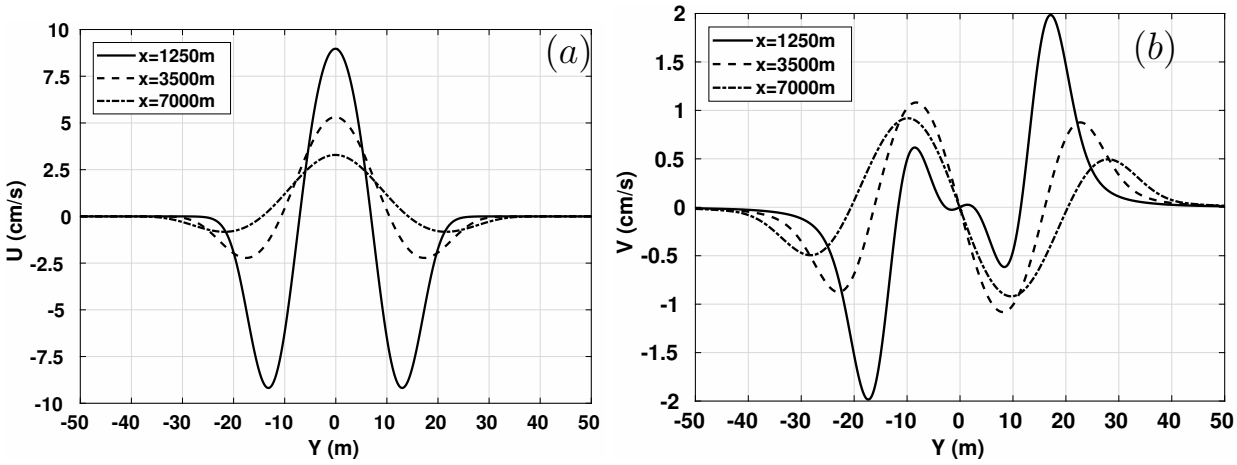

Figure 3.11: Evolution of surface currents in head seas at $Fr = 0.35$. Surface waves with $\lambda = 10\,\mathrm{m}$ and $a_s = 0.25\,\mathrm{m}$. a) axial velocity b) transverse velocity.

of the transverse flow related to the outer pair of LTC does decrease slowly as the width of these circulations increases. The LTC persist long ($O(10km)$) after the circulatory flows caused by the propellers disappear, as seen in the distribution of transverse surface velocity on the (x,y) plane in Figure 3.12. The role of ambient surface waves and generation of LTC in forming the persistent wake is especially noticeable when Figure 3.12 is compared to Figure 3.4, which corresponds to the calm–seas case. The persistence of the LTC generated transverse velocity is due in part to the vortex force continuing to reinforce the LTC while the axial current exists and is in part due to the reduced level of turbulence in the region of the persistent wake. Before the LTC develop, the transverse component of the surface flow is dominated by propeller–generated circulatory flows that, for this ship, rotate outward (Figure 3.4). The transition from the region of dominance of propeller–induced flow to the region of the persistent wake is reflected in Figure 3.12 by the centerline saddle–point region observed about 1000 m behind the ship.

For the head seas case, LTC that form the persistent wake produce a strong convergence zone along the center of the wake due to inward–rotating inner circulations. Also, there are two divergence zones produced between the inner– and outer–rotating circulations. Additionally, there are two so–called weak convergence zones at the outer edges of the wake, which are produced by the two outer, outward–rotating circulations. While the transverse surface velocity induced by the LTC is relatively low and cannot strongly affect the short surface waves directly, the existence of persistent regions of convergence and divergence can cause significant redistribution of the SAS films, which in turn will modify the short surface waves. In the case of head seas, the convergence zone near the centerline will create a region of high SAS concentration, which will reduce the amplitude of the short surface waves and, correspondingly, produce a dark centerline wake in SAR imagery. In addition, SAS concentration will also occur along the outer weak convergence zones, but the strength of these outer convergence zones is clearly weaker than the centerline convergence zone. Depending

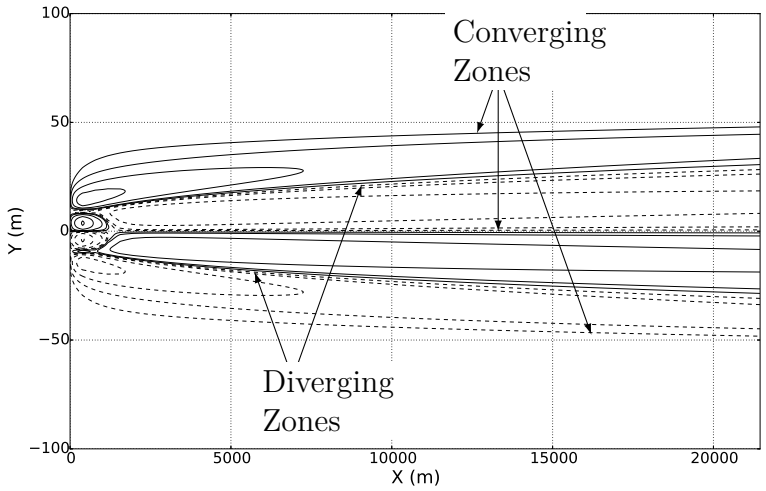

Figure 3.12: Contour map of transverse–component of velocity on ocean surface, in head seas at $Fr = 0.35$. Surface waves with $\lambda = 10\,\text{m}$ and $a_s = 0.25\,\text{m}$. Contours = +/- 0.05, 0.15, 0.5, 1.5, 3.5, 5 cm/s. Dashed lines are negative contours.

on the strength of the outer LTC, these outer convergence zones can form an additional set of streaks in SAR imagery.

3.3.4 Wake evolution for ship in following seas

In comparison to the case of head seas, the horizontal component of the vortex force in following seas reverses sign, Figure 3.13, but shows a similar magnitude and shape with four regions with alternating sign. These regions gradually spread, but at a slower rate than in the case of head seas. The outermost regions act inwards towards the centerline, thus reducing the rate of spreading in comparison to the case of head seas where the current is pushed further outboard by the outboard–acting forces. The vortex force in following seas also dissipates sooner than in head seas, Figure 3.14. The slight discontinuity in the peak vortex force again appears as the peak force transitions from outboard to inboard as seen through comparision of figures 3.13a and 3.13b.

The development of the transverse flow in the persistent wake for the case of following seas is shown in Figure 3.15 for the same distances behind the ship as presented in Figure 3.9 for the case of head seas. Parameters of the ambient surface waves are taken to be the same as in the previous case: sinusoidal wave with amplitude of 0.25 m and wavelength of 10 m. Here the development of four LTC with structure similar to the case of head seas can be observed, but with an important difference: the directions of the circulations are the opposite to the direction of the circulations in the head seas case. Specifically, the pair of inner circulations rotate outward and outer pair rotate inward. Since the initial fluid motions induced by the two propellers are outward rotating, they quickly merge with the inner LTC, unlike the

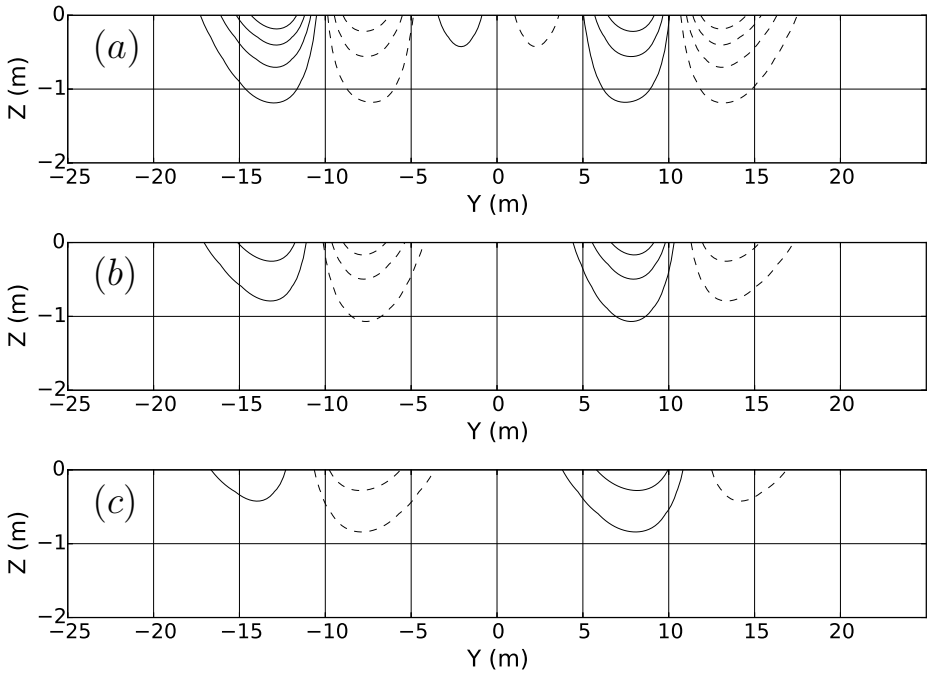

Figure 3.13: Contour maps of the horizontal component of the vortex force F_y at (a) $x =$ 450m, (b) $x = 850$m, and (c) $x = 1250$m in following seas at Fr $= 0.35$. Surface waves with $\lambda = 10m$ and $a_s = 0.25m$. Contour spacing $= 0.001$ N/kg. Peak vortex force at x=450m is 0.0049 N/kg. Dashed lines are negative contours.

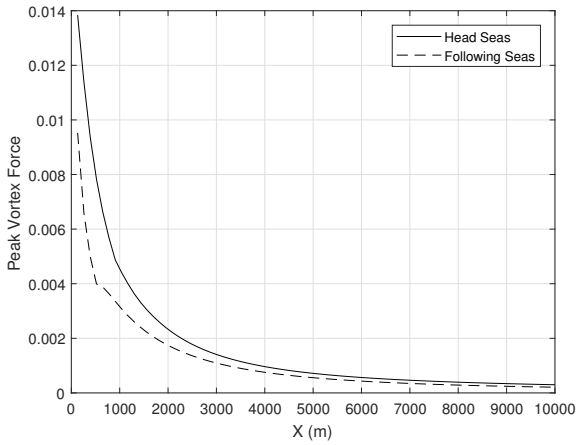

Figure 3.14: Decay of the peak horizontal component of vortex force (N/kg) in head and following seas at Fr=0.35. Surface waves with $\lambda = 10m$ and $a_s = 0.25m$.

propeller–induced motions in the head seas case.

The inner LTC in following seas grow faster in magnitude and size than in head seas. The inner LTC generate greater transverse velocities than the decaying propeller swirl by x=500m. Despite the lower magnitude vortex forces, the case of following seas generates greater transverse velocities than the head seas case for the range of study, Figure 3.10, due to these larger inner circulations. The LTC continue to grow in strength for several hundred meters beyond where they surpass the propeller swirl, before asymptotically approaching an equal decay rate to the head seas case with the transverse velocity in the persistent wake again proportional to $x^{-0.4}$. In following seas, the persistent wake is observed to begin around x=5000m, 1000m sooner than the head seas case.

The surface velocities in the ship wake in following seas are presented in Figure 3.16. Figure 3.16a shows the evolution of the axial velocity, which is fairly similar to its behavior in the previous cases of calm seas (Figure 3.3a) and head seas (Figure 3.11a). The presence of the upwelling zone along the centerline is observed to increase the persistence of the surface centerline axial velocity while the outboard surface drag current is suppressed by the downwelling zones. These differences in the near–surface axial velocity contribute to the stronger inner LTC and weaker outer LTC observed in Figure 3.15, compared to the case of head seas (Figure 3.9). In following seas, the transverse velocity at the surface (Figure 3.16b) has a direction opposite to the direction of the velocity in the head seas case (Figure 3.11b). The LTC extend well beyond the far wake as shown in Figure 3.17, which presents the distribution of the transverse surface velocity on the (x, y) plane. Because of the change in the sign of the circulations, LTC in the persistent wake for the case of following seas create a divergence zone along the centerline of the wake, two strong convergence zones on each side of the centerline and two weak divergence zones at the outer edges of the wake. The distribution of the SAS films due to these LTC will be different from the case of head seas. The two strong convergence zones offset from the centerline will create bands with high SAS concentration and, correspondingly, dark streaks in the SAR images, producing a railroad–track wake.

3.3.5 Effect of propeller rotation direction and propeller count

From the previous discussion, it is obvious that the exact configuration of the ship and the propellers are not the main factors in the formation of the persistent wake. Peltzer [115] reported similarity in wake evolution between a twin–propeller destroyer and a single–propeller frigate. Thus, the effects of propeller–rotation direction and a change in the number of propellers were considered. The simulations show that the structure of the persistent wake generated by same ship model (twin propellers) does not appreciably change when the direction of propeller rotation is changed.

To examine the effect of the propeller configuration on the structure of the persistent wake, the IDP of the present model was changed from a twin–propeller configuration to a single–

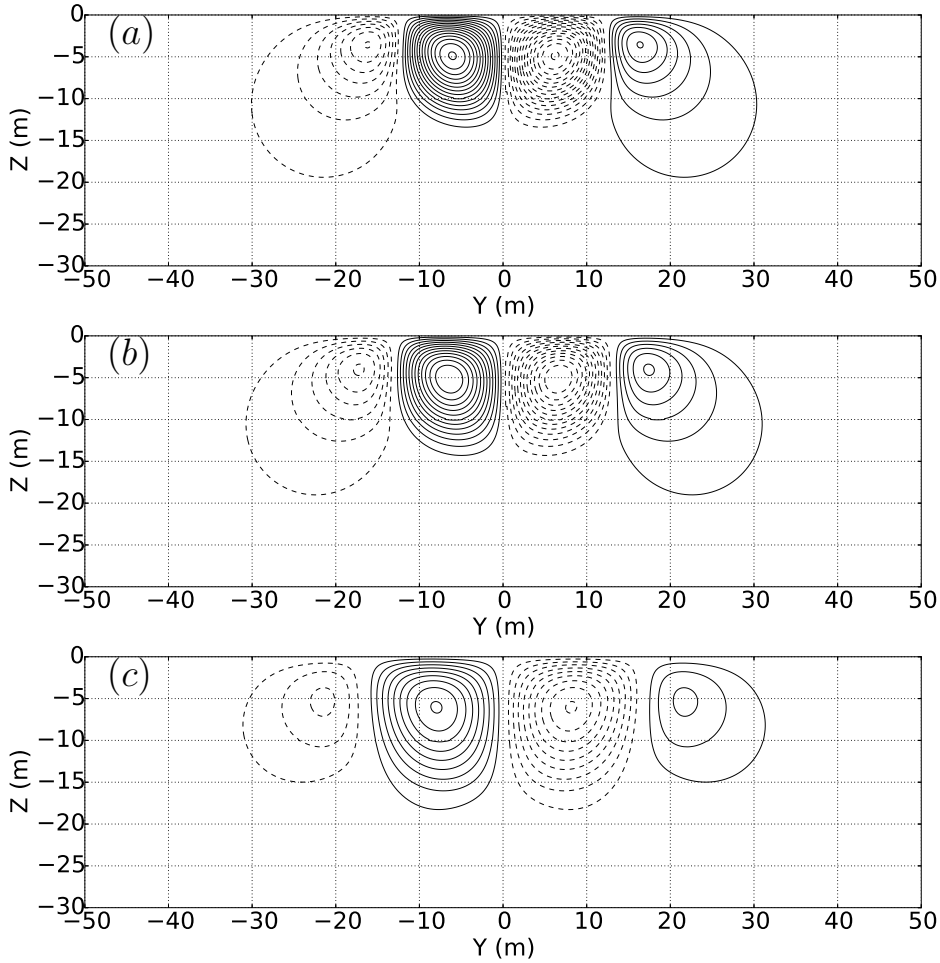

Figure 3.15: Contour maps of streamfunction at (a) $x = 1250\,\mathrm{m}$, (b) $x = 1650\,\mathrm{m}$, and (c) $x = 3500\,\mathrm{m}$, in following seas at $Fr = 0.35$. Surface waves with $\lambda = 10\,\mathrm{m}$ and $a_s = 0.25\,\mathrm{m}$. Contour spacing $= 0.005\,\mathrm{m}^2/\mathrm{s}$. Propeller swirl and inner LTC are reinforcing in following seas.

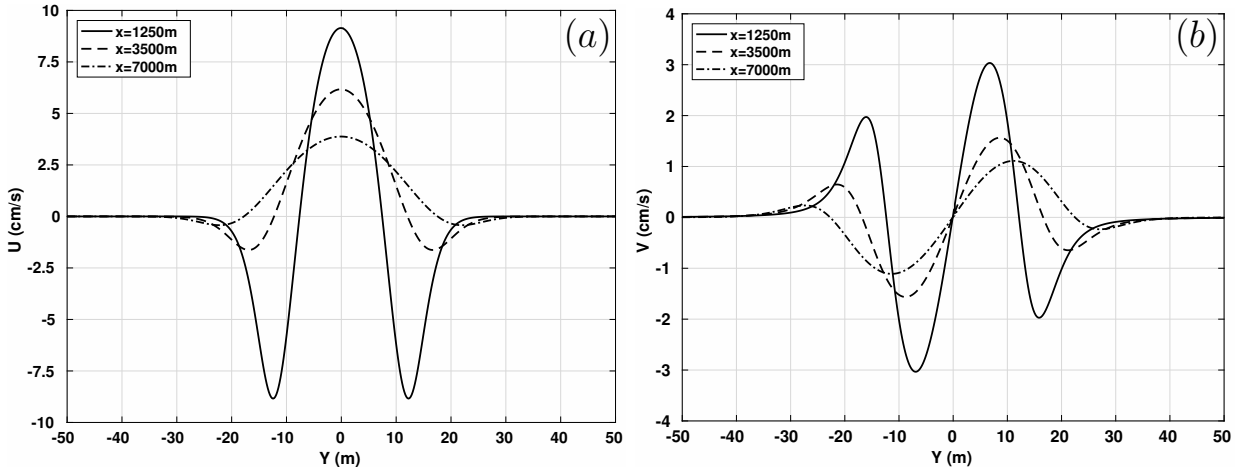

Figure 3.16: Evolution of surface currents in following seas at $Fr = 0.35$. Surface waves with $\lambda = 10\,\mathrm{m}$ and $a_s = 0.25\,\mathrm{m}$. a) axial–component of velocity b) transverse–component of velocity.

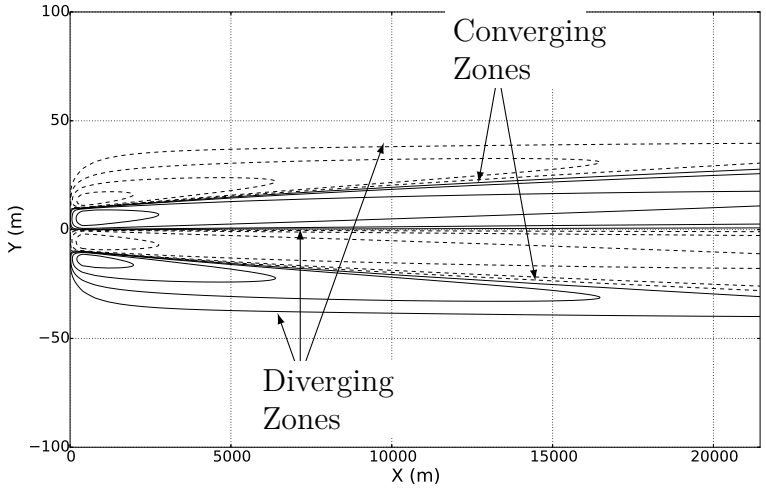

Figure 3.17: Contour map of transverse–component of velocity on ocean surface, in following seas at $Fr = 0.35$. Surface waves with $\lambda = 10\,\mathrm{m}$ and $a_s = 0.25\,\mathrm{m}$. Contours = +/- 0.05, 0.15, 0.5, 1.5, 3.5, 5 cm/s. Dashed lines are negative contours.

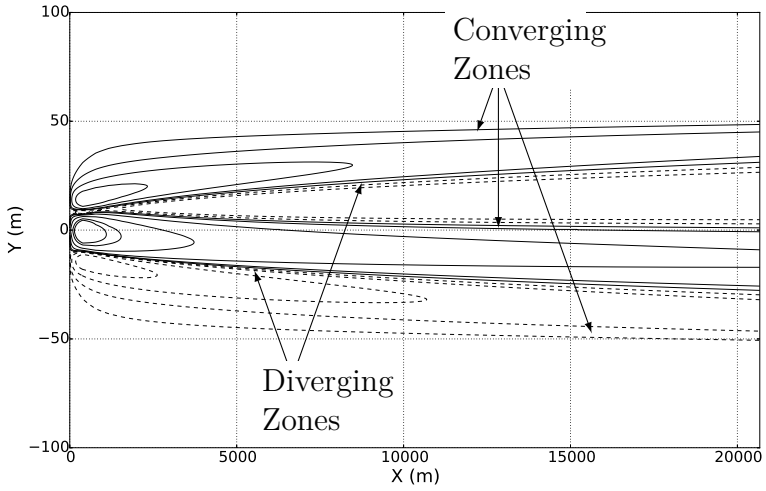

Figure 3.18: Contour map of the transverse–component of velocity on ocean surface, in head seas at $Fr = 0.35$ with a single propeller. Surface waves with $\lambda = 10\,\text{m}$ and $a_s = 0.25\,\text{m}$. Contours = +/- 0.05, 0.15, 0.5, 1.5, 3.5, 5 cm/s. Dashed lines are negative contours.

propeller configuration, and simulations were run for the head seas condition. The single propeller was sized to have an equal loading to the previously modeled twin propeller configuration.

The contours of the transverse component of surface velocity for the single propeller on the (x,y) plane is shown in Figure 3.18. This distribution is different from the two-propeller configuration shown in Figure 3.12 as the centerline convergence zone is initially offset due to the circulatory flow produced by the single propeller. However, as the distance behind the ship increases and initial propeller–induced circulatory flow decays, the developing LTC start to define the structure of the persistent wake and the distributions of transverse surface velocity in figures 3.18 and 3.12 (single versus twin propellers, both head seas) become similar, but with reduced symmetry in the single–propeller case. This result is to be expected as the LTC are driven by the axial velocity profile, which behaves as a single jet in the twin propeller configuration, once the two thrust currents merge (Figure 3.2).

3.4 Comparison with experimental data

The experimental data that contains detailed measurements of parameters of persistent wakes is very limited. For example, as was mentioned previously, Ermakov et al. [36] detected the presence of circulations by registering transverse velocities on the order of centimeters per second far behind a passing ship. However, the salient parameters of the axial current and of surface waves were not reported. There are many papers that provide SAR images of ship wakes (see, for example, [88, 106, 133, 147]), but often sea conditions and ship parameters at

the time the images were obtained are not well documented, making it difficult to compare these experimental results with the present theory.

The best documented series of full-scale experiments, to which we have access, was conducted during the 1989 Office of Naval Research Field Experiment [115] as discussed in chapter 2. During these experiments, *in situ* measurements of the ocean surface tension were collected to coincide with the collection of airborne SAR imagery of the ocean surface. The wind and surface wave conditions were also recorded.

Most of the experimental data collected for the US Navy destroyer was obtained in conditions of following seas. *In situ* measurements of surface tension across the ship wake were taken from a small boat that crossed the wake. Several bands with a high concentration of SAS films were registered. Not all bands registered with the *in situ* measurements can be clearly identified, since not each of them can be seen in the accompanying SAR imagery (see Figure 1.4). Nevertheless, the *in situ* measurements do confirm that the SAS concentration is low along the centerline of the wake and that there are two bands, one on each side of the wake centerline, where SAS concentration is high. These two bands correlate with the position of the two dark streaks that are seen in Figure 1.4. The length of the wake in the image is about 7 km. Based on the description of Figure 1.4 by Milgram et al. [97], the distance between the dark streaks (railroad tracks) in the image is roughly estimated to be about 70 m. The formation of such a railroad–track wake for the case of following seas has been described in this chapter. The transverse surface current generated in the simulation of the case of following seas (Figure 3.17) shows the distance between converging zones is about 50 m. This value is in reasonably good agreement with the estimate obtained from the SAR image. The difference can be caused by many factors such as an imperfect model of initial current at the IDP, uncertainty in the ambient surface–wave parameters, or the potential effect of ocean stratification on the development of LTC and other factors.

It also should be noted that the railroad–track structure of the persistent wake in the SAR image begins only beyond the distance of about 3 km behind the ship. At shorter distances, the wake appears as a centerline wake. Such behavior is observed in the region of the far wake, where the ship–generated perturbations are still relatively strong and the turbulence has a more significant damping effect than does the SAS film on the amplitude of the short surface waves. Once the turbulence decays, then the LTC–induced structure of the wake becomes more apparent.

Although the following seas case was the focus of the systematic study of the ONR set of experiments, a SAR image of the wake of the same US Navy destroyer in head seas was also obtained. That image is presented in Figure 1.3. Only a centerline wake is seen in the SAR image, which is in agreement with the predictions for the case of head seas made in this chapter. The dark centerline streak is the manifestation of a strong convergence zone, which is produced by the LTC at the center of the wake (see figure 3.12). Notice that initially the centerline wake is wide, which is caused by the presence of turbulence in the far wake region behind the ship. As the far wake transforms into a persistent wake, which is defined by the

evolving LTC, the centerline streak narrows.

3.5 Conclusions

An extended region of a surface ship wake far behind the ship, where original perturbations produced by the motion of the hull and propellers have decayed significantly, has been identified and characterized. The existence and configuration of this wake segment, which we refer to as the *persistent wake*, is as much the result of ocean dynamics as of ship configuration and operating parameters. The persistent wake arises as a result of the interaction between ship–induced currents and an energetic surface–wave field, which produces large–scale, nearly–inviscid secondary circulatory flows orthogonal to the direction of the ship drag and thrust currents. The interaction with the surface–wave field induces a so–called vortex force [26] on ship–generated non–uniform currents, which then generates the circulations. These circulations, first described by Basovich [13], are similar in character to the well–known Langmuir circulations [81]; therefore, we identify them as Langmuir–type circulations (LTC). Unlike naturally–generated Langmuir circulations, which arise as a result of an instability in the wind–driven surface currents, LTC are formed around a ship–induced non–uniform current system comprised of thrust currents (direction opposite to the ship motion) and drag currents (direction same as the ship motion). The structure and magnitude of the resultant LTC depend on the magnitude and relative direction of the ship–induced currents and the ambient surface–wave field. The description of the ship–induced currents follow the computational approach to establish an initial data plane (IDP) introduced by Miner et al. [102].

Numerical simulations reveal several important features of the development of a persistent wake. First, when LTC are considered as the primary mechanism, the persistent wake does not develop in the absence of a surface–wave field or if the direction of the ship–induced currents and the propagation direction of the surface–wave field are nearly orthogonal. Second, the effects of the interaction of the ship currents and surface–wave field are not immediately apparent, since it takes time for LTC to develop. Third, the structure of LTC and, correspondingly, of the persistent wake is different for the case with head seas (ship heads into the waves) than for the case with following seas (ship travels with the waves). This difference occurs because the sign of the vortex force depends on the direction of the surface waves relative to the direction of the ship–induced currents. For the particular model of the ship studied in the present chapter, the development of the large–diameter circulations can take minutes to form, and the magnitude of the transverse (cross–track) surface flows induced by the LTC are on the order of centimeters per second. At five to eight kilometers downstream of the IDP, the cross–track extent of the system of circulations can be three to four times the width of the beam of the ship. The resulting system of circulations can exist for tens of kilometers behind the ship, which is consistent with their large size and the relatively low eddy viscosity of the background fluid.

Previous experiments [36, 115] confirm that the appearance of the persistent wake is defined in remote SAR and optical imagery by the change in spectral density of the short surface waves, which is a result of the redistribution of SAS films by the LTC–induced surface flow in the wake. In the case of head seas, the LTC–induced flow at the surface creates a strong convergence zone at the center of the wake. The concentration of SAS films in this region is increased, thereby forming a centerline wake and producing a dark streak in SAR imagery. In the case of following seas, the LTC–induced flow at the surface creates two convergence zones on each side of the centerline, several tens of meters apart. Due to an increase in the concentration of the SAS film at these zones, dark streaks are produced in the SAR images, which appear as so–called railroad–track ship wakes. These simulation results are in good agreement with the experiment–based observations presented by Peltzer [115].

There are some other possible LTC related effects of potential importance for understanding the physics of the wake. For example, developing LTC can strongly affect the lifetime of bubble clouds created by the ship propellers, since LTC can create converging zones (downwelling) or diverging zones (upwelling) at the centerline of the wake for head and following seas, respectively. The lifetime of the bubble clouds depends on the time for the bubbles to rise to the surface. LTC-generated flow will inhibit the upward motion of the bubble in head seas and contribute to this motion in following seas. Thus, the lifetime of the bubble clouds can be expected to be noticeably shorter in the case of following seas, for ship configurations similar to the one studied here.

The present chapter is the first step in the study of the role of LTC in the physics of ship wakes. A comprehensive model of SAS film–induced effects is required. It should include the mechanisms of film redistribution by surface flows and turbulence, film degradation and diffusion, the effect of scavenging of SAS on film concentration, as well as the effects of bubbles and other contaminants on these processes. Present models of the persistent wake can be measurably improved by better describing the effects of SAS films and near–surface turbulence on the spectrum of short surface waves, which are responsible for the manifestation of ship–induced anomalies in sea–surface imagery. Several of these topics are the focus of the following chapters.

Chapter 4

Effect of Ship–Induced Langmuir–Type Circulations on Distribution of Surface–Active Substances and Damping of Short Wind Waves

(Work adapted from Somero et al. [136].)

4.1 Introduction

In the previous chapter a mechanism for the generation of large scale circulations in the wake of a surface ship was discussed. It was shown that these circulations, referred to as Langmuir-type circulations (LTC), induced significant transverse currents in the wake of the ship that could persist for tens of kilometers. In the persistent wake the ship–produced currents and turbulence have decayed significantly, while the surface currents produced by LTC, which are on the order of O(1 cm/s), decrease more slowly. These LTC–induced currents can sufficiently change the concentration of surface active substances (SAS) due to the presence of strong convergence and divergence zones. The change in the local SAS concentration in turn affects the damping factor of short surface waves as energy is dissipated by increased viscous damping in the interface boundary layer in regions of increased SAS concentration [5, 96]. Therefore, the main focus of this chapter is to describe the redistribution of the SAS by LTC–induced surface currents in the region of the persistent ship wake and to compute the corresponding SAS–induced damping effect on the short surface waves, $\lambda \sim$ 0.01-0.2m. Analysis of the change in the short surface–wave spectra will then be discussed in the next chapter.

This chapter is organized as follows. First, a model, employed to simulate the dynamics of the SAS films in the ship wake, is described. This model includes advection of the films by the surface currents and diffusion of SAS. Next, the distribution of the wind–wave damping factor, due to the presence of SAS films in the region of the persistent wake, is computed.

In this section, two different models developed independently by different research groups [29, 100] are compared and found to be in good agreement. Therefore, we can select one of the models [100] for implementation and have higher confidence in its accuracy. Finally, the results of our investigation into the redistribution of the SAS and its effect on the wind–wave damping factor (for a specific frequency) are presented and discussed in the context of available experimental data. It should be noted that local SAS composition and concentration vary by geographic region and season, but the results presented here provide a framework for analysis assuming the local conditions are known.

4.2 Mathematical Model

4.2.1 Redistribution of Surface–Active Substances

The redistribution of SAS on the ocean surface is modeled as a passive scalar subject to a scalar transport equation,

$$\frac{d\Gamma}{dt} + \frac{\partial\left(U_j\Gamma\right)}{\partial x_j} - \frac{\partial}{\partial x_j}\left(D\frac{\partial\Gamma}{\partial x_j}\right) = Source - Sink \tag{4.1}$$

where Γ is the concentration of SAS at the surface, U_i is a vector of the mean surface current, and D is a diffusion coefficient. Several authors [24, 29] have modeled the redistribution of SAS by the surface flow using this equation. In most of the previous studies the effect of diffusion of SAS was neglected. It is justified, for example, in the case of the surface current produced by internal waves [29], in which the characteristic time of velocity change is much smaller than characteristic time of diffusion of SAS. In the case considered in this chapter, the presence of strong stationary convergence zones requires taking diffusion into account in order to limit the increase of concentration of SAS in such zones. The diffusion of SAS at the surface is caused by several phenomena: molecular diffusion, turbulent diffusion, and diffusion related to the presence of the surface waves due to fluctuations of the wave-induced Stokes drift velocity [58]. There is significant uncertainty in the value of the SAS diffusion coefficient, thus in the model we use the turbulent diffusion as the strongest factor of diffusion of SAS and assume that coefficient of diffusion is the same as eddy viscosity.

For generality, equation 4.1 includes a term on the right–hand side that describes a source and a sink of the SAS concentration at the surface. The sink can occur due to natural degradation of the SAS and desorption from the surface to the bulk fluid. The source of SAS at the surface can be related to scavenging of the SAS from the water column due to the effect of the LTC and to the SAS transport by rising bubbles [132, 138]. In the current analysis, adsorption from, and desorption to, the bulk fluid are both neglected. Inclusion of these effects are the focus of future efforts, but it is shown here that the current model provides reasonable correlation with experimental results. In the absence of the source and sink terms, equation 4.1 describes conservation of the concentration of SAS at the surface.

4.2.2 Damping of Short Wind Waves

The impact of SAS redistribution on short–wave attenuation can be evaluated with a model based on the wave action balance equation [55, 62], which can be written as

$$\frac{\partial N}{\partial t} + (C_{gi} + U_i)\frac{\partial N}{\partial x_i} - k_i \frac{\partial U_i}{\partial x_j}\frac{\partial N}{\partial x_j} = (\beta - \gamma)\, N - \alpha N^2 \tag{4.2}$$

where N is the spectral density of wave action, k_i denotes a wave vector of wind waves , C_{gi} is the wind–wave group velocity, and U_i is the velocity of the surface currents. The right–hand side follows the formulation of Hughes [62] where β is the wind–wave growth rate, γ accounts for the damping of the waves due to surface films and turbulence, and α is a phenomenological coefficient to account for the nonlinear effects that limit the wave growth. The influence of LTC on the wave action balance appears primarily through the induced surface currents and damping of short wind waves by SAS films.

Wave damping due to SAS films is included through the damping factor γ_s, which is part of the overall damping factor γ. We adopt the damping–factor model presented in Milgram et al. [100], which follows the formulation developed by Cini et al. [23] and Alpers and Hühnerfuss [5]. The expression for γ_s can be written as

$$\gamma_s = 4\nu k^2 \frac{X + XY - 2X^2}{1 - 2X + 2X^2} \tag{4.3}$$

where,

$$X = \frac{Ek^2}{\rho(2\nu)^{1/2}(2\pi f)^{3/2}} \tag{4.4}$$

and

$$Y = \frac{Ek}{8\pi\rho\nu f}. \tag{4.5}$$

Here, E is the film elasticity (in Pascals), ρ is the density of seawater, ν is the kinematic viscosity of seawater, and f is the wave frequency calculated based on the wave number k as,

$$f = \frac{1}{2\pi}\sqrt{gk + \frac{\tau}{\rho}k^3}, \tag{4.6}$$

where g is the gravitational acceleration and τ is the surface tension given as $\tau = \tau_w - \Pi$. The surface tension of clean water is assumed to be constant $\tau_w = 72\,\mathrm{mN/m}$ [118], and the film pressure Π as a function of SAS concentration Γ is described by a 6th–order polynomial fit [98]

$$\begin{aligned}\Pi = {} & 8.8539 \\ & - 15.8969(\ln(A) - 5) - 8.221(\ln(A) - 5)^2 \\ & + 1.8225(\ln(A) - 5)^3 + 40.3451(\ln(A) - 5)^4 \\ & - 0.1023(\ln(A) - 5)^5 - 30.2724(\ln(A) - 5)^6,\end{aligned} \tag{4.7}$$

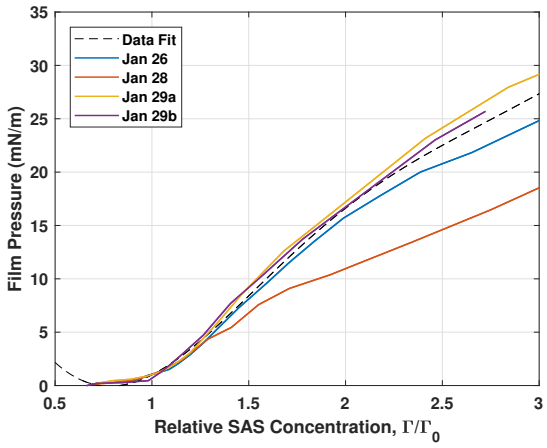

Figure 4.1: Film pressure Π dependence on SAS concentration ratio Γ/Γ_0 based on data of [118]. The Data–Fit curve is a 6th order polynomial fit to the values of Jan 26, Jan 29a, and Jan 29b.

where A is the film area described here by

$$A = A_0 \left(\frac{\Gamma}{\Gamma_0} \right), \tag{4.8}$$

and A_0 is the unperturbed film area and (Γ/Γ_0) is the concentration of SAS relative to the unperturbed concentration. The film elasticity is related to the film pressure by the following expression [118]

$$E = \frac{26.3\Pi}{\Pi + 2.4}. \tag{4.9}$$

It should be noted that the polynomial fit of equation 4.7 is based on a single set of data taken with a minimum measured film pressure of 1 mN/m. However, ambient film samples were collected at sea over a range of days for laboratory testing, and curves relating the film pressure to the film area were established for each day when samples were taken [118]. General agreement between the curves was found, but with significant variability in the initial film areas. Normalizing the data by the initial film areas provides an improved comparison between the data sets as shown in Figure 4.1. Here, each curve is normalized to an initial film pressure of 1 mN/m at a concentration ratio of 1. Film samples of Jan 26, Jan 29a, and Jan 29b show good agreement with each other, while film sample data from Jan 28 shows lower film pressure when compared to the other three curves, especially for concentration ratios greater than 1.4. Furthermore, it is noted that the coefficients in equation 4.7 were computed by Milgram et al. [100] using the outlier data from Jan 28.

Given the observed variability in film pressure vs. concentration, it was decided to study the effect of the film–sample data on the damping factor. Figure 4.2 shows two curves.

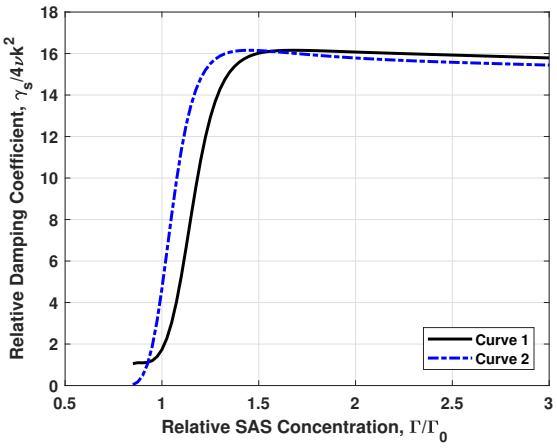

Figure 4.2: Relative damping factor ($\gamma_s/4\nu k^2$) dependence on SAS concentration Γ/Γ_0, which is described by equation 4.3. Curve 1 is computed using Π with coefficients based on Peltzer et al. [118] data from Jan 28, i.e., equation 12. Curve 2 is computed using Π with coefficients based on averaged data from Jan 26, Jan 29a, and Jan 29b.

"Curve 1" is plotted by directly using equation 4.7, which was fit by Milgram et al. [100] to the Jan 28 data. "Curve 2", on the other hand, is least–squares fit to the other three datasets. In general, the curves show a fast increase in the damping factor over concentration ratios between 1-1.5, with relatively constant values at greater concentration ratios. Since the film pressure curves of Figure 4.1 have good agreement through a concentration ratio up to approximately 1.4, the deviation in film pressure for greater concentration ratios is shown to not significantly impact the damping factor as it is relatively insensitive to the concentration ratio for values greater than 1.5. This allows the use of either curve for the purpose of estimating the relative damping factor. In this study, we will continue with the curve of Milgram et al. [100] as it corresponds to the day on which the SAR imagery, which we will compare with, was taken.

Alternative models for estimating the damping factor have been suggested by other authors. A comparison of the models of Milgram et al. [100] and of Da Silva et al. [29] for two initial film pressures ($\Pi_0 = 0.5$ and $1.0\,\mathrm{mN/m}$) at a wave number of $k = 125\,\mathrm{m}^{-1}$ is presented in Figure 4.3. The level of agreement between the models at the initial film pressure of $1\,\mathrm{mN/m}$ is remarkable, considering they were developed independently using film data from different sources. Extrapolation of expression 4.7 below the minimum measured value of $1\,\mathrm{mN/m}$ is not suggested due to the nature of the 6th–order polynomial. Considering the agreement between the two models at $1\,\mathrm{mN/m}$, description of the case of initial film pressure $0.5\,\mathrm{mN/m}$ was conducted following the method of Milgram et al. [100], while using data for the initial film area based on the curve presented in Da Silva et al. [29]. The level of agreement noted above does not hold across all wave numbers of the surface waves with increased discrepancy at lower wave numbers, but does provide a level of confidence in the model for the wave

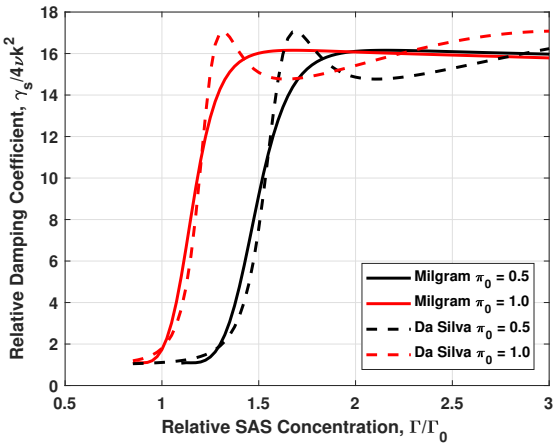

Figure 4.3: Comparison of relative damping factor ($\gamma_s/4\nu k^2$) from [100] and [29] for wave number $k = 125m^{-1}$ and initial film pressures of 0.5 mN/m and 1.0 mN/m.

numbers studied here.

Both models show a fast increase in the damping factor when relative SAS concentration changes between 1 and 1.5. The model employed in Da Silva et al. [29] predicts a slightly higher peak damping factor with a small drop following, compared to the model used in Milgram et al. [100], which uses a smooth curve that peaks and then gradually declines. The relative insensitivity to SAS concentration above these initial peaks is noteworthy and is reflected at both values of initial film pressure. Decreasing the initial film pressure shifts the curve to the right, requiring greater concentration levels to achieve the same level of damping. Increasing the initial film pressure above 1.0 mN/m, however, is shown by Da Silva et al. [29] to have less of an impact on the damping factor.

4.3 Computational Model

The computational model is based upon the assumption of one–way coupling between the hydrodynamics and the SAS redistribution. This enables a two–step process that is schematically shown in Figure 4.4: 1) solve for the hydrodynamics over large time and space using a 2D+t approach; and 2) solve for the SAS redistribution on the ocean surface using a transient 2D simulation of SAS concentration.

For step 1, the 2D+t approach results in surface currents that are steady in the ship–fixed frame of reference. For step 2, the simulation is transient, albeit with a frozen velocity field and steady boundary conditions. While there may be certain aspects of the time evolution of SAS redistribution and concentration that are important, we focus on the data after sufficient time has elapsed such that a stationary concentration field has been achieved.

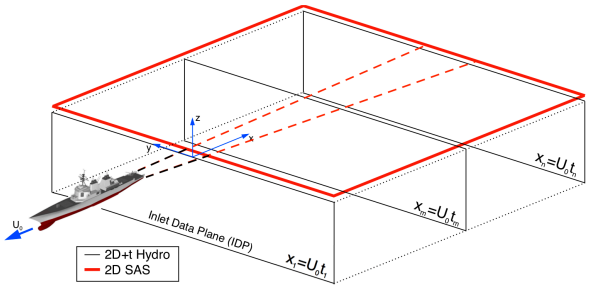

Figure 4.4: Computational domains for 2D (y,z) plus time hydrodynamics and 2D (x,y) SAS redistribution

4.3.1 Domains and Meshing

As shown in Figure 4.4, there are two computational domains, and therefore two meshes to construct. For the hydrodynamics, the computational mesh is identical to that described in chapter 3. For the SAS redistribution, a 2D domain is created on the ocean surface [(x, y) plane at $z = 0$] with dimensions that are inherited from the hydrodynamics simulation, although this is not explicitly required. Therefore, the size of the 2D domain in meters is $0 < x < 20,000$ and $-1000 < y < 1000$. The mesh uses 2000 equally spaced cells in each direction, for a total cell count of 4 million cells with mesh resolution of $\Delta x = 10\,\text{m}$ and $\Delta y = 1\,\text{m}$ in the axial and transverse directions, respectively.

4.3.2 Numerical methods

The numerical methods implemented for SAS redistribution are similar to those used for the 2d+t hydrodynamic simulations discussed in chapter 3. Solution of the linear advection–diffusion equation, given by equation 4.1, is achieved using a straight forward implicit time–marching scheme. Since both the surface currents from the hydrodynamics simulation and boundary conditions are steady, the time-marching algorithm is used as an iteration loop to a steady concentration field. As would be expected, treatment of the diffusion coefficient D in equation 4.1 has a large influence on the speed at which this convergence takes place. As previously mentioned, we assume that $D = \nu + \nu_t$, where ν_t is the turbulent eddy viscosity.

The governing partial–differential equation is discretized using a cell–centered finite–volume method. Gradients at the cell faces are computed using weighted interpolation between the adjacent cell centers. To limit numerical dissipation, a second–order energy–conserving scheme was used for the divergence operator in the advection term of equation 4.1. The Laplacian term was discretized with a second–order linear scheme. The equation is solved using a pre–conditioned bi–conjugate gradient (PBiCG) scheme, with absolute and relative convergence criterion of 10^{-8} and 10^{-5}, respectively.

4.3.3 Initial and boundary conditions

For the SAS redistribution, the velocity field is directly mapped from the hydrodynamics simulations using bi-linear interpolation, and the initial conditions are prescribed such that the relative concentration $\Gamma/\Gamma_0 = 1$. The boundary conditions for this transient 2D simulation include a steady inlet boundary with $\Gamma/\Gamma_0 = 1$, i.e., the ship is sailing into a continuous field of constant SAS concentration, far–field boundaries with $\partial\Gamma/\partial y = 0$, and an exit boundary with $\partial\Gamma/\partial x = 0$.

Damping of the short wind waves is calculated using a wave number of $k = 125\,\mathrm{m}^{-1}$, which corresponds to a wave length of $\lambda = 0.05\,\mathrm{m}$.

4.4 Results

In this section, we present simulation results for the redistribution of the SAS due to the surface currents presented in chapter 3, and its impact on the wind–wave damping factor.

4.4.1 Redistribution of Surface–Active Substances

The redistribution of SAS on the ocean surface due to surface currents in calm seas is shown in Figure 4.5 (top). The propeller–induced surface currents clear the local SAS away from the centerline and form two weak convergence zones to either side of the centerline. Note that the color–map scale of concentrations for the case of calm seas is reduced relative to other cases to allow some structure to be observed. If visualized on the same scale, the redistribution would be hard to see. As already discussed, the surface currents generated due to the propellers alone do not persist in the same manner as those generated by LTC. The case of calm seas does not extend beyond the far wake, and therefore significantly limits the downstream distance for which SAS is redistributed compared to the head and following seas cases.

The redistribution of SAS on the ocean surface in the condition of head seas is shown in Figure 4.5 (middle). In the far wake, the effects of the outboard rotating propellers, along with the outboard rotating drag–current induced LTC, redistribute SAS to the edges of the wake. As the effects of propellers dissipate and LTC develop, LTC–induced surface currents, Figure 3.12(middle), redistribute SAS into streaks along the convergence zones and remove SAS from the diverging zones. The case of head seas has a strong LTC–induced centerline converging zone and two weaker outboard converging zones in the persistent wake. The SAS concentration in the centerline convergence zone is observed to increase with increasing distance behind the ship for the range of study. This effect is caused by the decrease in turbulent diffusion of SAS with distance behind the ship, while LTC related surface current decreases slower. It was shown in chapter 3 that the maximum value of transverse velocity

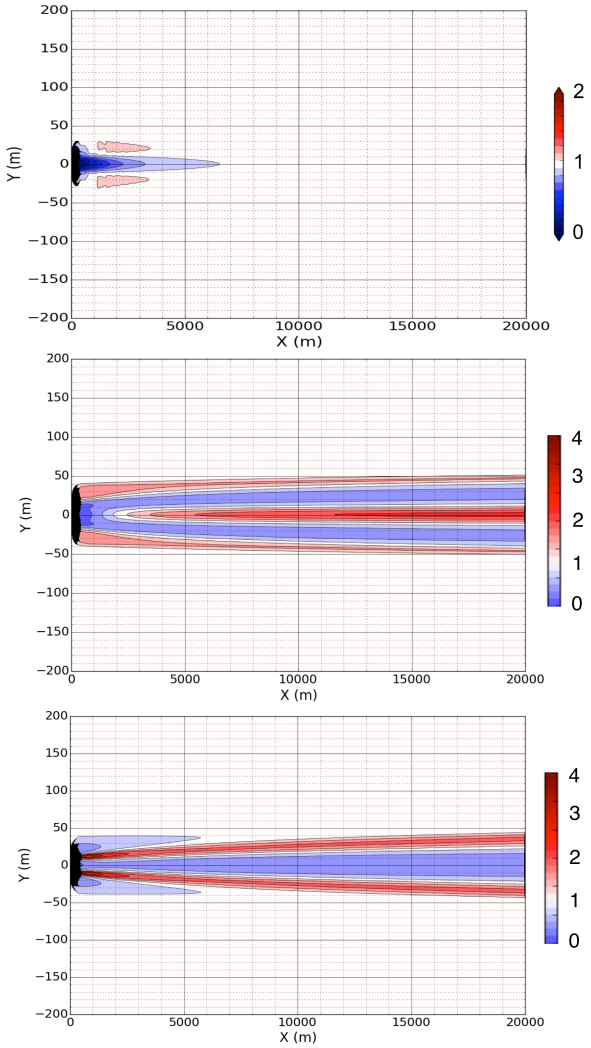

Figure 4.5: Relative SAS distribution (Γ/Γ_0) in calm seas (top), head seas (middle) and following seas (bottom).

produced by LTC in the region of the persistent wake decays as $x^{-0.4}$. It was found that for the case studied here it decreases by an order of magnitude over a distance of about 10 km, while the turbulent kinetic energy in the ship wake decreases by an order of magnitude over about 3 km. It should be noted also that while the turbulence generated by a ship decays with the distance behind the ship there is always some level of turbulence in the upper layer and, correspondingly, of turbulent diffusion due to the presence of the surface waves. Thus, the concentration of SAS in the streaks caused by LTC will eventually start to decrease as LTC decay.

The redistribution of SAS in the case of following seas is shown in Figure 4.5 (bottom). In the near field, the outboard rotating propellers again redistribute SAS away from centerline, but the width is somewhat reduced by the now inboard rotating drag-current induced by the LTC. It is important to note that this predicted initial width is only due to the effects of surface currents and neglects the breaking bow and stern waves, which can cause significant redistribution in the far wake. As LTC develop, the twin converging zones compact SAS into symmetric streaks with widths on the order of 90 m at distances 20 km downstream.

4.4.2 Impact of SAS Redistribution on Wind–Wave Damping Factor

Prediction of the relative damping factor using the SAS concentrations of Figure 4.5, is shown in Figure 4.6. The damping factor is shown relative to pure viscous damping ($4\nu k^2$), for a wave number of $125m^{-1}$ and with an initial film pressure of $\Pi_0 = 1.0\,\mathrm{mN/m}$. It should be noted that the wave numbers dampened by SAS are much higher than those that generate the Stokes drift velocity. Dampening of these short wind waves do not impact the formation or persistence of LTC.

The case of operating in calm seas predicts the formation of two weak damping bands offset from centerline [Figure 4.6 (top)] in line with the weak convergence zones of Figure 4.5 (top). An area of reduced damping relative to ambient level is also predicted along the centerline diverging zone. This condition is expected to form two weak dark streaks along with a brighter streak down centerline in SAR imagery due to the damping of the short wind waves. It is important to note that damping of the short waves is only considered by redistribution of SAS films due to surface currents. SAS films can be significantly redistributed in the near wake by breaking bow and stern waves. In the case of calm seas and extremely light wind, the disturbance of the SAS film by the ship can persist for a long time, even in the absence of LTC.

The structure of the damping factor in the wake of a ship operating in a sea state is highly dependent on the location of converging/diverging surface currents. The convergence zones in the case of head seas form three distinct streaks with strong relative damping, Figure 4.6 (middle). The edge streaks form the edges of the wake on the order of 100m width, while

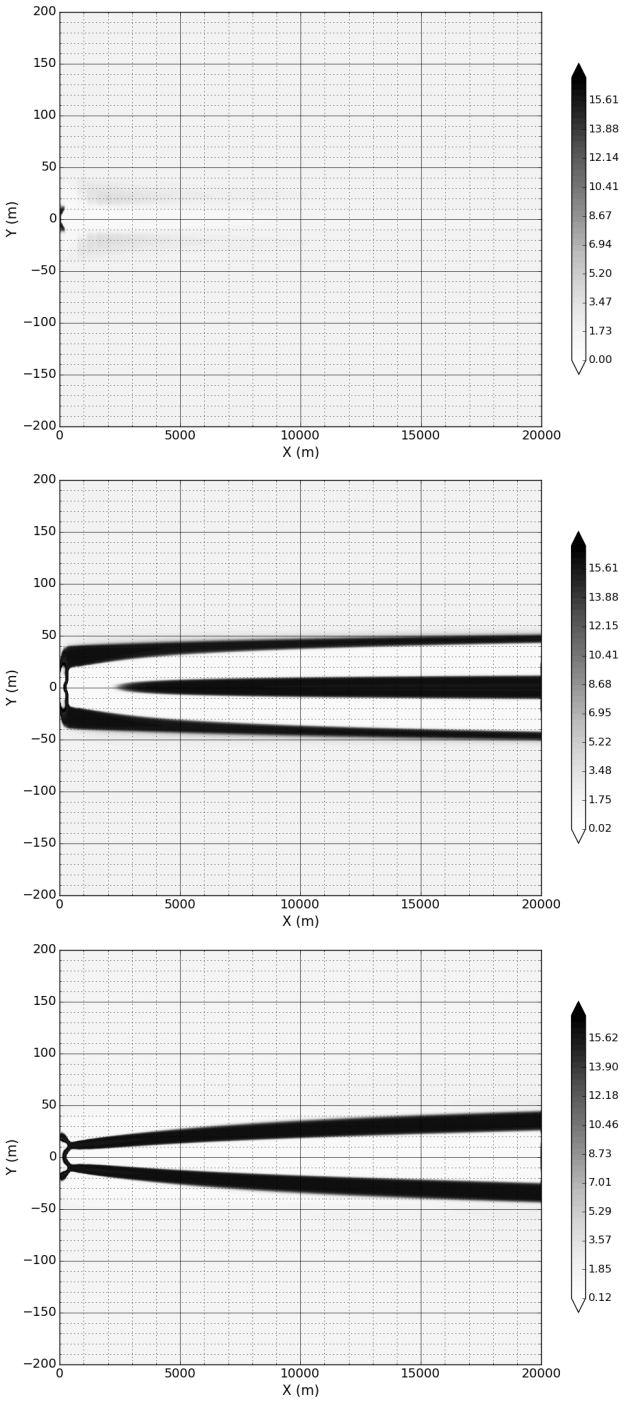

Figure 4.6: Relative damping factor ($\gamma_s/4\nu k^2$) in calm seas (top), head seas (middle), and following seas (bottom) for $\Pi_0 = 1.0\,\mathrm{mN/m}$.

the strong centerline streak spans on the order of the ship beam. These regions of high wave damping would appear as dark streaks on SAR images. The diverging zones exhibit reduced damping relative to the ambient level, which would appear as bright streaks on SAR images between the dark streaks. The appearance of the edge bands in SAR imagery though is highly sensitive to the initial film pressure. The relative concentration in the bands is around 1.3, which is in the range of the steep change in damping with changing film concentration, Figure 4.3. Lower values of initial film pressure reduce the damping factor in the outer bands while the centerline streak remains strong, Figure 4.7. The reduced initial film pressure also reduces the difference in concentration between the diverging zones and the background, which would reduce the relative brightness of the diverging zones in SAR imagery. The appearance of the side bands in SAR imagery is also highly dependent on the strength of the LTC. When the ship travels at some angle to the propagation direction of the surface waves, the magnitude of the vortex force would be reduced relative to direct head seas, generating weaker LTC, and in turn reduced SAS concentrations. The reduced SAS concentration in the outer bands could fall below the required level of concentration to generate significant damping. The centerline streak would persist because it is supported by two converging surface currents, which would generate a single streak on SAR imagery.

Predictions of the relative wave damping in following seas, Figure 4.6 (bottom), show strong damping in the twin converging zones forming the dark railroad track seen in SAR imagery. The centerline diverging zone again shows reduced damping relative to ambient, which would appear as a bright streak on SAR imagery. The regions of high damping can persist for tens of kilometers as even increased SAS concentrations on the order of 1.5 are shown to generate significant damping, Figure 4.3. The railroad track wake is less sensitive to initial film pressure than the outer bands in head seas. SAS concentrations in the twin converging zones are greater than 2.0, limiting its sensitivity to the initial pressure. The railroad–track wake is also less sensitive to the relative ship heading than the outer bands in head seas as they are supported by twin converging circulations in a similar manner as the centerline streak in head seas.

4.5 Comparison with Experimental Data

Comparisons here are again made to the 1989 ONR Field Experiment [118]. During these experiments, data was taken on the variation in surface tension behind the USS Chandler, a US Navy destroyer. This variation in surface tension was converted to film pressure in order to estimate change of the SAS concentration. The peak film pressure based on the data was 12 mN/m, which corresponds to a SAS concentration ratio on the order of 2.1. Unfortunately, the actual peak film pressure could not be determined, since the full range of surface tension measuring oils was not functional during the experiment. Laboratory testing of water samples established film pressures of 21 mN/m, corresponding to a concentration ratio on the order of 3.4. Both the available in–situ data and the laboratory test results

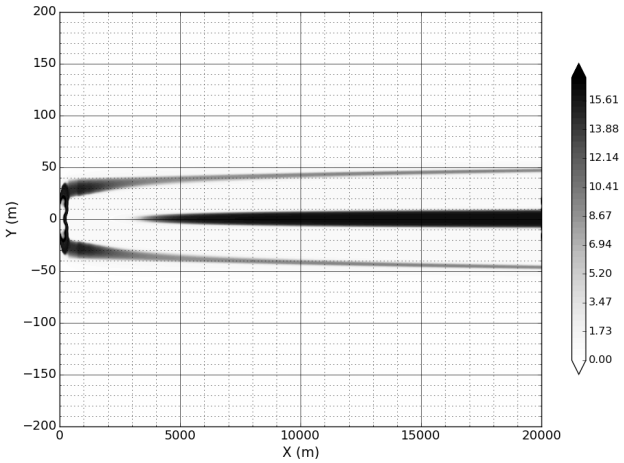

Figure 4.7: Relative damping factor ($\gamma_s/4\nu k^2$) in head seas for $\Pi_0 = 0.5\,\mathrm{mN/m}$. Comparison to Figure 4.6 reveals the sensitivity of the outer bands to the initial film pressure.

compare well with the SAS concentrations, in both head and following seas conditions, obtained in our simulations.

Comparison of structure of the damping factor of short surface waves obtained here is also in good agreement with the SAR image (Figure 1.3) presented in Milgram et al. [98] corresponding to the experimental run for the head seas case. Only one centerline streak (no side streaks) is observed in this case, which may result from lower initial SAS film pressure as well as lower, than predicted, magnitude of the LTC in the experiment. It should be noted that the persistent wake in the SAR image does not form into the more concentrated centerline streak for several kilometers behind the ship. In the far wake, where initial ship–induced perturbations still exist, the short waves are attenuated primarily due to effect of the turbulence. Therefore, the observed wake is initially wider in the far–wake region and then transforms into a narrower persistent wake.

Figure 1.4 shows the same ship operating in following seas, generating a railroad-track persistent wake, which is again in agreement with the predictions made here. Milgram et al. [98] reports that the two smaller vessels that are seen in Figure 1.4 are 0.75 km apart with a total wake length of 7 km. These scales allow the width between the railroad tracks to be estimated on the order of 70 m. Simulations shown here predict a width of 50 m at a distance of 7 km, which is in relatively good agreement with the SAR image of Milgram et al. [98], considering the uncertainty in the parameters of the ship–produced current model and in the record of the ambient conditions during the experiment. As in the head seas case, the surface wave dampening in the far–wake region is believed to be dominated by the effect of the turbulence. Therefore, the persistent railroad track wake in the SAR image in Figure 1.4 is formed at a distance that is on the order of 3-4 km behind the ship.

4.6 Conclusions

The damping of short wind waves due to redistribution of surface–active substances by LTC has been presented as a mechanism of the persistent ship wake observed in remote sensing imagery. These LTC, which are generated by the interaction of ship–induced currents with an ambient wave field, generate surface currents that form converging and diverging zones on the ocean surface. It is within these converging zones that SAS are concentrated and dampen the short wind waves, appearing as dark streaks on SAR imagery. The diverging zones are shown to form areas of reduced damping, which can appear as bright streaks on SAR imagery.

A model relating the concentration of SAS to the short wave damping factor as presented by Milgram et al. [100] has been implemented and compared to the method of Da Silva et al. [29]. Remarkable agreement between the two models was observed for the wave number of a study with an initial film pressure of 1.0 mN/m, providing confidence in the reliability of the model. Both models show a sharp rise in the dampening factor for relative SAS concentrations between 1 and 1.5, with relatively steady values of the damping factor for higher concentrations. Both models also show a dependence of the damping factor on the initial ambient film pressure, which shifts the sharp rise of the corresponding curve towards lower concentrations with higher initial film pressures.

Using the model of Milgram et al. [100], a ship operating in head seas has been shown to form a persistent centerline streak in agreement with SAR imagery presented in Milgram et al. [98]. Two weaker outboard convergence zones are also predicted in the head seas case, but their appearance in SAR imagery is highly dependent on the strength of LTC as well as the initial ambient film pressure.

Using the same model, a ship operating in following seas has been shown to form a persistent railroad–track wake, also in agreement with the SAR image presented in Milgram et al. [98]. The railroad–track wake is also shown to be less sensitive to initial film pressure than the outer bands in head seas.

The simulations presented in this chapter have focused on the damping of short surface waves by SAS films redistributed by ship–generated surface current. The effect of SAS on the short waves is dominant in the region of the persistent ship wake where the surface current is mainly LTC–induced. As was noted in the far–wake region, where initial ship–induced perturbations are still pronounced, the damping of short waves is believed to be primarily caused by turbulence, and the direct effect of the initial current on propagation of the surface waves is also important. Thus, in order to correctly describe the change in the spectral density of the short surface waves everywhere in the wake, all these factors need to be taken into account and the wave action balance model, equation 2.2, has to be solved. These factors will addressed in the following chapter.

Chapter 5

Relative Importance of Turbulence, Surface-Active Substances,and Surface Currents on Roughness Modification of Short Surface Waves in Ship Wakes

(Work adapted from Somero and Paterson [134].)

5.1 Introduction

In the preceding chapters, three distinct regions of ship wakes have been identified: near wake, far wake, and persistent wake. The near wake is defined as the region immediately behind the ship where the wake is dominated by ship induced perturbations from the hull, propellers, and appendages. Within the far wake, these perturbations evolve and decay. The persistent wake is then the region beyond where the initial ship induced perturbations have disappeared. In situ measurements, [98], have found that the edges of the far and persistent wake are defined by the compacting of surface active substances (SAS) into streaks which dampen the surface roughness. The persistence of the streaks are due to surface currents transverse to the direction of travel that compact the SAS, thus increasing SAS concentration and its impact on short-wave damping.

It was demonstrated in chapter 3 that persistent surface currents are generated by Langmuir-type circulations (LTC) when the ship is operating in an ambient wave field. These circulations have been demonstrated to redistribute SAS sufficiently to dampen short wind waves and to form wake structure that compared well with SAR imagery. Comparison to experimental data of Milgram et al. [98] and Peltzer et al. [118], however showed the width of the wake to be under predicted. Due to their size, LTC persist for long distances and as the circulations are induced by the vortex force, the direction of rotation is dependent on the angle between the relative ship heading and the wave vector. This causes the surface currents in the persistent wake, and in turn the redistribution of SAS, to be different depending on

if the ship is operating in head or following seas. Ships operating in head seas were shown to have three streaks in the persistent wake, one strong centerline streak and two weaker edge streaks, while those operating in following seas would have only two edge streaks. The initial film pressure of the ambient SAS field was also shown to impact the persistent wake, especially in head-sea conditions. Lower ambient film pressure requires greater levels of compacting to achieve equal dampening factors. The appearance of the weaker edge streaks in head-sea conditions were shown to be subject to the strength of the LTC and the ambient film pressure.

An additional source of surface currents transverse to the direction of motion was presented by Walker et al. [156] as discussed in chapter 2. It was shown that the presence of the free surface would dampen the vertical velocity fluctuations and redistribute its energy to the lateral fluctuations. Transverse surface currents then would be induced by gradients in the vertical and lateral Reynolds stresses as a function of $\left(\overline{w'^2} - \overline{v'^2}\right)$, where w' and v' are the vertical and transverse velocity fluctuations. As this effect is limited to a thin near surface layer and is dependent on the ship-induced turbulence, its persistence had yet to be quantified, but is addressed here.

In the near and far wake, where ship-induced turbulence still exists, it was hypothesized that turbulence dampens small wind waves through the wake center, giving the appearance of a single wide streak. As the ship-induced turbulence decays, the wide centerline wake transitions into the SAS streak dominated persistent wake. In addition to turbulence, ship-induced surface currents in the near and far wake directly impact the amplitude of short surface waves. Surface currents that travel opposite the short wind waves increase their amplitude and in turn increase their backscatter.

Several authors [93, 100, 126, 149] have formulated models to solve the wave-action balance in the wake of surface ships, but none previously have considered the combined effects of LTC, near-surface Reynolds-stress anisotropy, turbulence, and surface currents that are addressed here. The focus of this chapter is to demonstrate that the structure of the wake is not only due to a single phenomena, but is a function of several effects, each having regions of dominance that change based on ship and environmental conditions. As the near wake is primarily ship dependent, we focus on the far and persistent wakes on phenomena that are universal to wakes across ship types: turbulence, SAS, and surface currents.

This chapter is organized as follows. First a brief description of the model used to predict the hydrodynamic processes in the wake is provided with focus on a range of turbulence models that have been investigated for their ability to predict the formation of surface currents due to near surface Reynolds-stress anisotropy. Next, the model used for redistributing ambient SAS is briefly discussed. Third, a description of the wave-action balance equation is provided along with discussions on the formulations used to account for damping due to SAS and turbulence. Next, results are presented for the turbulence models' predictions of turbulent round jets near a free surface at several laboratory scales. The chosen redistribution model is then used to provide comparison between LTC and near-surface turbulence induced surface

currents. Results of the relative spectral density are presented over a range of ship heading and wave conditions with discussion on the relative importance and range of dominance of each feature discussed.

5.2 Mathematical Model

5.2.1 Hydrodynamics

The governing equations for the hydrodynamic wake are described by the conservation of mass and linear momentum for an unsteady incompressible flow, equations 3.1 and 3.2

$$\frac{\partial U_j}{\partial x_j} = 0, \tag{3.1}$$

$$\frac{\partial U_i}{\partial t} + \frac{\partial (U_i U_j)}{\partial x_j} = -\frac{1}{\rho_0}\frac{\partial \hat{p}}{\partial x_i} + \nu \frac{\partial^2 U_i}{\partial x_j \partial x_j} + \frac{\partial}{\partial x_j}\overline{u_i' u_j'} + \frac{\Delta \rho}{\rho_0} g_j \delta_{ij} + \epsilon_{ijk} U_j^{St} \omega_k. \tag{3.2}$$

In this chapter, to compute the Reynolds stresses, $\overline{u_i' u_j'}$, we explore a range of models for their ability to predict both the subsurface and surface flow field. The base model, used in chapters 3 and 4, is the standard eddy–viscosity model $-\overline{u_i' u_j'} = 2\nu_t S_{ij} - \frac{2}{3}k\delta_{ij}$, which is a linear closure relating the Reynolds stresses to the mean rate of strain $S_{ij} = \frac{1}{2}\left(\frac{\partial U_i}{\partial x_j} + \frac{\partial U_j}{\partial x_i}\right)$. The eddy viscosity ν_t is computed from a standard $k - \varepsilon$ model.

Walker [154] presented a model based on the standard k-ε model to account for the anisotropy induced by the free surface. The standard k-ε model results in essentially isotropic turbulence as $\nu_t S_{ij}$ tends to be small in comparison to k. To account for the redistribution of energy from the vertical stresses to the horizontal, Walker [154] implements a form of the wall reflection term, Φ_{ij}^w, from Daly and Harlow [30] and Shir [128] given as:

$$\Phi_{ij} = \frac{\varepsilon}{k}\left(\overline{u_3' u_3'}\delta_{ij} - \overline{u_i' u_3'}\delta_{3j} - \overline{u_3' u_j'}\delta_{i3}\right) f(z) \tag{5.1}$$

where

$$f(z) = \frac{C l_t}{z - \eta}, \tag{5.2}$$

$l_t = k^{3/2}/\varepsilon$, and η is the local free surface elevation. The value of the coefficient C was not provided, but through extensive experimentation, $C = 0.04$ has been adopted here. This wall-reflection term yields a series of energy redistribution expressions in the thin near-surface

layer for the 'corrected' Reynolds stresses,

$$\begin{aligned}
\overline{w'^2}_{corr} &= \frac{\overline{w'^2}_{k\varepsilon}}{1+2f(z)} \\
\overline{u'^2}_{corr} &= \overline{u'^2}_{k\varepsilon} + \frac{\overline{w'^2}_{k\varepsilon}}{2+1/f(z)} \\
\overline{v'^2}_{corr} &= \overline{v'^2}_{k\varepsilon} + \frac{\overline{w'^2}_{k\varepsilon}}{2+1/f(z)} \\
\overline{u'v'}_{corr} &= \overline{u'v'}_{k\varepsilon} \\
\overline{u'w'}_{corr} &= \frac{\overline{u'w'}_{k\varepsilon}}{1+3f(z)/2} \\
\overline{v'w'}_{corr} &= \frac{\overline{v'w'}_{k\varepsilon}}{1+3f(z)/2}.
\end{aligned} \tag{5.3}$$

The terms identified similar to $\overline{w'^2}_{k\varepsilon}$ are the terms from the standard k-ε model. As the free surface is approached, the vertical stress components approach zero and the horizontal normal stresses each increase by $\overline{w'^2}_{k\varepsilon}/2$. A source term, $-\frac{\partial}{\partial x_j}\Delta\overline{u'_i u'_j}$, is then added to equation 3.2 to account for the redistributed Reynolds stresses, where $\Delta\overline{u'_i u'_j} = \overline{u'_i u'_j}_{corr} - \overline{u'_i u'_j}_{k-\varepsilon}$.

Launder [84] specifies a wall reflection term using a more generic wall distance modification of

$$f(z) = \left(C\frac{k^{3/2}}{\varepsilon x_n}\right)^a \tag{5.4}$$

where x_n is the distance to the surface and a is traditionally taken as 1 such as in the case of Walker [154]. Naot and Rodi [108] found improved agreement in cases of channel flow using a non-linear wall reflection term with $a = 2$ as this caused the wall echo effect to decrease more rapidly with distance from the wall. In order to investigate this effect, models similar to Walker [154] were used with a=2 and 3. Again the value of the coefficient C in equation 5.2 was explored and values of 0.07 and 0.08 were selected for a=2 and a=3 respectively.

These Reynolds-stress redistribution models equally distribute the energy from the vertical normal stress to the horizontal normal stresses. Experimental data of Walker et al. [156] showed that roughly two-thirds of the energy in the vertical velocity w-fluctuations is distributed to the u-fluctuations, with one-third distributed to the v-fluctuations. An additional set of models are therefore explored where equation 5.3 is modified to more accurately

redistribute the energy from the vertical Reynolds stress as

$$\overline{u'^2}_{corr} = \overline{u'^2}_{k\varepsilon} + \frac{2\overline{w'^2}_{k\varepsilon}}{3 + 1/f(z)} \tag{5.5}$$
$$\overline{v'^2}_{corr} = \overline{v'^2}_{k\varepsilon} + \frac{\overline{w'^2}_{k\varepsilon}}{3 + 1/f(z)}.$$

5.2.2 Redistribution of Surface–Active Substances

The redistribution of SAS on the ocean surface is modeled as a passive scalar, as detailed in chapter 4, with a transport equation of

$$\frac{d\Gamma}{dt} + \frac{\partial\left(U_j\Gamma\right)}{\partial x_j} - \frac{\partial}{\partial x_j}\left(D\frac{\partial\Gamma}{\partial x_j}\right) = Source + Sink \tag{4.1}$$

where Γ is the concentration of SAS at the surface, U_i is a vector of the mean surface current, and D is a diffusion coefficient. While in a real ocean environment SAS would also be diffused by wave action, the diffusion coefficient is modeled purely based on the effective eddy viscosity ($D = \nu_t + \nu$). In addition, a real ocean environment would involve sources and sinks of SAS on the surface due to adsorption from rising bubbles and desorption back into the bulk fluid. Both of these effects are neglected but are currently under research. Despite these approximations, chapter 4 presented reasonable correlation with experimental results.

5.2.3 Wave Action Balance

The relative impact of SAS redistribution, turbulence, and surface currents on short–wave attenuation can be evaluated with a model based on the wave action balance equation [55, 62], which can be written as

$$\frac{\partial N}{\partial t} + \left(C_{gi} + U_i\right)\frac{\partial N}{\partial x_i} - k_i\frac{\partial U_i}{\partial x_j}\frac{\partial N}{\partial x_j} = \left(\beta - \gamma\right)N - \alpha N^2 \tag{2.2}$$

where N is the spectral density of wave action, k_i denotes a wave vector of wind waves, C_{gi} is the wind–wave group velocity, and U_i is the velocity of the surface currents. The right–hand side follows the formulation of Hughes [62] where β is the wind–wave growth rate, γ accounts for the damping of the waves due to surface films and turbulence, and α is a phenomenological coefficient to account for the nonlinear effects that limit the wave growth such as wave breaking.

The wind wave growth rate is modeled according to Plant [120] as

$$\beta = 0.04\omega\left(\frac{u_\star}{c}\right)^2 \tag{5.6}$$

where $u_\star$ is the friction velocity and c is the phase velocity, $c = \omega/k$. The friction velocity is given as $u_\star = 0.03U_{wind}$.

The wave-damping term, γ, is modeled as the sum of damping due to SAS films and turbulence as

$$\gamma = \gamma_s + \gamma_t. \tag{5.7}$$

Milgram [96] found that the small-wave decay rate due to the presence of both SAS and turbulence was equal to the sum of the decay rates of SAS and turbulence alone, at least for turbulence levels that could be generated in the laboratory. The damping effect of SAS is caused by increased viscous damping in the interface boundary layer [5]. This effect occurs over a very thin layer at the surface (O(1mm)) that exists within the viscous sublayer of the free-surface boundary layer. The damping effect of turbulence is due to downward convection of wave kinetic energy, which acts over a region that is significantly greater (O(50mm)) than the influence depth of SAS. As the wave-damping effect of SAS is limited to the viscous sublayer, it is relatively unaffected by turbulence, allowing for the use of wave-decay superposition.

Damping due to surface films using the method of Milgram et al. [100] is described in detail in chapter 4. A slight modification has been made here as the method of Milgram et al. [100] approaches zero for low concentration conditions, which would signify damping lower than the clean water condition. The method of Da Silva et al. [29] approaches 1 as the concentration ratio falls below 1. Based on this observation, equation 4.3 is modified here as

$$\gamma_s = 4\nu k^2 \left(\frac{X + XY - 2X^2}{1 - 2X + 2X^2} + 1 \right). \tag{5.8}$$

This equation is equivalent to the form of Da Silva et al. [29] and that given by equation 2.10. The film elasticity is related to the film pressure by

$$E = -A\frac{d\Pi}{dA} = -\frac{d\Pi}{d(ln(A))}. \tag{5.9}$$

In chapter 4 the film elasticy, was modeled using a simplified relationship provided by [118] based on samples taken from a range of sources from Barger and Klusty [11] as

$$E = \frac{26.3\Pi}{\Pi + 2.4}. \tag{5.10}$$

In chapter 4 comparison to the method of Da Silva et al. [29] was presented for a wavenumber of 125, between S and C-Band, for SAS concentrations 0.85-3. Comparison across the wavenumber spectrum is shown in Figure 5.1. Damping relative to pure viscous damping is shown on the left. Higher wavenumbers show higher levels of damping for low SAS concentrations, but peak relatively quickly. X-Band in particular shows a significant rise

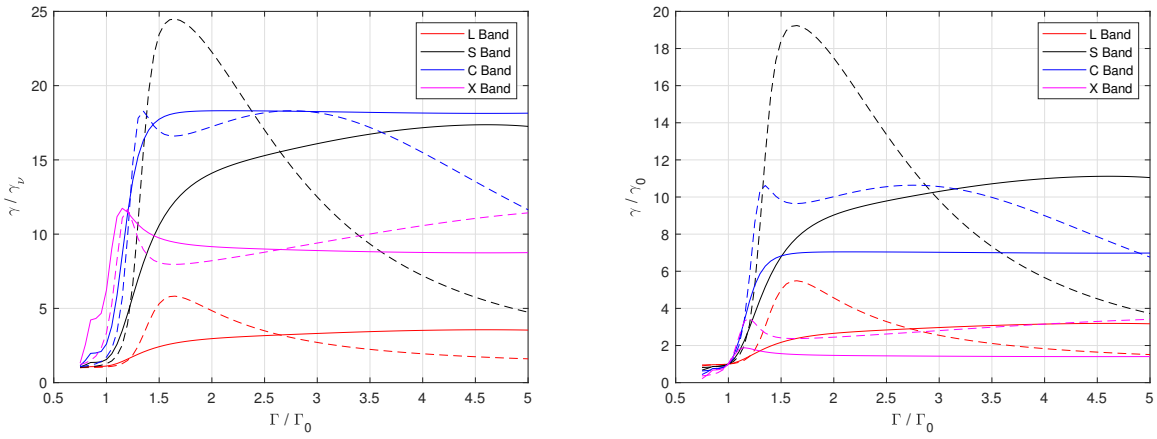

Figure 5.1: Relative damping ratios using film property data from Milgram (solid) and Da Silva (dashed). Left - Damping relative to clean water damping. Right - Damping relative to ambient ($\Gamma/\Gamma_0 = 1$).

in damping levels at low concentrations, but peaks and levels off for concentration ratios greater than 2. This produces significantly higher levels of ambient damping where $\Gamma/\Gamma_0 = 1$ than the lower wave numbers. Comparison against the level of damping outside the wake is shown on the right of Figure 5.1. X-Band shows small relative damping compared to the lower wavenumbers due to its significantly higher level of ambient damping. While C-Band shows the highest levels of absolute damping, S-Band produces the highest levels of damping relative to ambient for all concentration values above 1.5. S-Band also shows increasing damping up to concentration values of 4.5, while C-Band plateaus beyond concentrations of 1.5. L-Band shows increasing damping levels for the full range of concentration levels studied, but is significantly lower than both S and C-Band.

It should be noted though that the elasticity properties of ambient SAS can vary significantly. Elasticity properties taken during the ONR Field Experiment ([115]) varied from day to day with minimum film pressures occurring at film areas ranging from $220cm^2$ to $400cm^2$ over a three day span. Mass and Milgram [94] collected water samples for testing from four locations: Cohasset, MA, Woods Hole, MA ,San Diego, CA, and Hampton Harbor, NH. Variations in the film pressure-elasticity relationship were found across the samples. With the elasticity of each sample known, the agreement between measured wave damping and theory was quite good for all samples.

Chapter 4 found concentration ratios in the wake edge bands between 2.5-3.5 for ships operating in direct head/following seas. In these ranges, the variation between SAS data sets is smaller than for lower concentration values, suggesting that the edge bands would be less sensitive to the local SAS properties over the range of study. Here, equation 5.10 is primarily used along with SAS data from [100], but comparison is made to the properties from Da Silva et al. [29].

Milgram et al. [100] modeled the damping of short wind waves by turbulence based on the experimental results of Ölmez and Milgram [111] and Milgram [96] as

$$\gamma_t = 0.06 \frac{u_1' K^{2/3}}{L_1^{1/3}} \tag{5.11}$$

where K is the wavenumber, u_1' is the root mean square velocity of one of the horizontal components of turbulence, and L_1 is the integral length scale. Assuming w' to be zero at the surface and u' and v' to be of similar magnitude, this model can be transformed into one appropriate for use with a k-ε turbulence model as

$$\gamma_t = 0.06 \left(\frac{K^2 \varepsilon}{C_\mu} \right)^{1/3} \tag{5.12}$$

True et al. [149] calculated a theoretical coefficient of 0.137 based on the mixing rate and a mean value of the vertical velocity fluctuations over the mixing scale length, which is remarkably close to the value used here of 0.134 when $C_\mu = 0.09$.

5.3 Computational Model

The first set of computational models used in this analysis are of a near-surface turbulent jet. This analysis models the experiments of Walker et al. [156] in order to compare the ability of modified k-ε models to simulate the formation of surface currents due to anisotropy of the Reynolds stresses.

The computational models for the ship wake and SAS redistribution are described in chapters 3 and 4. Finally, as the surface currents, SAS field, and rate of turbulence dissipation are steady from the perspective of the ship, a steady-state solution for the spectral density N is obtained.

5.3.1 Domains and Meshing

The domain for the near-surface jet simulations were set to match the experimental setup of Walker et al. [156]. Two domains were used to model the low and moderate Reynolds number cases each with Froude number = 1. The low Reynolds number case ($Re = 1.27 \times 10^4$) had domain limits of $0 < x < 3\,\text{m}$, $-0.75 < y < 0.75\,\text{m}$, and $-1.2 < z < 0\,\text{m}$. Due to the low Froude number, Walker et al. [156] noted that the surface was mostly undisturbed, enabling it to be approximated as a flat boundary. Walker [154] and Miner et al. [101] also treated the surface as a fixed flat boundary. The mesh is constructed of 14 million hexahedron cells with 201 in the x-direction, 351 in the y-direction, and 200 in the z direction, Figure 5.2. Cells in the y-z plane are clustered near the jet centerline and the surface. The jet diameter was

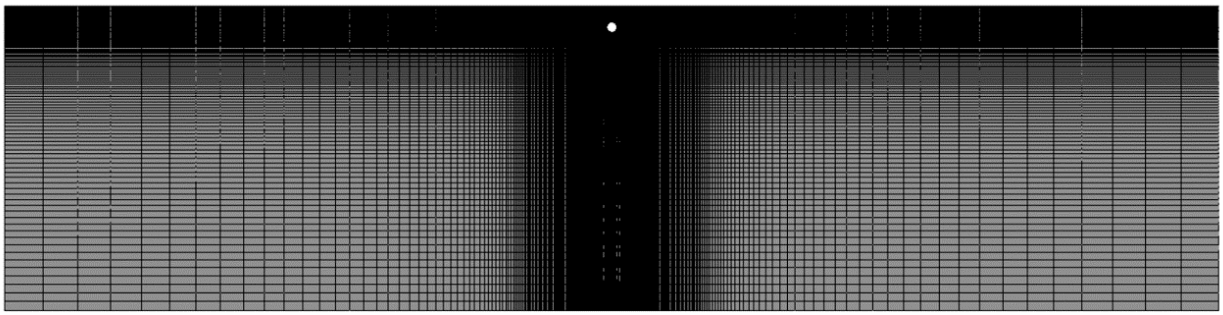

Figure 5.2: Near surface jet simulation mesh.

0.0254 m with the centerline positioned 0.051 m below the surface. The moderate Reynolds number case ($Re = 1.02 \times 10^5$) had domain limits of $0 < x < 12.24$ m, $-3.35 < y < 3.35$ m, and $-3.1 < z < 0$ m. Identical mesh clustering and cell count were used as the low Reynolds number case. The jet diameter was 0.1 m with the centerline positioned 0.2 m below the free surface.

The domain and mesh for the 2d+t hydrodynamic simulations are detailed in chapter 3. For the SAS redistribution, a 2D domain is created on the ocean surface [(x, y) plane at $z = 0$] with dimensions that are inherited from the hydrodynamics simulation. In these simulations, the wake a full 1 hour late is evaluated. Therefore, the size of the 2D domain in meters is $0 < x < 46,000$ and $-1000 < y < 1000$. The mesh uses 4600 equally spaced cells in the axial direction and 2000 equally spaced cells in the transverse direction, for a total cell count of 9.2 million cells with mesh resolution of $\Delta x = 10$ m and $\Delta y = 1$ m in the axial and transverse directions, respectively.

The spectral density of wave action is solved on a 4D grid of the ocean surface: 2 dimensions in space (x,y), wave number (K), and wave angle (ϕ). The limits of the domain are $0 < x < 20.000$ m, $-150 < y < 150$ m, $0 < \phi < 2\pi$, and $0.6 < K < 280$. The spacial domain uses constant spacing of 20 m in the x direction and 0.5 m in the y direction. The wave angle uses 12 equally spaced points and the wave number uses 24 points distributed on a logarithmic scale due to the range being across several order of magnitude.

5.3.2 Numerical methods

The numerical methods for the ship-wake hydrodynamics that solve equations 3.1-3.2 and SAS redistribution that solves equation 4.1 are described in chapters 3 and 4. The near-surface jet simulations also solve equations 3.1-3.2, but exclude the effects of gravity and the vortex force. In order to ensure the performance of the turbulence models would translate to the ship-wake simulations, identical numerical methods were used between the simulations.

The wave-action-balance equations are solved using a modified form of the ERIM Ocean

Model (EOM) ([93]). The code uses a modified upwind finite-difference method for the advective and wave-current interaction terms. Here the spectral density is solved at fixed wave number and spatial coordinates, termed as the action spectral density (A), to permit use of a sweeping algorithm where each grid point is solved each iteration only if it had not reached a converged state the previous iteration. Solutions are considered converged once residuals are reduced to less than 10^{-6}. Also, to account for the need to resolve high wavenumbers, $\partial A/\partial K$ is solved as a perturbation function where $A = A_{eq} + \Delta A$, where A_{eq} is the equilibrium value and ΔA is the difference from equilibrium. This modification is required as the action spectrum falls off as $K^{-4.5}$ at high wavenumbers, which are of utmost interest when simulating SAR response.

5.3.3 Initial and boundary conditions

Initial and boundary conditions must be specified for the primitive variables from all governing equations. This includes $U, k, \varepsilon, T, S, p, \Gamma$, and A.

Initial conditions for the near-surface jet simulations were based on the experimental setup of Walker et al. [156]. The $Re = 1.27 \times 10^4$ case used an initial jet velocity $U = 0.5\,\mathrm{m/s}$, $k = 9.4 \times 10^{-6}\,\mathrm{m^2/s^2}$, and $\varepsilon = 1.45 \times 10^{-6}\,\mathrm{m^2/s^3}$. The $Re = 1.02 \times 10^5$ case used an initial jet velocity $U = 1\,\mathrm{m/s}$, $k = 4 \times 10^{-5}\,\mathrm{m^2/s^2}$, and $\varepsilon = 1.45 \times 10^{-5}\,\mathrm{m^2/s^3}$. The surface was treated as a slip boundary (zero gradient for all variables, except for the normal component of velocity which is set to zero) and the outlet was treated as an inlet/outlet pressure boundary which ensures flow may only leave through the boundary, preventing back-flow.

The initial conditions for the ship wake hydrodynamic simulations at $t = 0\,\mathrm{s}$ are described in detail in chapter 3. Of unique interest here is the flat slip-wall boundary at the free-surface. As our primary area of interest is the persistent wake, the use of a flat-slip free surface is considered valid, as in this region the ship induced currents have decayed sufficiently to be considered low Froude number, similar with the conditions of the near-surface jet simulations. The use of such a boundary condition, however, should be limited to low to moderate sea-state conditions where significant wave breaking would not occur. This requirement is consistent with the derivation of the vortex force that assumes monochromatic irrotational waves. It is also consistent with the approximation made here that SAS is diffused only through turbulent eddy viscosity. Conditions of moderate to high sea-states would act to dissipate SAS concentrations, significantly limiting the detectability of a persistent wake. The initial conditions for the SAS redistribution are described in chapter 4.

The initial conditions for the wave-action balance solver are based on the hydrodynamic and SAS redistribution simulations. The surface currents, SAS concentrations, and turbulence dissipation rate distributions are mapped to the spacial grid using bi-linear interpolation. The action spectral density is set to the equilibrium conditions at the spacial boundaries as well as the ends of the spectral domain. Here the damping is limited to viscous damping, given as $\gamma_\nu = 4\nu K^2$, damping due to ambient SAS ($\Gamma/\Gamma_0 = 1$), and damping due to ambient

surface turbulence.

5.3.4 Fluid properties and flow conditions

The fluid properties are described by the density and the kinematic viscosity. For the near-surface jet simulations, the kinematic viscosity and density were set to $\nu = 1 \times 10^{-6}\,\mathrm{m^2/s}$ and $\rho = 1000\,\mathrm{kg/m^3}$.

The kinematic viscosity is set to $\nu = 1.0 \times 10^{-6}\,\mathrm{m^2/s}$ with a density of $\rho = 1025\,\mathrm{kg/m^3}$ for the ship wake simulations. The ambient turbulent kinetic energy for the ship wake simulations is set to $k = 2 \times 10^{-4}\,\mathrm{m^2/s^2}$ and turbulent dissipation rate is set to $\varepsilon = 2 \times 10^{-7}\,\mathrm{m^2/s^3}$ based on the observations of Wu et al. [160].

Surface wave parameters are set to explore a range of ocean conditions under which SAS streaks could reasonably be expected to persist. In order to provide additional comparison with figures 1.3 and 1.4, longer surface waves than those used in chapters 3 and 4, as observed in the figures, are used. Here, wave amplitudes between 0 and 1.5 m and wavelength of 50 m are used. It is known that the exact form of the wind-wave spectra is not crucial for the effect of the vortex force on the non-uniform current [13], so the surface waves are approximated as monochromatic waves.

Relative wave–ship heading angles of 0° and 180° are used to simulate head– and following–seas conditions as these are the limiting cases. Angles between 0° and 180° can also be simulated, but mesh domain considerations must be made for wake drift at alternate angles. Full–scale ship parameters are used with $Fr = 0.35$, $Re = 1.85 \times 10^9$, and a ship speed of $U_0 = 13\,\mathrm{m/s}$.

Damping of the short wind waves is calculated using a surface roughening wind speed of 2 m/s to provide comparison with the SAR data reported by [100]. Sea wavenumbers are set to the Bragg resonant values for L,S,C, and X Band to explore the variation with frequency. The Bragg resonant water wave frequency (f_w) is related to the radar frequency (f_r) as given by [98]:

$$f_w = \sqrt{\frac{g f_r sin\theta}{\pi c} + \frac{16\pi\tau f_r^3 sin^3\theta}{\rho c^3}} \tag{5.13}$$

where θ is the incidence angle of the radar beam, c is the electromagnetic wave speed, τ is the surface tension, and ρ is the sea water density.

An ambient surface turbulent dissipation rate of $1 \times 10^{-5}\,\mathrm{m^2/s^3}$ is used for the surface wake simulations. This is based on a balance of available data. In addition to Wu et al. [160], St. Laurent and Merrifield [137] provides mean dissipation rates with near surface values on the order of $2 \times 10^{-7}\,\mathrm{m^2/s^3}$. St. Laurent and Merrifield [137] also shows data over a two week period with significant fluctuations in the near surface dissipation rate due to solar heating

where peaks of $1 \times 10^{-4}\,\mathrm{m}^2/\mathrm{s}^3$ are observed during the day. Sutherland and Melville [141] report measured values as high as $1 \times 10^{-2}\,\mathrm{m}^2/\mathrm{s}^3$ for higher wind conditions (17 m/s) where significant wave breaking occurs. Dissipation rates for more moderate wind speeds (10 m/s) are on the order of $4 \times 10^{-4}\,\mathrm{m}^2/\mathrm{s}^3$ at a depth of 5 cm and decaying to $1 \times 10^{-5}\,\mathrm{m}^2/\mathrm{s}^3$ at a depth of 1 m. As the majority of the turbulent dissipation occurs in the upper 5 cm of the ocean boundary layer, the higher dissipation rates are primarily used here with a range investigated to demonstrate the impact of the ambient surface turbulence.

5.4 Results

In this section, we present simulation results for the hydrodynamics of the far and persistent wake and the impact of SAS, turbulence, and surface currents on the spectral density in the wake. First, the accuracy of a range of turbulence models are explored and compared to the experimental results of Walker et al. [156]. The turbulence model of choice is then implemented and used in the simulation of the far/persistent wake. Here, there are two primary outputs: turbulent dissipation rate (ε) and surface currents. The simulated surface currents then are used to redistribute SAS and establish the steady state SAS concentrations. Finally, the surface currents, SAS distribution, and turbulent dissipation rate are used to simulate the impact on surface roughness as measured through the wave-action spectral density.

5.4.1 Near-Surface Turbulence Modeling

Implementation of a near-surface Reynolds-stress redistribution model requires balancing the prediction of the induced surface currents with the impact on the subsurface flow. Walker et al. [156] demonstrated that the formation of the surface currents is due to the redistribution of energy from the vertical normal Reynolds stress to the horizontal normal Reynolds stresses and that this redistribution acts over a thin near-surface layer. It is important then to ensure the Reynolds-stress redistribution is limited to this thin layer to minimize the impact on the subsurface flow. The redistribution model of Walker [154] uses a linear wall reflection term, equation 5.4, that is shown to not provide sufficient decay rates away from the surface, Figure 5.3. The use of non-linear wall reflection terms (a=2,3) though show improved agreement with the experimental results. Here, Reynolds stresses, as calculated using the standard $k-\varepsilon$ model at $x/d = 32$, are redistributed using equation 5.3.

The simulated surface currents for $Re = 1.02 \times 10^5$ that use the 2/3-1/3 redistribution model of equation 5.5 are shown in Figure 5.4. The centerline axial-velocity profiles are shown in Figure 5.5. Setting the coefficient C in equation 5.2 is a balance between capturing the peak surface currents, the decay in the surface currents away from centerline, and the subsurface axial-velocity profile. Increasing C raises the level of Reynolds-stress redistribution, which

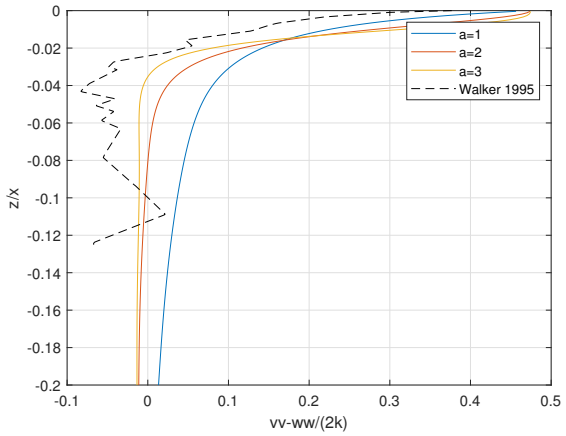

Figure 5.3: Vertical distribution of $\left(\overline{w'^2} - \overline{v'^2}\right)$ for the near surface turbulent jet of [156] at Re=102,000 using wall reflection exponents (Equation 5.4) ranging from 1-3 at x/d=32.

increases the peak surface current, but also decreases axial velocities. Larger coefficients also delay the outboard decay of the surface currents, leading to higher predicted currents outboard of the peaks.

The root-mean-square error for the surface currents and axial-velocity profiles of each model for $Re = 1.02 \times 10^5$ are shown in Table 5.1. Here '2/3' designates the 2/3-1/3 redistribution models of equation 5.5. The first three redistribution models are based on equation 5.2. The baseline $k - \varepsilon$ model produced the best sub-surface axial-velocity profile at the downstream station of $x/d = 32$. At $x/d = 16$, the peak of the velocity profile was under predicted. It should be noted that the standard $k - \varepsilon$ model uses $C_\mu = 0.09$. Use of $C_\mu = 0.08$ for the redistribution models is based on the improved agreement in capturing the centerline axial-velocity peak. Each redistribution model was was able to be tuned to predict reasonable surface currents, but the linear wall reflection term used by Walker [154] significantly under predicted the axial-velocity profile. The non-linear wall reflection models were able to be tuned to similar performance. The quadratic model had slightly better prediction of the surface currents while the cubic model showed a better centerline axial-velocity profile. The quadratic model also showed slightly better agreement with the y-position of the surface current peak and outboard decay. Similar performance was achieved between the models that used equal redistribution to the normal stresses and the models that provided 2/3 of the vertical normal stress to the axial normal stress.

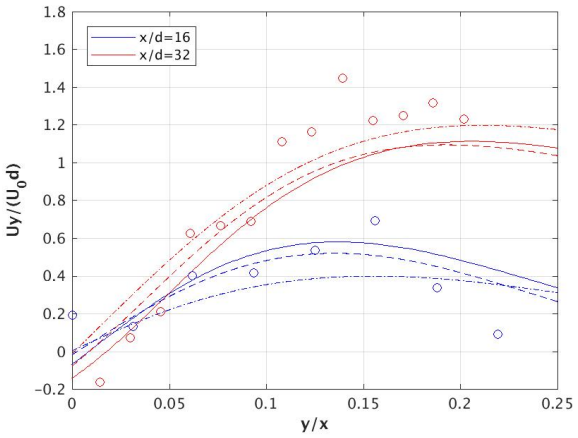

Figure 5.4: Transverse surface currents for the near-surface turbulent jet at $x/d = 16$ and 32 at $Re = 1.02 \times 10^5$. Dash-dot lines: $a = 1$, Dashed lines: $a = 2$, Solid lines: $a = 3$, o: [156]

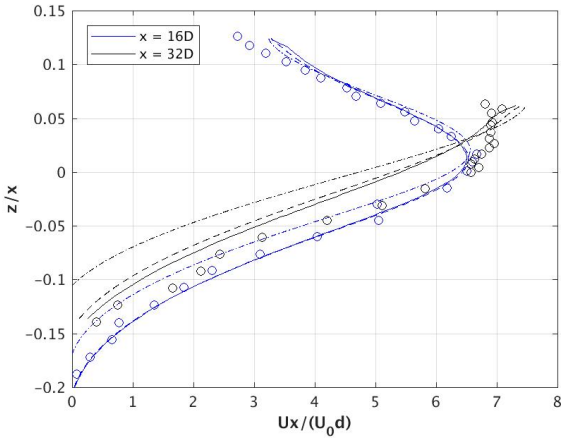

Figure 5.5: Centerline axial-velocity profiles for the near-surface turbulent jet at $x/d = 16$ and 32 at $Re = 1.02 \times 10^5$. Dash-dot lines: $a = 1$, Dashed lines: $a = 2$, Solid lines: $a = 3$, o:[156]

Table 5.1: Root-mean-square error of the simulated surface currents and centerline axial velocity profiles for the near surface turbulent jet at $Re = 1.02 \times 10^5$.

	Surface Currents		Centerline Velocity	
Model	x/d=16	x/d=32	x/d=16	x/d=32
$k - \varepsilon$	0.448	0.908	0.347	0.420
a=1	0.175	0.199	0.361	1.352
a=2	0.1758	0.1788	0.226	0.826
a=3	0.172	0.241	0.291	0.466
2/3 (a=1)	0.1736	0.1781	0.425	1.321
2/3 (a=2)	0.1462	0.1951	0.223	0.803
2/3 (a=3)	0.1737	0.2029	0.245	0.676

The turbulence models were also tested against a near-surface jet at $Re = 1.27 \times 10^4$ with the root-mean-square errors presented in Table 5.2. The surface current and subsurface-velocity profiles were similar to those of the higher Reynolds number case. Again, the linear wall-reflection model significantly under predicts the centerline axial-velocity profile while the non-linear models produce similar results.

Table 5.2: Root-mean-square error of the simulated surface currents and centerline axial-velocity profiles for the near-surface turbulent jet at $Re = 1.27 \times 10^4$

	Surface Currents		Centerline Velocity	
Model	x/d=16	x/d=32	x/d=16	x/d=32
$k - \varepsilon$	0.390	0.812	0.339	0.350
a=1	0.173	0.166	0.374	1.265
a=2	0.142	0.164	0.298	0.594
a=3	0.174	0.220	0.281	0.528
2/3 (a=1)	0.202	0.196	0.376	1.183
2/3 (a=2)	0.199	0.211	0.156	0.462
2/3 (a=3)	0.1516	0.1571	0.3018	0.5028

The most significant variation between Reynolds numbers was the prediction of the outboard decay rate of the surface currents. The higher Reynolds number case under predicted the decay rate, while the lower Reynolds number case showed much better agreement with the experimental data at the outboard locations.

One potential shortcoming of these models is the use of the turbulent length scale to determine the depth of redistribution as it is not constant across the surface, Figure 5.6. Each case shows a variation in the length scale across the jet of approximately 20%. This leads to the depth of redistribution being greater at the edges of the jet current than along the centerline. Miner et al. [101] used a length scale based on $1/4^{th}$ of the jet half-width to determine the

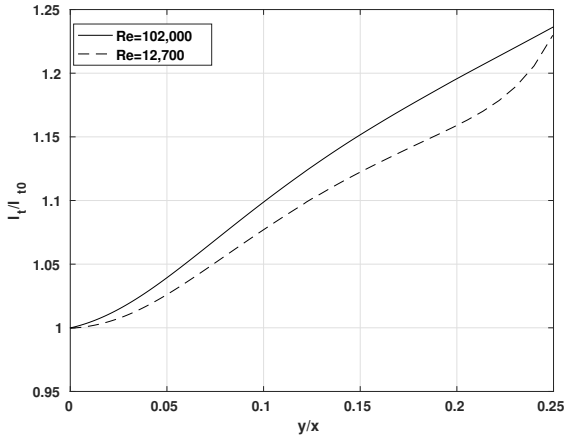

Figure 5.6: Turbulent length scale on the surface for the near-surface jet simulation at $x/d = 32$ using the quadratic wall reflection 2/3-1/3 redistribution model.

depth of redistribution and achieved reasonable results compared to the $Re = 1.27 \times 10^4$ case using an algebraic stress model. Miner's model also incorporated a near-surface modification to the turbulent dissipation rate that is not accounted for here. Establishing the local half-width for a constantly evolving ship wake would be challenging though, and results at higher Reynolds numbers were not presented. As the primary quantity of interest for the ship-wake simulations is the formation of surface currents, the quadratic model is chosen to be used. Also, since no significant difference in performance was observed between the models with equal vertical normal stress redistribution and those with 2/3 redistribution to the axial normal stress, the 2/3 redistribution model is chosen due to the experimentally observed redistribution.

5.4.2 Hydrodynamics

The observable structure of the persistent wake is due to the compacting of surface active substances into streaks by surface currents that are transverse to the direction of ship motion ([118],[98]). It was demonstrated in chapter 3 that persistent surface currents could be induced by Langmuir-type circulations (LTC) in the wake of a ship operating in an ambient wave field. LTC are formed by the interaction of the ship–induced drag and thrust current with the ambient waves, where the direction of rotation is dependent on the ship heading relative to the wave field. The case of the ship operating in head seas was shown to form an inner pair of LTC that rotate top-inboard and an outer pair that rotate top-outboard. These submerged circulations induce a strong centerline convergence zone due to the inboard rotating circulations and two weak outer convergence zones. The ship operating in following seas was shown to form persistent circulations that rotate in the opposite direction to the head seas case. The inboard circulations rotate top-outboard and the outboard pair rotate

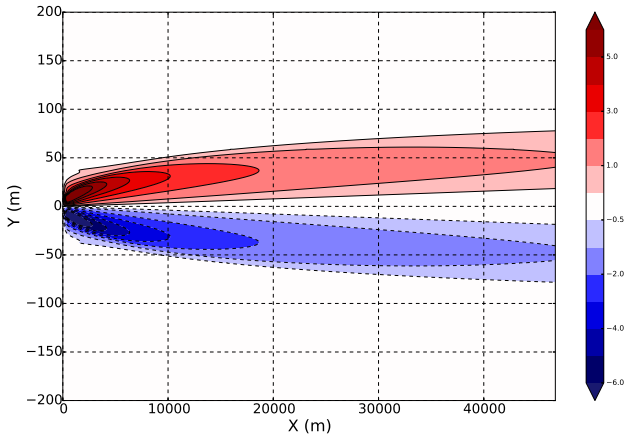

Figure 5.7: Transverse surface velocity (cm/s) for a ship operating in calm seas.

top-inboard. The induced surface currents in following seas form two strong convergence zones that are offset from the centerline with a diverging zone between them.

Here, we combine the effects of surface currents due to LTC and those induced by near-surface Reynolds-stress anisotropy and examine the impact of each based on changing ambient wave conditions. As evident by equation 3.3, the strength of the LTC, and in turn their induced surface currents, is a function of the ambient wave field.

First, we examine the induced surface currents for calm seas, where the wave amplitude is zero, Figure 5.7. The surface currents induced by the near-surface Reynolds-stress anisotropy form currents away from ship centerline and reinforce the outboard currents generated by the propellers. It was demonstrated in chapter 3 that the surface currents induced by the propellers mostly decay by 6000m. Here, outboard currents O(1cm/s) are shown to be maintained well into the persistent wake.

Next we examine the impact of a ship operating in following seas over a range of wave amplitudes. As the ship in following seas generates LTC that induce surface currents away from centerline, they reinforce the outboard currents due to the near-surface Reynolds-stress anisotropy. It was shown in chapter 3 that the set of inboard circulations formed in following seas was significantly stronger than the outboard circulations. The induced surface currents of the outboard circulations dissipated by 10km. Here, the surface currents due to Reynolds-stress anisotropy are shown to cancel the inboard current generated by the outboard LTC, while the growing inner LTC reinforce the outboard Reynolds-stress anisotropy induced current. The surface currents are observed to increase in magnitude and width with increasing wave amplitude due to the increased vortex force.

Finally, the condition of a ship operating in head seas is considered. The surface currents for wave amplitudes of 0.5 m to 1.5 m are shown in Figure 5.9. At low wave amplitude (0.5 m), the inner LTC are only sufficiently strong to dampen the turbulence anisotropy induced outboard currents. With increasing wave amplitude, the inner LTC strengthen and form the centerline

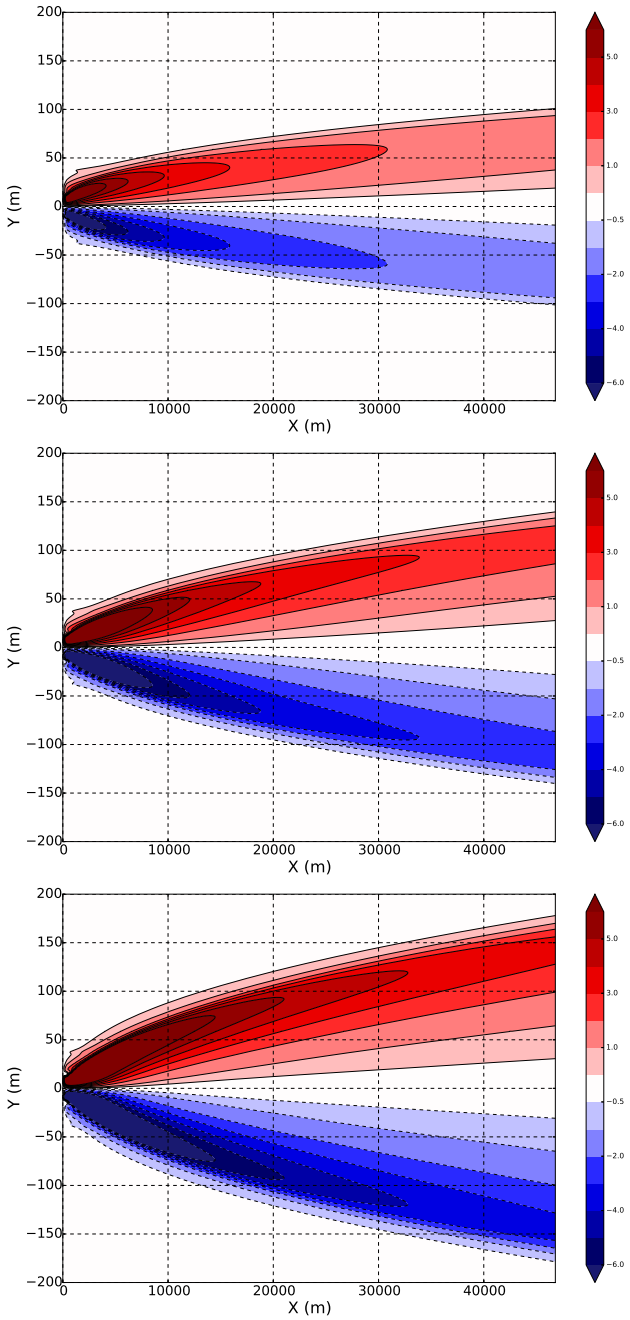

Figure 5.8: Transverse surface velocity (cm/s) for a ship operating in following seas with wavelength of 50 m and wave amplitudes of 0.5 m, 1.0 m and 1.5 m.

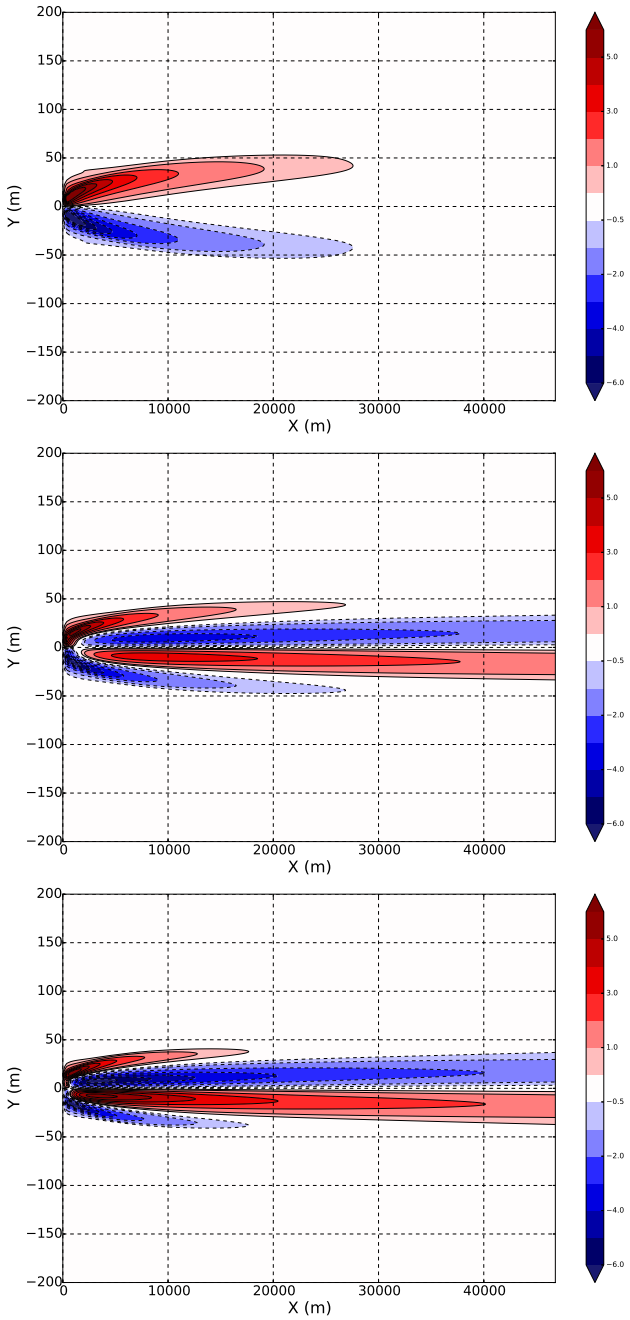

Figure 5.9: Transverse surface velocity (cm/s) for a ship operating in head seas with wavelength of 50 m and wave amplitudes of 0.5 m, 1.0 m and 1.5 m.

convergence zone observed at 1 m and 1.5 m wave amplitudes. Simultaneously, the outboard surface currents are dampened and are mostly dissipated by 20 km with wave amplitude of 1.5 m. Aft of this position, a single centerline convergence zone persists. Forward of this point though, three convergence zones exist. The centerline convergence zones for the 1 m and 1.5 m wave amplitudes are similar in magnitude and persistence. The primary difference between the centerline convergence zones is in the far wake where the 1.5 m wave amplitude case shows the formation of strong surface currents around 4000 m, where as the 1 m wave amplitude case peaks around 10 km with reduced magnitude.

5.4.3 SAS Redistribution

Ambient SAS is redistributed in the wake by the induced transverse surface currents. Concentration ratios for calm seas, following seas, and head seas are shown in Figure 5.10 at locations 3.5 km and 10 km behind the ship. The cases of following seas and head seas are both for a 1.0 m wave amplitude. At a distance of 3.5 km, the structure of the edge bands is similar between all three conditions with following seas showing stronger concentrations that have moved slightly more outboard. Both head seas and calm seas predict SAS concentrations around 3 at this distance with following seas predicting concentrations around 4. Head seas also shows a strong centerline streak also with a concentration ratio of 3. The reduction in concentration through the wake center, other than the head seas centerline streak, is similar between head and following seas where almost all SAS is redistributed into one of the streaks. Greater than half the SAS through the center is redistributed in the case of calm seas.

At a distance of 10 km, the SAS concentration edge streaks have moved outboard and reduced in magnitude. Here, the following seas edge band has separated from the calm and head seas cases and maintained higher concentration levels. The centerwake region is similar between following and calm seas. The edge bands of the head seas case remain similar in magnitude to the calm seas condition, but move less outboard due to the growing inboard rotating LTC. The centerline streak in head seas now dominates the wake with SAS concentration ratios similar to following seas at 3.5 km. The reduction in SAS concentration in the centerwake, outside the streaks, is now greatest for head seas due to the strong centerline convergence zone. The SAS concentration levels predicted here at 10 km for calm and following seas now fall into the range where the SAS film pressure-film area relationship is significantly variable across the cases studied and would impact the observed persistence of the edge bands, Figure 2.2.

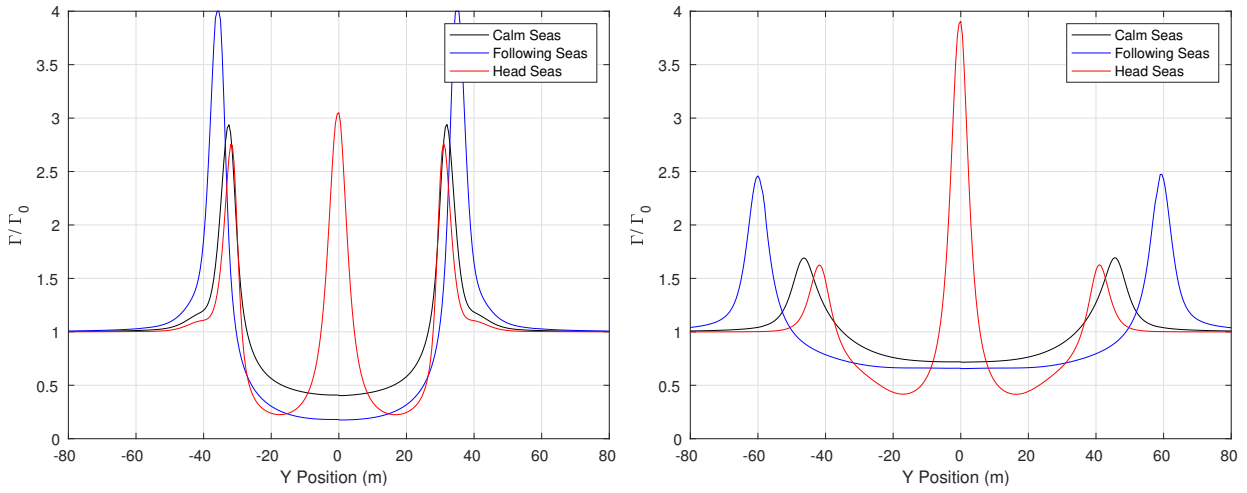

Figure 5.10: SAS concentration ratios 3.5 km (left) and 10 km (right) downstream for calm, following, and head seas cases. Following seas and head seas cases use a wave amplitude of 1.0 m each.

5.4.4 Impact of SAS, Turbulence, and Surface Currents on Surface Roughness

The impact of SAS, turbulence, and surface currents on surface roughness is evaluated through the spectral density from the wave-action balance, equation 2.2. Here the spectral density is measured relative to the ambient equilibrium value taken outside the wake. In a similar fashion to the hydrodynamic results, we present the spectral density plots based on ambient-wave conditions. First, we present the case of calm seas, where LTC are not formed. In order to establish the direct impact of surface currents, we initially set turbulence levels and SAS to their ambient conditions everywhere, Figure 5.11. Values of the spectral density are shown for conditions where the wave energy is traveling across the wake (left) and along the wake (right) and at wavenumbers corresponding to Bragg resonant wavenumbers for L, S, C, and X band radar. As expected, the wave energy is significantly modified across the wake due to the strong transverse velocity gradients induced by the near surface Reynolds stress anisotropy, Figure 5.12. The effect is observed to be strongest for lower wavenumbers (L and S). At L band, the centerline sees strong damping due to the positive transverse velocity gradients with bright bands of amplified roughness defining the wake edges due to the negative gradients outboard. As wavenumber increases, the relative impact of the edge bands decreases in comparison to the centerline damping. The observed asymmetry is due to the direction of wave energy. Wave energy traveling in the opposite direction mirrors the images shown here. Wave energy along the wake is significantly less impacted by the wake across the frequency spectrum. At L band, near field structure from the velocity gradients induced by the propeller and breaking waves are visible. At higher wave numbers these details are lost and primarily replaced by centerline damping with short lived edge bands of

elevated energy.

The inclusion of ship induced turbulence, Figure 5.13, is similar in structure to the case without it for energy traveling across the wake, but with increased dampening through the wake center where ship-induced turbulence is strong. The bright streaks of elevated wave energy due to the transverse velocity gradients persist and define the wake edges. Similar to the case with only surface currents, Bragg-resonant wavenumbers for L-band radar show higher sensitivity to turbulent dampening than X-band as $\gamma_t \propto K^{2/3}$. Since the spectral density is measured relative to the ambient environment, the impact of turbulent dampening decreases moving from L-band to X-band. The roughness amplification due to the outboard currents is partially damped and the turbulent centerline wake now shows longer persistence than the outboard amplified roughness for frequencies greater than L band. The structure of energy traveling along the wake is simplified with the inclusion of turbulent damping. The nearfield details observed with only surface currents included have been covered by the centerline damping.

Including SAS redistribution significantly changes the surface roughness modification, Figure 5.14. The transverse surface currents shown in Figure 5.7 redistribute SAS to the wake edges and form streaks where the spectral density is damped into the persistent wake. Strong damping due to SAS is primarily observed at wavenumbers less than X-Band, with the maximum relative damping at S band. Under conditions with reduced ambient SAS and where SAS sources are included, X-Band damping would be expected to be more pronounced than the lower wavenumbers due to the higher absolute damping.

The surface-roughness amplification due to the outboard current gradients has now been mostly damped by SAS. At higher wavenumbers though, the centerwake is dominated by the brightness of the amplified roughness due to wind where the SAS has been removed and redistributed to the wake edge. At X band, the centerline amplification exceeds the damping due to SAS along the edge bands. The structure of the wake centerline at lower wave numbers is similar to the case without SAS redistribution, with elongated centerline damping of wave energy across the wake compared to the damping of energy along it. Wake widths of 110 m at 10 km and 140 m at 20 km behind the ship are predicted.

The spectral density using elasticity data from Da Silva et al. [29], Figure 5.16, shows the wake structure to be quite similar to Figure 5.14. At a downstream distance of 5 km, the edge bands are similar in magnitude as the SAS concentration ratios in the near/far field are around 3. Use of the SAS properties from Da Silva et al. [29] predicts a reduced centerline roughness amplification as the ambient SAS damping (γ_0) is lower than that from Milgram et al. [98]. Further downstream, the delta between the edge bands grows as the concentration ratios begin to diminish. This has implications on both the strength and persistence of the edge bands with changing SAS elasticity characteristics.

The spectral density distribution in the wake of the ship operating in following seas is shown in Figures 5.17-5.19. The structure of the wake is similar to the case of calm seas for a wave amplitude of 0.5 m. Turbulence and surface currents dissipate short waves in the

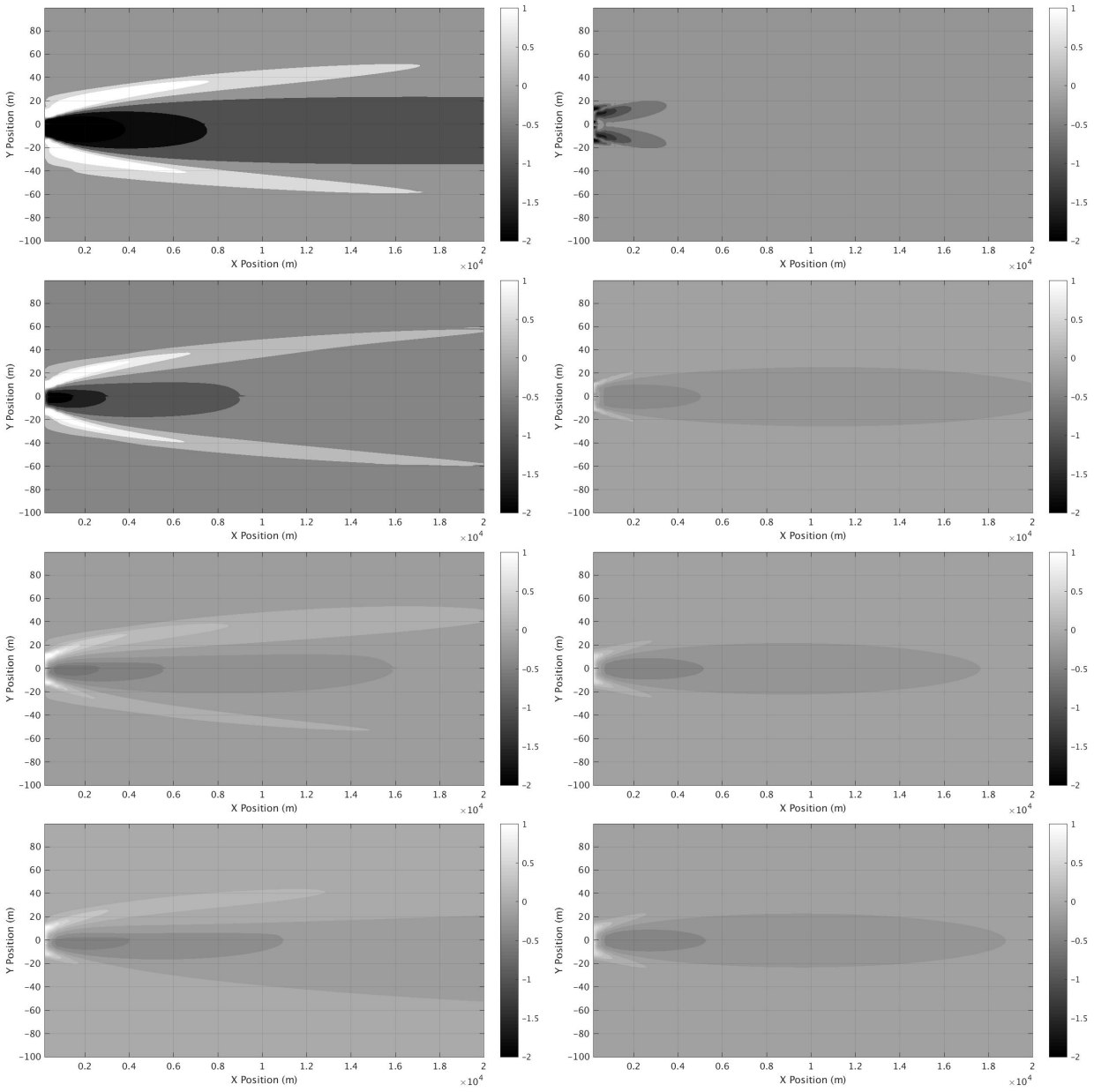

Figure 5.11: Spectral Density (dB) for a ship operating in calm seas with turbulence and SAS set to ambient conditions everywhere at L, S, C, and X Band. Spectral energy is taken across wake (left) and along wake (right).

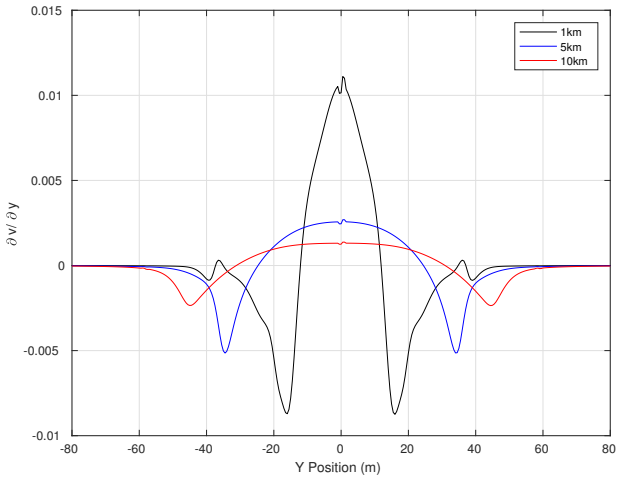

Figure 5.12: Transverse gradient in transverse surface current at 1km, 5km, and 10km downstream in calm seas.

near/far wake, while streaks of SAS provide persistent damping for distances greater than 20 km. Streaks of amplified surface roughness are again observed between the center wake and the edge bands where SAS has been removed, but outside the turbulent damping zone. The impact of LTC amplifying the spectral energy in this region is most easily observable for L-Band with reduced amplification at higher frequencies. As expected, higher wave amplitudes, which generate stronger LTC, further enhance the amplification due to larger velocity gradients, Figure 5.20.

Cross-sections of the spectral density at distances 3.5 and 10 km behind the ship are shown in Figure 5.21. Damping due to SAS along the outboard edges of the wake is clearly observed with lower spectral density values in the along wake direction. The damping characteristics of SAS are not impacted by the direction of wave energy, but the amplification of surface roughness in the across wake direction due to surface currents reduces the reduction of spectral density relative to the ambient. The strong centerline damping at 3.5 km due to turbulence and surface currents is clearly observed in the across wake direction with reduced modification in energy along the wake. At a downstream distance of 10 km, the centerline damping due to turbulence and surface currents has mostly diminished, while the damping due to SAS along the edge bands persists. At this 1 m wave amplitude, wake widths of 140 m and 185 m are predicted at 10 km and 20 km behind the ship for damping values of -0.5 dB. Increasing wave amplitude also increases both the width and the persistence of SAS damping.

It was demonstrated in chapter 3 that the centerline upwelling zone formed by LTC in following seas decreased the decay rate of the axial surface current induced by the ship propellers, which in turn supports increased LTC persistence. The outboard currents along centerline were also shown in chapter 3 to widen the thrust current with increasing distance. This effect forms a centerline region in the persistent wake where outboard velocities are no

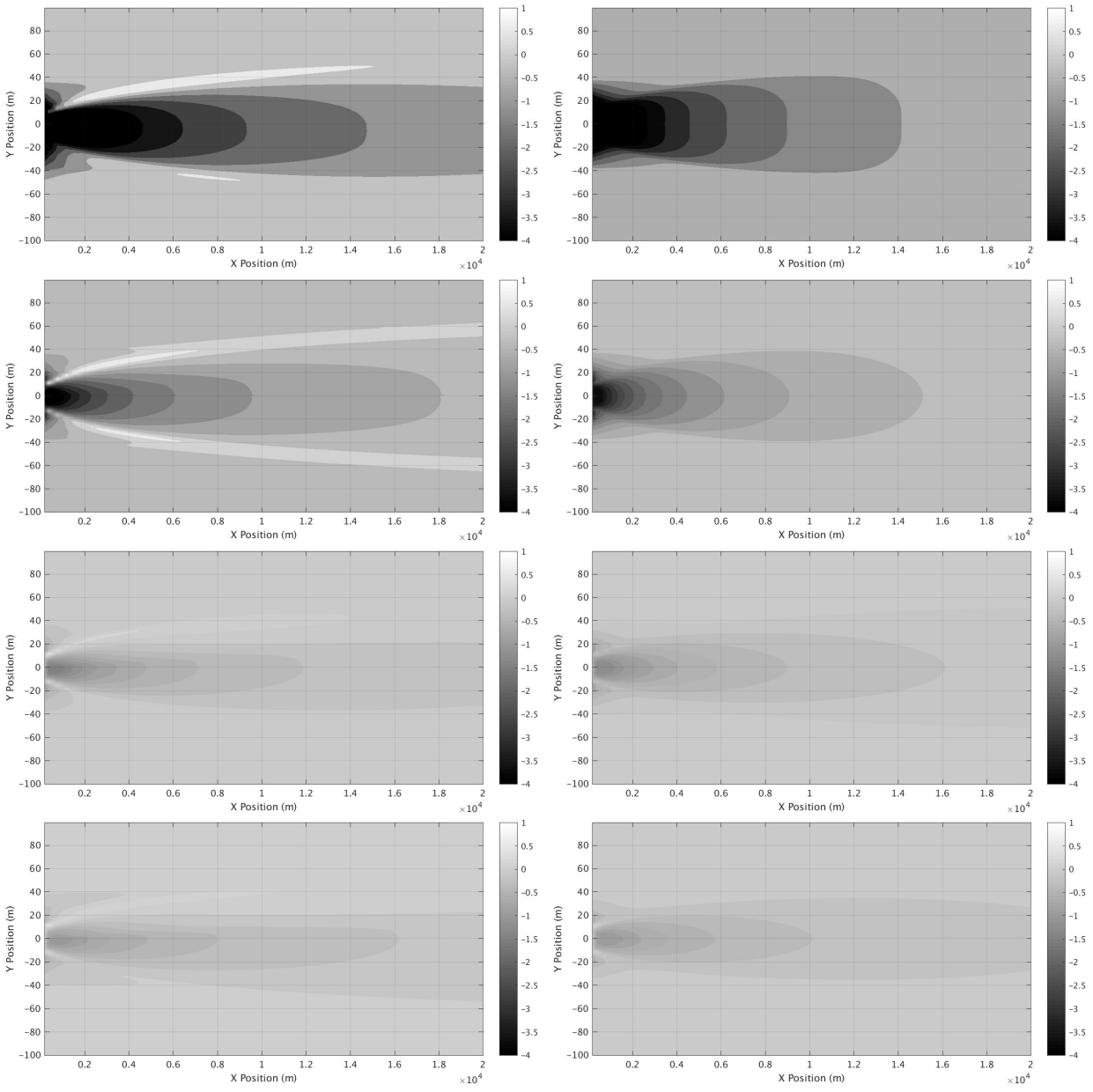

Figure 5.13: Spectral Density (dB) for a ship operating in calm seas with turbulent damping, but no SAS redistribution at L, S, C, and X Band. Spectral energy is taken across wake (left) and along wake (right).

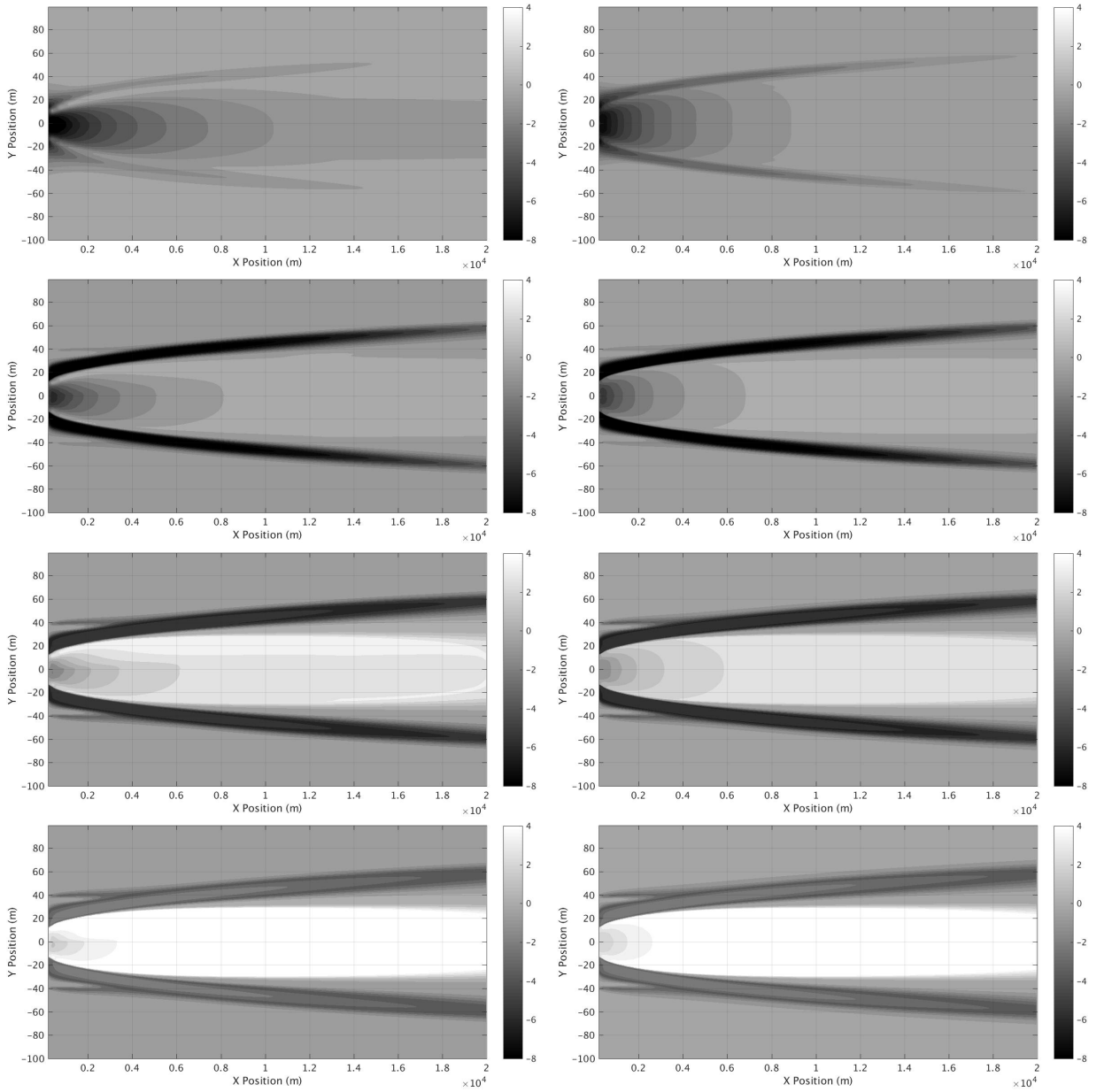

Figure 5.14: Spectral Density (dB) for a ship operating in calm seas with surface roughness modifications due to surface currents, turbulence, and SAS redistribution at L, S, C, and X Band using elasticity properties from Milgram et al. [100]. Spectral energy is taken across wake (left) and along wake (right).

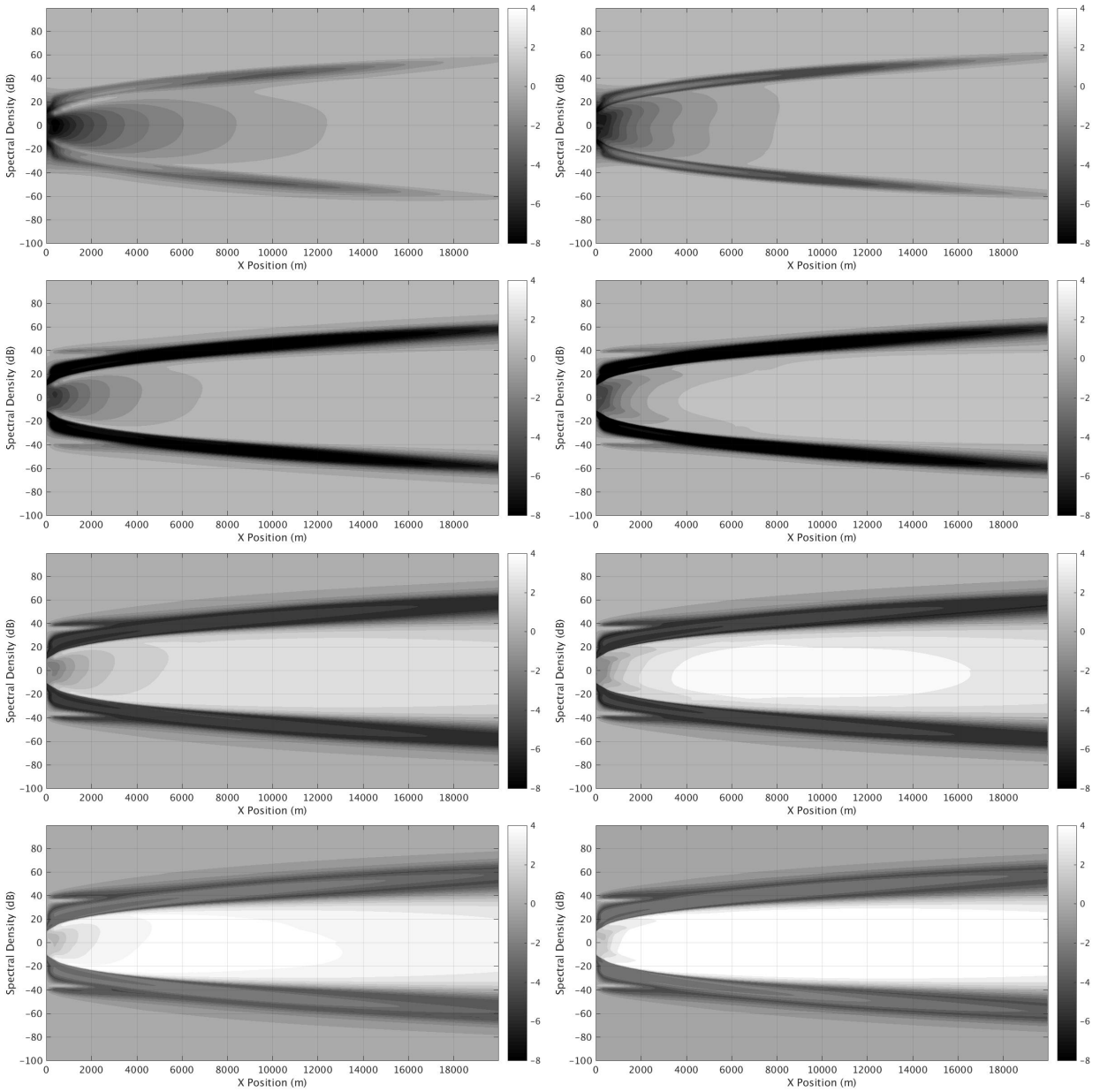

Figure 5.15: Spectral Density (dB) for a ship operating in calm seas with surface roughness modifications due to surface currents, turbulence, and SAS redistribution at L, S, C, and X Band using SAS elasticity properties from Da Silva et al. [29]. Spectral energy is taken across wake (left) and along wake (right).

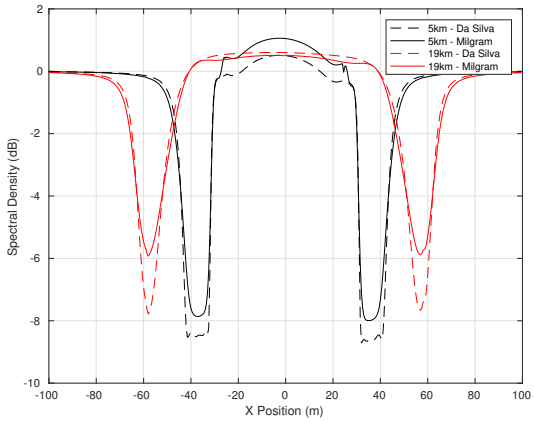

Figure 5.16: Spectral Density (dB) of wave energy traveling across the wake at S-Band for a ship operating in calm seas with elasticity properties given by Da Silva et al. [29] and Milgram et al. [98] at 5km and 19km behind the ship.

longer sufficient to redistribute SAS to the wake edges. This is most clearly observed for an ambient wave height of 1.5 m, where a center damping region remains starting around 15 km behind the ship. In the absence of SAS sources, this region of SAS would in actuality have been previously redistributed by the ship wake and is a current limitation of the model employed here, but does demonstrate that with the inclusion of SAS sources, additional damping regions can form within the wake center where redistributing currents have become small.

Finally, the spectral density in the wake of a ship operating in head seas is shown in Figures 5.22-5.24. In conditions with small wave amplitude (0.5 m) (Figure 5.22), the far-wake structure is similar to the case in calm seas at L band as the surface currents induced by near surface Reynolds stress anisotropy are stronger than the weak LTC. The transverse gradients of the surface currents, Figure 5.25, show similar structure to calm seas for the 0.5m wave amplitude condition. The weak, but growing LTC resist the redistribution of SAS away from centerline, forming a centerline band further downstream in the persistent wake that is observable in all but L-Band. Overall though, these combined effects make the ship operating in a head seas condition with small wave amplitudes have a less persistent wake than one operating in calm seas at L-band, but of similar persistence for higher wavenumbers. Additionally, the centerline wake structure in the near/far wake is similar to the calm seas condition where at higher wavenumbers the wake centerline is dominated by amplified higher frequency roughness up to approximately 7 km.

As wave amplitude increases, the wake structure changes. A wave amplitude of 1 m shows significant damping to occur along the centerline convergence zone that now begins within the turbulent damping zone and extends well beyond 20 km. Along the edges, damping also persists beyond 20 km. The wake width now is observed to decrease with increasing

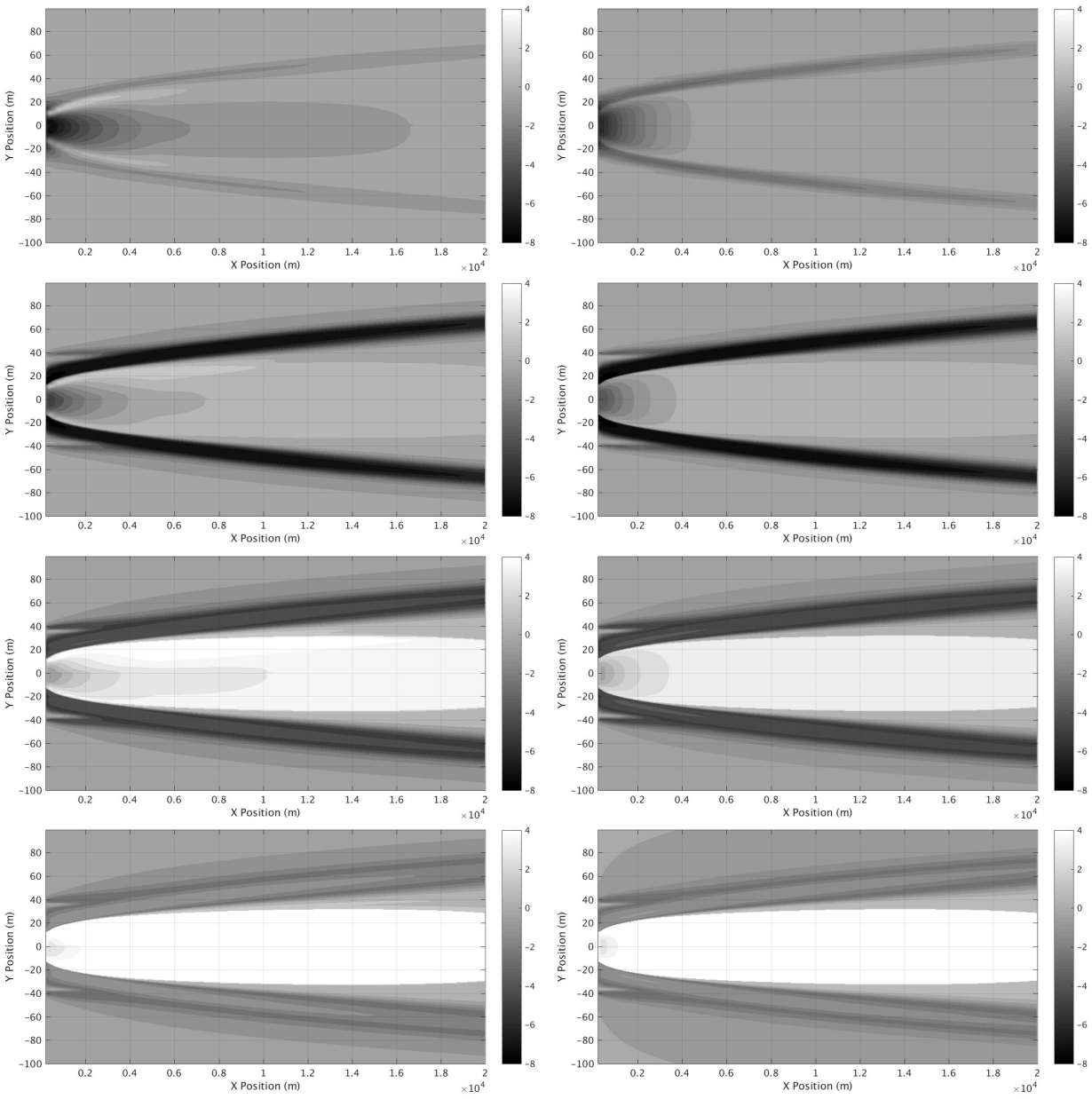

Figure 5.17: Spectral Density (dB) for a ship operating in following seas with wavelength of 50 m and wave amplitude of 0.5 m at L, S, C, and X Band. Spectral energy is taken across wake (left) and along wake (right).

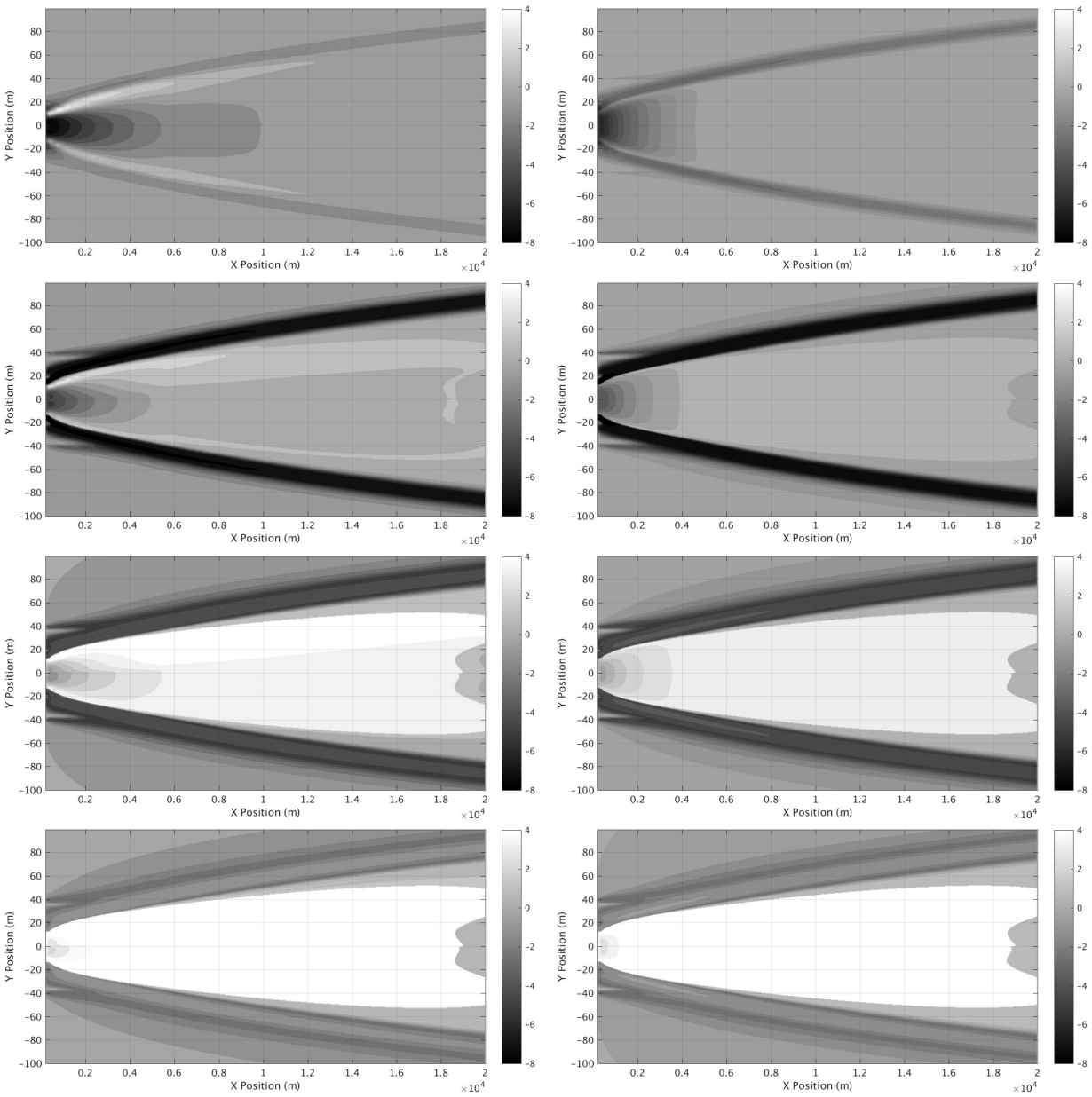

Figure 5.18: Spectral Density (dB) for a ship operating in following seas with wavelength of 50 m and wave amplitude of 1.0 m at L, S, C, and X Band. Spectral energy is taken across wake (left) and along wake (right).

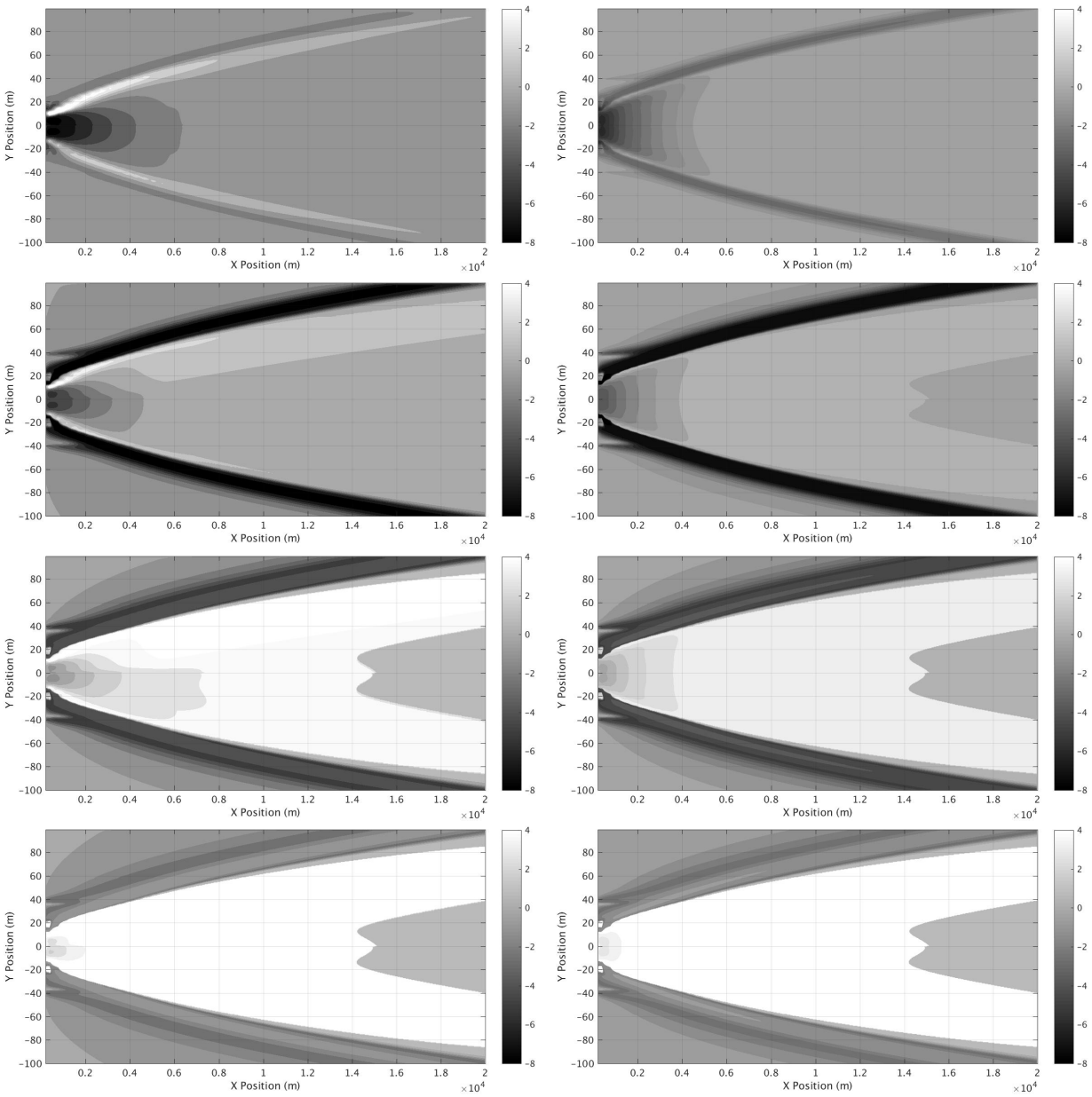

Figure 5.19: Spectral Density (dB) for a ship operating in following seas with wavelength of 50 m and wave amplitude of 1.5 m at L, S, C, and X Band. Spectral energy is taken across wake (left) and along wake (right).

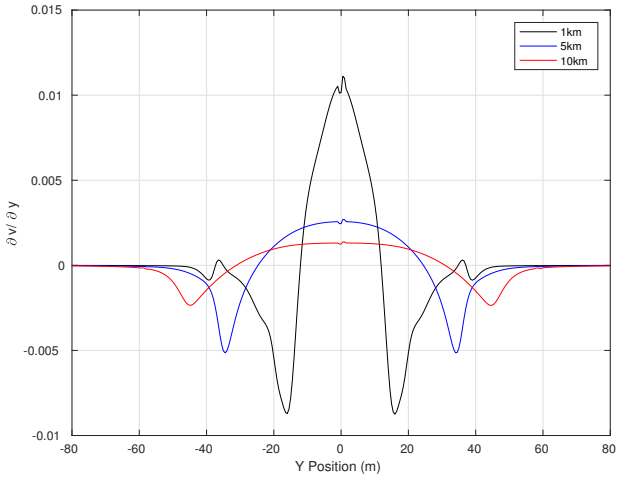

Figure 5.20: Transverse gradient in transverse surface current at 1km, 5km, and 10km downstream in following seas with 1.0m wave amplitude.

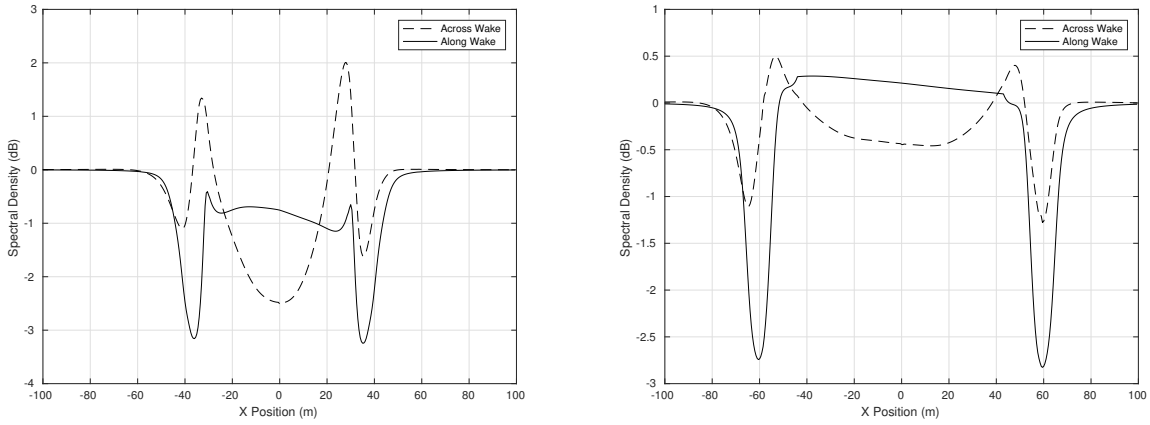

Figure 5.21: Spectral density (dB) in the wake at distances of 3.5 km (left) and 10 km (right) for wave energy along the wake and across the wake.

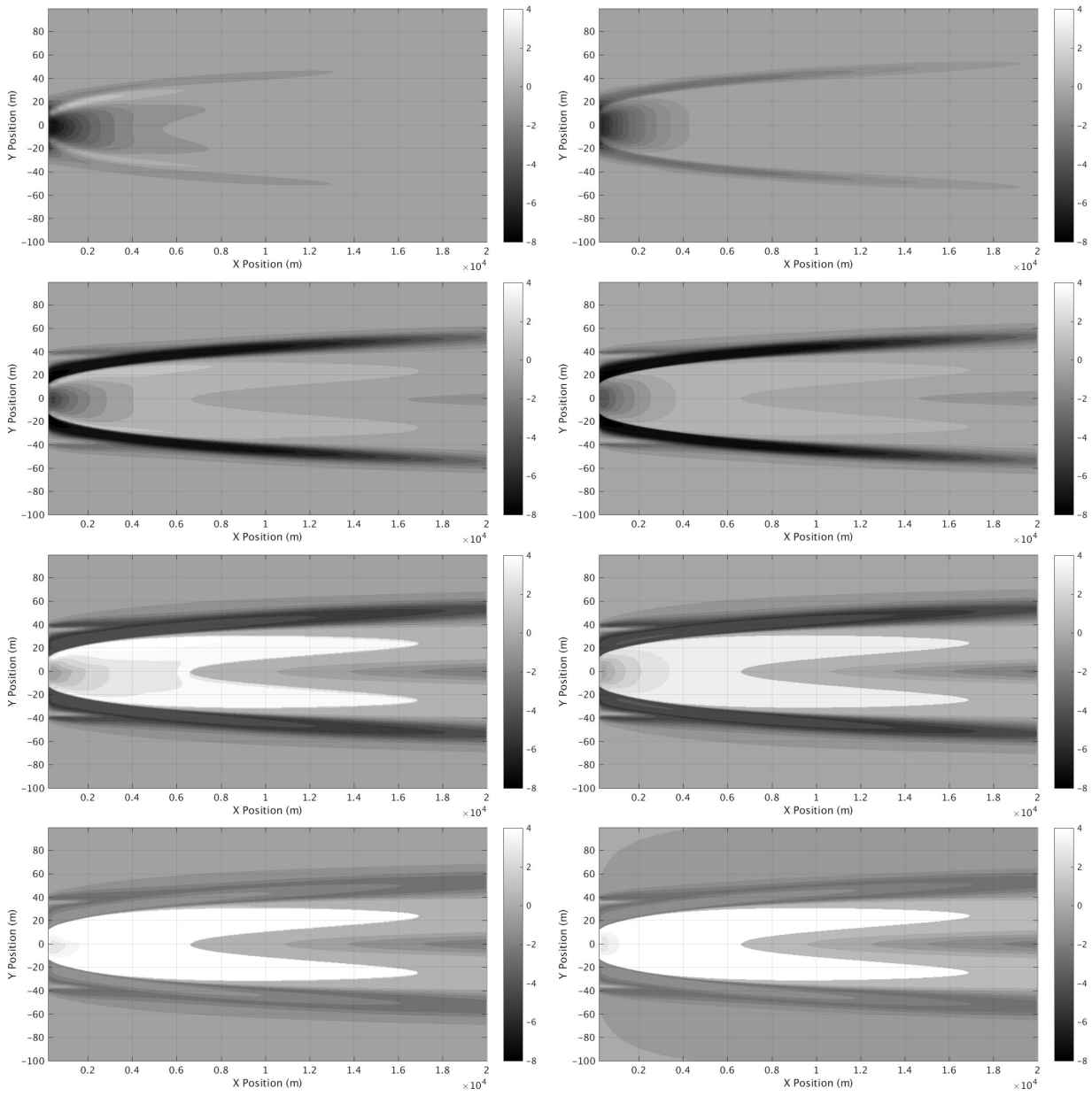

Figure 5.22: Spectral Density (dB) for a ship operating in head seas with wavelength of 50 m and wave amplitude of 0.5 m at L, S, C, and X Band. Spectral energy is taken across wake (left) and along wake (right).

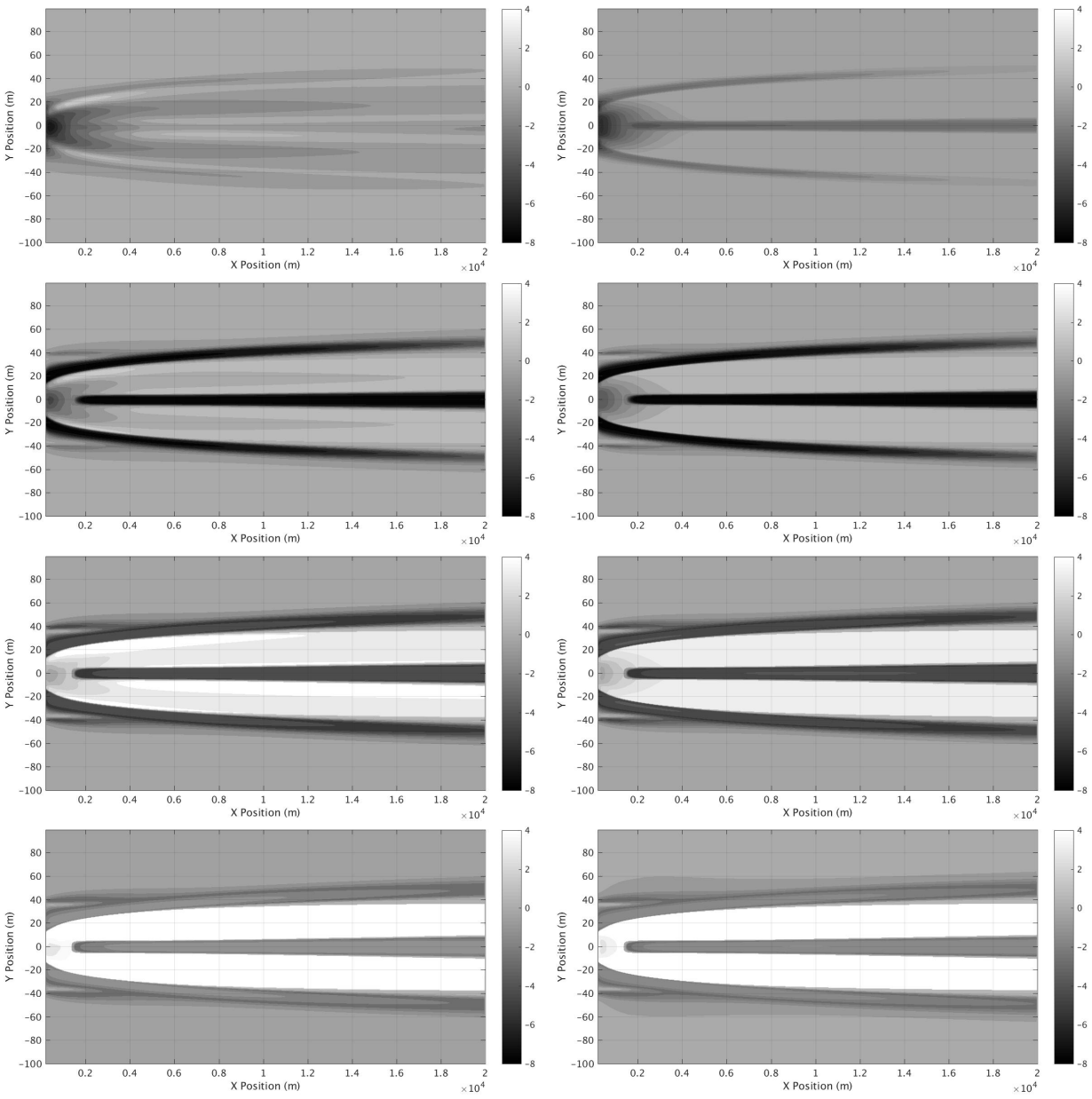

Figure 5.23: Spectral Density (dB) for a ship operating in head seas with wavelength of 50 m and wave amplitude of 1.0 m at L, S, C, and X Band. Spectral energy is taken across wake (left) and along wake (right).

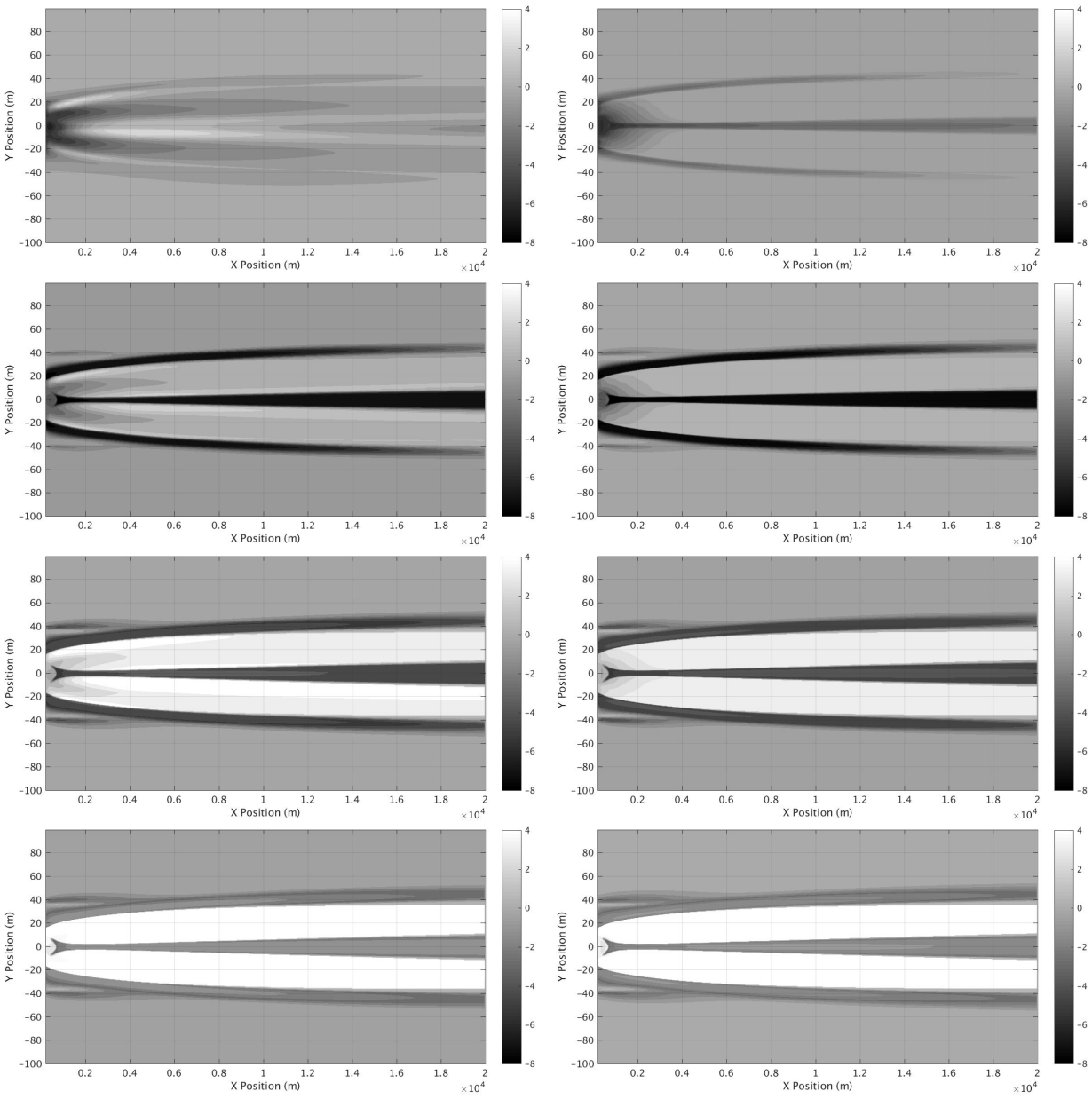

Figure 5.24: Spectral Density (dB) for a ship operating in head seas with wavelength of 50 m and wave amplitude of 1.5 m at L, S, C, and X Band. Spectral energy is taken across wake (left) and along wake (right).

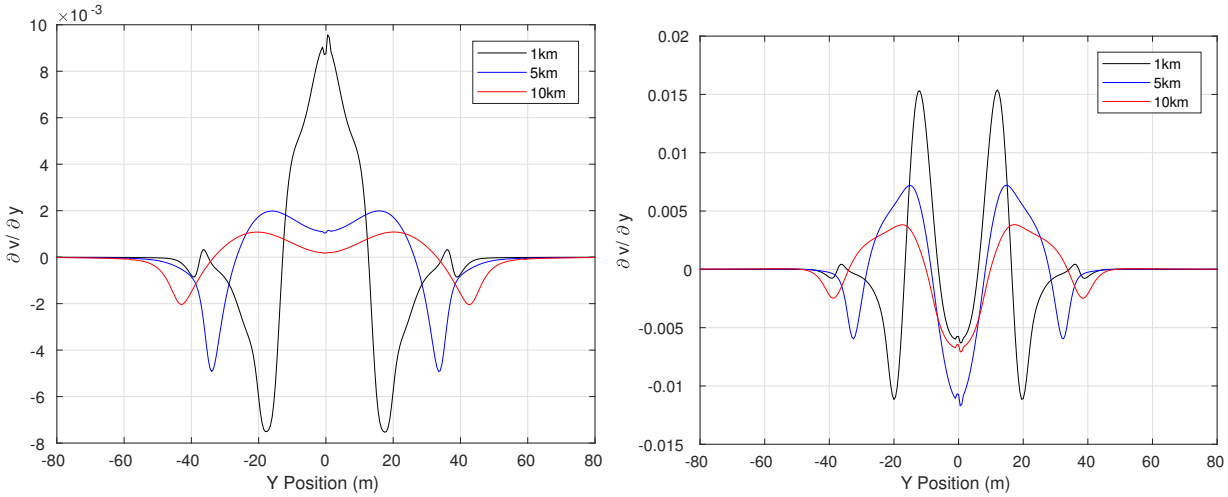

Figure 5.25: Transverse gradient in transverse surface current at 1km, 5km, and 10km downstream in head seas with 0.5m (left) and 1.5m (right) wave amplitudes.

wave amplitude due to the strong inboard rotating LTC. The case of 0.5 m wave amplitude shows a wake width of 95 m at 10 km downstream and 115 m at 20 km downstream. The width decreases to approximately 85 m at 10 km and 100 m at 20 km downstream with 1.5 m wave amplitude. It is also observed that at the highest wave amplitude (1.5m), the L-Band wave energy traveling across the wake is dominated by surface currents due to the strong gradients across the wake, Figure 5.25. Here, the positive gradients well exceed those of the 0.5m wave amplitude case and persist over 10 km downstream. Roughness amplification due to the negative current gradients also exceed the lower wave amplitude conditions both in magnitude and persistence.

As wavenumber increases, the impact of SAS over surface currents increases such that at X-Band there is minimal difference between the energy traveling across the wake and energy traveling along the wake.

It should be highlighted that the relative impact of each phenomena is a function of the wave number of interest. Bragg-resonant wave numbers for L-band radar show higher relative sensitivity to turbulent dampening than C-band as $\gamma_t \propto K^{2/3}$, while the ambient short wave damping due to viscosity is $\gamma_\nu \propto K^2$. Since the spectral density is measured relative to the ambient environment, the impact of turbulent dampening decreases moving from L-band to C-band. The impact of SAS is highest at S-Band for concentration ratios greater than 1.5 as shown in Figure 5.1. SAS also produces a strong relative damping factor at C-Band, with relative damping decreasing for L and X-Band. It's important to note that these conditions assume the presence of SAS in the ambient field. Under circumstances were the ambient SAS levels are low, but SAS is brought to the surface by the passage of the ship, the relative damping in the edge bands would be significantly greater.

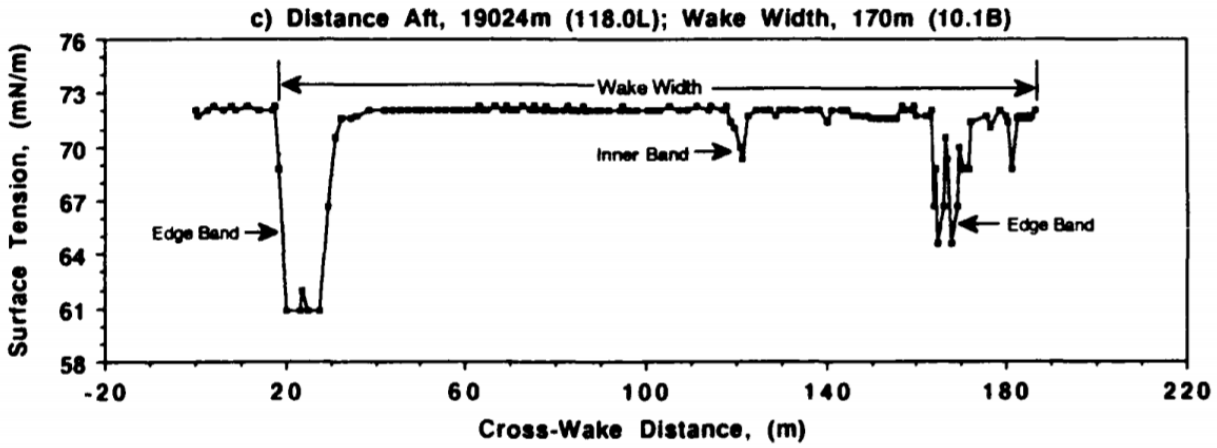

Figure 5.26: Surface tension measurement in the wake of DDG-996 19km downstream of the ship. Peltzer [115]

5.5 Comparison with Experimental Data

Here, comparison is again made to the 1989 ONR Field Experiment [118]. During these experiments, data was taken on the variation in surface tension behind the USS Chandler, a US Navy destroyer. The variation in surface tension was caused by the compacting of SAS into streaks in the wake which formed concentrated regions of reduced surface tension along the edges of the wake. Wake widths were estimated based on the distance between these regions of reduced surface tension as well as on video recordings of the experiment. In the persistent wake, wake widths on the order of 150 m and 170 m were measured 10 km and 20 km behind the destroyer at 25 knots, Figure 5.26. Milgram et al. [98] noted that during these tests the wind was coming from the port stern quarter, signifying a following-seas condition. Comparison of these measured wake widths with Figure 5.14 shows that surface currents due to Reynolds-stress anisotropy alone do not generate wakes of sufficient width to explain those observed in the experiment. Considering the combined effect of turbulence anisotropy and LTC, Figure 5.18, reveals wakes of sufficient width with ambient waves with approximately 1.0 m wave amplitude. It should also be noted that measured wake widths in the field experiment showed a level of variability, also suggesting a partial dependency on environmental conditions. Of the two 25 knot cases studied, a wider wake width was observed with higher wind speeds as measured by the ship. This would lead to larger wave amplitudes and stronger LTC.

During the same tests, SAR imagery was taken by aircraft, Figure 1.4. The image shows the formation of a persistent "rail-road track" wake beyond about 3.5 km. Forward of the small research vessel shown in the center of the image, the wake is attenuated across the width. These findings are mostly in agreement with Figure 5.18, where the spectral density is attenuated by turbulence and surface currents along the wake center with persistent SAS

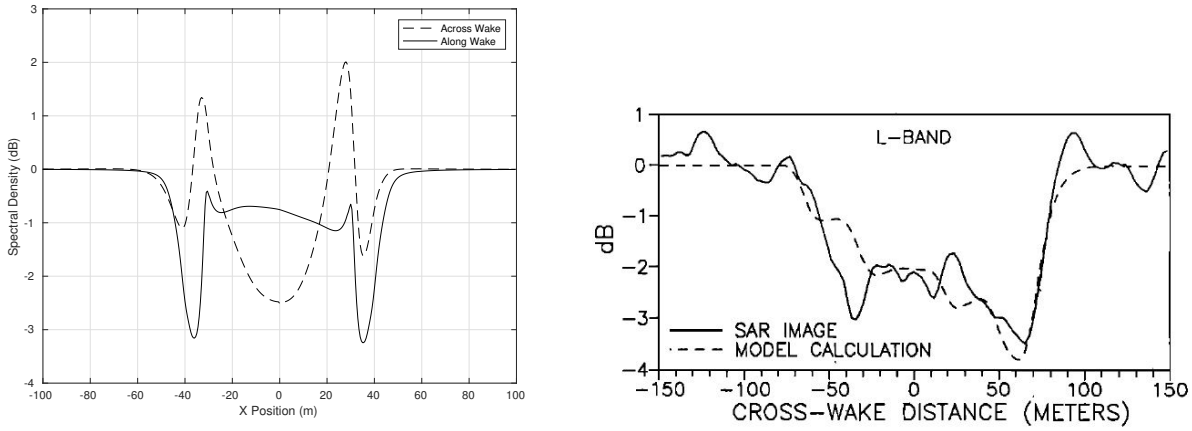

Figure 5.27: Left - Spectral density (dB) in the wake at L-Band at distance of 3.5 km (left) for wave energy along the wake and across the wake for a ship operating in following seas with wavelength of 50 m and wave amplitude of 1.0 m. Right - SAR image intensity in wake of DDG-996 3652m behind the ship [98].

streaks defining the wake beyond. As the ship was operating in an oblique seas condition, the strength of LTC would be less than that predicted here, which would reduce the magnitude of the outboard surface currents and in turn reduce the regions of amplified roughness. It should also be noted that in the current model the wind energy input across the wake is uniform regardless of SAS concentration. Mitsuyasu and Honda [103] observed a reduction in the friction velocity of wind over a surface film compared to clean water. Inclusion of this effect would further reduce the observed regions of amplified roughness.

Milgram et al. [98] showed peak attenuation of spectral density across the SAS streaks of 3 dB to 3.5 dB 3563 m behind the ship with an L-Band SAR. Here we predict attenuation in this range in the along wake direction, but the impact of surface currents reduce the attenuation in the across wake direction, Figure 5.27. This result also gives credence to the results of Anthony et al. [9] being applicable at low Froude numbers in addition to the high Froude number case. In this scenario, the surface currents, and more importantly their gradients, would be reduced as the impact of Reynolds stress anisotropy would be partially mitigated by the surface film. At the same distance, Milgram et al. [100] showed damping around 2 dB through the wake centerline. This level of damping is observed in the across-wake direction, with reduced damping in the along wake direction. Direct comparison here is difficult as the spectral density is measured relative to the ambient condition, which is not fully known for the experimental data. In particular, the ambient surface turbulent dissipation rate is unknown. Milgram et al. [100] imposes an initial condition where the L-Band spectral density is reduced 7 dB for a full ship beam on either side of centerline to account for complex near field effects (wave breaking, bubbles, etc). Our IDP model also predicts a reduction of the spectral density of 7 dB along centerline at a distance of 4 ship lengths (500 m), but not extending a full ship beam to either side of centerline. This is

mostly attributed to the lack of inclusion of these complex, ship specific, near field effects. Unfortunately, the published SAR data is limited to this single run with data only in the near/far wake region. Despite these comparative limitations, the predicted wake widths and wake structure show good agreement with the published data and images.

An additional image of the same ship in a head seas condition is also provided by Milgram et al. [98], Figure 1.3. In a similar manner as the case in following seas, the wake is initially attenuated through the wide center wake due to turbulence and surface currents, as predicted by Figure 5.23. Several kilometers behind the ship, the turbulence dissipates and a narrower centerline streak is observed, also as predicted by Figure 5.23. Milgram et al. [98] noted that the sea waves were coming from the starboard bow quarter. Chapter 4 demonstrated that the structure of the persistent wake in a head seas condition is highly sensitive to the strength of the LTC and the initial film pressure of the ambient SAS field. The predicted outboard streaks are weakened when the ship is not directly into the waves. The outboard streaks were also shown to dissipate sooner with lower initial film pressures in the ambient SAS field as higher levels of SAS compacting are required to achieve the same level of short wave damping. These combined effects suggest that the less persistent edge bands predicted in Figure 5.23 may not appear in many conditions and only the strong centerline streak may be observed.

5.6 Conclusions

The structure of the far and persistent wake of surface ships has been shown to be a combined function of several hydrodynamic phenomena. Specifically, the effects of surface currents, turbulence, and surface active substances have been presented here with their relative impact on each region of the wake. Two primary mechanisms that generate surface currents that compact SAS were studied: near-surface Reynolds-stress anisotropy and Langmuir-type circulations. Turbulence models that utilize the $k-\varepsilon$ formulation were modified to incorporate the redistribution of the vertical Reynolds stress to the axial and transverse Reynolds stresses over a thin surface layer. The use of non-linear redistribution models were found to provide improved agreement with experimental data over linear redistribution models. A quadratic redistribution model was implemented into the persistent wake solver to allow predictions of surface currents due to the combined effects of near surface Reynolds stress anisotropy and Langmuir-type circulations.

In the far wake, it has been shown that turbulence and surface currents contribute to the dampening of short wind waves through the center of the wake, while SAS is compacted along the edges. The direct impact of surface currents on the spectral density was observed to be small relative to the dampening effect of turbulence for the wind/wave conditions used here. Wind conditions directly across the wake generate enhanced surface roughness due to interaction with the outboard induced currents, but limited data exists for these conditions. It should be noted that operation in areas with low SAS concentrations or low initial film

pressures would also enable the amplification of surface roughness due to surface currents and the formation of the sometimes observed bright streaks along the edges of the turbulent center wake. Incorporation of a friction velocity modification, though, is recommended to account for reduced amplification in regions where SAS is concentrated. A more complete model of this region would also need to account for the effects of bow/stern wave breaking and bubbles.

In the persistent wake, calm and following seas show similar wake structure, but the effects of LTC in following seas increase the width of the wake. Comparisons to wake widths measured by Peltzer et al. [118] show good agreement with the cases of following seas, highlighting the importance of inclusion of both turbulence anisotropy and LTC-induced surface currents. In head-sea conditions, the formation of a persistent centerline streak along with two weaker outboard streaks are predicted. The outboard streaks are not as persistent as the centerline streak and, as highlighted in chapter 4, their existence is highly dependent on both the strength of LTC and the ambient SAS film pressure.

While reasonable agreement with available data was achieved here, the need of quality full-scale data can not be overstated where complete environmental parameters are known. Model improvements such as the inclusion of SAS sources/sinks and consideration of near field effects will enhance model comparisons. In addition, for actual wake predictions, it is recommended to utilize a more complete Reynolds-stress transport model that incorporates environmental forcing such as the work of [157]. as the work of Wall and Paterson [157].

Chapter 6

Simulating SAR images of Surface Ship Wakes

6.1 Introduction

The application of SAR to the study of surface ship wakes has been prominent since the days of SEASAT in the 1970's. Early research was focused on the near/far field wake features (Kelvin wake, centerline tubulent wake, breaking bow/stern waves) as they were the most prominently observed in these early images. Advances in sensor and data processing have enabled detection of distinct features within the wake. Here focus is primarily on the structure of the persistent wake and the impacts of Langmuir type circulations (LTC), near surface Reynolds stress anisotropy, SAS redistribution, and turbulence.

The approach to SAR (Synthetic Aperture Radar) modeling taken here is a multi-step approach that involves initially solving for the radar cross section (RCS) where the ocean waves are averaged and also without consideration for actual instrumentation limitations. In this analysis, a composite approach is taken where the influence of the small scale wind waves are accounted for through Bragg scattering and the larger scale waves are accounted for through a specular component. The impact of the randomness of the ocean surface is then incorporated by considering the change in RCS with the inclination angle and finally the impact of the sensor altitude, speed, and resolution are included.

This chapter is organized as follows. First a description of the electromagnetic model used to predict the composite response due to Bragg scattering and specular components is provided. A discussion on the methods used to account for the randomized ocean realization is provided next to complete the perfect SAR model. A description of the Simulated SAR model is then described including the full SAR process from signal detection to image processing. Results on the perfect SAR and simulated SAR images are presented for the ship operating in calm seas, head seas, and following seas with the same conditions as discussed in chapter 5. Results here are also compared to the spectral density distributions discussed in chapter 5. Results are also compared to experimental data from the 1989 ONR Field Experiment [115] followed by recommendations for further model development.

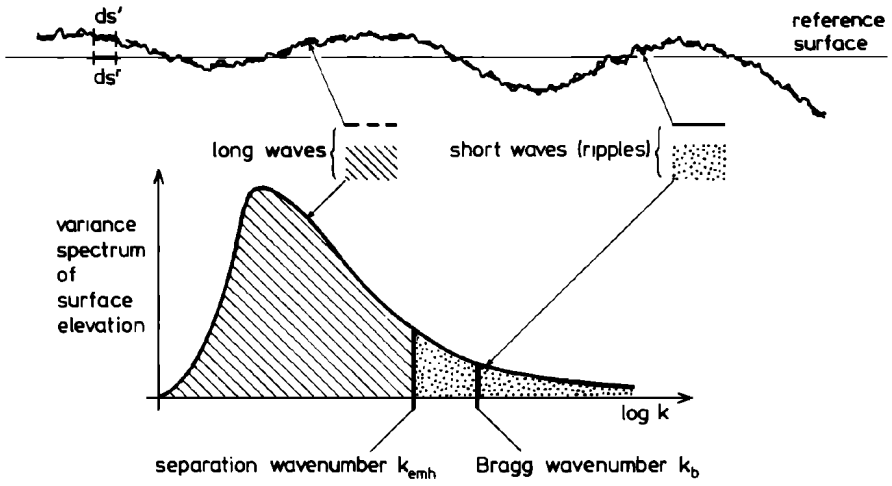

Figure 6.1: Two scale model of surface waves as presented by Hasselmann et al. [56]. The separation wave number must be large in comparison to the Bragg wavenumber, but sufficiently small to satisfy the requirements of a perturbation analysis.

6.2 Mathematical Model

6.2.1 Electromagnetic modeling

The radar cross section is modeled using a composite approach where the contributions of the small scale structure are solved based on Bragg scattering and the large scale structure contribute to the physical optics. These two regimes are demonstrated in Figure 6.1. The cutoff frequency between the two scales is taken to satisfy the requirements of a perturbation analysis,

$$4k_0^2\zeta_s^2 \ll 1 \tag{6.1}$$

where k_0 is the electromagnetic wave number and ζ_s is the mean-square height of the small scale structure. Lyzenga and Bennett [93] found there to be a smooth transition between the large scale and small scale contributions if the cutoff frequency was set as $k_d = k_0/3$, which corresponded to $4k_0^2\zeta_s^2 \approx 0.1$. Hasselmann et al. [56] used a value of $k_d = k_0/5$ and commented that this choice marginally satisfies the geometric optical condition for long waves, $k_d << k_0 \sin(\theta)$, where θ is the incidence angle of the electromagnetic radiation on the surface. Here, we follow the methodology of Hasselmann et al. [56] and use $k_d = k_0/5$.

The radar cross section due to Bragg scattering for a roughened surface is given by Wright [159] and Plant [121] as

$$\sigma_B(\theta,\phi) = 16\pi k_0^4 |G(\theta)|^2 S(k_b,\phi) \tag{6.2}$$

where $G(\theta)$ is a polarization-dependent scattering coefficient, $S(k_b, \phi)$ is the surface elevation spectral density at the Bragg resonant wave number, and ϕ is the radar look direction (view azimuth). The Bragg resonant wave number is $k_b = 2k_0 \sin\theta$.

The polarization-dependent scattering coefficients are given by Wright [159] based on the Fresnel reflection coefficients as

$$G(\theta) = G_{vv} = -R_v \cos^2(\theta) + \frac{1}{2}\left(\frac{\varepsilon - 1}{\varepsilon}\right)(1 + R_v)^2 \sin^2(\theta) \tag{6.3}$$

$$G(\theta) = G_{hh} = -R_h(\theta) \cos^2(\theta) \tag{6.4}$$

R_v for vertical polarization is given as

$$R_v(\theta) = \frac{\varepsilon \cos(\theta) - \sqrt{\varepsilon - \sin^2(\theta)}}{\varepsilon \cos(\theta) + \sqrt{\varepsilon - \sin^2(\theta)}} \tag{6.5}$$

and R_h for horizontal polarization is given as

$$R_h(\theta) = \frac{\cos(\theta) - \sqrt{\varepsilon - \sin^2(\theta)}}{\cos(\theta) + \sqrt{\varepsilon - \sin^2(\theta)}} \tag{6.6}$$

where ε is the relative dielectric constant of the ocean as given by Klein and Swift [78]. The second term on the right hand side of equation 6.3 is not included by all authors. A numerical study found this term to have a small impact for L-band, but increasing influence at higher frequencies.

The surface elevation spectral density at the Bragg wave number is given as $S(k_b, \phi) = \omega\left[A(k_b, \phi') + A(k_b, \phi' + \pi)\right]$ where ω is the water wave frequency, $A(k, \phi')$ is the action spectral density, and ϕ' is the wave propagation direction relative to the view azimuth. Since the action spectral density is solved at discrete wave numbers and the value and derivative at the Bragg wave number are needed, the spectrum is modeled as a power law function

$$S(k, \phi) = Bk^{-c} \tag{6.7}$$

where B and c are fitted around the Bragg wave number.

In reality, the small scale waves ride on top of the large scale waves and in effect are tilted relative to the incoming radiation beam. This effect is accounted for by treating the surface as a series of facets that are tilted by angles α and γ relative to the mean surface where α is the angle between the vertical and the projection of the surface normal onto the plane of incidence and γ is the angle between the vertical and the projection of the surface normal onto a vertical plane perpendicular to the plane of incidence. The tilt angle α modifies the local incidence angle, while the tilt angle γ impacts the polarization of the incident radiation. Considering the randomness of the ocean, the tilt angles are normally distributed with a probability density function given as

$$p(\alpha)\, d\alpha d\gamma = \frac{0.06}{\sqrt{2\pi}} \exp\left\{ -\frac{1}{2}\left(\frac{\alpha}{\sigma_{\xi_x}}\right)^2 \right\} \tag{6.8}$$

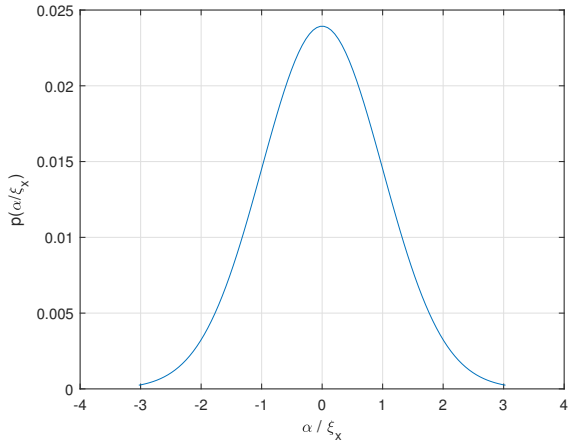

Figure 6.2: Surface facet tilt angle probability distribution as a function of the local surface slope.

and distributed as shown in Figure 6.2 where ξ_x is the surface slope in the plane of incidence. The standard deviation of the surface slope, σ_{ξ_x}, is taken as the square root of the variance, which, assuming a zero mean slope, is the mean square slope, $< \xi_x^2 >$, obtained from the surface elevation spectrum by integrating over wave numbers smaller than k_d as done by Lyzenga and Bennett [93] as

$$< \xi_x^2 >= \int_0^{\pi} \int_0^{k_d} k^2 \cos^2(\phi') S(k, \phi') \, k dk d\phi' \tag{6.9}$$

$$< \xi_y^2 >= \int_0^{\pi} \int_0^{k_d} k^2 \sin^2(\phi') S(k, \phi') \, k dk d\phi'. \tag{6.10}$$

The local incidence angle is then taken as $\theta' = \theta + \alpha$. The tilt angle γ is calculated as

$$\gamma = \alpha \frac{\sigma_{\xi_x \xi_y}}{\sigma_{\xi_y}^2} \tag{6.11}$$

where $\sigma_{\xi_x \xi_y}$ is the covariance of the surface slopes.

The titled Bragg radar cross section is then modeled as

$$\sigma_B(\theta', \phi) = 16\pi k_0^4 \int \int |G(\theta', \gamma)|^2 S(k_b, \phi) \, p(\alpha, \gamma) \, d\alpha d\gamma. \tag{6.12}$$

The scattering coefficient for vertical polarization is not impacted by the tilt angle γ, but the horizontal polarization scattering coefficient is modified as

$$G_{hh}(\theta', \gamma) = G_{hh}(\theta') + \frac{\tan^2(\gamma)}{\sin^2(\theta')} G_{vv}(\theta') \tag{6.13}$$

The large scale contribution from the specular component is given based on Barrick [12] and Wright [159] as

$$\sigma_s(\theta,\phi) = \frac{\pi}{\cos^4\theta}|R(0)|^2\left[\frac{1}{2\pi\xi_x\xi_y}\exp\left(-\frac{\theta^2}{2{\xi_x}^2}\right)\right] \tag{6.14}$$

where $|R(0)|$ is the Fresnel reflection coefficient at normal incidence given as

$$R(0) = \frac{1-\varepsilon}{1+\varepsilon}. \tag{6.15}$$

The total radar cross section is then sum of the small scale contribution from Bragg scattering and the large scale specular component,

$$\sigma_0 = \sigma_B + \sigma_s. \tag{6.16}$$

6.3 Ocean Realization

The actual ocean surface at any given moment is a randomized realization of the surface height. In order to generate this realization, the wave heights in Cartesian space are calculated based on the spatially varying wave height spectral density given in polar-wavenumber coordinates ($S(k,\phi)$). A sampling window is passed over the hydrodynamic grid where the the spectral density at the center of each window is taken through bilinear interpolation where the wave height spectrum is the square root of the interpolated spectral density. The window is discretized into a grid of spatial wavenumbers, described by Lyzenga [90] as

$$k_m = \frac{2\pi}{L_x}\left(m - \frac{M}{2}\right), m = 1..., M-1 \tag{6.17}$$

$$k_n = \frac{2\pi}{L_x}\left(n - \frac{N}{2}\right), n = 1..., N-1 \tag{6.18}$$

where L_x and L_y are the x and y dimensions of the window. The number of nodes (M,N) within each window is determined by the ratio of the maximum resolved water wavelength and the pixel size in each direction. The size of each window (L_x, L_y) is determined by the number of nodes and the pixel size, e.g. $L_x = MP_x$, where P_x is the pixel size in the x–direction. Each spatial wavenumber (k_m, k_n) corresponds to a deep-water wave with frequency $\omega_{mn} = \sqrt{gk}$, where g is gravitational acceleration and k is the magnitude of the spatial wavenumber. The wave height spectrum from the center node is distributed over the window based on each node's spatial wavenumber and polar angle ϕ relative to the center. The distributed wave height spectrum is multiplied by a random complex amplitude and phase and passed through a Hanning window function to reduce edge effects described as

$$w_m = \sqrt{\frac{1}{2} - \frac{1}{2}\cos\left(\frac{2\pi m}{M}\right)}. \tag{6.19}$$

The surface height at each location within the window can then be described as

$$z\left(m,n\right)=\left[\frac{4\pi^{2}}{L_{x}L_{y}}S\left(m,n\right)\right]^{1/2}w_{m}w_{n}re^{i\psi} \tag{6.20}$$

where r is the magnitude of the random complex number that ranges between -1 and 1 and ψ is the random phase ranging between 0 and 2π.

The window is translated half a window length ($L_x/2$) and repeated with all windows finally summed to achieve the total surface realization. The half–window translation allows each location in the total surface realization to be the sum of four $z\left(x,y\right)$ values.

6.3.1 Perfect SAR

Consideration for a perfect SAR (pSAR) image (no limitations of instrumentation) is given by generating an image that incorporates the randomness of the ocean realization. As previously discussed, the local tilt angle α modifies the inclination angle θ. The randomized surface realization is accounted for by multiplying the local surface slope of the realization with the partial derivative of the total RCS with respect to the inclination angle and adding this to the total RCS calculated with averaged wave characteristics as

$$\sigma_{pSAR}=\sigma_{B}+\sigma_{s}+\frac{\Delta z_{x}}{P_{x}}\frac{\partial\sigma_{0}}{\partial\theta} \tag{6.21}$$

where Δz_x is the change in surface height across a pixel from the ocean realization, $\Delta z_x = z\left(x_1,y_1,t\right)-z\left(x_2,y_1,t\right)$, and P_x is the pixel size in the x–direction.

6.3.2 Simulated SAR

SAR achieves fine azimuth resolution by taking many returns from the same location at various phase changes and processing the returns. A schematic demonstrating this methodology is shown in Figure 6.3. Each pulse sends a beam of electromagnetic energy that spreads across the beam width based on the antenna pattern such that elements at the edges of the beam have less power than those in the beam center. The return at each element is stored as a phase history. The platform moves forward a distance Vt, where t is the pulse duration and V is the platform velocty, and emits another pulse. The antenna pattern has shifted the distance of one element such that the x-position of element j is now located at the x-position of j+1 from the previous pulse. Once the position x has been passed over by the full antenna pattern, the returns can be processed to provide the required azimuthal resolution.

The antenna gain pattern is given as

$$H\left(x-Vt\right)=\exp\left(-\pi\left(\frac{x-Vt}{\beta R}\right)^{2}\right) \tag{6.22}$$

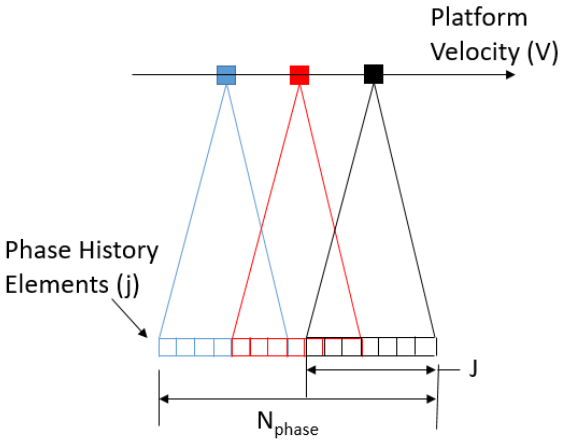

Figure 6.3: SAR phase history schematic. Antenna patterns are shown every fifth pulse. The length of the antenna pattern J is notional. N_{phase} is the total number of locations where the phase history is recorded.

where β is the beam width in radians and R is the slant range. It is assumed that the image is sufficiently resolved in range and that the azmithal swath can be described as βR. The term $(x - Vt)$ is the distance on the ground between each phase history element, j, as depicted in Figure 6.3, and the position of the platform or the beam center, which is given as $x = Vt$ or $J/2$ in the phase history.

Due to the motion of the platform, a Doppler phase shift is experienced across the antenna pattern

$$D(x - Vt) = \exp\left(i\frac{k_0}{R}(x - Vt)^2\right) \tag{6.23}$$

where k_0 is the electromagnetic wavenumber.

The scattering properties of the surface, including the effects of random surface motions, are modeled as a complex reflectivity as

$$r(x, y, j) = r(x, y, 1) + \frac{(Z_1 - Z_0)\, r(x, y, j - 1) + W}{Z_1 + Z_0} \tag{6.24}$$

where $r(x, y, 1)$, Z_1 and Z_0 are

$$r(x, y, 1) = \left(\frac{1}{2}\sigma_0(x, y)\right)^{1/2} \qquad Z_1 = \frac{\pi}{\alpha\sigma_\omega(x, y)t_p} \qquad Z_0 = \frac{1}{2}\left(1 - i\frac{\pi\omega_0(x, y)}{\alpha\sigma_\omega(x, y)}\right).$$

Here σ_0 is the total RCS from equation 6.16, α is the non–dimensional Lorentzian bandwidth scale factor taken as $\alpha = \sqrt{\pi}/2$, t_p is the pulse duration, and W is a complex variable serving

as a source of white noise with a random complex multiplier $a + ib$ that changes for each phase history element

$$W = \left(\frac{\pi \sigma_0(x,y)}{\alpha \sigma_\omega(x,y) t_p} \right)^{1/2} (a + ib)\,. \tag{6.25}$$

A Gaussian-like distribution has been used for the reflectivity with a center frequency of ω_0 and coherence bandwidth of σ_ω as

$$\omega_0 = 2k_0 V_r \qquad\qquad \sigma_\omega = \sqrt{\frac{\pi \sigma_v^2}{2\lambda^2}}.$$

Here, V_r is the mean radial velocity of the surface current and σ_v^2 is the variance of the radial velocity described by Lyzenga and Bennett [93] as

$$\sigma_v^2 = \int_0^{\pi} \int_{k_l}^{k_d} gk \left(\sin^2(\theta) \cos^2(\phi') + \cos^2(\theta) \right) S(k, \phi') k dk d\phi' \tag{6.26}$$

where k_l is the lowest resolved water wavenumber and ϕ' is the angle between the wave propagation direction and the view azimuth.

The received antenna pattern is passed over the complex reflectivity function in a fashion similar to a convolution to form the SAR recieved signal as

$$s(l,y) = \sum_{y=1}^{Y} \sum_{x=1}^{X} \sum_{j=1}^{J} r(x,y,j)\, H(x - Vt)\, D(x - Vt) \tag{6.27}$$

where X and Y are the number of pixels in the x and y directions in the final SAR image and l is the azimuth location of the summed phase history elements within N_{phase}.

The processed signal is then convolved with a matched filter,

$$B(l) = \frac{1}{N_{phase}} \exp\left(i \frac{R}{4k_0} \left((l-1) \frac{2\pi}{N_{phase} P_x} \right)^2 \right). \tag{6.28}$$

This function is applied in the frequency domain as a multiplicative operation and an inverse Fourier transform is taken of the resulting signal providing $i(l,y)$. The final image intensity, $I(x,y)$, is retrieved as the square of the modulus of the processed signal,

$$I(x,y) = |i(l,y)|^2 \qquad\qquad \frac{J}{2} < l < N_{phase} - \frac{J}{2} \tag{6.29}$$

where $J/2$ is the location of the first pulse in the total phase history and $N_{phase} - \frac{J}{2}$ is the location of the final pulse that covers the scene of interest.

6.4 Computational Model

6.4.1 Domains and Meshing

The spectral density of wave action is solved on a 4D grid of the ocean surface: 2 dimensions in space (x,y), wave number (K), and wave angle (ϕ). The limits of the domain are $0 < x < 20\,000\,\text{m}$, $-150 < y < 150\,\text{m}$, $0 < \phi < 2\pi$, and $0.6 < K < 280$. The spacial domain uses constant spacing of 20 m in the x direction and 0.5 m in the y direction. The wave angle uses 12 equally spaced points and the wave number uses 24 points distributed on a logarithmic scale due to the range being across several order of magnitude.

6.4.2 Numerical methods

The wave-action-balance equations are solved using a modified form of the ERIM Ocean Model (EOM) ([93]). The code uses a modified upwind finite-difference method for the advective and wave-current interaction terms. Here the spectral density is solved at fixed wave number and spatial coordinates, termed as the action spectral density (A), to permit use of a sweeping algorithm where each grid point is solved each iteration only if it had not reached a converged state the previous iteration. Solutions are considered converged once residuals are reduced to less than 10^{-6}. Also, to account for the need to resolve high wavenumbers, $\partial A/\partial K$ is solved as a perturbation function where $A = A_{eq} + \Delta A$, where A_{eq} is the equilibrium value and ΔA is the difference from equilibrium. This modification is required as the action spectrum falls off as $K^{-4.5}$ at high wavenumbers, which are of utmost interest when simulating SAR response.

6.4.3 Initial and boundary conditions

The initial conditions for the wave-action balance solver are based on the hydrodynamic and SAS redistribution simulations. The surface currents, SAS concentrations, and turbulence dissipation rate distributions are mapped to the spacial grid using bi-linear interpolation. The action spectral density is set to the equilibrium conditions at the spacial boundaries as well as the ends of the spectral domain. Here the damping is limited to viscous damping, given as $\gamma_\nu = 4\nu K^2$, damping due to ambient SAS ($\Gamma/\Gamma_0 = 1$), and damping due to ambient surface turbulence.

6.4.4 Fluid properties and Instrumentation parameters

Damping of the short wind waves is calculated using a surface roughening wind speed of 2 m/s to provide comparison with the SAR data reported by Milgram et al. [100]. Sea

wavenumbers are set to the Bragg resonant values for L-Band (1.25 GHz), S-Band (3.1 GHz) , C-Band (5.3 GHz), and X-Band (9.6 GHz) to explore the variation with frequency. An ambient surface turbulent dissipation rate of $1 \times 10^{-5}\,\mathrm{m}^2/\mathrm{s}^3$ is used for the surface wake simulations. This is based on a balance of available data. In addition to Wu et al. [160], St. Laurent and Merrifield [137] provides mean dissipation rates with near surface values on the order of $2 \times 10^{-7}\,\mathrm{m}^2/\mathrm{s}^3$. St. Laurent and Merrifield [137] also shows data over a two week period with significant fluctuations in the near surface dissipation rate due to solar heating where peaks of $1 \times 10^{-4}\,\mathrm{m}^2/\mathrm{s}^3$ are observed during the day. Sutherland and Melville [141] report measured values as high as $1 \times 10^{-2}\,\mathrm{m}^2/\mathrm{s}^3$ for higher wind conditions (17 m/s) where significant wave breaking occurs. Dissipation rates for more moderate wind speeds (10 m/s) are on the order of $4 \times 10^{-4}\,\mathrm{m}^2/\mathrm{s}^3$ at a depth of 5 cm and decaying to $1 \times 10^{-5}\,\mathrm{m}^2/\mathrm{s}^3$ at a depth of 1 m. As the majority of the turbulent dissipation occurs in the upper 5 cm of the ocean boundary layer, the higher dissipation rates are primarily used here with a range investigated to demonstrate the impact of the ambient surface turbulence.

The SAR instrument is simulated as traveling 500 km above the surface at a velocity of 7500 m/s. The instrument has a resolution of 2 m in both the range and azimuth directions, which is consistent with modern space based SAR capabilities in spotlight mode and is aggressive for a surveillance scan. An inclination angle of 50 degrees is used with a total of 10,000 bins considered in the azimuth direction and 100 bins in the range direction.

6.5 Results

6.5.1 Perfect SAR

First we explore the predicted perfect SAR returns. These are the expected returns without limitations of the instrumentation or consideration of the operating conditions of the carrying vehicle. Perfect SAR returns for the case of calm seas are shown in Figure 6.4 for a hh polarization. The wake structure is nearly identical to the spectral density plots shown in Figure 5.14. The outer wake bands strongly define the edges of the wake, while the persistence of the center wake is diminished as the specular contribution and the randomized ocean realization are included. Streaks of amplified roughness at the wake edge are still observed on the windward side of the wake at L-Band. Wake widths of 120 m and 140 m are predicted here at 10 km and 20 km downstream based on an RCS of -0.5 dB. Similar to chapter 5, the structure of the wake is similar for conditions where the azimuth is along or across the wake, expect for the case of L-Band. At low frequency, the direct modification to the spectral density by surface currents and their gradients is the strongest influence on the observable wake.

The same ship condition is shown with a vv polarization in Figure 6.5. The variation in the wake is mostly observed as a reduction in damping of the centerwake. Reduction of

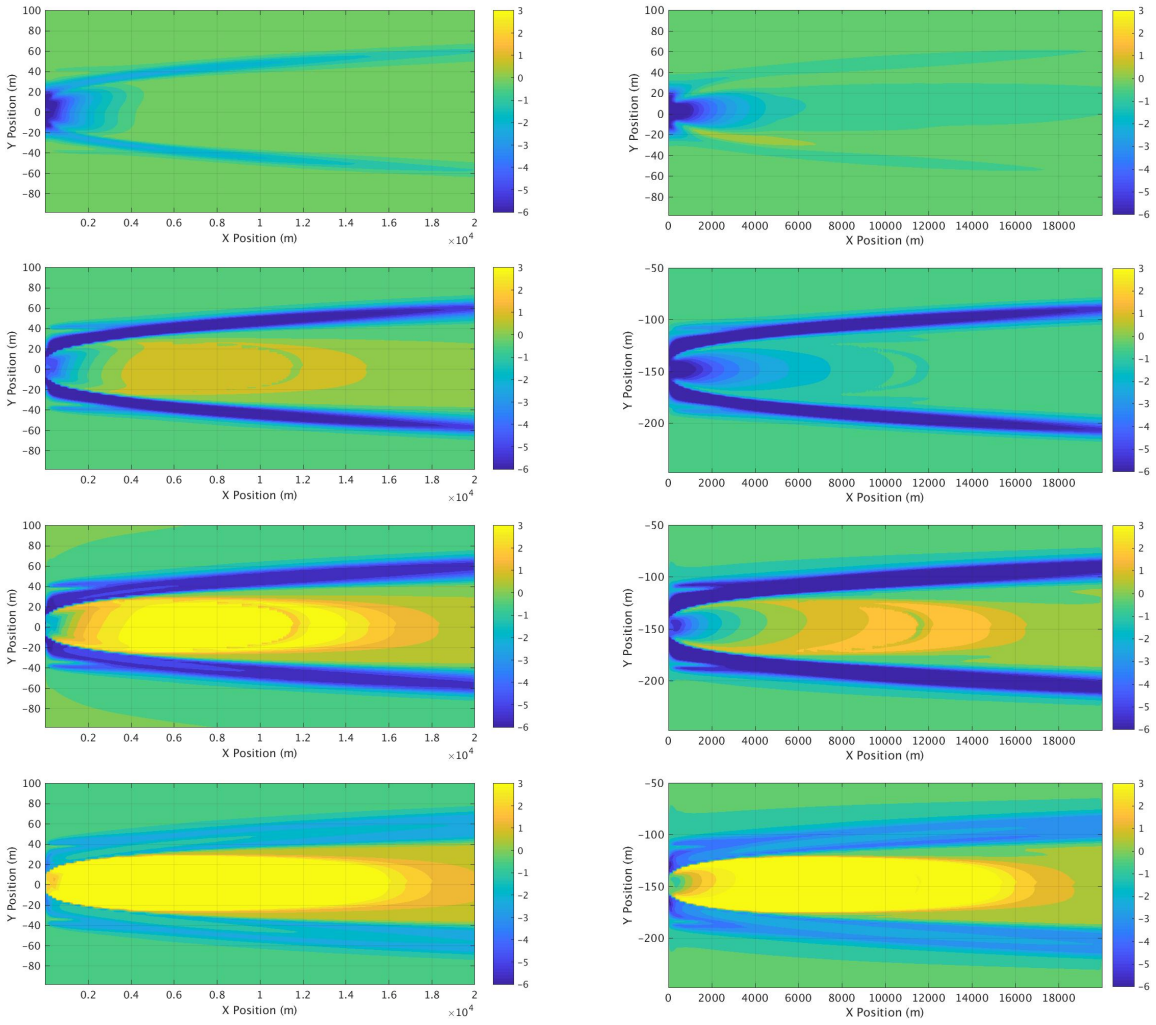

Figure 6.4: Perfect SAR images (dB) at L, S, C, and X band with hh polarization at 50 degree incidence with the azimuth along (left) and across (right) the wake for a calm seas condition.

the damping in the edge bands is also observed at X-Band, while no significant variation is observed in the edge bands for lower wavebands. These impacts are strongest for the case where the azimuth is along the wake.

A fundamental assumption made is that the maximum resolvable wave length is shorter than the nominal resolution. As resolution increases, the maximum long wave induced tilt angles decrease with the decreasing wave lengths. This influences the impact of polarization on the return. The tilt angle α effects both vertical and horizontal polarization, but considering that α is assumed small compared with the incidence angle, its impact is small and is shared by both hh and vv polarization. The out of plane tilt angle γ, however only effects the horizontal polarization scattering coefficient, introducing a variation in the return. Figure 6.6 shows the change in variation for maximum resolvable wave lengths ranging from 1-5m at 5 km and 15 km downstream. The variation between vv polarized images is observed to be much smaller than the hh polarized images. A change of less than 1 dB exists between the use of 1m and 5m maximum resolvable wave lengths for vv polarization at a downstream distance of 5 km . HH polarization exhibits a change of approximately 1.5 dB between 1m and 5m resolvable wave lengths. Centerline damping is increased with increasing resolvable wave length for both vv and hh polarizations, but all hh polarized cases showed greater centerline damping than even the highest resolvable wave length with vv polarization. While the 5m resolvable wave length simulations do not satisfy the requirement to be less than the nominal resolution (2m), they are shown here to reinforce the trend. At a distance of 15 km the variation in the centerline image has reduced, while the impact on the edge bands has increased. In the far wake (5 km), the edge bands are mostly unaffected by changes in resolvable wave length. At 15 km, the 5m resolvable wave length cases show reductions in the damping of the edge bands on the order of 3 dB.

The wake is also impacted by the wind speed, Figure 6.7 and direction, Figure 6.8. Conditions of low wind speed (0-1 m/s) show amplified roughness on the windward side of the wake compared to centerline in the far wake (5 km). As wind speed increases, the level of variation between the windward and leeward sides decrease as well as the relative energy reduction in the edge bands. In the persistent wake (15 km), regions of amplified roughness are observed in the centerwake for low wind speeds where damping due to turbulence and surface currents have dissipated. Higher wind speeds show relative ambient conditions through the wake center with decreasing strength of the edge bands as wind speeds increase. It should again be noted here that the current model does not account for reduced wind energy input in regions where SAS is concentrated as discussed in chapter 5. Inclusion of this effect would reduce the impact of higher wind speeds on the edge bands. It should also be noted that the change in wind speed is only considered for its energy input to the small wind waves in the wave action balance equation. Clearly, stronger sustained wind speeds would induce higher wave amplitudes and in turn stronger LTC, which would have a significant impact on the structure and persistence of the wake. The results shown here can be considered the effect of a freshening wind over a relatively calm day.

Wind direction is shown to have less of an impact than wind speed for the conditions studied

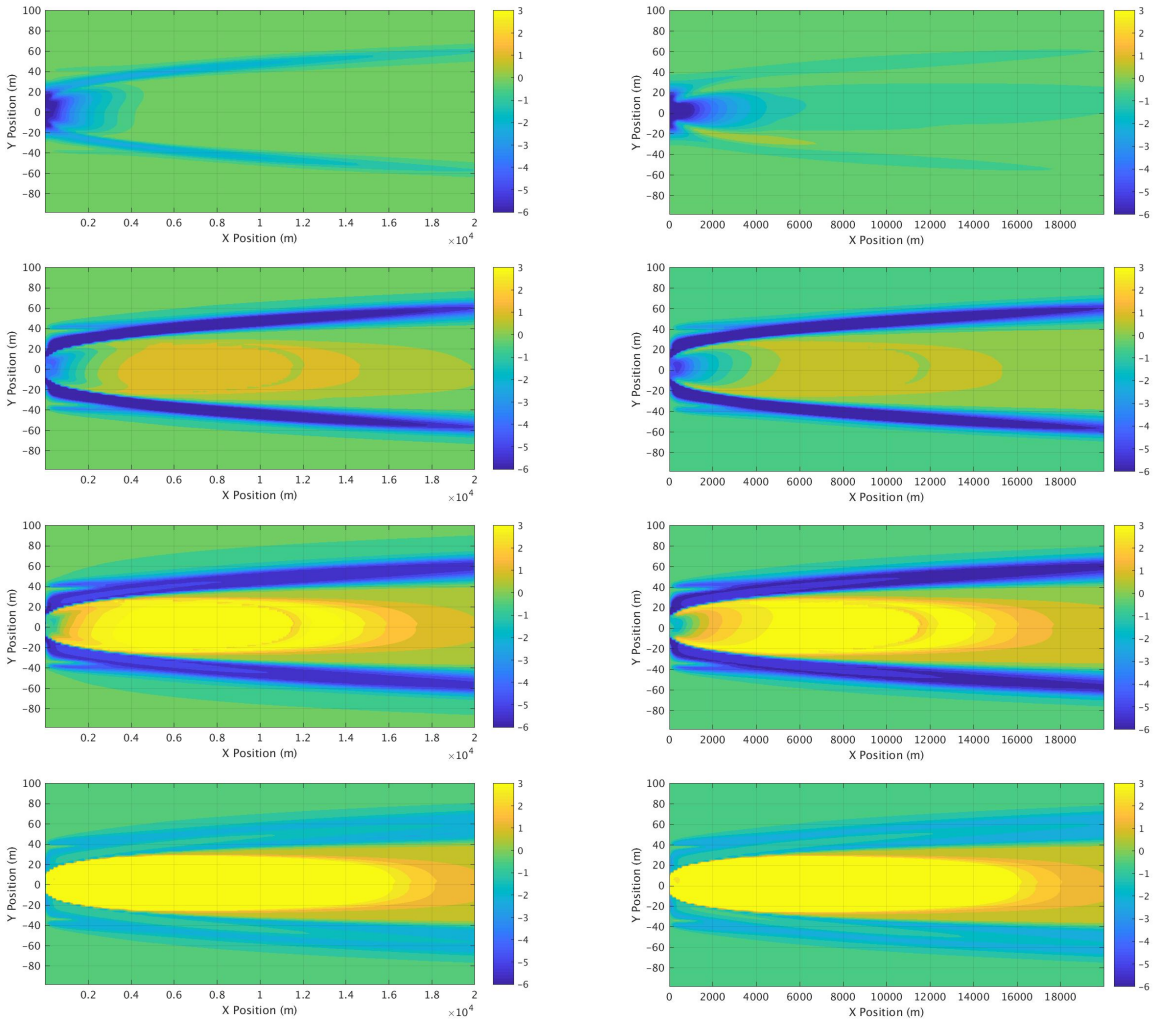

Figure 6.5: Perfect SAR images (dB) at L, S, C, and X band with vv polarization at 50 degree incidence with the azimuth along (left) and across (right) the wake for a calm seas condition.

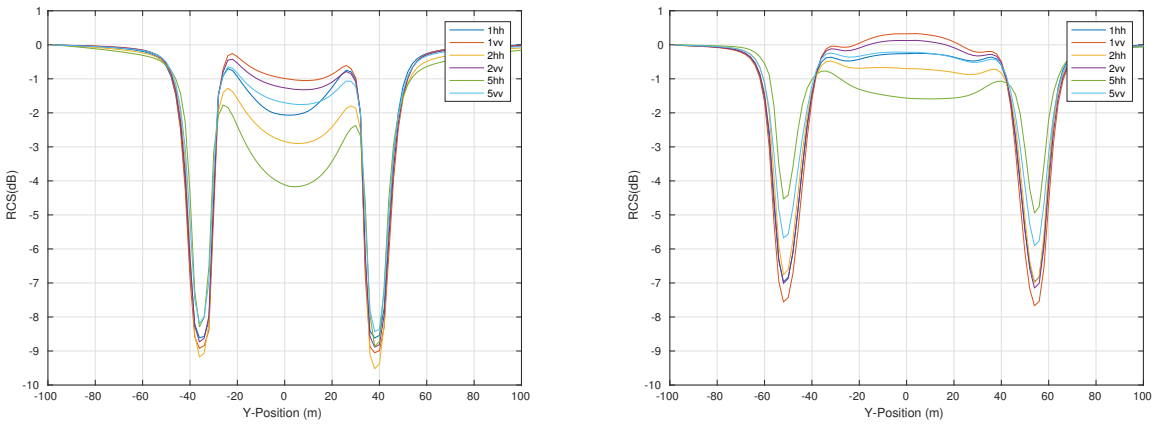

Figure 6.6: Impact of polarization on RCS return across the wake 5km (left) and 15 km (right) downstream for S-Band for a calm seas condition. Maximum resolvable wave lengths of 1, 2, and 5m are used with hh and vv polarization.

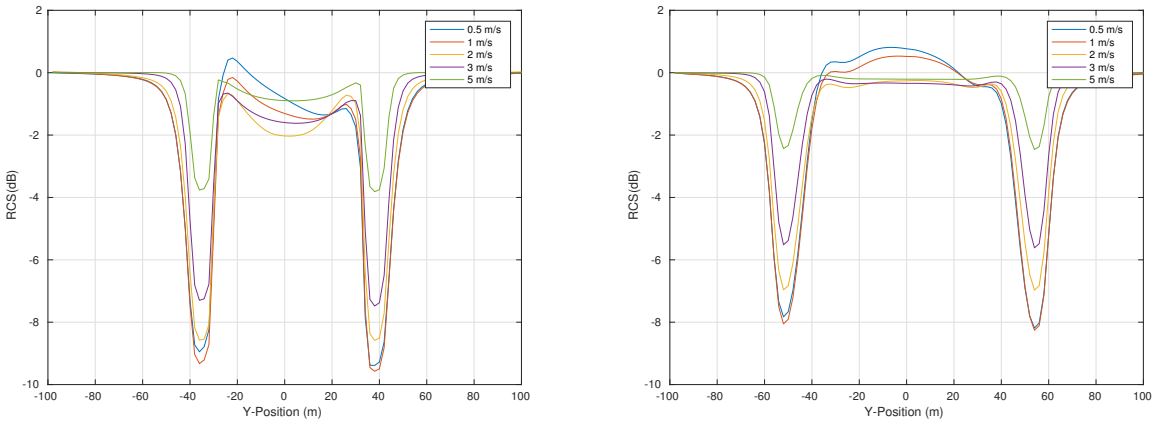

Figure 6.7: Impact of wind speed on perfect SAR images (dB) at S-Band with hh polarization for distances of 5 km and 15km in calm seas.

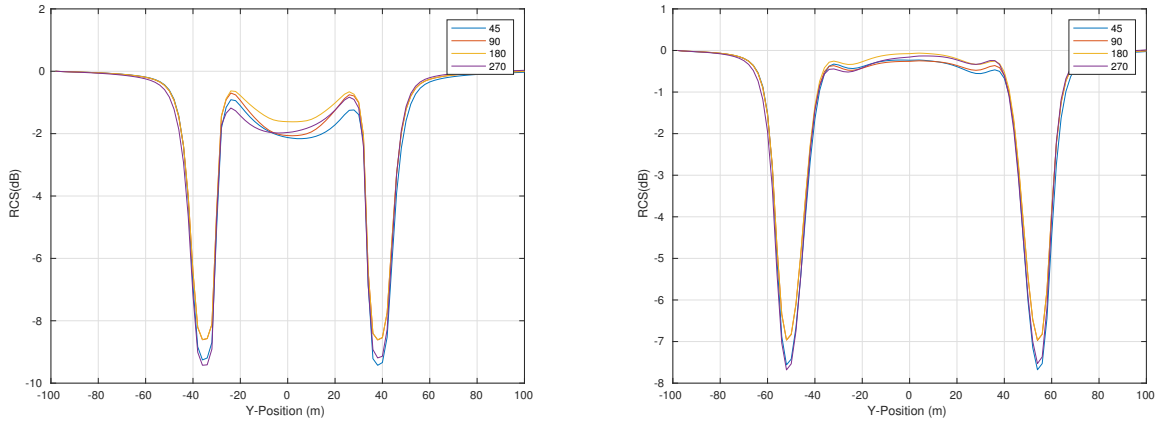

Figure 6.8: Impact of wind direction on perfect SAR images (dB) at S-Band with hh (right) polarization for distances of 5 km and 15km in calm seas with a wind speed of 2 m/s.

here, Figure 6.8. Conditions where the wind is at an angle across the wake shows the greatest levels of centerline damping in the far wake (5 km). Here the wind interfaces with the both the transverse and axial currents such that the peak dampening is offset from centerline on the leeward side of the wake. Conditions where the wind is orthogonal to the wake shows a similar response where the roughness is amplified on the windward side and dampened on the leeward side. The condition where the wind is along the wake shows the lowest level of damping. This condition is symmetric about centerline. The edge bands are slightly impacted by the wind direction, the impact is slight in comparison to wind speed. In the persistent wake (15 km), the impact on the wake due to wind direction is small. True et al. [149] highlights the impact of wind direction on the wake 1000m downstream where SAS bands are not considered and demonstrates relevant variation for a 9 knot wind speed. Additional data, either numerical or experimental, are not provided for distances downstream, but the impact on the near field at higher wind speeds at a minimum is highlighted.

The ambient turbulent dissipation rate at the surface is an area of uncertainty as discussed in chapter 5. The relative RCS in the wake is taken using a range of dissipation rates in Figure 6.9. As expected, the magnitude of damping in the edge bands and center wake is increased with lower ambient surface turbulent dissipation. Relative damping in the center wake is similar for ambient dissipation rates of $\varepsilon = 1x10^{-4}$ and $\varepsilon = 1x10^{-5}$ as contributions of ship induced turbulence are lost into the ambient. At the lower value of $\varepsilon = 2x10^{-7}$, the ship induced turbulence is high relative to ambient and shows a stronger manifestation of the center turbulent wake. The edge bands are impacted as expected with reduced relative damping with increasing ambient turbulent dissipation. At a distance of 5 km the impact shows variability of 3 dB between ambient values of $\varepsilon = 2x10^{-7}$ and $\varepsilon = 1x10^{-4}$ and variability of 2.5 dB at 15 km. The structure of the wake is not impacted by the change in ambient turbulent dissipation, but direct quantitative comparison with experimental data would require an understanding of this environmental condition.

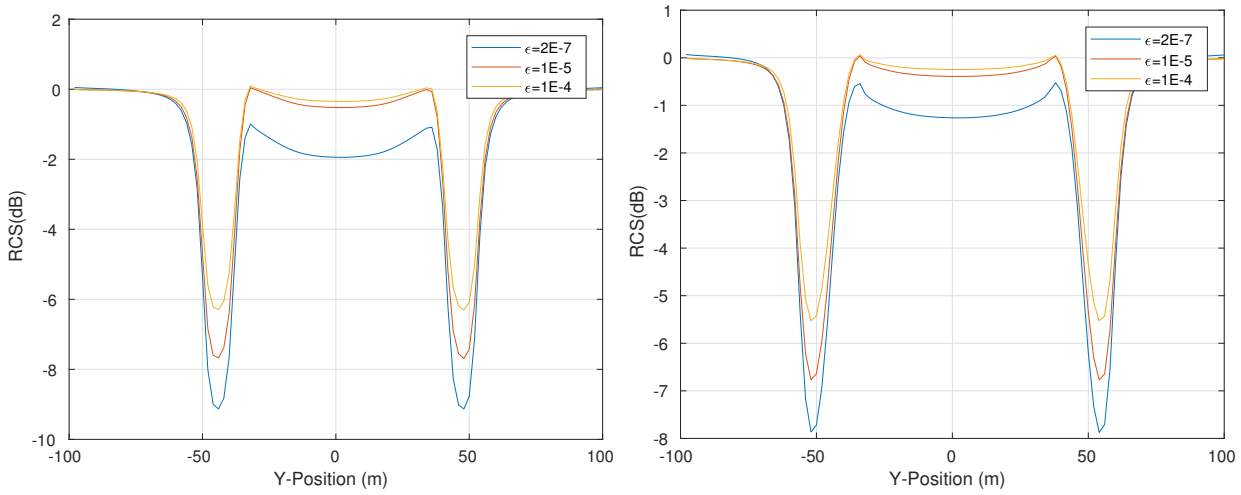

Figure 6.9: Impact of ambient turbulent dissipation on perfect SAR images (dB) at S-Band with hh (right) polarization for distances of 5 km and 15km in calm seas with a wind speed of 2 m/s.

The other primary environmental condition that impacts the wake is the ambient SAS film pressure/area. Cuts through the wake at 5 km and 15 km downstream with ambient film area ranging from 240-300 cm^2 is shown in Figure 6.10. The film area is not a directly measurable quantity in an ocean environment, but is correlated to the film pressure through laboratory evaluations of collected material samples. The film area is used here as it corresponds to the level of SAS concentration ($\Gamma = {}^{A_0}/_{A}$). In a similar fashion to the variations in ambient turbulent dissipation rate, the structure of the edge bands are not impacted by the ambient film area, but the magnitudes are. Variations greater than 2 dB are observed in the edge bands over the range of film areas studied with higher levels of damping in the edge bands with higher ambient film areas. Higher ambient film areas corresponds with lower ambient film pressures and lower ambient damping due to SAS. Within the center wake, ambient film areas of 275 cm^2 and 300 cm^2 show similar results with close to ambient conditions. Lower ambient film areas ($250cm^2$ and $240cm^2$) show areas of amplified roughness compared to ambient. Here, SAS has been redistributed to the wake edges, significantly reducing the levels of short wave damping. As the ambient film area decreases, the ambient SAS damping increases, which leads to the higher relative RCS in areas where SAS has been removed. Within the persistent wake (15 km) the edge band with an ambient film area of 300 cm^2 has reduced in magnitude to a level similar to the case with an ambient film pressure of $250cm^2$. The SAS concentrations in the edge bands here have reduced to the point where the absolute damping is partially a function of the ambient film pressure/area as discussed in chapter 4 and shown in Figure 4.3. At 5 km the absolute damping in the edge bands is relatively equal at S-Band for SAS concentrations around 3.

Next we consider the case where the ship is operating in following seas with wave amplitudes between 0.5 m and 1.5 m, figures 6.11-6.13. In conditions of low wave amplitude (0.5 m), the

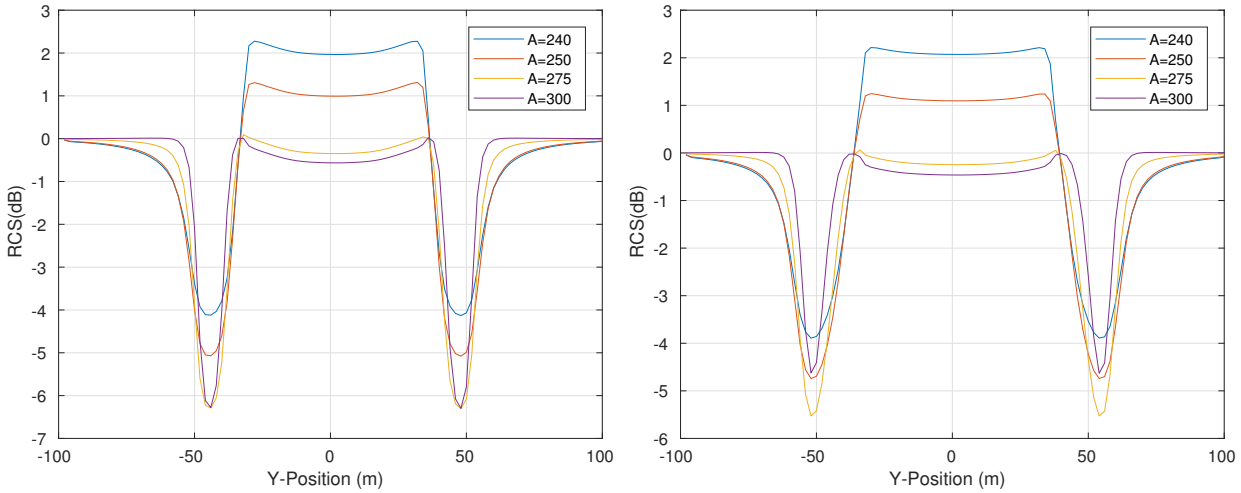

Figure 6.10: Impact of ambient SAS film area (cm^2) on perfect SAR images (dB) at S-Band with hh (right) polarization for distances of 5 km and 15km in calm seas with a wind speed of 2 m/s.

wake structure is similar to the case of calm seas with slightly wider edge bands (126m and 144m at 10 km and 20 km). As wave amplitude increases, LTC induce stronger transverse surface currents, widening the width of the the edge bands. Wake widths of 144 m and 194 m are predicted here at 10 km and 20 km downstream based on an RCS of -0.5 dB for the 1.0 m wave amplitude. The streaks of amplified roughness observed in L-Band increase in magnitude also due to the increased outboard surface currents. In addition, as the width of the wake increases the transverse surface currents along centerline decrease with distance downstream, leaving regions of SAS in the center of the wake as discussed in chapter 5. The variation due to polarization is similar to that showed in calm seas. Perfect SAR images for vv polarization are provided in Appendix C.

Finally, we examine the perfect SAR images for a ship operating in a head seas condition, figures 6.14-6.16. Conditions of low wave amplitude appear similar to the calm seas condition at L-Band, in particular when the range is along the wake. At higher wavenumbers, the centerline streak becomes visible for distances beyond 8 km while the edge bands due to surface currents induced by Reynolds stress anisotropy are strong and persist for the range of study. As wave amplitude increases, the centerline streak strengthens and its formation point moves forward into the turbulent near wake, while the edge bands weaken and are pulled inboard.

6.5.2 Simulated SAR

Predictions of the simulated SAR returns are now explored for a space based system operating at an altitude of 500 km. Images are generated with the azimuth both along and across the

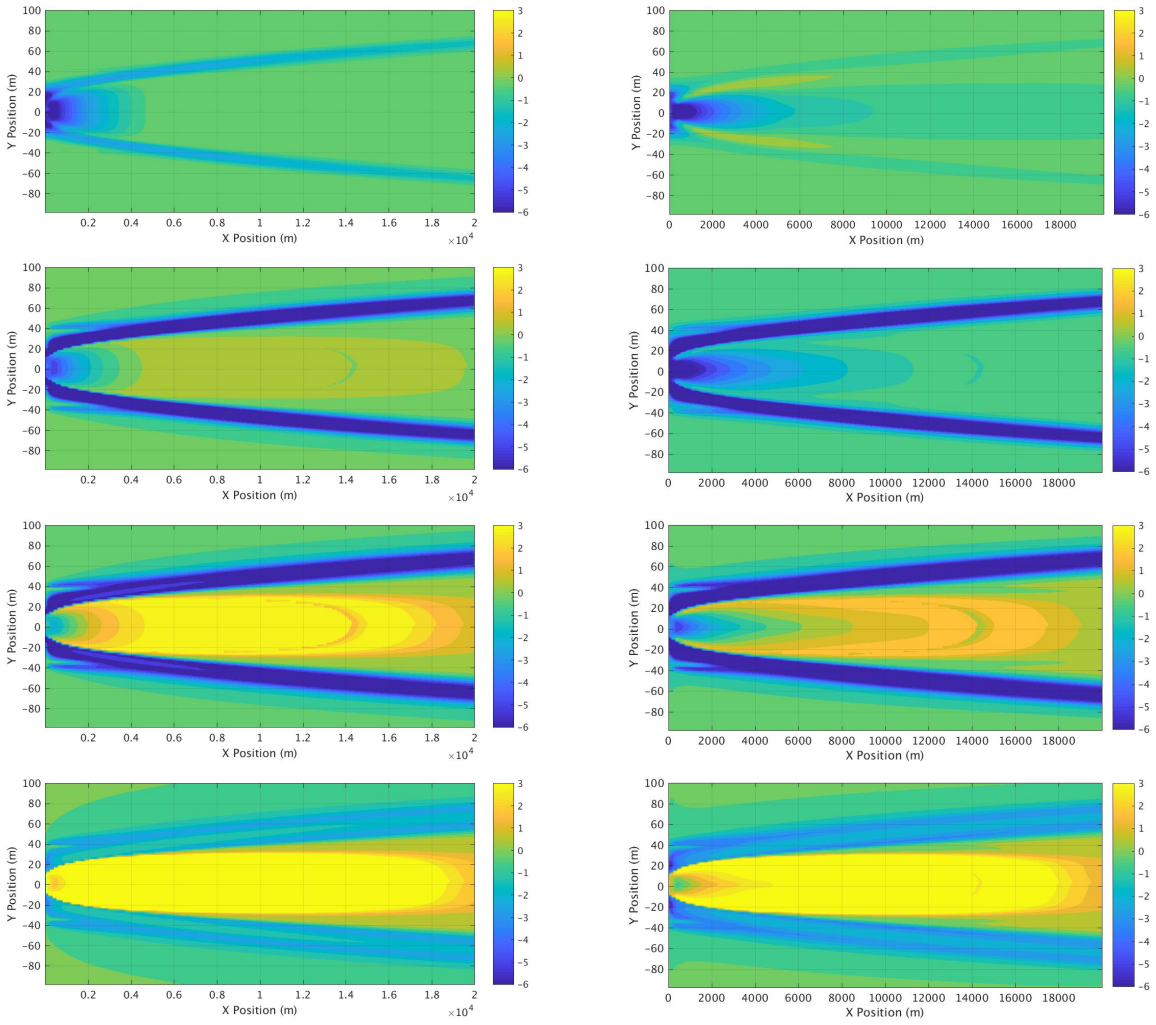

Figure 6.11: Perfect SAR images (dB) at L, S, C, and X band with hh polarization at 50 degree incidence with the azimuth along (left) and across (right) the wake for a 0.5 m wave amplitude in following seas.

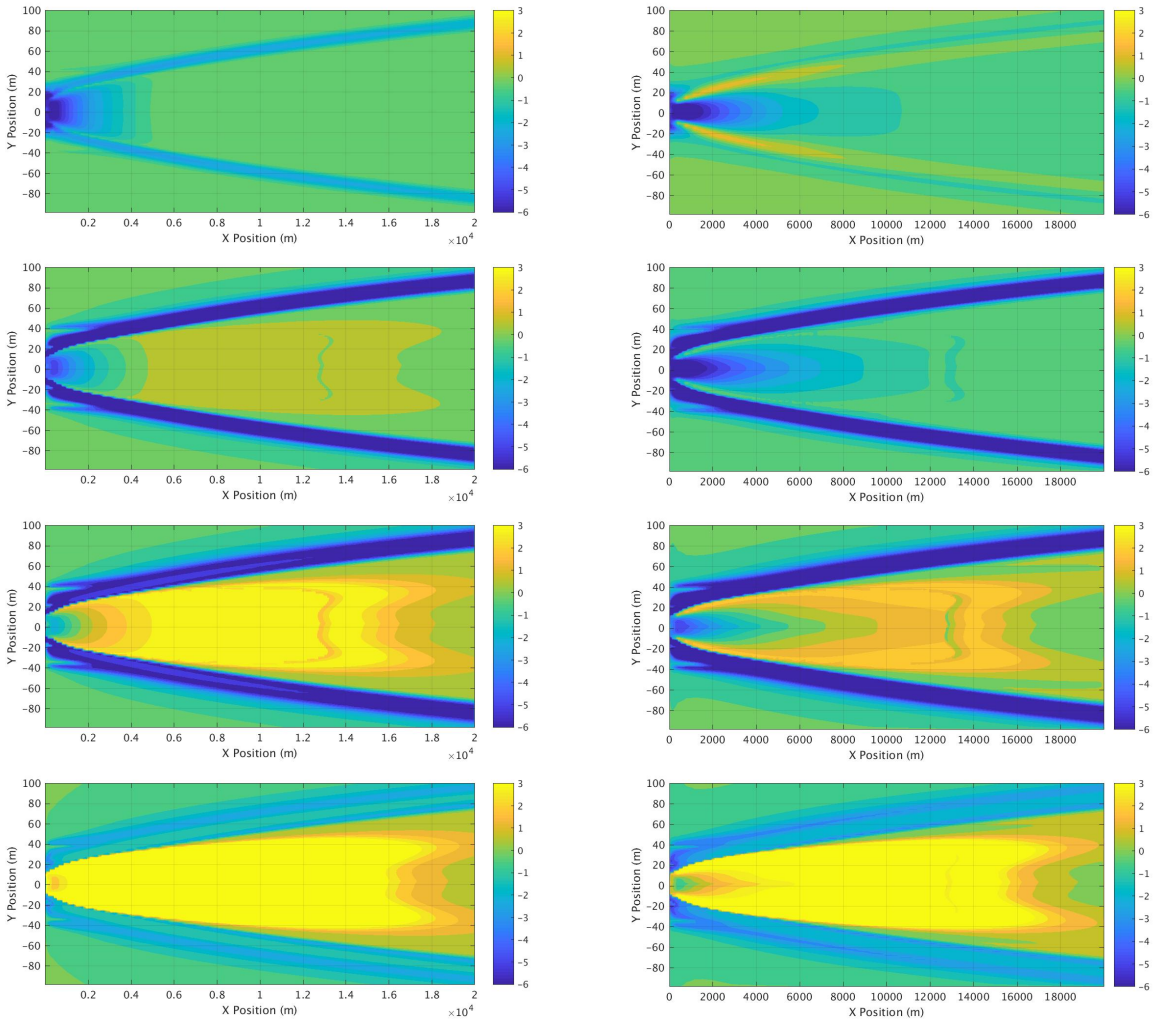

Figure 6.12: Perfect SAR images (dB) at L, S, C, and X band with hh polarization at 50 degree incidence with the azimuth along (left) and across (right) the wake for a 1.0 m wave amplitude in following seas.

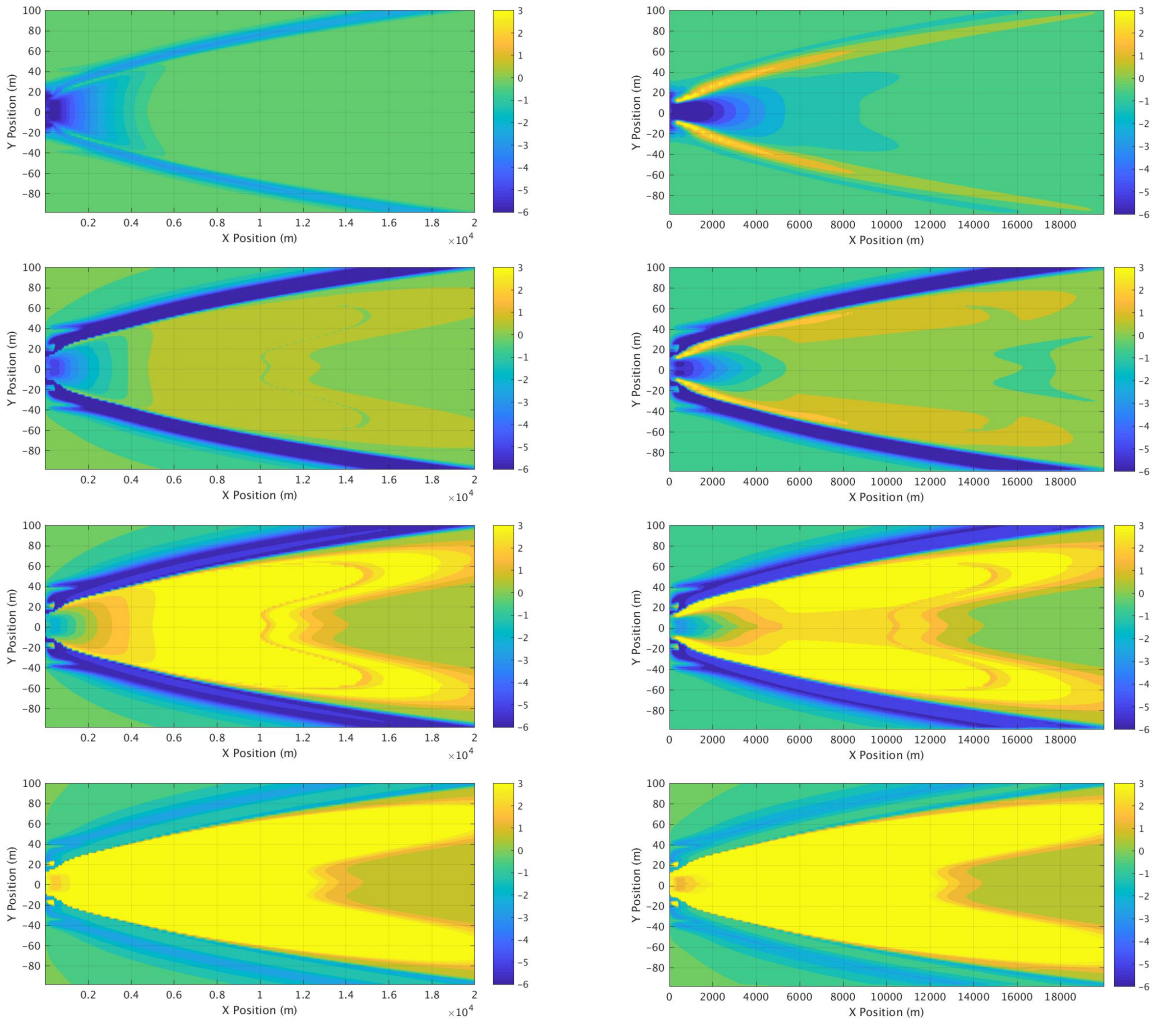

Figure 6.13: Perfect SAR images (dB) at L, S, C, and X band with hh polarization at 50 degree incidence with the azimuth along (left) and across (right) the wake for a 1.5 m wave amplitude in following seas.

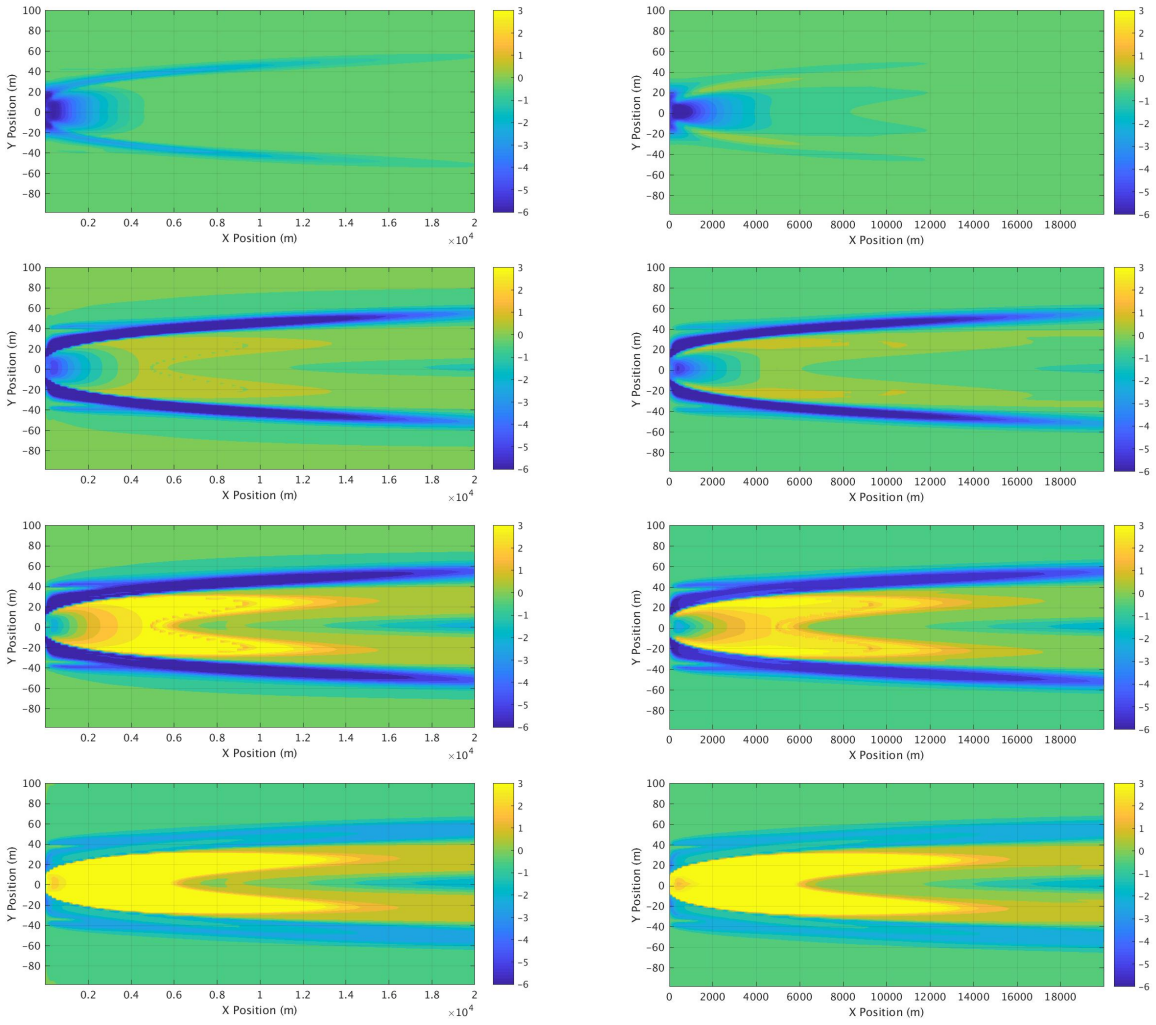

Figure 6.14: Perfect SAR images (dB) at L, S, C, and X band with hh polarization at 50 degree incidence with the azimuth along (left) and across (right) the wake for a 0.5 m wave amplitude in head seas.

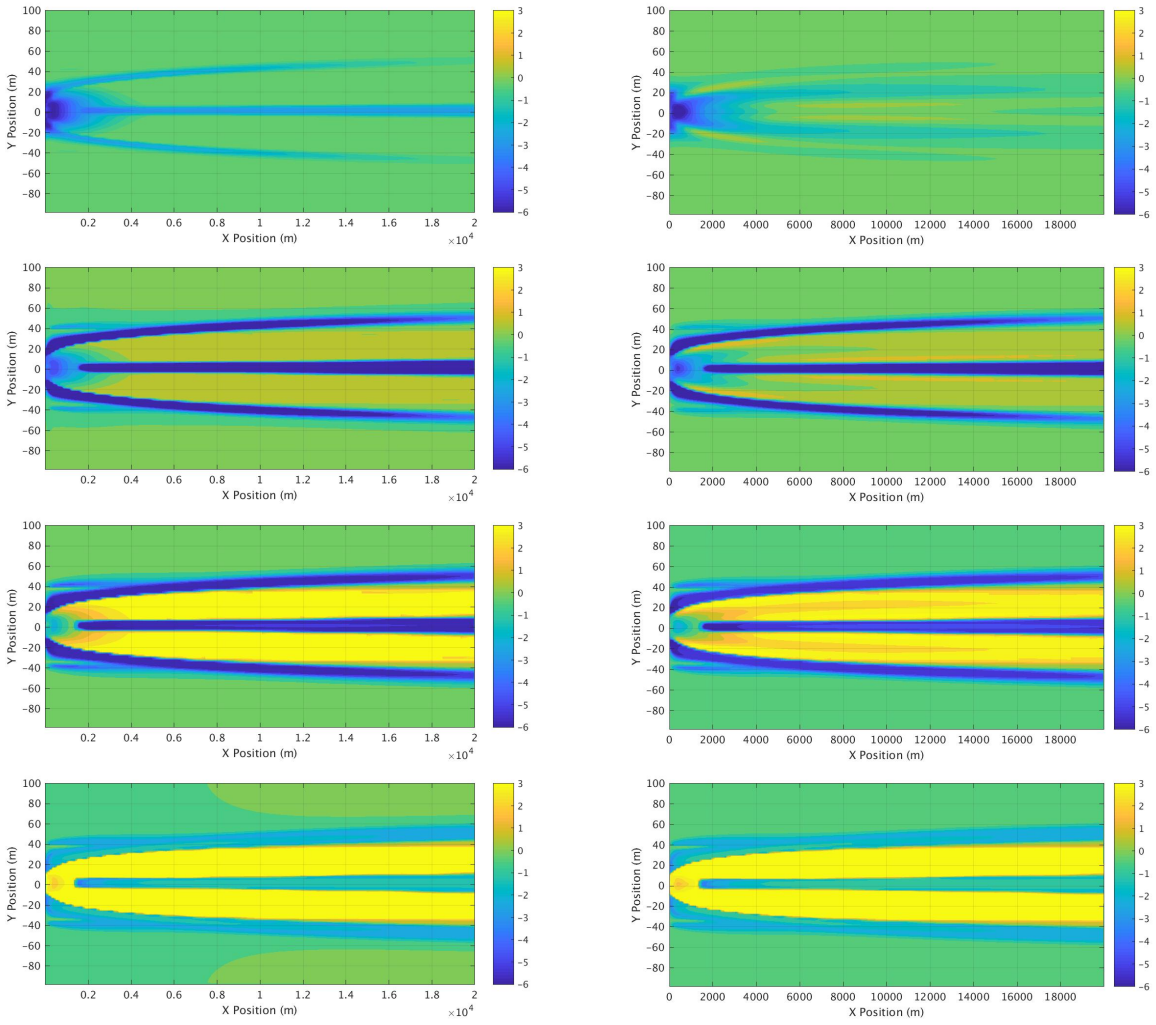

Figure 6.15: Perfect SAR images (dB) at L, S, C, and X band with hh polarization at 50 degree incidence with the azimuth along (left) and across (right) the wake for a 1.0 m wave amplitude in head seas.

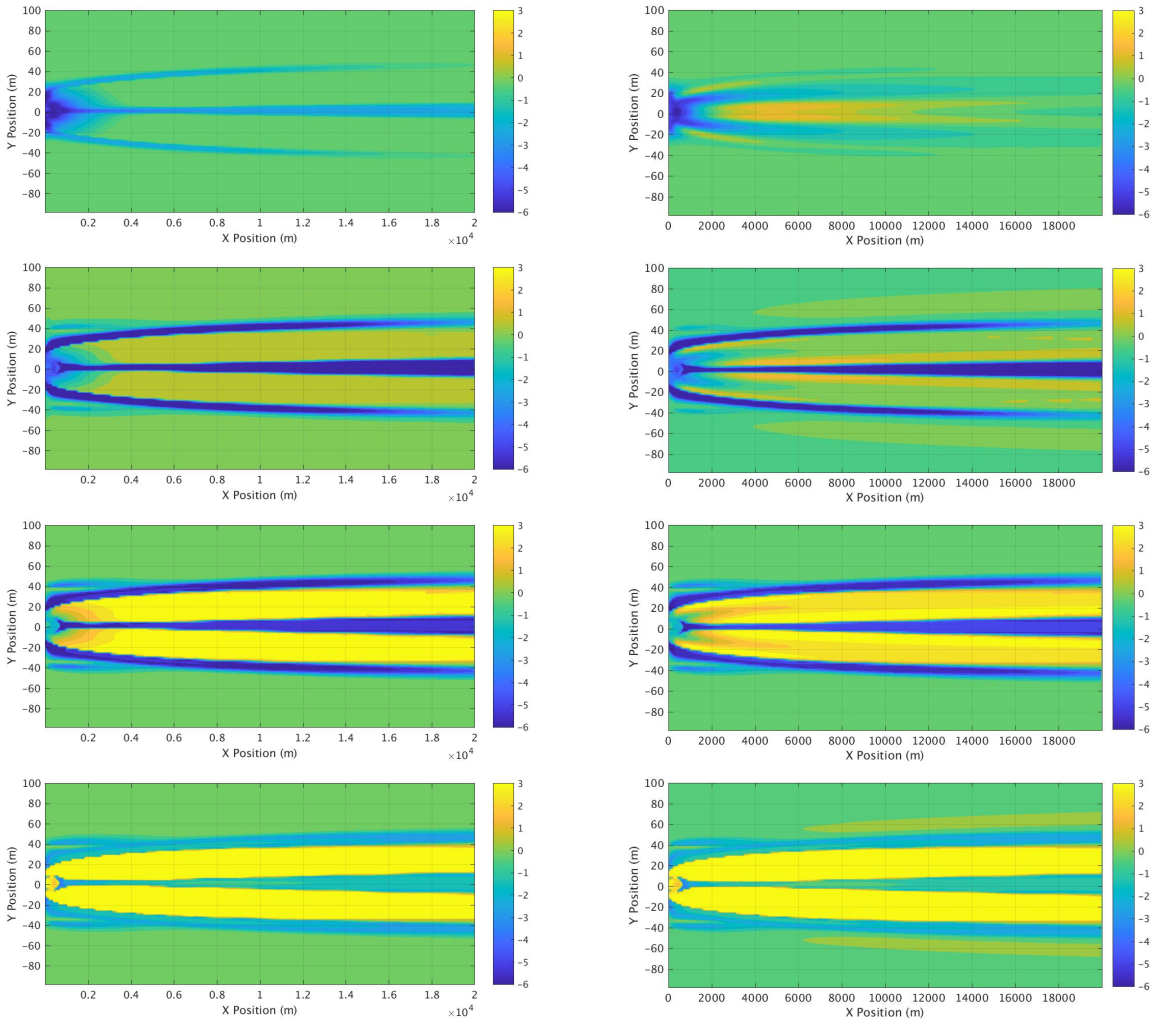

Figure 6.16: Perfect SAR images (dB) at L, S, C, and X band with hh polarization at 50 degree incidence with the azimuth along (left) and across (right) the wake for a 1.5 m wave amplitude in head seas.

wake with a reference value taken as the mean of the RCS along the first 1000 m of the image edge. Predictions of the simulated SAR returns for calm seas are shown in Figure 6.17. The simulated SAR returns under these conditions are dominated by the damping due to SAS in the persistent wake for wave numbers greater than L-Band. The damping due to surface currents and turbulence is observed in the near/far wake, but any resolvable structure is lost here. At L-Band, the near/far wake damping is evident, but the edge bands are mostly lost. Similar returns are generated for conditions where the azimuth is along or across the wake, but with distortions of the near wake due to the image windowing process. Images with vv polarization are similar to hh polarization as the primary impact in Figure 6.5 was observed through the center wake, which is mostly washed out here. Images of the vv polarized returns are provided in Appendix C.

Next, the simulated SAR returns for the ship operating in following seas are shown in Figure 6.18. Here we focus on the returns where the azimuth is along the wake with hh polarization. Images with vv polarization are provided Appendix C. The structure of the wake in following seas is similar to the case in calm seas with increasing width between the edge bands. As wave amplitude increases, the streaks of amplified roughness become evident as transverse velocity gradients increase. The near ambient conditions through the wake center in the persistent wake are also evident where the LTC have moved sufficiently outboard to form a region that is relatively quiescent.

Comparing across wake cuts of the simulated SAR images to the perfect SAR images highlights the variability in the wake due to the randomized ocean realization, Figure 6.19. Here the areas of SAS damping are clearly observed, but determination of the wake structure with only the isolated wake cuts would not be possible here due to the high levels of variability. Determination of the wake width here would prove difficult as regions of reduced RCS are also observed on the edges of the domain at 5 km and on one side at 15 km.

Finally, the case of the ship operating in head seas is examined. At low wave amplitude (0.5m), L-Band shows attenuation in the near/far wake with minimal resolvable features in the persistent wake. As discussed in 5, the wake here is less persistent than the case of calm seas. With increasing wave amplitude, the L-Band return shows a pair of narrow bands, approximately 40m in width, into the persistent wake. The case of calm seas showed edge bands approximately 110 m at 10km downstream and 140m at 20km downstream. At S-Band, the wake at low wave amplitudes strongly resembles the return for calm seas with slightly lower wake widths. Wave numbers of C and X-Band begin to show the formation of the centerline streak in the persistent wake, signifying a head seas condition.

Techniques that use SAR images of ship wakes to classify the source would significantly under predict the ship size while using purely an L-Band return in head-seas conditions.

Comparison to cuts across the perfect SAR image for the 1.0 m wave amplitude case is similar to the case of following seas. The SAS streaks are observable amongst the clutter with low RCS values again appearing on the wake edges at 5 km and on one side at 15 km downstream. The strength of the centerline damping is highlighted even beyond that

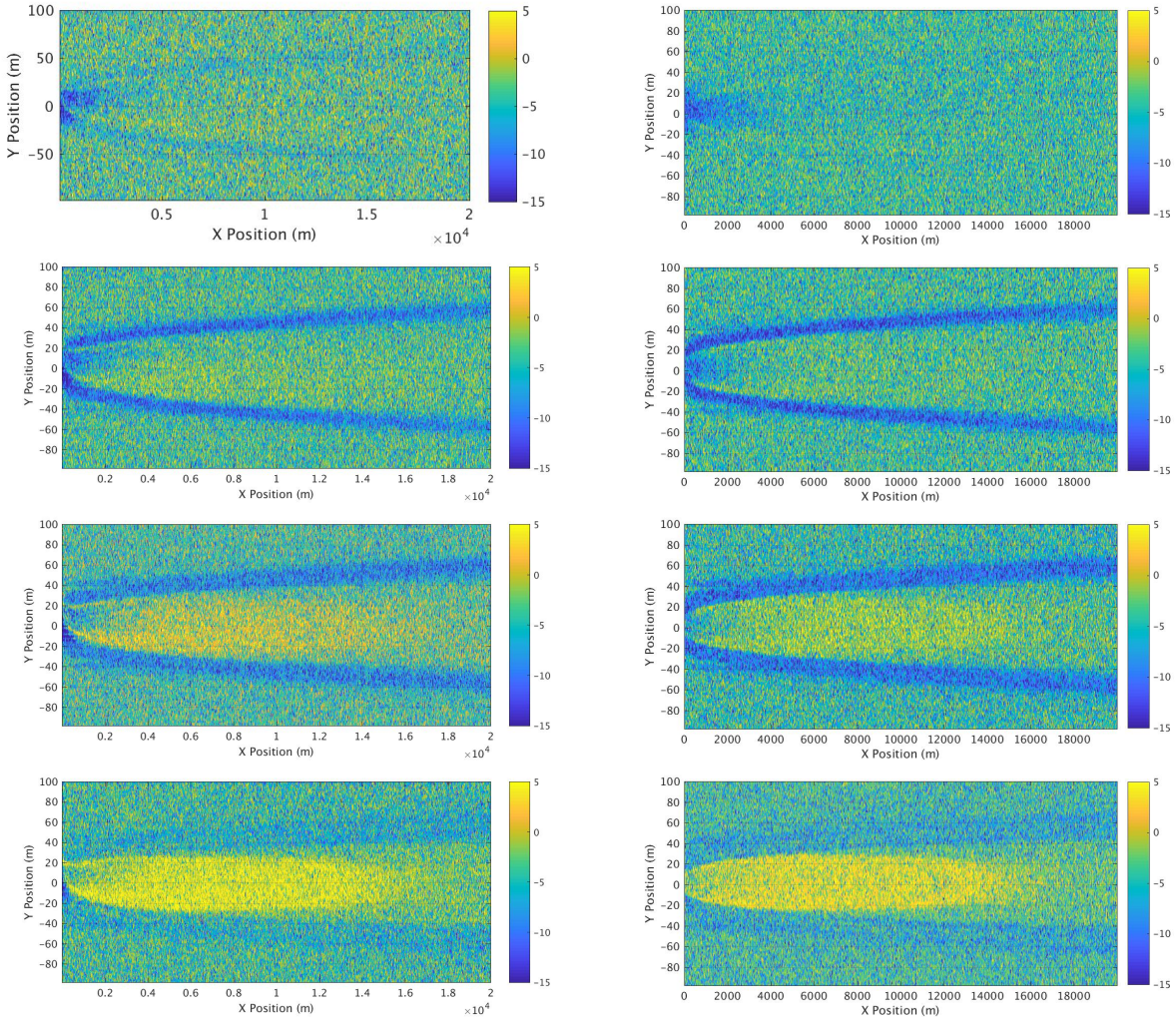

Figure 6.17: Simulated SAR images (dB) at L, S, C, and X band with hh polarization at 50 degree incidence with the azimuth along (left) and across (right) the wake for a calm seas condition.

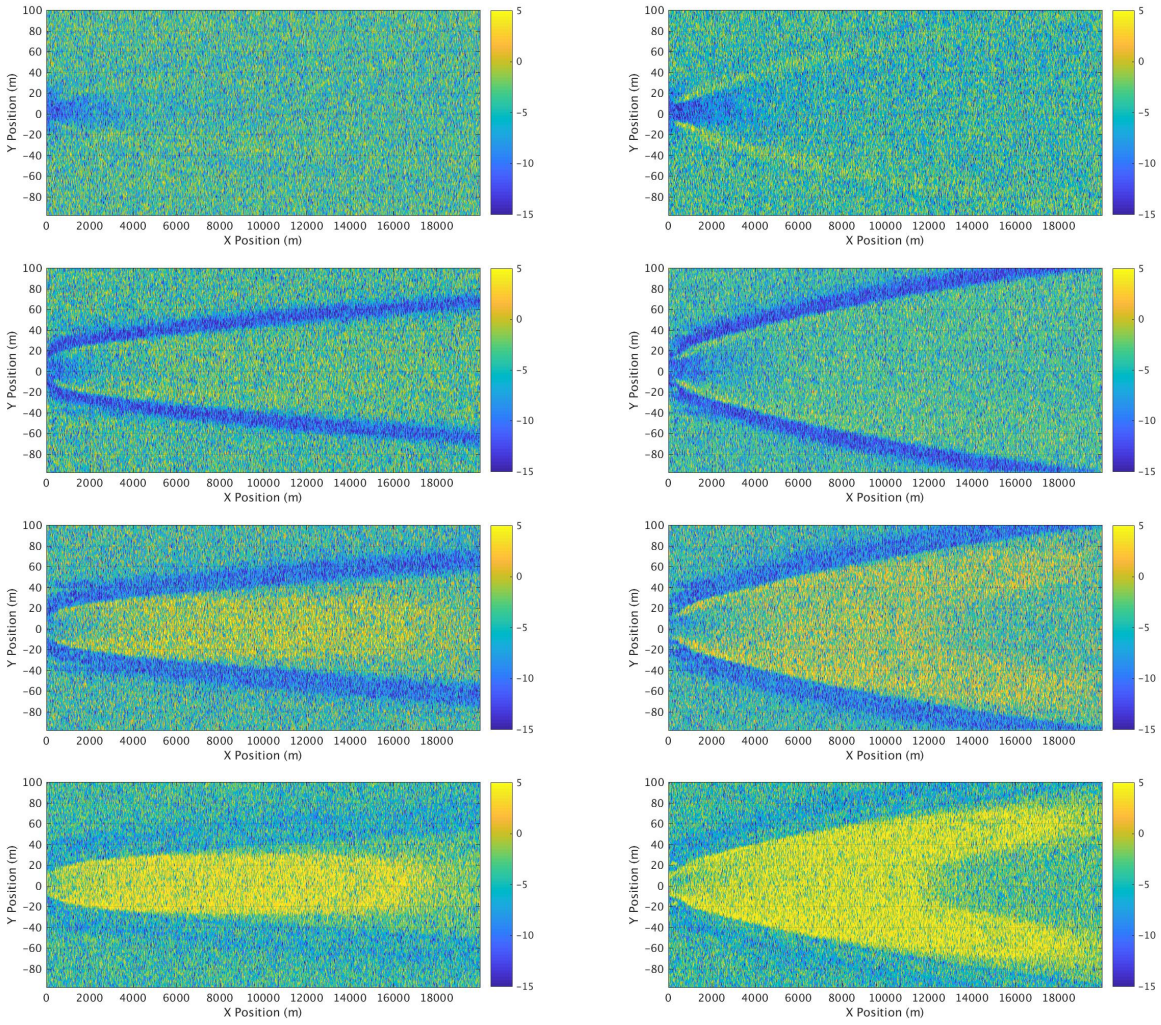

Figure 6.18: Simulated SAR images (dB) at L, S, C, and X band with hh polarization at 50 degree incidence with the azimuth along the wake for a following seas with 0.5m (left) and 1.5m (right) wave amplitudes.

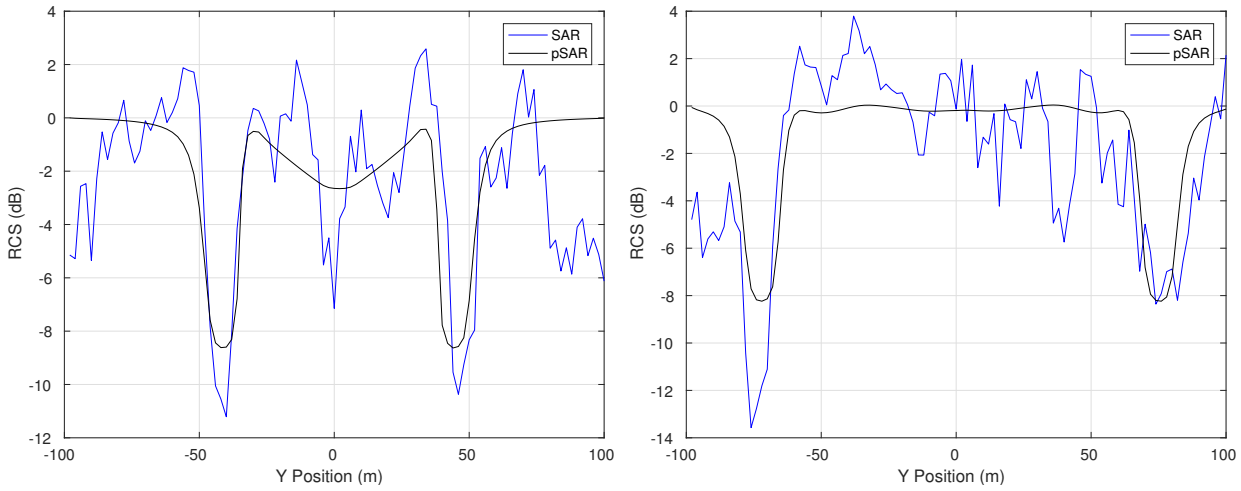

Figure 6.19: Comparison of simulated SAR return and perfect SAR return at S-Band with hh polarization at 50 degree incidence with the azimuth along the wake for following seas with a 1.0m wave amplitude at distances of 5 km (left) and 15 km downstream. Simulated SAR images are averaged over 10 m windows across the wake.

predicted by the perfect SAR return and the edge are also observable into the persistent wake.

6.6 Comparison with Experimental Data

During the 1989 ONR Field Experiment [115] wake widths were measured in the wake of the USS Chandler (DDG-996) based on the distance between SAS edge bands measured by a smaller research vessel transiting across the wake. Wake widths of 150 m and 170 m were measured at distances of 10 km and 20 km behind the ship during 25 knot runs in seas coming from the stern quarter (following seas), Figure 5.26. Perfect SAR predictions here show these widths to correspond well to conditions with wave amplitudes between 0.5-1.0 m. It is again noted wake widths in calm seas, without LTC, predicted wake widths much less than those observed in the experiment, highlighting the complementary nature of LTC and near surface Reynolds stress anisotropy induced currents.

SAR imagery of the wake was also processed by Milgram et al. [99] at L and C-Band and averaged over 12 m windows, Figure 6.22. Similar to results from chapter 5, perfect SAR returns at 3.5 km show damping through the wake center of 2.5-3 dB at L-Band in good agreement with Milgram et al. [100]. The damping due to SAS along the edge bands at L-Band though are again under predicted due to the roughness amplification induced the by strong surface current gradients. Incorporation of a wave energy reduction model to account for the reduction in friction velocity in areas of SAS concentration would help in locally reducing the wind energy input in these areas. In addition, further study into the impact of

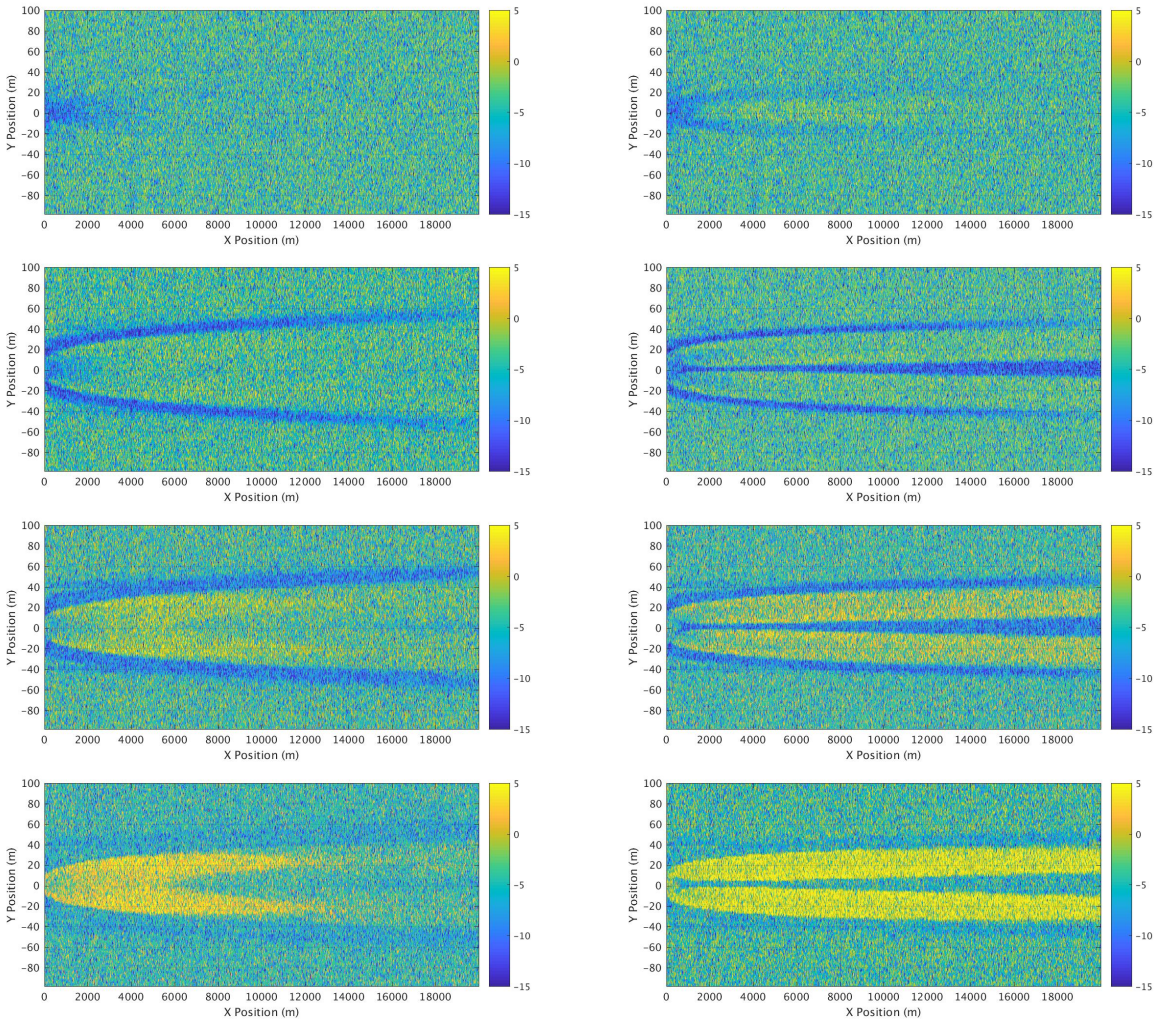

Figure 6.20: Simulated SAR images (dB) at L, S, C, and X band with hh polarization at 50 degree incidence with the azimuth along the wake for a head seas with 0.5m (left) and 1.5m (right) wave amplitudes.

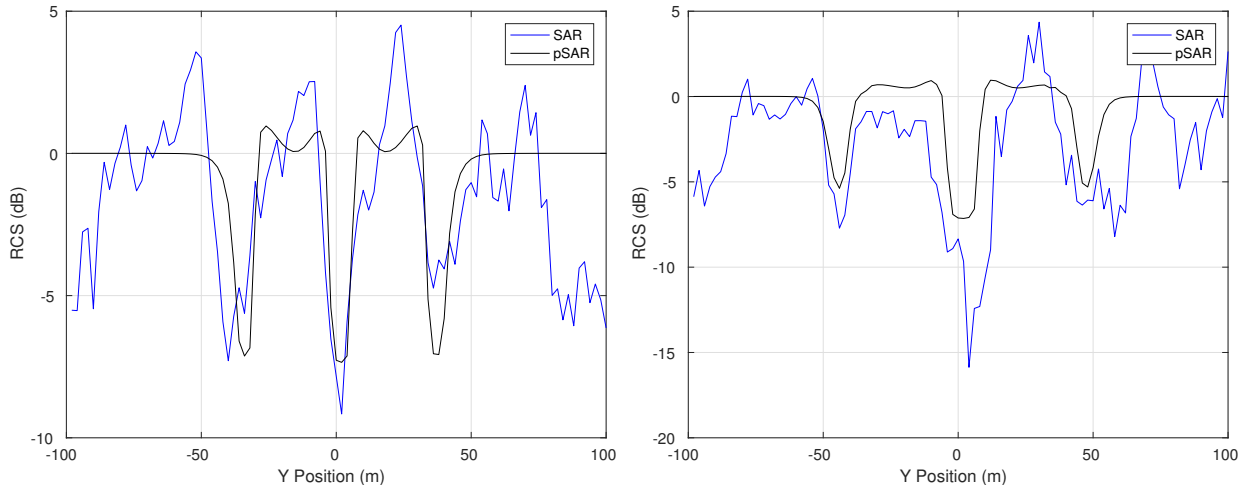

Figure 6.21: Comparison of simulated SAR return and perfect SAR return at S-Band with hh polarization at 50 degree incidence with the azimuth along the wake for head seas with a 1.0m wave amplitude at distances of 5 km (left) and 15 km downstream. Simulated SAR images are averaged over 10 m windows across the wake.

SAS on surface currents induced by near surface Reynolds stress anisotropy in line with work accomplished by Anthony et al. [9] would further improve model prediction capabilities.

Comparisons to C-Band show similar agreement through the wake center, but the predicted damping in the edge bands is greater than that in the measured data. It should also be noted that the model of Milgram et al. [100] also over predicts edge damping in C-Band. The predicted reduction in SAR intensity in the edge bands in Figure 6.22 is limited to -2 dB at C-Band. Milgram et al. [100] later decrease the lower limit to -3 dB at C-Band and observe the edge bands to also be capped by this limit. No attempt is made to find the actual lower bound of the model as it is commented that no regions in the experiment showed depressions of SAR intensity greater than 3 dB. No significant change was observed

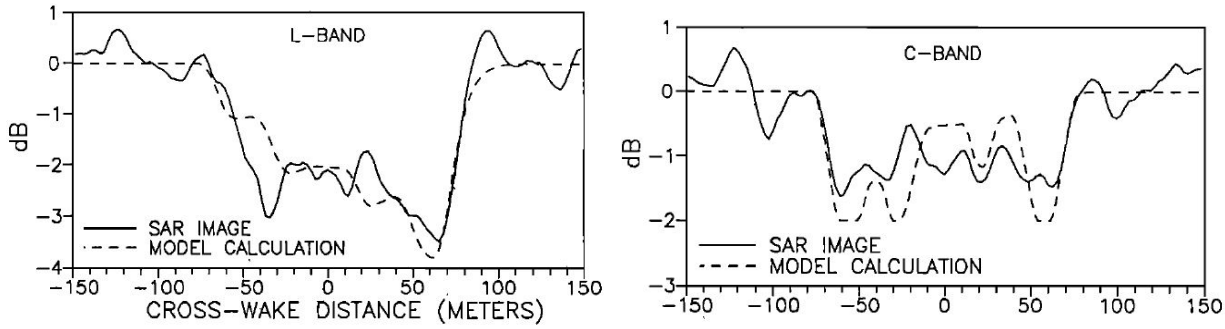

Figure 6.22: SAR image intensity measured 3563 m behind the ship at L-Band (left) and C-Band (right) from Milgram et al. [100]. Data was averaged over 12 m across the wake.

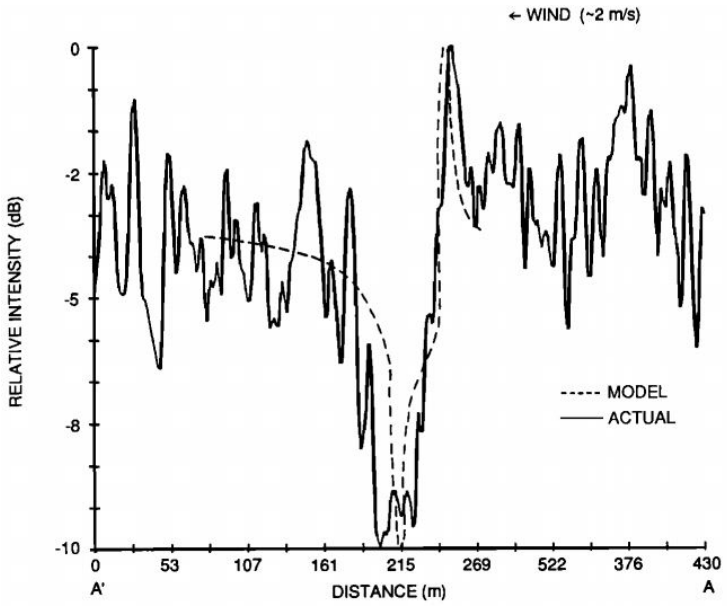

Figure 6.23: Radar backscatter measured in the wake of USS Quapaw approximately 1 km downstream during the 1983 U.S.-Canda Joint Ocean Wave Investigation Project (JOWIP). (Lyden et al. [88])

by decreasing the lower limit of the L-Band prediction. Milgram et al. [100] comments that it is unclear if these measured results are accurate at C-Band or if the recorded energy levels are impacted by the background noise. It should also be noted that the film pressure values used in Milgram et al. [100] were set to 12 mN/m based on the experimental data. Peltzer [115] notes that the oils used to measure higher values of surface tension reduction were not operating properly, limiting the maximum measurable reduction in surface tension to 12 mN/m. The actual peak of surface tension reduction was found to be some value between 11.3 mN/m and a value greater than 27.2 mN/m. These peak film pressures would be more in line with the levels of SAS concentrations predicted here.

Variations in the SAR data of approximately 0.5 dB was measured in Figure 6.22. The scatter in the simulated SAR data predicted here significantly exceeds this observed variability and is more in line with that measured during the 1983 U.S.-Canda Joint Ocean Wave Investigation Project (JOWIP), Figure 6.23 [89]. Improvements in the prediction of the ocean realization as well as methods of image processing would reduce this variability and improve the simulated SAR images.

6.7 Conclusions

A model for predicting the SAR return of a surface ship wake has been presented here. The model is based on a composite approach where Bragg scattering accounts for the small scale structure and a specular component accounts for the larger scale wave structure. Two primary results are generated, the perfect SAR image and the fully simulated SAR image. The perfect SAR image is the result when limitations of the SAR instrument are neglected, while the fully predicted SAR image simulates the full SAR process from signal reception through image processing including the range and speed of the instrument. The perfect SAR images show good agreement with the structure of observed wakes along with good quantitative agreement over several important areas such as damping of the centerwake region by turbulence and surface currents and the measured growth of the wake width. Damping due to SAS tends to be over predicted compared to C-Band data. This is attributed to several factors. First, the SAS redistribution model neglects any sources/sinks and allows surface currents to redistribute until a steady state condition is achieved without consideration of significant sources of diffusion. Secondly, surface currents induced by Reynolds stress anisotropy have been shown to be reduced in the presence of surface films. Areas of peak near surface turbulence occur in areas where the ambient SAS has been redistributed, reducing any reduction in the induced surface currents, but this may potentially be offset by the inclusion of sources of SAS in the model. It is unclear if the SAR data at C-Band was accurate as the authors questioned its values, but the above model modifications would still provide improvements to the predictions made here.

Predicted SAR returns show the primary wake structure, but the majority of center wake features are lost due to the scatter in the predictions. This excessive scattering is due to a combination of the randomized ocean realization and the image processing methods incorporated in the model. It is recommended that prior to extensive use of the SAR simulation model, an improved method for processing the SAR data is incorporated. The use of the perfect SAR model provides insight into the future detectability of the wake as instrumentation and signal processing advance. As such, further additional research is warranted. Inclusion of SAS in the hydrodynamic simulation will improve both SAS concentration predictions as well as surface current predictions. Inclusion of improved ambient environmental conditions such as TKE and dissipation rate vertical profiles to go along with distributions of SAS, temperature, and salinity within the water column would improve simulated distributions of surface SAS and currents. Incorporation of a wind-energy input reduction over areas of SAS potentially based on the work of Mitsuyasu and Honda [103] will also improve predictions.

Chapter 7

Conclusions and Future Work

7.1 Summary

A range of mechanisms responsible for features observed in remote sensing imagery of surface ship wakes have been discussed. The focus has been placed on mechanisms that would exist across ship types as some previously suggested mechanisms have been shown to be highly ship dependent. The application of the Craik–Leibovich vortex force has been shown to generate large scale circulations in the wake of the ship due to the interaction of the ship induced vorticity with an ambient wave field in a similar fashion to Langmuir circulations and are hence called Langmuir-type circulations (LTC). LTC have been shown to generate surface currents on the order of O(1 cm/s) well into the persistent ship wake. These surface currents have been shown to compact surface active substances (SAS) into streaks in the wake that are capable of damping the short wind waves and form the dark streaks that are often observed in SAR imagery. It was shown that the structure of the persistent wake is partially a function of the angle between the relative ship heading and the ambient wave vector. In the case of a ship operating in following seas, twin streaks are predicted to form as the often observed "rail-road" track streaks. In the case of operating in head-seas, one or three streaks may appear depending on the relative strength of the LTC and the initial film pressure of the ambient SAS. For all but lightest of sea states, a strong centerline streak forms while the two outboard streaks are highly dependent on the ambient environmental conditions.

In addition to LTC, persistent surface currents have been shown to form due to near-surface Reynolds stress anisotropy. Walker et al. [156] showed that surface currents would be induced due to gradients in the Reynolds stresses that are forced by the free surface boundary condition. As the surface is approached, the vertical velocity fluctuations are damped and their energy is redistributed to the horizontal components. This redistribution induces momentum gradients that are ultimately responsible for the formation of the transverse surface currents. A modified form of the k-ε turbulence model has been incorporated that redistributes the vertical Reynolds stress to the axial and transverse directions using a form of a non-linear wall-reflection term from the pressure-strain correlation in full Reynolds stress transport models. Good agreement with experiment was achieved using the model to simulate laboratory scale near surface jets. Implementation of this turbulence model into the ship wake simulations demonstrated that this effect is also capable of generating currents

sufficient to compact SAS into the persistent wake even in the case of calm seas.

The combined effects of LTC and near-surface Reynolds stress anisotropy have been demonstrated to play complimentary roles in the formation of the persistent wake structure where individual components under predict experimental wake width measurements, but the combined effects provide good agreement.

The short wave damping effects of turbulence and the direct modification effects of surface currents have also been incorporated into the far and persistent wake model. It has been shown that turbulence plays a significant role in the far wake as the short waves are damped across the wake center while ship induced turbulence remains strong. Direct modification of the surface roughness by transverse velocity gradients has also been shown to play a key role in the near/far wake. In regions where velocity gradients are positive, surface smoothing is observed, while negative gradients amplify surface roughness. In the near/far wake turbulence and surface currents have been shown to also complement each other in the damping of the center wake. As ship induced turbulence and currents decay, streaks due to compacted SAS transition into the rail-road or thin centerline wake depending on environmental conditions and relative ship heading.

In addition to the importance of ambient film pressure, the physical properties of SAS have been shown to be highly variable for different parts of the world and even for the same location on different days. Changes in SAS properties impact the relative level of damping that is achievable with varying SAS concentration levels. This would signify that the same ship at the same operational conditions would generate different damping magnitudes in the wake for various locations/times. Ships operating in following seas have shown to be relatively insensitive to the environmental conditions as far as the structure is concerned, but head seas conditions are highly sensitive to both the environmental and operational conditions.

Finally, a model for the prediction of SAR returns has been demonstrated with two outputs: perfect SAR and simulated SAR. A two-part composite approach is taken where the impacts of the short wind waves are accounted for through Bragg scattering and the long waves are accounted for through a specular component. In the case of the perfect SAR, the ocean realization is accounted for through a modification to the total radar cross section (RCS) by the gradient of the total RCS with respect to the inclination angle. The randomized change in local surface height across each resolution pixel modifies the inclination angle and in turn induces a level of randomness into the perfect SAR images. The impact of polarization is also included with the perfect SAR images. It was observed that relatively small variations were induced by the change in polarization and were localized to the wake center. The structure of the wake due to turbulence/surface current gradients in the near/far wake and SAS streaks in the persistent wake was not impacted by the polarization. Here the influence was limited to the magnitude of damping/roughness amplification in the center wake with small impacts on the amplitude of SAS damping. Impacts due to wind speed and direction were also analyzed. The impact due to wind direction was found to be small here, but

with the assumption that the wind direction would not impact the ambient wave field. In reality, the wind-wave vectors are usually in the same direction, but the effect was studied here for completeness. The magnitude of the wind showed a stronger influence on the wake. Again, here it was assumed that the magnitude of the wind did not directly correspond to a change in the ambient wave amplitude such as a condition of a newly freshening wind on an otherwise calm day. The magnitude of the wind was shown to impact the symmetry of the wake. At low wind speeds, amplified roughness was observed on the windward side of the wake with higher smoothing on the leeward side. As wind speed increased, wake symmetry increased signifying that the energy input by the wind became greater than that due to the surface current gradients. The structure of the edge bands was not impacted by changes in wind speed or direction, but magnitude of relative damping was reduced with increased wind speed as the ambient RCS levels rose.

The fully simulated SAR images showed significant levels of scatter such that the majority of any detailed wake structure was lost. The near/far field damping due to turbulence and surface current gradients remained observable and the streaks due to SAS also remained observable, but transitions became difficult to identify. Also, L-band returns were mostly limited to the near/far wake damping due to turbulence/surface current gradients with edge bands mostly lost to the clutter. Overall, it is recommended that use of these models be limited to the perfect SAR until limitations of the simulated SAR model are addressed.

7.2 Model Limitations

Streaks of amplified surface roughness have been predicted to occur in the region just outboard of the strong turbulent damping, but inboard of the SAS streaks. These areas of amplified surface roughness were not observed in the SAR data from the experiment. In this region, the model shows that SAS has been redistributed to the wake edges, reducing the damping directly in the area of the largest negative surface gradients, leading to these areas of amplified roughness. During the 1989 ONR Field Experiment it was observed that surface tension was usually similar to the ambient conditions everywhere not in the streaks of compacted SAS. A few cases in the experiment were observed where the ship did pass through an ambient SAS slick, but SAR data was not collected in these conditions. The current model assumes the ship is operating in an ambient SAS field that is then redistributed with no sources or sinks of SAS in the redistribution model. As the spectral density is measured relative to the ambient condition, the areas inside the wake where SAS concentrations are less than 1 due to redistribution into the SAS bands, predict roughness amplification in the persistent wake once the ship induced turbulence and surface currents have decayed. The experimental results would suggest in most cases that the redistributed SAS is replaced by SAS coming up from the water column to maintain a close to equilibrium condition with the ambient environment.

The current model assumes a one-way coupling between the hydrodynamics and SAS redis-

tribution. Anthony et al. [9] and Shen et al. [127] demonstrate the presence of a surface film would reduce the levels of Reynolds stress redistribution due to the elasticity of the film absorbing some amount of the turbulent velocity fluctuations and also supporting shear stress at the surface, modifying the zero-stress boundary condition. This in turn reduces the formation of transverse surface currents in the near surface jet wake in regions with the surface film. This would impact the magnitude of surface currents and hence both the surface current gradients, which directly modify the surface roughness, and also the SAS concentration ratios. It is noted that the initial passage of the ship and LTC in following seas would act to redistribute SAS away from the wake centerline, reducing the surface film concentration in way of the strongest levels of near surface turbulence and in turn reducing any reduction in Reynolds stress redistribution.

The presence of surface films has also been shown to reduce the transfer of energy from the wind to the waves due to a reduction in the friction velocity [103]. Currently no mechanism has been implemented to account for this reduction in wind energy input.

The levels of variability in the full SAR predictions are also a limitation of the current model. Scatter on the order of several dBs is observed even in the case of calm seas with low wind conditions. These results are believed to be due to limitations in the data/image processing model.

7.3 Future Work

There are opportunities for continued work in several areas to improve the models presented here. First, the inclusion of SAS into the hydrodynamics model is recommended. This inclusion will provide an improved method for establishing the distribution of SAS on surface after the passage of a ship where SAS is able to be transported to the surface through scavenging by bubbles and surface currents. The model should include the ability for SAS to be adsorbed to the surface and redistributed by surface currents with realistic distributions of SAS within the water column. The model should also consider the impact of a surface film on the redistribution of near surface Reynolds stresses. Additional experimental data is most likely needed here to establish the impact of a surface film at low Froude numbers. The relationship between film pressure and Reynolds stress redistribution would also need to be established. Shen et al. [127] have conducted DNS studies of this effect, but for Reynolds numbers several orders of magnitude less than full scale.

Second, the inclusion of a model to account for reductions in wind energy input in areas of surface films should be added. A reduction in the boundary layer friction velocity due to the surface films would reduce the wind energy input and also aid in reducing areas of amplified roughness where SAS had been redistributed.

Third, improved methods of image processing should be incorporated into the simulated SAR model. Methods currently implemented are based on capabilities from the early 1990's.

Significant advancements in image processing have occurred since these methods were developed.

Forth, stratification of the water column should be considered. The current simulations assume the ship is operating fully within the mixed layer. This is not a limitation of the model, but was a simplifying assumption to isolate the influences studied here. Distributions of temperature, salinity, turbulent kinetic energy, and turbulent dissipation rate should be included in future simulations to include the impacts of internal waves on the wake.

Finally, the need for modern experimental data to provide model validation can not be overstated. Ideally, full scale data would be collected where all relevant environmental parameters are recorded such as wind speed and direction, wave amplitude and length, ambient SAS properties and turbulence quantities both at the surface and within the water column, and distributions of temperature and salinity within the water column. Experiments would measure surface tension in the wake as well as surface and subsurface currents. Overhead SAR imagery would be taken for ships operating in calm, head, and following seas with measurements of the surface and submerged conditions taken. Relevant findings would also come from model scale tests of the surface and submerged velocity profiles in the ship wake where the ambient wave conditions could be accurately controlled and wall wave reflections could be minimized. These tests could provide validation data on the formation of surface currents due to LTC and near surface Reynolds stress anisotropy. The inclusion of fans could also simulate a wind roughened surface to provide data on the impact of surface currents and surface current gradients on roughness modification.

Bibliography

[1] Canadian Space Agency. Radarsat satellites: Technical comparison, Dec 2019. URL https://www.asc-csa.gc.ca/eng/satellites/radarsat/technical-features/radarsat-comparison.asp.

[2] European Space Agency. Sentinel-1. URL https://sentinel.esa.int/web/sentinel/missions/sentinel-1.

[3] TL Ainsworth, ME Cannella, SR Chubb, RA Fusina, RW Jansen, GO Marmorino, and GR Valenzuela. Insar imagery of surface currents, wave fields and fronts. In *Proceedings of IGARSS'94-1994 IEEE International Geoscience and Remote Sensing Symposium*, volume 3, pages 1720–1722. IEEE, 1994.

[4] Nicholas Allan, Clifford L Trump, Dennis B Trizna, and David J McLaughlin. Dual-polarized doppler radar measurements of oceanic fronts. *IEEE transactions on geoscience and remote sensing*, 37(1):395–417, 1999.

[5] Werner Alpers and Heinrich Hühnerfuss. The damping of ocean waves by surface films: A new look at an old problem. *Journal of Geophysical Research: Oceans*, 94 (C5):6251–6265, 1989.

[6] D Gr Andrews and ME McIntyre. An exact theory of nonlinear waves on a lagrangian-mean flow. *Journal of Fluid Mechanics*, 89(4):609–646, 1978.

[7] D G Andrews and ME McIntyre. An exact theory of nonlinear waves on a lagrangian-mean flow. *Journal of Fluid Mechanics*, 89(4):609–646, 1978.

[8] DG Anthony and WW Willmarth. Turbulence measurements in a round jet beneath a free surface. *Journal of Fluid Mechanics*, 243:699–720, 1992.

[9] Douglas G Anthony, Amir Hirsa, and William W Willmarth. On the interaction of a submerged turbulent jet with a clean or contaminated free surface. *Physics of Fluids A: Fluid Dynamics*, 3(2):245–247, 1991.

[10] John R Apel. An improved model of the ocean surface wave vector spectrum and its effects on radar backscatter. *Journal of Geophysical Research: Oceans*, 99(C8): 16269–16291, 1994.

[11] WR Barger and MA Klusty. Common features of natural surface films from the coastal waters of maine, virginia, and bermuda, i, pressure and modulus data. *J. Geophys. Res*, 1992.

[12] D Barrick. Rough surface scattering based on the specular point theory. *IEEE Transactions on Antennas and Propagation*, 16(4):449–454, 1968.

[13] A Basovich. Circulations caused by interaction of underwater currents and surface waves. *Dynamics of Atmospheres and Oceans*, 51(3):151–164, 2011.

[14] A. Basovich. The effect of contaminant drag reduction on the onset and evolution of Langmuir circulations. *Journal of Physical Oceanography*, 44(10):2739–2752, 2014.

[15] NRRC Booij, Roeland C Ris, and Leo H Holthuijsen. A third-generation wave model for coastal regions: 1. model description and validation. *Journal of geophysical research: Oceans*, 104(C4):7649–7666, 1999.

[16] AG Boyev. The damping of surface waves by intense turbulence. *Izv. Atmos. Ocean Phys*, 7:31–36, 1971.

[17] K.A. Brucker and S. Sarkar. A comparative study of self-propelled and towed wakes in a stratified fluid. *Journal of Fluid Mechanics*, 652:373–404, 2010.

[18] Michael Bruno, Kil Woo Chung, Hady Salloum, Alexander Sedunov, Nikolay Sedunov, Alexander Sutin, Hans Graber, and Paul Mallas. Concurrent use of satellite imaging and passive acoustics for maritime domain awareness. In *2010 International Waterside Security Conference*, pages 1–8. IEEE, 2010.

[19] K Case, C Callan, R Dashen, R Davis, and W Munk. Seasat iii and iv. Technical report, MITRE CORP MCLEAN VA, 1984.

[20] G.G. Chernykh and O.F. Voropayeva. Numerical modeling of momentumless turbulent wake dynamics in a linearly stratified medium. *Computers & Fluids*, 28(3):281 – 306, 1999.

[21] Scott R Chubb, Farid Askari, Timothy F Donato, Roland Romeiser, Susanne Ufermann, Arnold L Cooper, Werner Alpers, Stephen A Mango, and Jong-Sen Lee. Study of gulf stream features with a multifrequency polarimetric sar from the space shuttle. *IEEE transactions on geoscience and remote sensing*, 37(5):2495–2507, 1999.

[22] Renato Cini and Pietro P Lombardini. Damping effect of monolayers on surface wave motion in a liquid. *Journal of Colloid and Interface Science*, 65(2):387–389, 1978.

[23] Renato Cini, Pietro Paolo Lombardini, Claudia Manfredi, and Enrico Cini. Ripples damping due to monomolecular films. *Journal of colloid and interface science*, 119(1): 74–80, 1987.

[24] Arnold L Cooper, Colin Y Shen, George O Marmorino, and T Evans. Simulated radar imagery of an ocean" spiral eddy". *IEEE transactions on geoscience and remote sensing*, 43(10):2325–2331, 2005.

[25] Cortana Corporataion. Oceanographic and atmospheric science, 2020. URL https://www.cortana.com/oceanPhysics/. [Online; accessed Feburary 14, 2020].

[26] A.D.D. Craik and S. Leibovich. A rational model for Langmuir circulations. *Journal of Fluid Mechanics*, 73(03):401–426, 1976.

[27] Alex DD Craik and Sidney Leibovich. A rational model for langmuir circulations. *Journal of Fluid Mechanics*, 73(3):401–426, 1976.

[28] PL Croot, Uta Passow, Philipp Assmy, Sandra Jansen, and VH Strass. Surface active substances in the upper water column during a southern ocean iron fertilization experiment (eifex). *Geophysical research letters*, 34(3), 2007.

[29] JCB Da Silva, SA Ermakov, IS Robinson, DRG Jeans, and SV Kijashko. Role of surface films in ERS SAR signatures of internal waves on the shelf: 1. short-period internal waves. *Journal of Geophysical Research: Oceans*, 103(C4):8009–8031, 1998.

[30] Bart J Daly and Francis H Harlow. Transport equations in turbulence. *The Physics of Fluids*, 13(11):2634–2649, 1970.

[31] P.J. Diamessis, J.A. Domaradzki, and J.S. Hesthaven. A spectral multidomain penalty method model for the simulation of high reynolds number localized incompressible stratified turbulence. *Journal of Computational Physics*, 202(1):298 – 322, 2005.

[32] D. G. Dommermuth, J. W. Rottman, G. E. Innis, and E. A. Novikov. Numerical simulation of the wake of a towed sphere in a weakly stratified fluid. *Journal of Fluid Mechanics*, 473:83–101, 2002.

[33] Mark A Donelan and Willard J Pierson Jr. Radar scattering and equilibrium ranges in wind-generated waves with application to scatterometry. *Journal of Geophysical Research: Oceans*, 92(C5):4971–5029, 1987.

[34] Mark A Donelan and William J Plant. A threshold for wind-wave growth. *Journal of Geophysical Research: Oceans*, 114(C7), 2009.

[35] S.A. Ermakov and I.A. Kapustin. Experimental study of turbulent-wake expansion from a surface ship. *Izvestiya Atmospheric and Oceanic Physics*, 46(4):524–529, 2010.

[36] S.A. Ermakov, I.A. Kapustin, and T. Lazareva. Ship wake signatures in radar/optical images of the sea surface: observations and physical mechanisms. *Proc. SPIE*, 9240: 1–6, 2014.

[37] SA Ermakov, IA Kapustin, and OV Shomina. Laboratory investigation of damping of gravity-capillary waves on the surface of turbulized liquid. *Izvestiya, Atmospheric and Oceanic Physics*, 50(2):204–212, 2014.

[38] D Ewing. Decay of round turbulent jets with swirl. In *Engineering Turbulence Modelling and Experiments 4*, pages 461–470. Elsevier, 1999.

[39] Kenneth W Fischer and Robert A Shuchman. Satellite observations of deep water convection. Technical report, Environmental Research Institute of Michigan, Ann Arbor, 1996.

[40] Kenneth W Fischer, Catherine A Russel, and RA Schuchman. Spatial characterization of deep ocean convection in the labrador sea using ers-2 sar imagery. In *IGARSS'98. Sensing and Managing the Environment. 1998 IEEE International Geoscience and Remote Sensing. Symposium Proceedings.(Cat. No. 98CH36174)*, volume 2, pages 580–582. IEEE, 1998.

[41] Lee-Leung Fu and Benjamin Holt. *Seasat views oceans and sea ice with synthetic-aperture radar*, volume 81. California Institute of Technology, Jet Propulsion Laboratory, 1982.

[42] A. Fujimura, A. Soloviev, S.H. Rhee, and R. Romeiser. Coupled model simulation of wind stress effect on far wakes of ships in SAR images. *IEEE Transactions on Geoscience and Remote Sensing*, 54(5):2543–2551, 2016.

[43] C. Garrett. Generation of Langmuir circulations by surface waves–a feedback mechanism. *J. Mar. Res.*, 34:117–130, 1976.

[44] WD Garrett. The organic chemical composition of the ocean surface. In *Deep Sea Research and Oceanographic Abstracts*, volume 14, pages 221–227. Elsevier, 1967.

[45] Blaženka Gašparović and Božena Ćosović. Distribution of surface-active substances in the northern adriatic sea. *Marine chemistry*, 75(4):301–313, 2001.

[46] Simon Gareth George. *Satellite measurement of ocean turbulence*. PhD thesis, University of Southampton, 2014.

[47] Ephim Golbraikh, Alexander Eidelman, and Alex Soloviev. On helical behavior of turbulence in the ship wake. *Journal of Hydrodynamics, Ser. B*, 25(1):83–90, 2013.

[48] M.J. Gourlay, S.C. Arendt, D.C. Fritts, and J. Werne. Numerical modeling of initially turbulent wakes with net momentum. *Physics of Fluids*, 13(12):3783–3802, 2001.

[49] M Daniela Graziano, Giancarlo Rufino, and Marco D'Errico. Wake-based ship route estimation in high-resolution sar images. In *SAR Image Analysis, Modeling, and Techniques XIV*, volume 9243, page 92430T. International Society for Optics and Photonics, 2014.

[50] Maria Daniela Graziano, Marco D'Errico, and Giancarlo Rufino. Ship heading and velocity analysis by wake detection in sar images. *Acta astronautica*, 128:72–82, 2016.

[51] Maria Daniela Graziano, Marco D'Errico, and Giancarlo Rufino. Wake component detection in x-band sar images for ship heading and velocity estimation. *Remote Sensing*, 8(6):498, 2016.

[52] Maria Daniela Graziano, Marco Grasso, and Marco D'Errico. Performance analysis of ship wake detection on sentinel-1 sar images. *Remote Sensing*, 9(11):1107, 2017.

[53] Harm Greidanus and Carlos Santamaria. First analyses of sentinel-1 images for maritime surveillance. *Publications Office of the European Union: Luxembourg*, 2014.

[54] The Wamdi Group. The wam model—a third generation ocean wave prediction model. *Journal of Physical Oceanography*, 18(12):1775–1810, 1988.

[55] K. Hasselmann. Weak-interaction theory of ocean waves. Schrieftenreihe Schiffbau 181, Technische Universitat Hamburg-Harburg (TUHH), 1967.

[56] K Hasselmann, RK Raney, WJ Plant, Werner Alpers, RA Shuchman, David R Lyzenga, CL Rufenach, and MJ Tucker. Theory of synthetic aperture radar ocean imaging: A marsen view. *Journal of Geophysical Research: Oceans*, 90(C3):4659–4686, 1985.

[57] S. Hassid. Collapse of turbulent wakes in stably stratified media. *Journal of Hydronautics*, 14:25–32, January 1980.

[58] K Herterich and K Hasselmann. The horizontal diffusion of tracers by surface waves. *Journal of Physical Oceanography*, 12(7):704–711, 1982.

[59] M. Hoekstra and A. Aalbers. Macro wake measurements for a range of ships. In *21st Symposium on Naval Hydrodynamics*, pages 278–290, 1997.

[60] Dennis Holliday, Gaetan St-Cyr, and Nancy E Woods. A radar ocean imaging model for small to moderate incidence angles. *International Journal of Remote Sensing*, 7 (12):1809–1834, 1986.

[61] Holthuijsen. *Waves in oceanic and coastal waters*. Cambridge university press, 2007.

[62] BA Hughes. The effect of internal waves on surface wind waves 2. theoretical analysis. *Journal of Geophysical Research: Oceans*, 83(C1):455–465, 1978.

[63] M. Hyman. Computation of ship wake flows with free-surface/turbulence interaction. In *22nd Symposium on Naval Hydrodynamics, Washington, DC*, pages 11–32, 1998.

[64] ICEYE. Iceye sar satellite capabilities. URL https://www.iceye.com/.

[65] R.I. Issa. Solution of the implicitly discretized fluid flow equations by operator-splitting. *Journal of Computational Physics*, 62:40–65, 1985.

[66] Robert W Jansen, Scott R Chubb, Robert A Fusina, and Gasper R Valenzuela. Modeling of current features in gulf stream sar imagery. Technical report, Naval Research Lab, Washington DC, 1993.

[67] JA Johannessen, AD Jenkins, OM Johannessen, S Sandven, EK Korsbakken, HA Espedal, R Romeiser, P Brandt, R Alpers, A Rubino, et al. Intercomparison and improvement of sar ocean imaging interaction models. In *IGARSS'98. Sensing and Managing the Environment. 1998 IEEE International Geoscience and Remote Sensing. Symposium Proceedings.(Cat. No. 98CH36174)*, volume 3, pages 1653–1655. IEEE, 1998.

[68] Johnny A Johannessen, Robert A Shuchman, G Digranes, DR Lyzenga, C Wackerman, Ola M Johannessen, and PW Vachon. Coastal ocean fronts and eddies imaged with ers 1 synthetic aperture radar. *Journal of Geophysical Research: Oceans*, 101(C3): 6651–6667, 1996.

[69] Ola M Johannessen, Heidi Espedal, and DB Akimov. Coastwatch'95: modeling of ocean fronts imaged by sar. In *IEEE 1999 International Geoscience and Remote Sensing Symposium. IGARSS'99 (Cat. No. 99CH36293)*, volume 4, pages 1957–1959. IEEE, 1999.

[70] P.B.V. Johansson, W.K. George, and M.J. Gourlay. Equilibrium similarity, effects of initial conditions and local Reynolds number on the axisymmetric wake. *Physics of Fluids*, 15(3):603–617, 2003.

[71] Vincent G Johnston and David T Walker. Experimentally observed features of the turbulent near-wake of a model ship. Technical report, University of Michigan, 1992.

[72] Matthew C Jones and Eric G Paterson. Evolution of stratified boundary-free shear flows under stokes-ekman forcing. In *45th AIAA Fluid Dynamics Conference*, page 2309, 2015.

[73] JA Kaiser, WD Garrett, SE Ramberg, RD Peltzer, and DM Andrews. Wakex 86: A ship wake/films exploratory experiment. Technical report, Naval Research Lab Washington DC, 1988.

[74] Oktay Karakuş and Alin Achim. Ship wake detection in x-band sar images using sparse gmc regularization. In *ICASSP 2019-2019 IEEE International Conference on Acoustics, Speech and Signal Processing (ICASSP)*, pages 2182–2186. IEEE, 2019.

[75] ES Kasischke, RA Shuchman, RW Larson, DR Lyzenga, and JC Clinthorne. Sar (synthetic aperture radar) data collection and processing summary-1984 sarsex (sar internal wave signature experiment) experiment. Technical report, Environmental Research Institute of Michigan Ann Arbor RADAR Division, 1985.

[76] SA Kitaigorodskii and JL Lumley. Wave-turbulence interactions in the upper ocean. part i: The energy balance of the interacting fields of surface wind waves and wind-induced three-dimensional turbulence. *Journal of physical oceanography*, 13(11):1977–1987, 1983.

[77] SA Kitaigorodskii, MA Donelan, JL Lumley, and EA Terray. Wave-turbulence interactions in the upper ocean. part ii. statistical characteristics of wave and turbulent components of the random velocity field in the marine surface layer. *Journal of Physical Oceanography*, 13(11):1988–1999, 1983.

[78] Lawrence Klein and C Swift. An improved model for the dielectric constant of sea water at microwave frequencies. *IEEE transactions on antennas and propagation*, 25 (1):104–111, 1977.

[79] Herbert J Kramer. *Observation of the Earth and its Environment*. European Space Agency, 2020. URL https://directory.eoportal.org/web/eoportal/satellite-missions.

[80] Vladimir Kudryavtsev, Danièle Hauser, Gérard Caudal, and Bertrand Chapron. A semiempirical model of the normalized radar cross-section of the sea surface 1. background model. *Journal of Geophysical Research: Oceans*, 108(C3):FET–2, 2003.

[81] I. Langmuir. Surface motion of water induced by wind. *Science*, 87(2250):119–123, 1938.

[82] Irving Langmuir. Surface motion of water induced by wind. *Science*, 87(2250):119–123, 1938.

[83] BE Launder and W Rodi. The turbulent wall jet measurements and modeling. *Annual Review of Fluid Mechanics*, 15(1):429–459, 1983.

[84] Brian Edward Launder. Second-moment closure and its use in modelling turbulent industrial flows. *International Journal for Numerical Methods in Fluids*, 9(8):963–985, 1989.

[85] Evgeniy Lebed and Ron Caves. Recent and ongoing developments in using radarsat-2 for maritime surveillance in canada. In *EUSAR 2018; 12th European Conference on Synthetic Aperture Radar*, pages 1–4. VDE, 2018.

[86] S Leibovich. On wave-current interaction theories of langmuir circulations. *Journal of Fluid Mechanics*, 99(4):715–724, 1980.

[87] Peter S Liss, Peter S Liss, and Robert A Duce. *The sea surface and global change*. Cambridge University Press, 2005.

[88] James D Lyden, Robert R Hammond, David R Lyzenga, and RA Shuchman. Synthetic aperture radar imaging of surface ship wakes. *Journal of Geophysical Research: Oceans*, 93(C10):12293–12303, 1988.

[89] JD Lyden, DR Lyzenga, RA Shuchman, and CV Swanson. Sar detection of ship-generated turbulent and vortex wakes. Technical report, Environmental Research Institute of Michigan, Ann Arbor, 1985.

[90] David R Lyzenga. Numerical simulation of synthetic aperture radar image spectra for ocean waves. *IEEE Transactions on Geoscience and Remote Sensing*, (6):863–872, 1986.

[91] David R Lyzenga. Interaction of short surface and electromagnetic waves with ocean fronts. *Journal of Geophysical Research: Oceans*, 96(C6):10765–10772, 1991.

[92] David R Lyzenga. Effects of intermediate-scale waves on radar signatures of ocean fronts and internal waves. *Journal of Geophysical Research: Oceans*, 103(C9):18759–18768, 1998.

[93] David R Lyzenga and John R Bennett. Full-spectrum modeling of synthetic aperture radar internal wave signatures. *Journal of Geophysical Research: Oceans*, 93(C10): 12345–12354, 1988.

[94] John T Mass and Jerome H Milgram. Dynamic behavior of natural sea surfactant films. *Journal of Geophysical Research: Oceans*, 103(C8):15695–15715, 1998.

[95] Sean P McKenna. Free-surface turbulence and air-water gas exchange. Technical report, Woods Hole Oceanographic Institution MA, 2000.

[96] Jerome H Milgram. Short wave damping in the simultaneous presence of a surface film and turbulence. *Journal of Geophysical Research: Oceans*, 103(C8):15717–15727, 1998.

[97] J.H. Milgram, R.D. Peltzer, and O.M. Griffin. Suppression of short sea waves in ship wakes: measurements and observations. *Journal of Geophysical Research*, 98(C4): 7103–7114, 1993.

[98] JH Milgram, RD Peltzer, and OM Griffin. Suppression of short sea waves in ship wakes: measurements and observations. *Journal of Geophysical Research: Oceans*, 98 (C4):7103–7114, 1993.

[99] J.H. Milgram, R.A. Skop, R.D. Peltzer, and O.M. Griffin. Modeling short sea wave energy distributions in the far wakes of ships. *Journal of Geophysical Research*, 98 (C4):7115–7124, 1993.

[100] JH Milgram, Richard A Skop, Rodney D Peltzer, and Owen M Griffin. Modeling short sea wave energy distributions in the far wakes of ships. *Journal of Geophysical Research: Oceans*, 98(C4):7115–7124, 1993.

[101] E Miner, M Stewart, and T Swean, JR. Modeling and computation of turbulent free-surface jets. In *31st Aerospace Sciences Meeting*, page 201, 1993.

[102] E.W. Miner, S.E. Ramberg, and T.F. Swean, Jr. A method for approximating the initial data plane for surface ship wake simulations. NRL Memorandum Report 6376, Naval Research Laboratory, Washington D.C., November 30 1988.

[103] H Mitsuyasu and T Honda. Wind-induced growth of water waves. *Journal of Fluid Mechanics*, 123:425–442, 1982.

[104] Darren G Muff. *Electromagnetic ray-tracing for the investigation of multipath and vibration signatures in radar imagery*. PhD thesis, UCL (University College London), 2018.

[105] CJ Mullenhoff, SK Lehman, and H Jones. Radar imagery from the 1994 lock linnhe ship wake experiment. Technical report, Lawrence Livermore National Lab., CA (United States), 1994.

[106] W.H. Munk, P. Scully-Power, and F. Zachariasen. The Bakerian lecture, 1986. ships from space. *Proceedings of the Royal Society of London A: Mathematical, Physical and Engineering Sciences*, 412(1843):231–254, 1987.

[107] M. Nakagawa and W. Dahm. Virtual origin of incompressible and supersonic turbulent bluff-body wakes. *AIAA Journal*, 43(3):697–700, 2005.

[108] Dan Naot and Wolfgang Rodi. Calculation of secondary currents in channel flow. *Journal of the Hydraulics Division*, 108(8):948–968, 1982.

[109] Adam O'Connor. Capella's advanced sar imagery products, May 2020. URL https://www.capellaspace.com/capellas-advanced-sar-imagery-products/.

[110] A. Olivieri, F. Pistani, A. Avanzini, F. Stern, and R. Penna. Towing tank experiments of resistance, sinkage and trim, boundary layer, wake, and free surface flow around a naval combatant INSEAN 2340 model. IIHR Report 421, Iowa Institute of Hydraulic Research, The University of Iowa, Iowa City, Iowa, 2001.

[111] Hasan S Ölmez and Jerome H Milgram. An experimental study of attenuation of short water waves by turbulence. *Journal of Fluid Mechanics*, 239:133–156, 1992.

[112] Y.H. Pao and J.T. Lin. Velocity and density measurements in the turbulent wake of a towed slender body in stratified and nonstratified fluids. Report 12, Flow Research Inc., December 1973.

[113] E.G. Paterson, M. Hyman, F. Stern, P. Carrica, F. Bonetto, and D. Drew. Near- and far-field CFD for a naval combatant including thermal stratification and two-fluid modeling. In *Proceedings of the 21st Symposium on Naval Hydrodynamics*, Trondheim, Norway, June 1996.

[114] R.D. Peltzer. White-water wake characteristics of surface vessels. NRL Memorandum Report 5335, Naval Research Laboratory, Washington D.C., 1984.

[115] R.D. Peltzer. The 1989 ONR field experiment: High resolution surfactant film measurements. NRL Memorandum Report 7226-93-7193, Naval Research Laboratory, Washington D.C., 1993.

[116] R.D. Peltzer, O.M. Griffin, W.R. Barger, and J.A.C. Kaiser. High-resolution measurement of surface-active film redistribution in ship wakes. *Journal of Geophysical Research: Oceans*, 97(C4):5231–5252, 1992.

[117] RD Peltzer, OM Griffin, WR Barger, and JAC Kaiser. High-resolution measurement of surface-active film redistribution in ship wakes. *Journal of Geophysical Research: Oceans*, 97(C4):5231–5252, 1992.

[118] RD Peltzer, OM Griffin, JA Kaiser, and WR Barger. The 1989 onr field experiment: High resolution surfactant film measurements. Technical report, Naval Research Lab, Washington DC, 1993.

[119] Owen Phillips. *The dynamics of the upper ocean / O. M. Phillips*. Cambridge University Press Cambridge ; New York, 2d ed. edition, 1977. ISBN 0521214211.

[120] William J Plant. A relationship between wind stress and wave slope. *Journal of Geophysical Research: Oceans*, 87(C3):1961–1967, 1982.

[121] William J Plant. A two-scale model of short wind-generated waves and scatterometry. *Journal of Geophysical Research: Oceans*, 91(C9):10735–10749, 1986.

[122] Fusina' RA, Chubb' SR, A Cooper, and GR Valenzuela. Comparison of data and model slope statistics for a current convergence feature. 1994.

[123] SE Ramberg, TF Swean Jr, and MA Plesnia. Turbulence near a free surface in a plane jet. Technical report, NAVAL RESEARCH LAB WASHINGTON DC, 1989.

[124] A.M. Reed and J.H. Milgram. Ship wakes and their radar images. *Annual Review of Fluid Mechanics*, 34(1):469–502, 2002.

[125] Maria T Rey, James K Tunaley, JT Folinsbee, PAUL A Jahans, JA Dixon, and Malcolm R Vant. Application of radon transform techniques to wake detection in seasat-a sar images. *IEEE Transactions on Geoscience and Remote Sensing*, 28(4):553–560, 1990.

[126] Roland Romeiser, Werner Alpers, and Volkmar Wismann. An improved composite surface model for the radar backscattering cross section of the ocean surface: 1. theory of the model and optimization/validation by scatterometer data. *Journal of Geophysical Research: Oceans*, 102(C11):25237–25250, 1997.

[127] Lian Shen, Dick KP Yue, and George S Triantafyllou. Effect of surfactants on free-surface turbulent flows. *Journal of Fluid Mechanics*, 506:79, 2004.

[128] CC Shir. A preliminary numerical study of atmospheric turbulent flows in the idealized planetary boundary layer. *Journal of the Atmospheric Sciences*, 30(7):1327–1339, 1973.

[129] A. Shiri, W.K. George, and J.W. Naughton. Experimental study of the far field of incompressible swirling jets. *AIAA journal*, 46(8):2002–2009, 2008.

[130] A Sirviente and VC Patel. Experiments in the swirling wake of a self-propelled axisymmetric body. In *Proc. of the 21st Symp. on naval hydrodynamics, Trondheim (Norway)*, pages 24–28, 1996.

[131] John D Skoda. The interaction of waves and turbulence in water. Technical report, California University Berkeley Hydraulic Engineering Lab, 1972.

[132] RA Skop, WG Lindsley, and JW Brown. Radiotracer studies of surfactant transport to the sea-air interface by submillimeter-size bubbles. *Experiments in Fluids*, 10(5): 251–256, 1991.

[133] A. Soloviev, M. Gilman, K. Young, S. Brusch, and S. Lehner. Sonar measurements in ship wakes simultaneous with TerraSAR-X overpasses. *IEEE Transactions on Geoscience and Remote Sensing*, 48(2):841–851, 2010.

[134] Ryan Somero and Eric Paterson. Relative importance of turbulence, surface-active substances,and surface currents on roughness modification of shortsurface waves in ship wakes. In *Thirty-Third Symposium on Naval Hydrodynamics*, 2020.

[135] Ryan Somero, Andre Basovich, and Eric G Paterson. Structure and persistence of ship wakes and the role of langmuir-type circulations. *Journal of Ship Research*, 62(4): 241–258, 2018.

[136] Ryan Somero, Andre Basovich, and Eric Paterson. Effect of ship-induced langmuir-type circulations on distribution of surface-active substances and damping of short wind waves. *Journal of Ship Research*, 2019.

[137] Louis St. Laurent and Sophia Merrifield. Measurements of near-surface turbulence and mixing from autonomous ocean gliders. *Oceanography*, 30(2):116–125, 2017.

[138] Ryan L Stefan and Andrew J Szeri. Surfactant scavenging and surface deposition by rising bubbles. *Journal of colloid and interface science*, 212(1):1–13, 1999.

[139] F. Stern, J. Longo, R. Penna, A. Olivieri, T. Ratcliffe, and H. Coleman. International collaboration on benchmark CFD validation data for surface combatant DTMB model 5415. In *Twenty-Third Symposium on Naval HydrodynamicsOffice of Naval ResearchBassin d'Essais des CarenesNational Research Council*, 2001.

[140] P.P. Sullivan and J.C. McWilliams. Dynamics of winds and currents coupled to surface waves. *Annual Review of Fluid Mechanics*, 42:19–42, 2010.

[141] Peter Sutherland and W Kendall Melville. Field measurements of surface and near-surface turbulence in the presence of breaking waves. *Journal of Physical Oceanography*, 45(4):943–965, 2015.

[142] Claude V Swanson. Radar observability of ship wakes. *Cortana Corp. Rep., Falls Church, VA, USA, Corp. Rep*, 87, 1984.

[143] T.F. Swean, Jr. Calculations of the turbulent wake behind a slender self-propelled double-body and comparisons with experiment. NRL Memorandum Report 6075, Naval Research Laboratory, Washington D.C., 1987.

[144] TF Swean Jr, SE Ramberg, and EW Miner. Anisotropy in a turbulent jet near a free surface. 1991.

[145] T. Talipova. The surface active sea films: properties and dynamics. In *Geoscience and Remote Sensing, 1997. IGARSS'97. Remote Sensing–A Scientific Vision for Sustainable Development., 1997 IEEE International*, pages 362–364, 1997.

[146] MAC Teixeira and SE Belcher. On the distortion of turbulence by a progressive surface wave. *Journal of Fluid Mechanics*, 458:229–267, 2002.

[147] J.V. Toporkov, P.A. Hwang, M.A. Sletten, G. Farquharson, D. Perkovic, and S.J. Frasier. Surface velocity profiles in a vessel's turbulent wake observed by a dual-beam along-track interferometric SAR. *IEEE Geoscience and Remote Sensing Letters*, 8(4): 602–606, 2011.

[148] MA True. Validation support of the erim ocean model. Technical report, Environmental Research Institute of Michigan Ann Arbor, 1994.

[149] MA True, DI Lyzenga, and JD Lyden. Centerline wake modeling. Technical report, Environmental Research Institute of Michigan, Ann Arbor, 1993.

[150] James KE Tunaley. Ships turbulent propeller wake: Combined swirling and linear momentum wake. *momentum*, 5(3/5), 2004.

[151] B Mete Uz, Tetsu Hara, Erik J Bock, and Mark A Donelan. Laboratory observations of gravity-capillary waves under transient wind forcing. *Journal of Geophysical Research: Oceans*, 108(C2), 2003.

[152] Domenico Velotto, Carlos Bentes, Björn Tings, and Susanne Lehner. First comparison of sentinel-1 and terrasar-x data in the framework of maritime targets detection: South italy case. *IEEE Journal of Oceanic Engineering*, 41(4):993–1006, 2016.

[153] John F Vesecky and Robert H Stewart. The observation of ocean surface phenomena using imagery from the seasat synthetic aperture radar: An assessment. *Journal of Geophysical Research: Oceans*, 87(C5):3397–3430, 1982.

[154] D Walker. Reynolds-averaged modeling of high-froude-number free-surface jets. In *Twenty-Third Symposium on Naval HydrodynamicsOffice of Naval ResearchBassin d'Essais des CarenesNational Research Council*, 2001.

[155] David T Walker. On the origin of the 'surface current'in turbulent free-surface flows. *Journal of Fluid Mechanics*, 339:275–285, 1997.

[156] DT Walker, C-Y Chen, and WW Willmarth. Turbulent structure in free-surface jet flows. *Journal of Fluid Mechanics*, 291:223–261, 1995.

[157] Dylan Wall and Eric Paterson. Anisotropic turbulence modeling for ship wakes in an active ocean environment. In *Thirty-Third Symposium on Naval Hydrodynamics*, 2020.

[158] K Weston, L Fernand, DK Mills, R Delahunty, and J Brown. Primary production in the deep chlorophyll maximum of the central north sea. *Journal of Plankton Research*, 27(9):909–922, 2005.

[159] JW Wright. A new model for sea clutter. *IEEE Transactions on antennas and propagation*, 16(2):217–223, 1968.

[160] Lichuan Wu, Anna Rutgersson, and Erik Sahlée. Upper-ocean mixing due to surface gravity waves. *Journal of Geophysical Research: Oceans*, 120(12):8210–8228, 2015.

[161] Oliver Wurl, Lisa Miller, Rüdiger Röttgers, and Svein Vagle. The distribution and fate of surface-active substances in the sea-surface microlayer and water column. *Marine Chemistry*, 115(1-2):1–9, 2009.

[162] WW3DG. User manual and system documentation of wavewatch iii version 6.07, the WAVEWATCH III development group. *Tech. Note 326 pp. + Appendices, NOAA/NWS/NCEP/MMAB*, 2019.

[163] Gregory Zilman, Anatoli Zapolski, and Moshe Marom. The speed and beam of a ship from its wake's sar images. *IEEE Transactions on Geoscience and Remote Sensing*, 42 (10):2335–2343, 2004.

[164] Gregory Zilman, Anatoli Zapolski, and Moshe Marom. On detectability of a ship's kelvin wake in simulated sar images of rough sea surface. *IEEE Transactions on Geoscience and Remote Sensing*, 53(2):609–619, 2014.

[165] Vera Žutić, Božena Ćosović, Elena Marčenko, Nevenka Bihari, and Frano Kršinić. Surfactant production by marine phytoplankton. *Marine Chemistry*, 10(6):505–520, 1981.

Appendices

Appendix A

Derivation of the Craik-Leiboich Vortex Force

A.1 Introduction

The formation of Langmuir circulations due to interactions between wind currents and ambient surface waves has been understood since the 1930's (Langmuir [82]). A theoretical explanation of the phenomena didn't arise, however, until Craik and Leibovich [27] where the mechanism for formation of circulations due to the interaction of vorticity generated by the wind and surface waves was first described by the Craik-Leibovich (CL) equations. This mechanism was then referred to as the Craik-Leibovich vortex force. The CL equations were originally developed based on perturbing and time-averaging the vorticity transport equations over intervals that are long relative to the dominate surface wave period, but short relative to the time-scales required to develop the driving surface waves. This original derivation, however, was somewhat restrictive as it required a specific ordering of perturbation effects and the use of multiple time-averaging scales. Simultaneously, Andrews and McIntyre [6], developed a mathematical model to describe the Generalized Lagranian-Mean (GLM) flow. The GLM provides a method for exact representation of wave, mean-flow interactions and the effect that oscillatory perturbations have on the mean flow. Leibovich [86] shows how the CL equations can be derived using the GLM in a more direct and less restrictive manner than originally presented.

Here the derivation of the mean flow equations through the use of the GLM is demonstrated based on the method of Andrews and McIntyre [6]. An introduction to the Stokes drift and its application to the mean-flow equations is presented with the derivation of the CL equations following.

Significant intermediary steps were omitted in the original formulations of both the mean flow and the CL equations, but are provided here to form full and complete derivations of each.

A.2 Generalized Lagrangian Mean

The Generalized Lagrangian Mean (GLM) is introduced by Andrews and McIntyre [6] and the process here will initially be outlined in the most general sense.

Defining a real-valued tensor field $\phi(x,t)$ and a perturbation based particle displacement field $\xi(x,t)$, the Lagrangian-mean operator $\overline{(\,)}^L$ is defined as the mean taken relative to the perturbed position, $\Xi(x,t) = x + \xi(x,t)$, such that

$$\overline{\phi(x,t)}^L = \overline{\phi\left\{\Xi,t\right\}}. \tag{1.1}$$

$\xi(x,t)$ is defined as a perturbation based quantity, requiring that

$$\overline{\xi(x,t)} = 0. \tag{1.2}$$

Defining a Lagrangian-mean velocity, $\overline{u}^L = \overline{u(\Xi,t)}$, the Lagrangian-mean material derivative can be written as

$$\overline{D}^L(\phi) = \frac{\partial\phi}{\partial t} + \overline{u}^L \cdot \nabla\phi. \tag{1.3}$$

Using the notation $\phi^\xi(x,t) = \phi(\Xi,t)$ it follows that

$$\overline{D}^L(\Xi) = u^\xi \tag{1.4}$$

and

$$\overline{D}^L(\xi) = u^l \tag{1.5}$$

where u^l is the Lagrangian disturbance velocity, written as

$$u^l(x,t) = u^\xi - \overline{u}^L. \tag{1.6}$$

Taking consideration of (1.2), (1.5), and the mean operator identities

$$\overline{\overline{\phi}\psi} = \bar{\phi}\bar{\psi}, \tag{1.7}$$

$$\overline{\phi+\psi} = \overline{\phi} + \overline{\psi}, \tag{1.8}$$

the Lagrangian disturbance velocity, u^l, can be shown to truly be a perturbation based velocity as

$$\overline{u^l} = \frac{\partial\overline{\xi}}{\partial t} + \overline{u}^L \cdot \bigtriangledown\overline{\xi} = 0 \tag{1.9}$$

and

$$\overline{u}^L = \overline{u^\xi}. \tag{1.10}$$

Further application of the GLM notation provides several important corollaries:

$$\left(\frac{D\phi}{Dt}\right)^\xi = \overline{D}^L\left(\phi^\xi\right) \tag{1.11}$$

and

$$\overline{\left(\frac{D\phi}{Dt}\right)^L} = \overline{D}^L\overline{\phi^L}. \tag{1.12}$$

A.3 Stokes Correction

The relationship between the Generalized Lagrangian-mean and the Eulerian-mean description is the Stokes correction, defined as

$$\overline{\phi}^s(x,t) = \overline{\phi}^L(x,t) - \overline{\phi}(x,t). \tag{2.1}$$

Assuming perturbations (ξ) are of small amplitude, Taylor series expansion of the general transformation provides

$$\phi^\xi = \overline{\phi} + \phi' + \xi_j \phi_{,j} + \frac{1}{2}\xi_j \xi_k \overline{\phi}_{,jk} + O(\xi^3) \tag{2.2}$$

where $(\ )_{,i} = \frac{\partial(\ )}{\partial x_i}$. Considering $\phi = \overline{\phi} + \phi'$ and averaging (2.2) provides

$$\overline{\phi}^s = \overline{\xi_j \phi'_{,j}} + \frac{1}{2}\overline{\xi_j \xi_k \phi}_{,jk} + O(\xi^3). \tag{2.3}$$

noting that (1.1) shows that $\overline{\phi^\xi} = \overline{\phi}^L$. Replacing ϕ with u, the Stokes drift is written as

$$\overline{u}^s = \overline{\xi_j u'_{,j}} + \frac{1}{2}\overline{\xi_j \xi_k} \overline{u}_{,jk} + O(\xi^3). \tag{2.4}$$

The Stokes drift provides the relation between the mean Eulerian and mean Lagrangian velocities

$$\overline{u}^L = \overline{u} + \overline{u}^s. \tag{2.5}$$

Assuming monochromatic, irrotational waves in deep water, the velocity potential is described by Phillips [119] as

$$\varphi = \frac{\omega}{k} a e^{kz} sin\left(kx - \omega t\right), \tag{2.6}$$

where k is the wave number, a is the amplitude of the surface waves, g is the acceleration of gravity, and the flow satisfies the deep water dispersion relation, $\omega = \sqrt{gk}$. The perturbation can then be described as

$$\xi_i = \int \varphi_{,i} dt, \tag{2.7}$$

such that

$$\xi_x = -a e^{kz} sin\left(kx - \omega t\right)$$

and

$$\xi_z = a e^{kz} cos\left(kx - \omega t\right).$$

Evaluating $u'_{,j}$ in (2.4) as $\left(\frac{\partial \xi}{\partial t}\right)_{,i}$, the Stokes drift, to the first order, can be related to the perturbation as

$$\overline{u}^s = \overline{\xi_j \left(\frac{\partial \xi}{\partial t}\right)_{,i}}. \tag{2.8}$$

Using the relations of (2.7), the Stokes drift can be described as

$$\overline{u}^s = \overline{\left(\xi_x \frac{\partial \xi_{x,x}}{\partial t} + \xi_z \frac{\partial \xi_{x,z}}{\partial t}\right)},$$

which after substitution and reduction gives

$$\overline{u}^s = \overline{\omega k a^2 \left[sin^2\left(kx - \omega t\right) + cos^2\left(kx - \omega t\right)\right]}. \tag{2.9}$$

Further reducing (2.9) and substituting $\omega = \sqrt{gk}$ provides the form of the Stokes drift used in this analysis as

$$\overline{u}^s = (ka)^2 \sqrt{\frac{g}{k}} e^{-2kz}. \tag{2.10}$$

A.4 Mean Flow Evolution

In order to derive an expression to describe the evolution of the mean flow, Andrews and McIntyre [6], apply the GLM to the conservation of momentum equation

$$\frac{Du_j}{Dt} + 2(\Omega \times u)_j + \frac{\partial \Phi}{\partial x_j} + \frac{1}{\rho}\frac{\partial P}{\partial x_j} + X_j = 0, \tag{3.1}$$

where Ω is the angular velocity of a rotating reference frame, Φ accounts for gravitational and centrifugal forces, ρ is the fluid density, P is the pressure, and X allows for additional contributions such as dissipative forces. This analysis assumes that gravitational and centrifugal forces are negligible and that the flow is incompressible with constant density. The equation that governs the mean flow evolution for this analysis is obtained by multiplying $(3.1)^{\xi}$ by $\Xi_{,i}$ and averaging. Taking the first term and applying (1.8) gives

$$\Xi_{j,i}\left(\frac{Du_j}{Dt}\right)^{\xi} = \Xi_{j,i}\overline{D}^L\left({u_j}^{\xi}\right). \tag{3.2}$$

Moving $\Xi_{j,i}$ into the Lagrangian mean material derivative on the RHS and expanding gives

$$\overline{D}^L\left(\Xi_{j,i}{u_j}^{\xi}\right) = \frac{\partial\left(\Xi_{j,i}{u_j}^{\xi}\right)}{\partial t} + \overline{u}^L \cdot \bigtriangledown\left(\Xi_{j,i}{u_j}^{\xi}\right)$$

$$= {u_j}^{\xi}\frac{\partial \Xi_{j,i}}{\partial t} + \Xi_{j,i}\frac{\partial {u_j}^{\xi}}{\partial t} + \overline{u}^L\left(\Xi_{j,i}\frac{\partial {u_j}^{\xi}}{\partial x_i} + {u_j}^{\xi}\frac{\partial \Xi_{j,i}}{\partial x_i}\right).$$

Distributing $\overline{u}^L$ and rearranging provides

$$\overline{D}^L\left(\Xi_{j,i}{u_j}^{\xi}\right) = {u_j}^{\xi}\frac{\partial \Xi_{j,i}}{\partial t} + \Xi_{j,i}\frac{\partial {u_j}^{\xi}}{\partial t} + \Xi_{j,i}\left(\overline{u}^L \cdot \bigtriangledown {u_j}^{\xi}\right) + {u_j}^{\xi}\left(\overline{u}^L \cdot \bigtriangledown \Xi_{j,i}\right).$$

This can be further rearranged to give

$$\overline{D}^L\left(\Xi_{j,i}{u_j}^\xi\right) = {u_j}^\xi\frac{\partial\Xi_{j,i}}{\partial t} + {u_j}^\xi\left(\overline{u}^L\cdot\bigtriangledown\Xi_{j,i}\right) + \Xi_{j,i}\frac{\partial {u_j}^\xi}{\partial t} + \Xi_{j,i}\left(\overline{u}^L\cdot\bigtriangledown {u_j}^\xi\right),$$

which reduces to

$$\overline{D}^L\left(\Xi_{j,i}{u_j}^\xi\right) = {u_j}^\xi\overline{D}^L\Xi_{j,i} + \Xi_{j,i}\overline{D}^L\left({u_j}^\xi\right). \tag{3.3}$$

Plugging (3.3) into (3.2) provides

$$\Xi_{j,i}\left(\frac{Du_j}{Dt}\right)^\xi = \overline{D}^L\left(\Xi_{j,i}{u_j}^\xi\right) - {u_j}^\xi\overline{D}^L\Xi_{j,i}. \tag{3.4}$$

Expanding the final term of (3.4):

$${u_j}^\xi\overline{D}^L\Xi_{j,i} = {u_j}^\xi\left[\frac{\partial}{\partial t}\frac{\partial\Xi_j}{\partial x_i} + \overline{u}_k^L\frac{\partial}{\partial x_i}\left(\frac{\partial\Xi_j}{\partial x_i}\right)\right]$$

Bringing $\overline{u}^L$ into the partial derivative and rearranging gives

$${u_j}^\xi\overline{D}^L\Xi_{j,i} = {u_j}^\xi\left[\frac{\partial}{\partial x_i}\frac{\partial\Xi_j}{\partial t} + \frac{\partial}{\partial x_i}\left(\overline{u}_k^L\frac{\partial\Xi_j}{\partial x_i}\right) - \frac{\partial\overline{u}_k^L}{\partial x_i}\frac{\partial\Xi_j}{\partial x_i}\right].$$

Plugging this into (3.4) provides (B1) from Andrews and McIntyre [6],

$$\Xi_{j,i}\left(\frac{\partial u_j}{\partial t}\right)^\xi = \overline{D}^L\left(\Xi_{j,i}{u_j}^\xi\right) - {u_j}^\xi\left[\left(\overline{D}^L\Xi_j\right)_{,i} - \bar{u}_{k,i}^L\Xi_{j,k}\right]. \tag{3.5}$$

Using (1.4) and the definition of the perturbation position, the RHS of (3.5) can be written as (B2) in Andrews and McIntyre [6],

$$\overline{D}^L\left[\left(\delta_{ji}+\xi_{j,i}\right){u_j}^\xi\right] - {u_j}^\xi\left({u_j}^\xi\right)_{,i} + \overline{u}_{k,i}^L\left(\delta_{jk}+\xi_{j,k}\right){u_j}^\xi. \tag{3.6}$$

Recalling (1.6) and averaging, the first term on the RHS of (3.6) becomes

$$\overline{\overline{D}^L\left[{u_j}^l + {u_j}^l\xi_{j,i} + \overline{u}_j^L + \xi_{j,i}\overline{u}^L\right]}.$$

Applying (1.2), (1.7) and (1.9), this is simplified to

$$\overline{D}^L\left[\overline{{u_j}^l\xi_{j,i}} + {u_j}^L\right]. \tag{3.7}$$

The term ${p_i}^0$, which will later be referred to as the first term of the pseudo-momentum per unit mass, is defined as

$$p_i^0 = -\overline{\xi_{j,i}{u_j}^l}. \tag{3.8}$$

Plugging (3.8) into (3.7) and moving ${u_j}^{\xi}$ into the partial derivative of the second term in (3.6), (B4) of Andrews and McIntyre [6] is written as

$$\overline{\Xi_{j,i}\overline{D}^{L}\left({u_j}^{\xi}\right)} = \overline{D}^{L}\left(\overline{u}_i^{L} - p_i^{0}\right) - \frac{1}{2}\overline{\left(u_j{}^{\xi}u_j{}^{\xi}\right)}_{,i} + \overline{u}_{k,i}^{L}\left(\overline{u}_k^{L} - p_k^{0}\right). \tag{3.9}$$

Taking the second term of $(3.1)^{\xi}$, multiplying by $\Xi_{j,i}$, averaging, and applying (1.5) and (1.6) gives

$$2\overline{\Xi_{j,i}\epsilon_{jmn}\Omega_m u_n^{\xi}} = 2\epsilon_{jmn}\Omega_m\overline{(\delta_{ji} + \xi_{j,i})\left(\overline{u}_n^{L} + \overline{D}^{L}\xi_n\right)}. \tag{3.10}$$

Expanding the RHS gives

$$2\epsilon_{jmn}\Omega_m\overline{\left[\delta_{ji}\overline{D}^{L}\xi_n + \delta_{ji}\overline{u}_n^{L} + \xi_{j,i}\overline{D}^{L}\xi_n + \xi_{j,i}\overline{u}_j^{L}\right]}.$$

Considering (1.2), (1.7), (1.8), (1.9), and simplifying provides

$$2\overline{\Xi_{j,i}\epsilon_{jmn}\Omega_m u_n{}^{\xi}} = 2\epsilon_{jmn}\Omega_m\overline{\left[\overline{u}_n^{L} + \xi_{j,i}\overline{D}^{L}\xi_n\right]}. \tag{3.11}$$

Bringing $\overline{D}^{L}\xi_n$ in the second term of (3.11) into the partial derivative of $\xi_{j,i}$ allows the second term to be written as

$$2\epsilon_{jmn}\Omega_m\overline{\xi_{j,i}\overline{D}^{L}\xi_n} = 2\epsilon_{jmn}\Omega_m\left(\overline{\xi_{j,i}\overline{D}^{L}\xi_n} - \overline{\xi_j\left(\overline{D}^{L}\xi_n\right)_{,i}}\right). \tag{3.12}$$

The second term on the RHS can be expanded as

$$\xi_j\left(\overline{D}^{L}\xi_n\right)_{,i} = \xi_j\frac{\partial}{\partial x}\left[\left(\frac{\partial\xi_n}{\partial t}\right) + u_n^{L}\cdot\bigtriangledown\xi_n\right].$$

Further expanding the final term and rearranging gives

$$\xi_j\left[\frac{\partial}{\partial t}\left(\frac{\partial\xi_n}{\partial x_i}\right) + u_n^{L}\left(\xi_{n,i}\right)_{,i} + \xi_{n,p}\overline{u}_{p,i}^{L}\right],$$

which can be written as

$$\xi_j\left(\overline{D}^{L}\left(\xi_{n,i}\right) + \overline{u}_{p,i}^{L}\xi_{n,p}\right).$$

Plugging into (3.12),

$$2\epsilon_{jmn}\Omega_m\overline{\xi_{j,i}\overline{D}^{L}\xi_n} = 2\epsilon_{jmn}\Omega_m\left[\overline{\xi_j\left(\overline{D}^{L}\xi_n\right)_{,i}} - \overline{\xi_j\overline{D}^{L}\xi_{n,i}} - \overline{\overline{u}_{p,i}^{L}\xi_j\xi_{n,p}}\right].$$

Interchanging j and n in the middle term, changing its sign, and adding half the LHS to half the RHS gives

$$2\epsilon_{jmn}\Omega_m\overline{\xi_{j,i}\overline{D}^{L}\xi_n} = \epsilon_{jmn}\Omega_m\left[\overline{\xi_j\left(\overline{D}^{L}\xi_n\right)_{,i}} + \overline{\xi_{j,i}\overline{D}^{L}\xi_n} + \overline{\xi_n\overline{D}^{L}\xi_{j,i}} - \overline{\overline{u}_{p,i}^{L}\xi_j\xi_{n,p}}\right],$$

which can be reduced by considering (1.5) and the chain rule to

$$2\epsilon_{jmn}\Omega_m\overline{\xi_{j,i}\overline{D}^L\xi_n} = \epsilon_{jmn}\Omega_m\left[\overline{\left(\xi_j u_n^l\right)_{,i}} + \overline{D}^L\left(\overline{\xi_{j,i}\xi_n}\right) - \overline{\overline{u}^L_{p,i}\xi_j\xi_{n,p}}\right]. \tag{3.13}$$

Defining

$$p_i{}^{\Omega} = -\epsilon_j mn\Omega_m\overline{\xi_{j,i}\xi_n} = -\overline{\xi_{j,i}\left(\Omega\times\xi\right)_j} \tag{3.14}$$

and considering

$$\epsilon_{jmn}\Omega_m\left(\overline{\xi_j u_n^l}\right)_{,i} = \epsilon_{jmn}\Omega_m\left(\overline{\xi_j u_n{}^{\xi}} - \overline{\xi_j\overline{u}_n^L}\right)_{,i} = \epsilon_{jmn}\Omega_m\left(\overline{\xi_j u_n{}^{\xi}}\right)_{,i},$$

(3.11) can be written as

$$2\overline{\Xi_{j,i}\epsilon_{jmn}\Omega_m u_n^{\xi}} = 2\left(\Omega\times\overline{u}^L\right)_i - \left(\overline{u^{\xi}\cdot\Omega\times\xi}\right)_{,i} - \overline{D}^L p_i^{\Omega} - \overline{u}^L_{k,i}p_k^{\Omega}. \tag{3.15}$$

The third term of (3.1) is neglected in this analysis, while the fourth term can be written as

$$\overline{\Xi_{j,i}\left(\frac{1}{\rho}P_{,j}\right)^{\xi}} = \overline{\frac{1}{\rho^{\xi}}\left(P^{\xi}\right)_{,i}}. \tag{3.16}$$

Assuming constant density, as done by Leibovich [86], and recalling (1.10), (3.16) can be written as

$$\overline{\Xi_{j,i}\left(\frac{1}{\rho}P_{,j}\right)^{\xi}} = \frac{1}{\rho}\overline{P}^L_{,i}. \tag{3.17}$$

The final term can be written as (B8) in Andrews and McIntyre [6]:

$$\overline{\Xi_{j,i}X_j{}^{\xi}} = \overline{\left(\delta_{ji}+\xi_{j,i}\right)\left(X_j{}^L + X_j{}^l\right)} = \overline{X_i}^L + \overline{\xi_{j,i}X_j{}^l}. \tag{3.18}$$

Combining (3.9), (3.15), (3.17), and (3.18) provides (1) of Leibovich [86]:

$$\overline{D}_i^L\left(\overline{u}_i^L - p_i\right) + \overline{u}^L_{k,i}\left(\overline{u}_k^L - p_k\right) + 2\left(\Omega\times\overline{u}^L\right)_i + \pi_{,i} + \overline{X_i}^L + \overline{\xi_{j,i}X_j{}^l} = 0 \tag{3.19}$$

where,

$$\pi = \frac{1}{\rho}\overline{P}^L - \frac{1}{2}\overline{u^{\xi}u^{\xi}} + \overline{\left(\Omega\times\xi\right)\cdot u^{\xi}}.$$

A.5 Craik-Leibovich Vortex Force

The derivation of the Craik-Leibovich (CL) vortex force begins with the equation governing mean flow evolution, (3.19). Andrews and McIntyre [6], in their derivation of the mean flow equation, introduced the wave pseudo-momentum per unit mass, p, defined in its full form as

$$p_i\left(x,t\right) = -\overline{\xi_{j,i}\left[u_j{}^l + \left(\Omega\times\xi\right)_j\right]}. \tag{4.1}$$

Assuming $\Omega = 0$, as done by [86], p reduces to

$$p_i = -\overline{\xi_{j,i} {u_j}^l}. \tag{4.2}$$

Applying (2.28) of [6], $\phi^l = \phi' + \xi_j \overline{\phi_{,j}} + O\left(\xi^2\right)$, (4.2) can be written as

$$p_i = -\overline{\xi_{j,i} \left(u'_j + \xi_j \overline{u}_{,j} + O\left(\xi^2\right)\right)}. \tag{4.3}$$

Expansion of (4.3) gives

$$p_i = -\overline{\xi_{j,i} u'_j} - \frac{1}{2}\overline{\xi^2_{j,i} \overline{u}_{,j}} + O\left(\xi^3\right).$$

Swapping the partials in the first two terms provides

$$p_i = \overline{\xi_j u'_{j,i}} + \frac{1}{2}\overline{\xi^2_j \overline{u}_{,jk}} + O\left(\xi^3\right). \tag{4.4}$$

Comparison of (4.4) with (2.4) readily shows

$$p_i = \overline{u}^s + O\left(\xi^3\right). \tag{4.5}$$

Considering (4.5) and (2.5), $\overline{u}^L - p$ can be replaced with $\overline{u}$ in (3.19) . Assuming $\Omega = 0$, (3.19) can be written as

$$\overline{D}^L_i \left(\overline{u_i}\right) + \overline{u}^L_{k,i} \left(\overline{u}_k\right) + \pi_{,i} = V_i. \tag{4.6}$$

where

$$\pi = \frac{1}{\rho}\overline{P}^L - \frac{1}{2}\overline{u^\xi u^\xi}$$

and V_i accounts for viscous dissipation. Expanding the first two terms in (4.6)

$$\frac{\partial \overline{u}_i}{\partial t} + \bar{u}^L_j \bar{u}_{i,j} + \overline{u}^L_{k,i} \overline{u}_k + \pi_{,i} = V_i. \tag{4.7}$$

Bringing $\overline{u}_k$ in the third term into the partial derivative, the middle two terms on the LHS become

$$\overline{u_j}^L \overline{u}_{i,j} + \overline{u}^L_{j,i} \overline{u}_j = \overline{u}^L_j \left(\overline{u}_{i,j} - \overline{u}_{j,i}\right) + \left(\overline{u}_j \overline{u}^L_j\right)_{,i}$$

Applying (2.5) and expanding produces

$$\bar{u}_j \bar{u}_{i,j} + \bar{u}^s_j \bar{u}_{i,j} - \bar{u}_j \bar{u}_{j,i} - \bar{u_j}^s \bar{u}_{j,i} + \left(\bar{u}_j + \bar{u}^s_j\right) \bar{u}_{j,i} + u_j \left(\bar{u}_j + \bar{u}^s_j\right)_{,i}.$$

Observing that the four center terms cancel, this reduces to

$$\bar{u}_j \bar{u}_{i,j} + \bar{u}^s_j \bar{u}_{i,j} + \bar{u}_j \bar{u}_{j,i} + \bar{u}_j \bar{u}^s_{j,i}.$$

Bringing $\bar{u}_j$ in the final term into the partial derivative, applying the chain rule, and rearranging gives

$$\bar{u}_j \left(\bar{u}_{i,j} + \bar{u}_{j,i}\right) + \bar{u}^s_j \left(\bar{u}_{i,j} - \bar{u}_{j,i}\right) + \left(\bar{u}_j \bar{u_j}^s\right)_{,i} = \bar{u} \cdot \bigtriangledown \bar{u} - \bar{u}^s \times \left(\bigtriangledown \times \bar{u}\right) + \bigtriangledown \left(\bar{u} \cdot \bar{u}^s\right). \tag{4.8}$$

Applying (4.8) to (4.7) gives

$$\frac{\partial \bar{u}}{\partial t} + \bar{u} \cdot \bigtriangledown \bar{u} + \bigtriangledown \left(\pi + \bar{u} \cdot \bar{u}^s\right) = \bar{u}^s \times \left(\bigtriangledown \times \bar{u}\right) + V_i, \tag{4.9}$$

where $\bar{u}^s \times \left(\bigtriangledown \times \bar{u}\right)$ is the Craik-Leibovich vortex force.

Appendix B

Theoretical model for a surface–combatant wake

An empirical–analytical representation of the wake one-half ship length downstream, Figure 3.1, is established based on a formulation similar to [102]. This model includes resistance contributions from the ship's hull, wave breaking, and rudder; in addition to the thrust current and swirl from the propellers. The total axial velocity in the wake is described as $u = u_p - (u_f + u_w + u_r)$, where u_p is the thrust current from the propellers, u_f is the velocity deficit due to the frictional resistance of the hull, u_w is the manifestation of the wave making resistance in the axial velocity profile, and u_r is the velocity deficit due to the resistance of the twin rudders.

The ship's frictional drag current is approximated as a double Gaussian profile of the form

$$u_f = u_{Fmax} \exp\left(-3.5\tilde{a}\left[\left(\frac{y \pm 0.3B}{y_h}\right)^2 + \left(\frac{z}{z_h}\right)^2\right]\right), \tag{B.1}$$

where u_{Fmax} is the maximum value of the velocity deficit due to the ship's frictional resistance at the initial data plane, B is the ship beam, y_h and z_h are the half widths of the initial wake, and $\tilde{a} = 2.6$ based on experimental data from [112]. This profile was adjusted relative to the standard Gaussian profile provided by Miner to more closely match the experimental data reported by [143].

The maximum value of the frictional velocity deficit, u_{Fmax}, is found based on

$$u_{Fmax} = \frac{\tilde{a} U_0 S C_f}{\pi y_h z_h}, \tag{B.2}$$

where $C_f = \frac{0.075}{(\log_{10}(Re)-2)^2}$ is the coefficient of frictional resistance described by the ITTC-1957 correlation, Re is the Reynolds number, S is the wetted surface area, and U_0 is the ship's velocity.

Due to the presence of the free surface, the wake half widths are estimated independently. The lateral length scale is approximated as an axisymmetric wake:

$$y_h = \theta c_\delta \left[\frac{x - x_0}{\theta}\right]^{\frac{1}{3}} \tag{B.3}$$

where θ is the momentum radius, x_0 is the virtual origin of the wake, x is the location of the initial data plane, and c_δ is a scaling constant. The initial data plane is taken x/L = 0.5 downstream of the transom to allow sufficient distance for the wake to reach nearly self–similar conditions.

The momentum radius for an axisymmetric wake as shown by [107] is

$$\theta^2 = \frac{1}{8} C_D B^2 \tag{B.4}$$

where C_D is the drag coefficient. In this analysis, $C_D = C_f \frac{S}{b^2}$ is the frictional resistance non-dimensionalized by a reference area of B^2. The virtual origin is then solved via

$$x_0/\theta = \left(\frac{-\sqrt{8}\alpha}{c_\delta \sqrt{C_D}} \right)^3 \tag{B.5}$$

where $\alpha = 0.5$ and $c_\delta = 1.14$ based on high Reynolds number data reported by [70]. Assuming the same virtual origin for the horizontal and vertical wakes, Miner provides the ratio of scales as $y_h/z_h = 2(B/(2D))^{\frac{2}{3}}$ where D is the ship draft.

The turbulent kinetic energy (TKE) of the ship's drag current exhibits a double peak, corresponding to the production of turbulence in the boundary layer on either side of the hull. Miner modeled the TKE as

$$k_d = k_{max} \left(\tilde{a_1} \exp\left\{ -\tilde{a_2} \left[\left(\frac{y}{y_h} \right)^2 + \left(\frac{z}{z_h} \right)^2 \right] \right\} - \tilde{a_3} \exp\left\{ -\tilde{a_4} \left[\left(\frac{y}{y_h} \right)^2 + \left(\frac{z}{z_h} \right)^2 \right] \right\} \right) \tag{B.6}$$

where k_{max} is the peak value of the turbulent kinetic energy, $\tilde{a_1} = 1.35$, $\tilde{a_2} = 1.0$, $\tilde{a_3} = 0.45$, and $\tilde{a_4} = 8.22$. Miner solves for k_{max} as $\sqrt{k_{max}}/u_{Fmax} = 0.3$. A portion of the wave–making resistance is also manifest in the velocity deficit based on formulation similar to Miner. Here the wave–breaking contribution to the velocity profile is estimated as

$$u_w = u_{Wmax} \exp\left[-6\tilde{a} \left\{ \left(\frac{z}{z_{hw}} \right)^2 + \left(\frac{y \pm 0.6B}{y_{hw}} \right)^2 \right\} \right], \tag{B.7}$$

where u_{Wmax} is the maximum value of the velocity deficit due to wave breaking, and y_{hw} and z_{hw} are the half widths of the wave–breaking wake. The maximum velocity deficit is calculated based on

$$u_{Wmax} = \frac{\tilde{a} R_{wave}}{\pi \rho U_0 y_{hw} z_{hw}} \tag{B.8}$$

where R_{wave} is the wave making resistance of the hull based on the experimental data of [110].

The ship propellers are modeled as thrust currents with swirl with an axial velocity profile given as

$$u_p = u_{pMax} exp\left[-2\tilde{a} \left(\frac{r}{r_h} \right)^2 \right] \tag{B.9}$$

where $\tilde{a} = 2.45$, the constant 2 is a profile tuning value, and $r_h = 0.086x$. The maximum axial velocity is given by

$$u_{pMax} = \frac{\tilde{a}T}{\pi\rho U_0 (r_h)^2} \tag{B.10}$$

where T is the total thrust of the propellers to overcome the combined frictional and wave–making resistance. The swirl velocity is based on the self-similar propeller velocity.

$$V_s = V_{sMax}\tilde{a_1}\left(\frac{r}{r_{sh}}\right)\exp\left[-\tilde{a_2}\left(\frac{r}{r_{sh}}\right)^2\right] \tag{B.11}$$

where $\tilde{a_1} = 4.34$, $\tilde{a_2} = 3.56$, and r_{sh} is half width of the swirl profile taken to be $r_{sh} = 0.095\sqrt{xB}$. The maximum swirl velocity, V_{sMax}, is a function of the propeller torque (Q)

$$V_{sMax} = \frac{Q}{\pi\rho U_0 \frac{\tilde{a_1}}{\tilde{a_2}}(r_{sh})^3}. \tag{B.12}$$

The propeller torque is a function of the swirl number, $\tilde{S}$, and the propeller diameter, D_p

$$Q = \tilde{S}\left(T\frac{D_p}{2}\right), \tag{B.13}$$

where the swirl number is taken to be $S = 0.3$.

The self–similar turbulent kinetic energy from the propeller wake is given by

$$k_p = k_{pMax}\exp\left[-\tilde{a}\left(\frac{r}{r_h}\right)^2\right], \tag{B.14}$$

where $k_{pMax} = (0.59u_{Fmax})^2$.

The rudders are modeled as NACA 0015, with $C_{d_0} = 0.0093$. Single Gaussian profiles are used to model the wake deficits as outlined by Miner.

$$u_r = u_{rMax}exp\left[-\tilde{a}\left\{\left(\frac{y \pm y_r}{y_{hr}}\right)^2 + \left(\frac{z - z_r}{z_{hr}}\right)^2\right\}\right] \tag{B.15}$$

where y_r and z_r are the rudder horizontal and vertical offsets from the surface centerline. The maximum velocity deficit due to the rudder is estimated as

$$u_{rMax} = \frac{\tilde{a_r}R_{rudder}}{\pi\rho U_0 y_{hr} z_{hr}} \tag{B.16}$$

where R_r is the resistance of the rudder and y_{hr} and z_{hr} are the wake half widths. The vertical half width, $z_{hr} = \frac{1}{2}b_r$, where b_r is the rudder span, while the horizontal half width, y_{hr} is set as

$$y_{hr} = \tilde{a}_r\sqrt{xt_r} + \frac{1}{2}t_r; \tag{B.17}$$

where t_r is the thickness of the rudder and $\tilde{a}_r = 0.23\sqrt{C_{dr}}$. The TKE due to the rudders is found by using equation (A6) with $\sqrt{k_{max}}/u_{rMax} = 1$.

Bilge keels are not included in the current model as their contribution to the velocity profile is considered negligible. Miner provides a formulation for the inclusion of bilge vortices, but the experimental data presented by [143] and [59] suggest that the pair of bilge vortices are ingested by the propellers and their rotation canceled.

The total turbulent kinetic energy is taken to be the sum of the contributions from ship drag current and the propeller

$$k = k_d + k_p. \tag{B.18}$$

The turbulent dissipation rate of the drag current ε_d and the thrust current ε_p are modeled based on [57] as:

$$\varepsilon_d = \sqrt{\frac{3}{A}} (k_d)^{\frac{3}{2}}, \varepsilon_p = \frac{\sqrt{12}}{B} (k_p)^{\frac{3}{2}} \tag{B.19}$$

where

$$A = C_d B^2 \frac{U_0}{8 u_{fMax}}. \tag{B.20}$$

Appendix C

Perfect and Simulated SAR images

Perfect SAR images for vv polarization in following and head seas with wave amplitudes between 0.5-1.5 m are provided. Wavelengths of 50 m are used in all simulated conditions here.

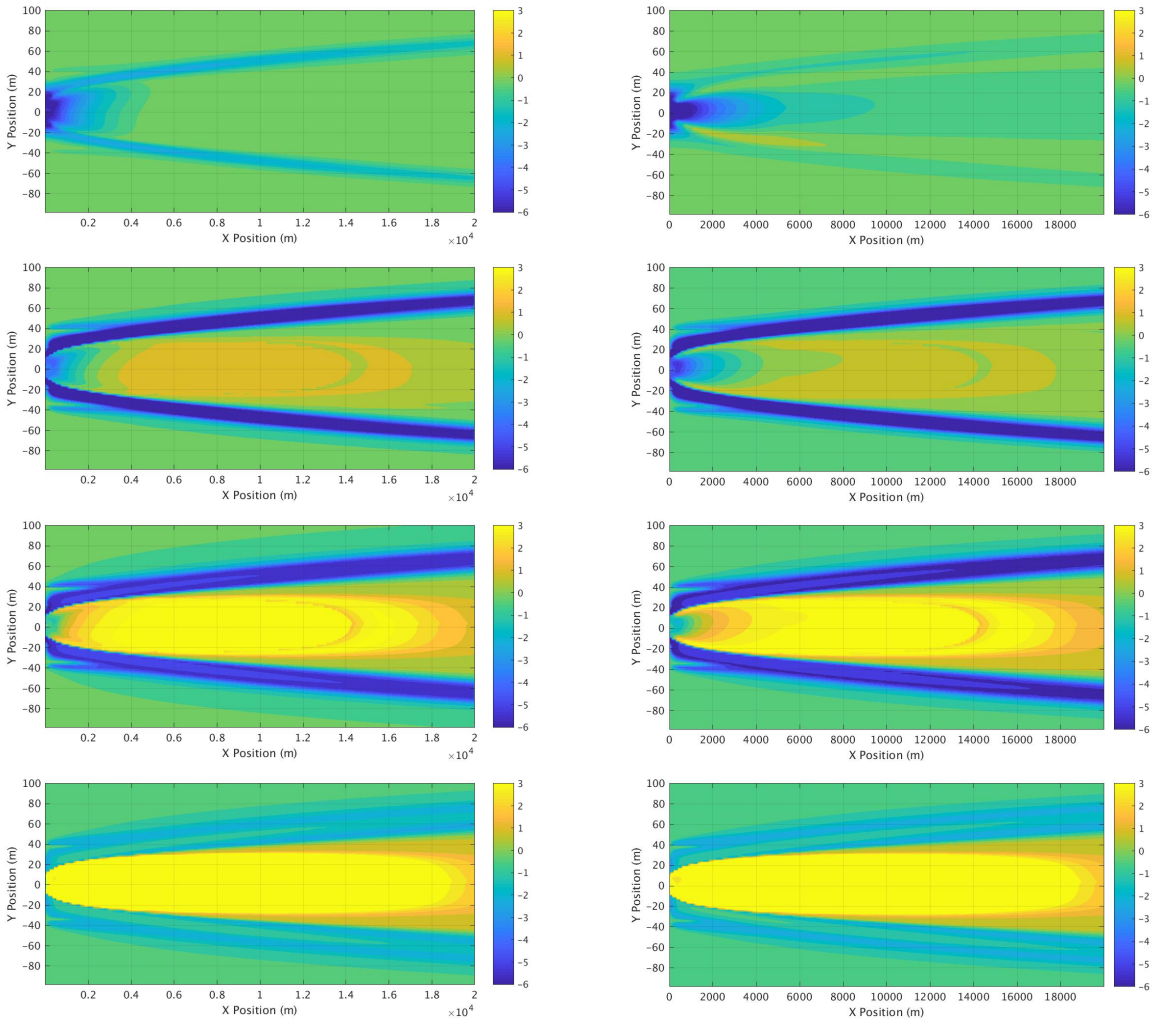

Figure C.1: Perfect SAR images (dB) at L, S, C, and X band with vv polarization at 50 degree incidence with the azimuth along (left) and across (right) the wake for a 0.5 m wave amplitude in following seas.

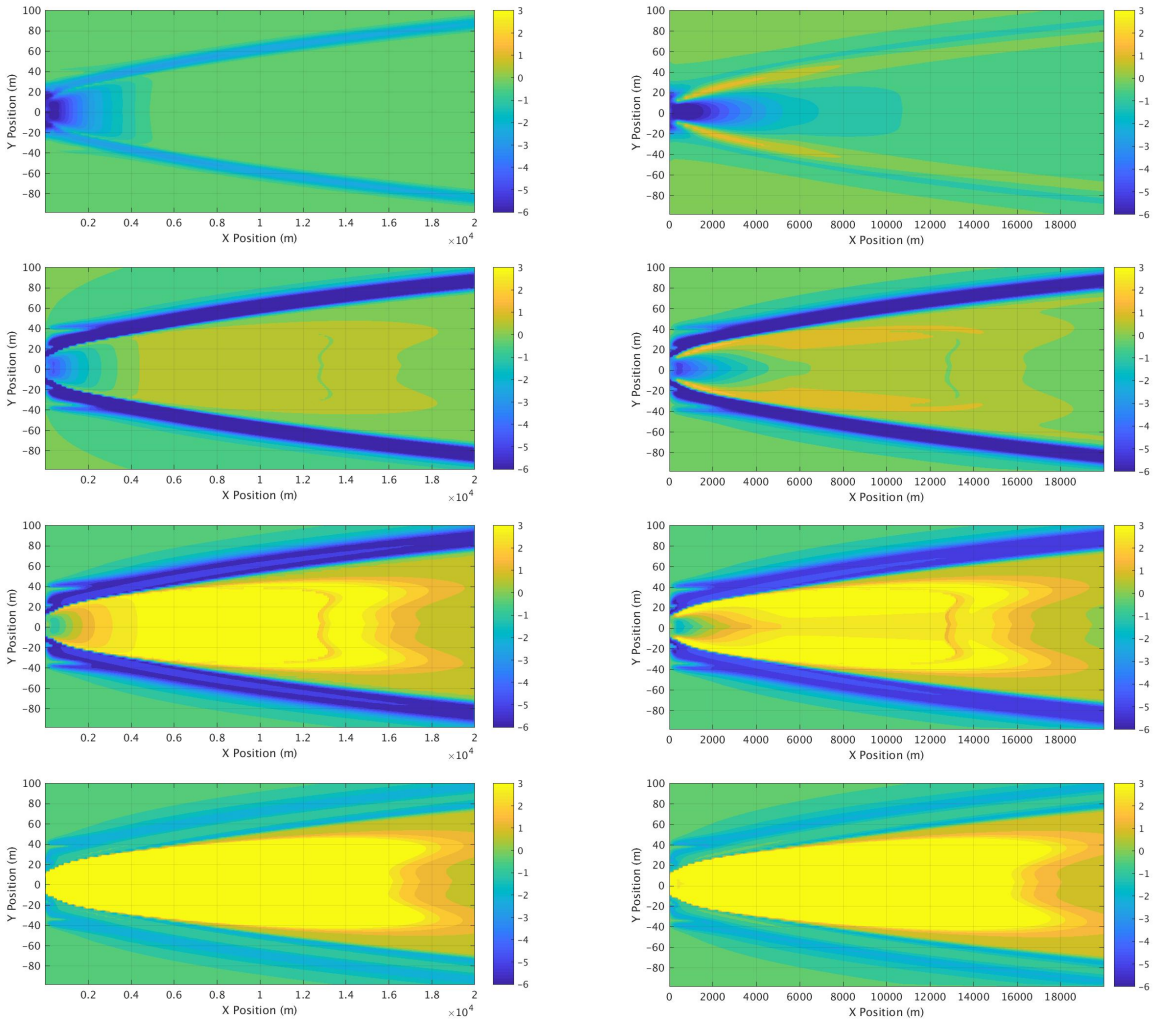

Figure C.2: Perfect SAR images (dB) at L, S, C, and X band with vv polarization at 50 degree incidence with the azimuth along (left) and across (right) the wake for a 1.0 m wave amplitude in following seas.

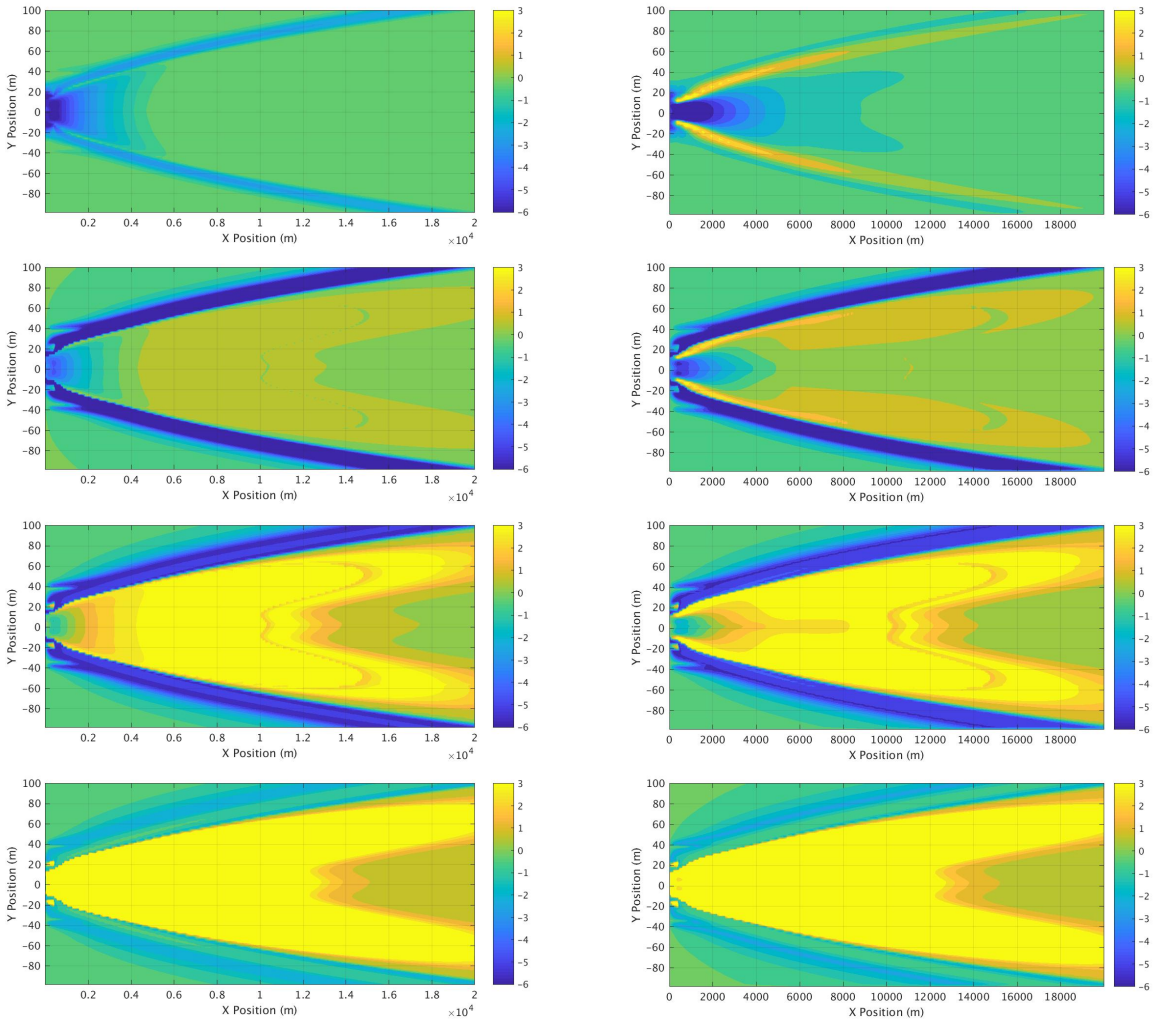

Figure C.3: Perfect SAR images (dB) at L, S, C, and X band with vv polarization at 50 degree incidence with the azimuth along (left) and across (right) the wake for a 1.5 m wave amplitude in following seas.

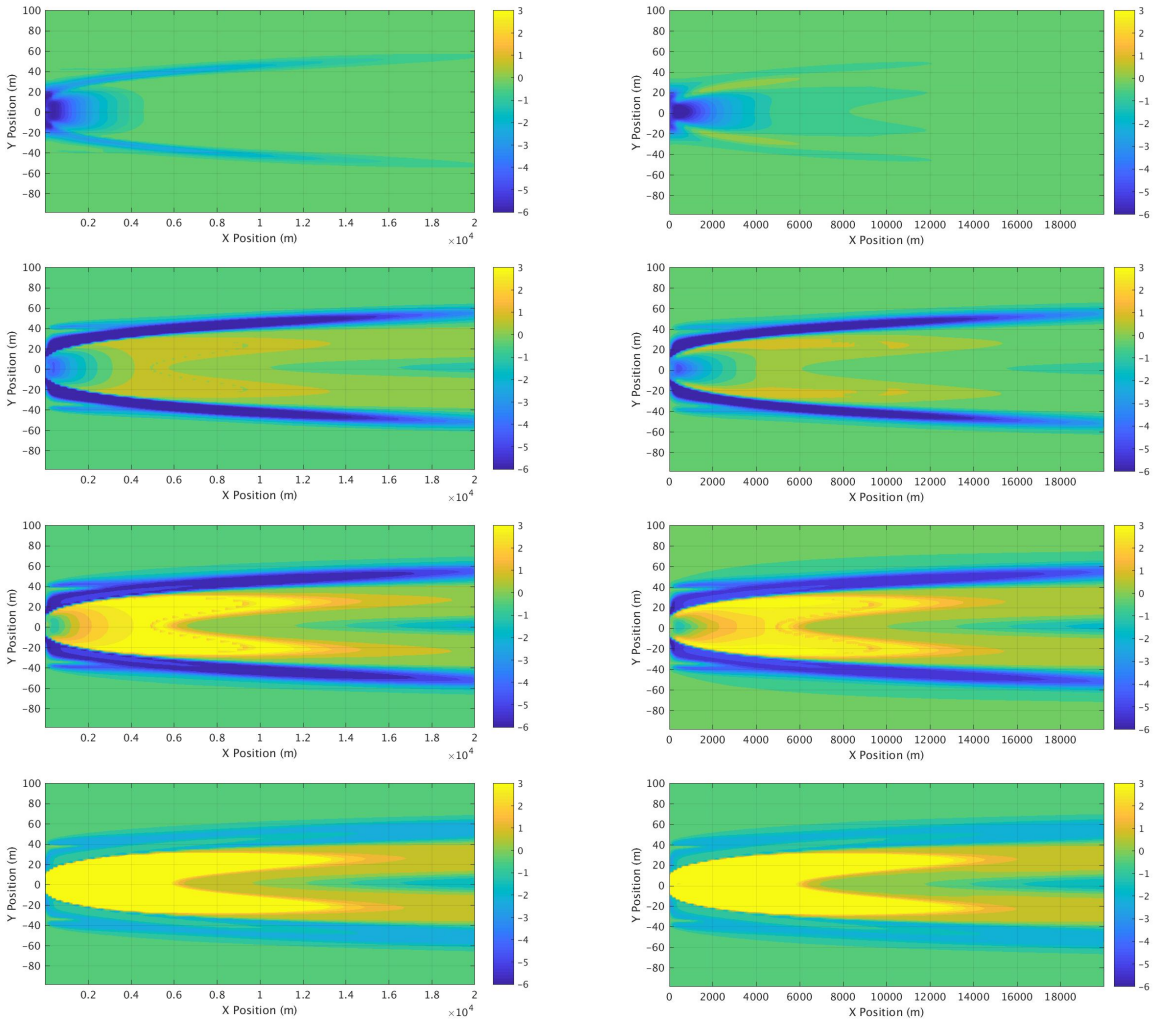

Figure C.4: Perfect SAR images (dB) at L, S, C, and X band with vv polarization at 50 degree incidence with the azimuth along (left) and across (right) the wake for a 0.5 m wave amplitude in head seas.

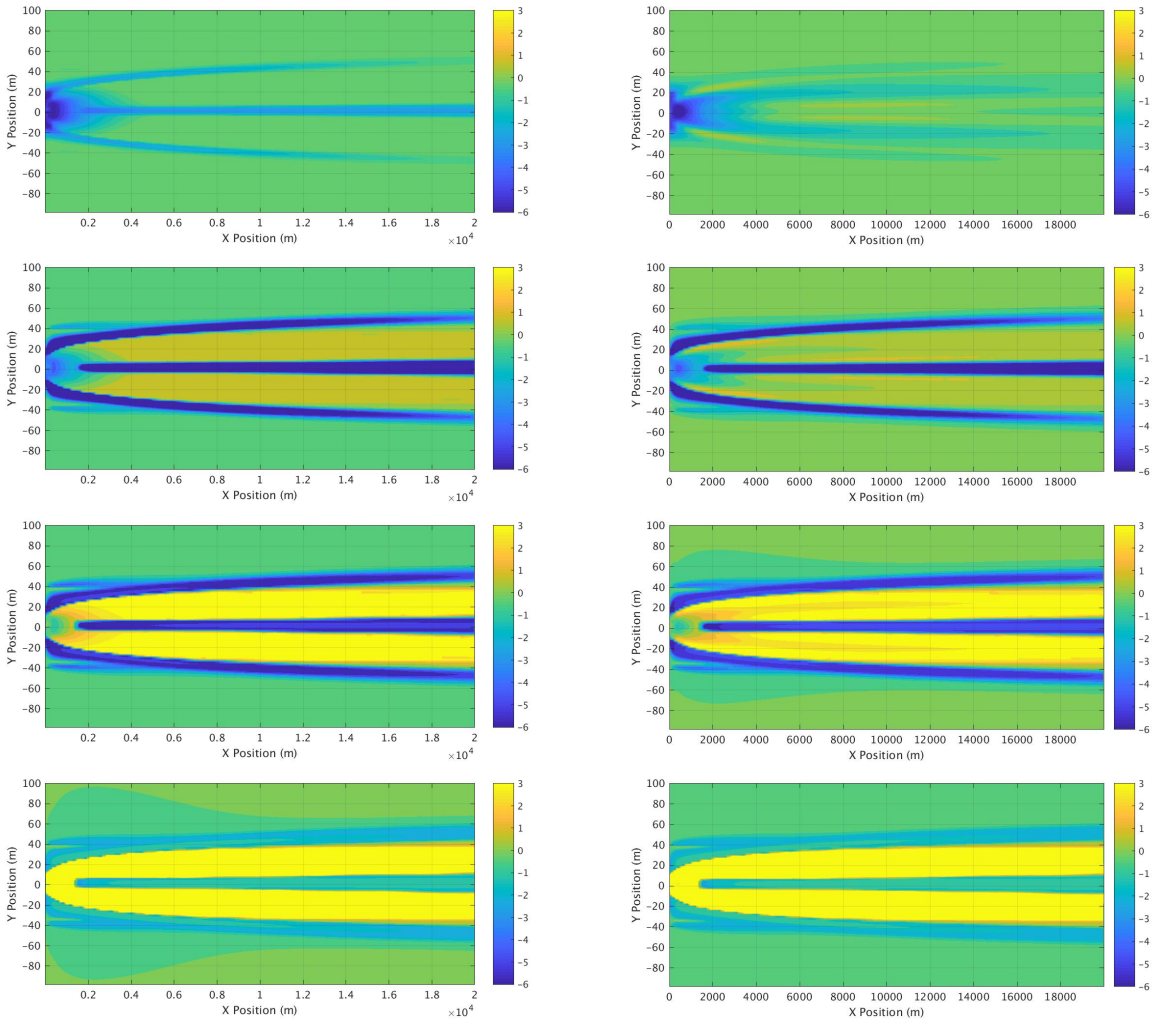

Figure C.5: Perfect SAR images (dB) at L, S, C, and X band with vv polarization at 50 degree incidence with the azimuth along (left) and across (right) the wake for a 1.0 m wave amplitude in head seas.

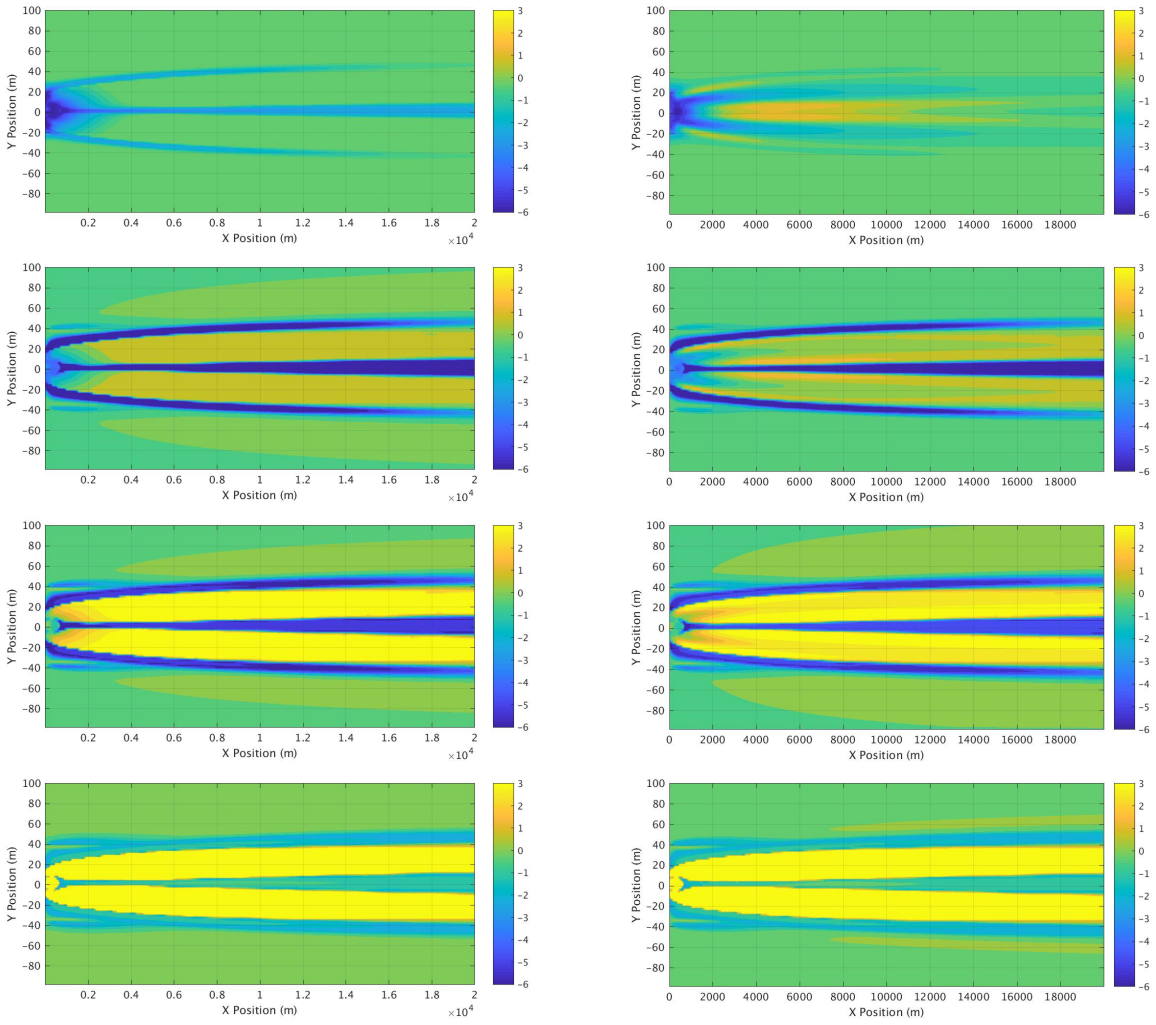

Figure C.6: Perfect SAR images (dB) at L, S, C, and X band with vv polarization at 50 degree incidence with the azimuth along (left) and across (right) the wake for a 1.5 m wave amplitude in head seas.

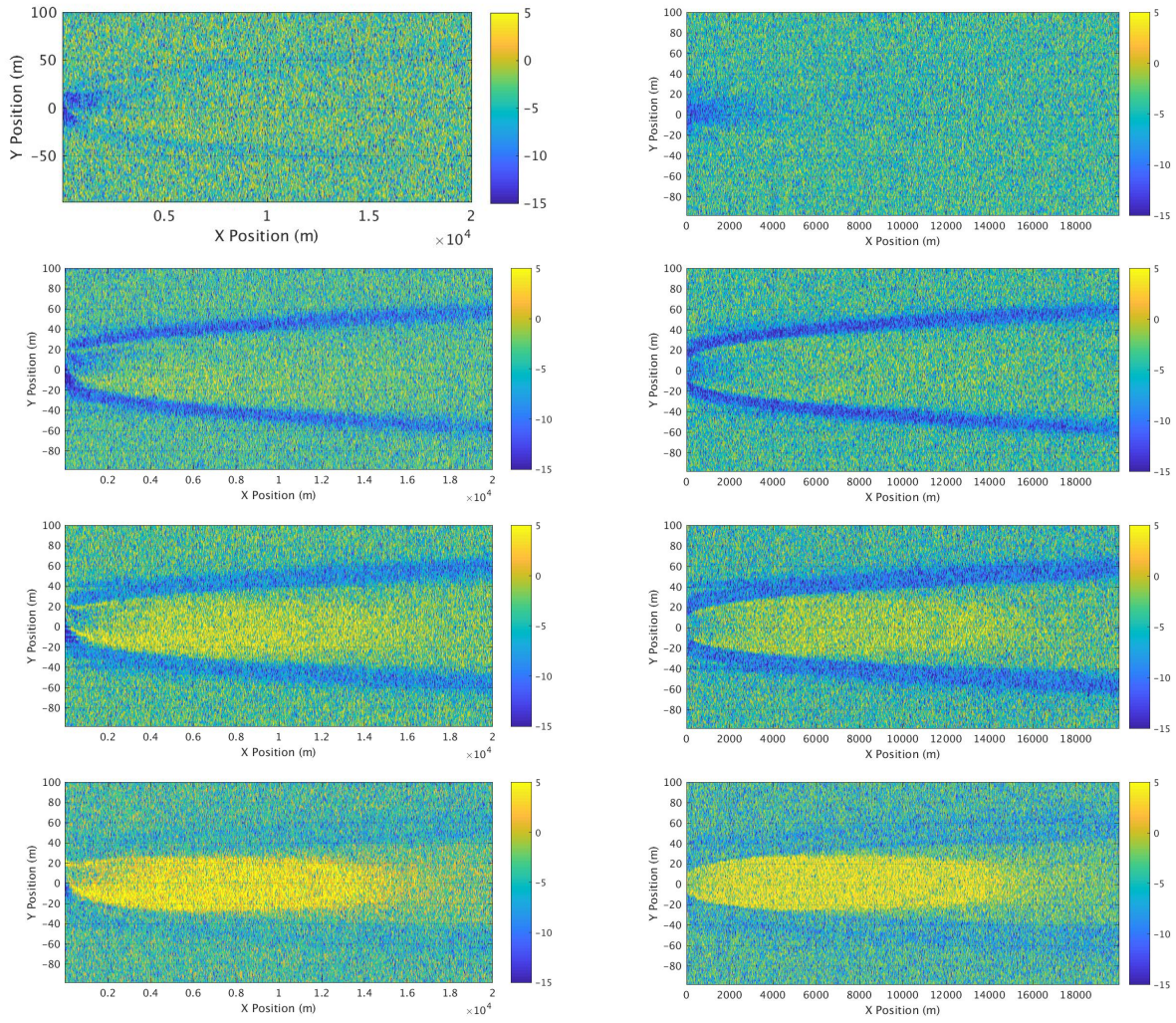

Figure C.7: Simulated SAR images (dB) at L, S, C, and X band with vv polarization at 50 degree incidence with the azimuth along (left) and across (right) the wake for a calm seas condition.

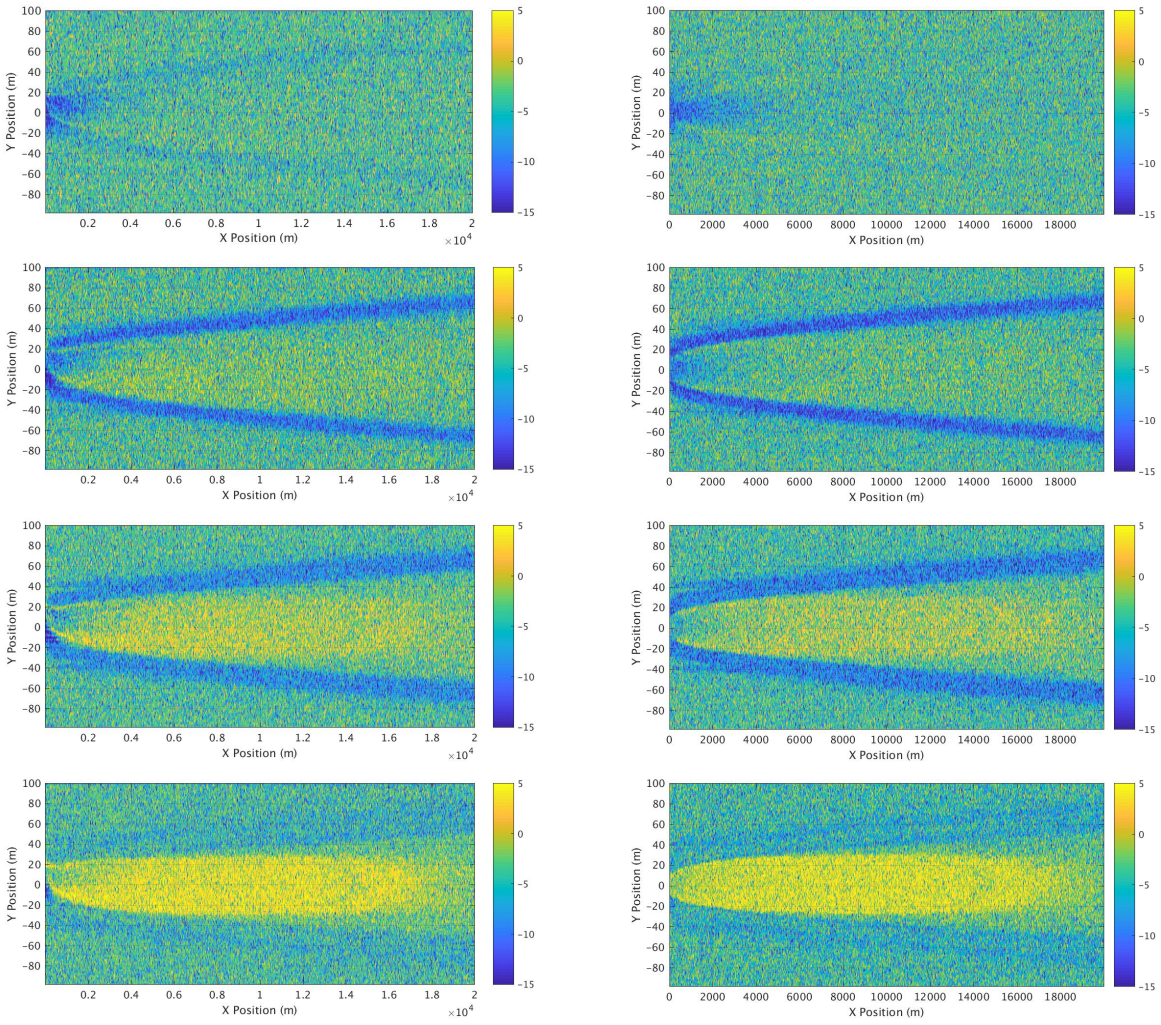

Figure C.8: Simulated SAR images (dB) at L, S, C, and X band with vv polarization at 50 degree incidence with the azimuth along (left) and across (right) the wake for a following seas condition with 0.5m wave amplitude.

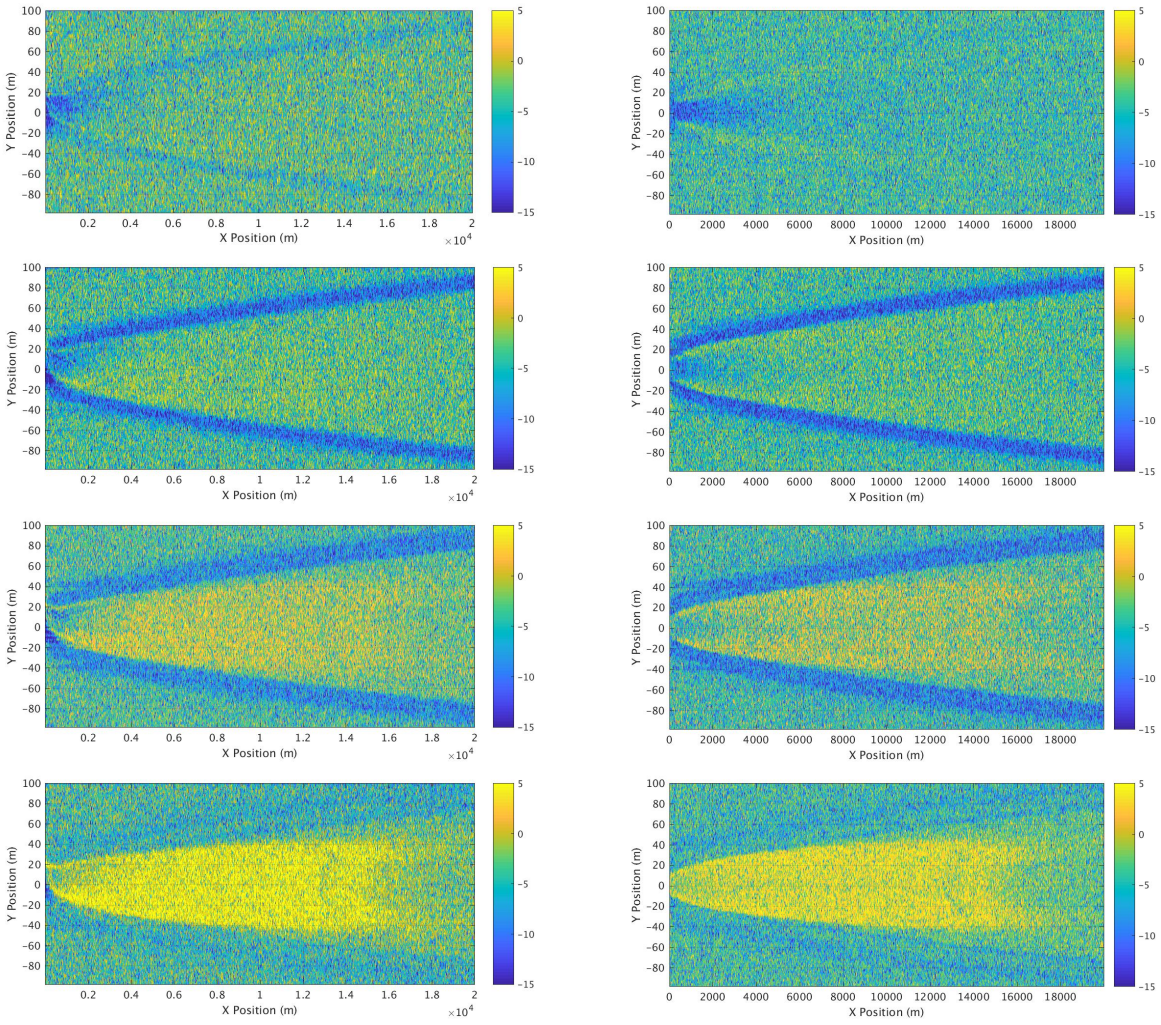

Figure C.9: Simulated SAR images (dB) at L, S, C, and X band with vv polarization at 50 degree incidence with the azimuth along (left) and across (right) the wake for a following seas condition with 1.0m wave amplitude.

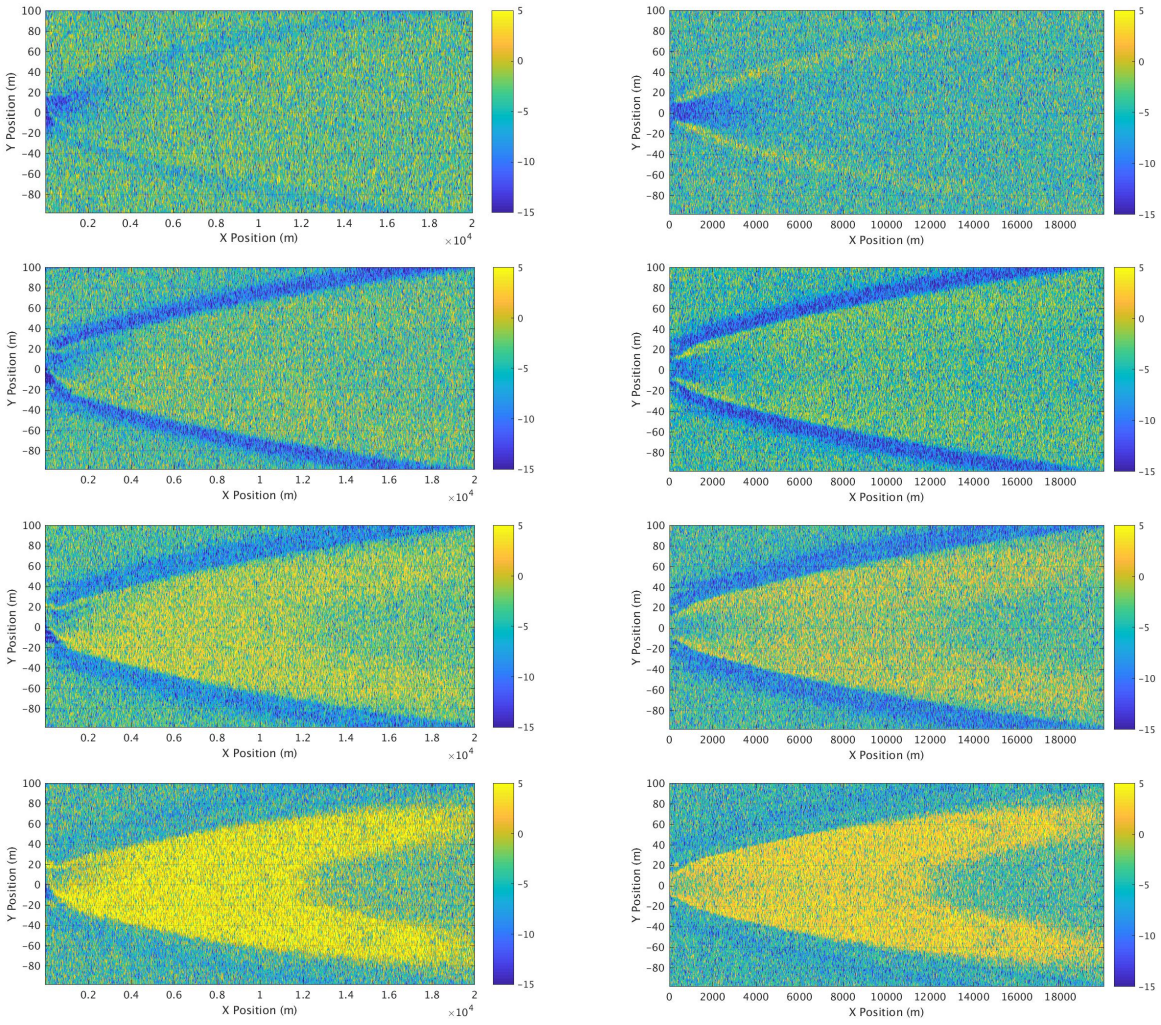

Figure C.10: Simulated SAR images (dB) at L, S, C, and X band with vv polarization at 50 degree incidence with the azimuth along (left) and across (right) the wake for a following seas condition with 1.5m wave amplitude.

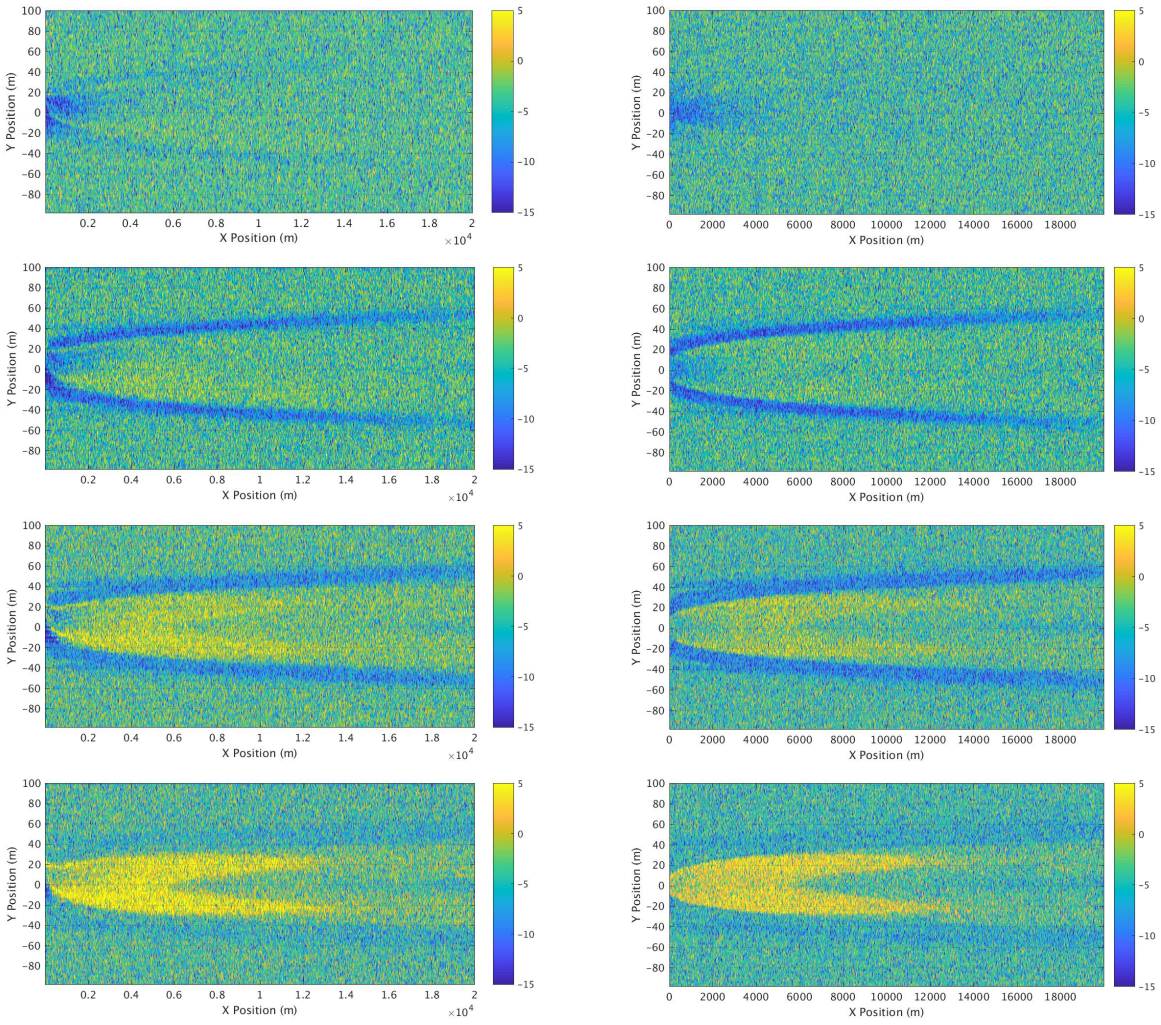

Figure C.11: Simulated SAR images (dB) at L, S, C, and X band with vv polarization at 50 degree incidence with the azimuth along (left) and across (right) the wake for a head seas condition with 0.5m wave amplitude.

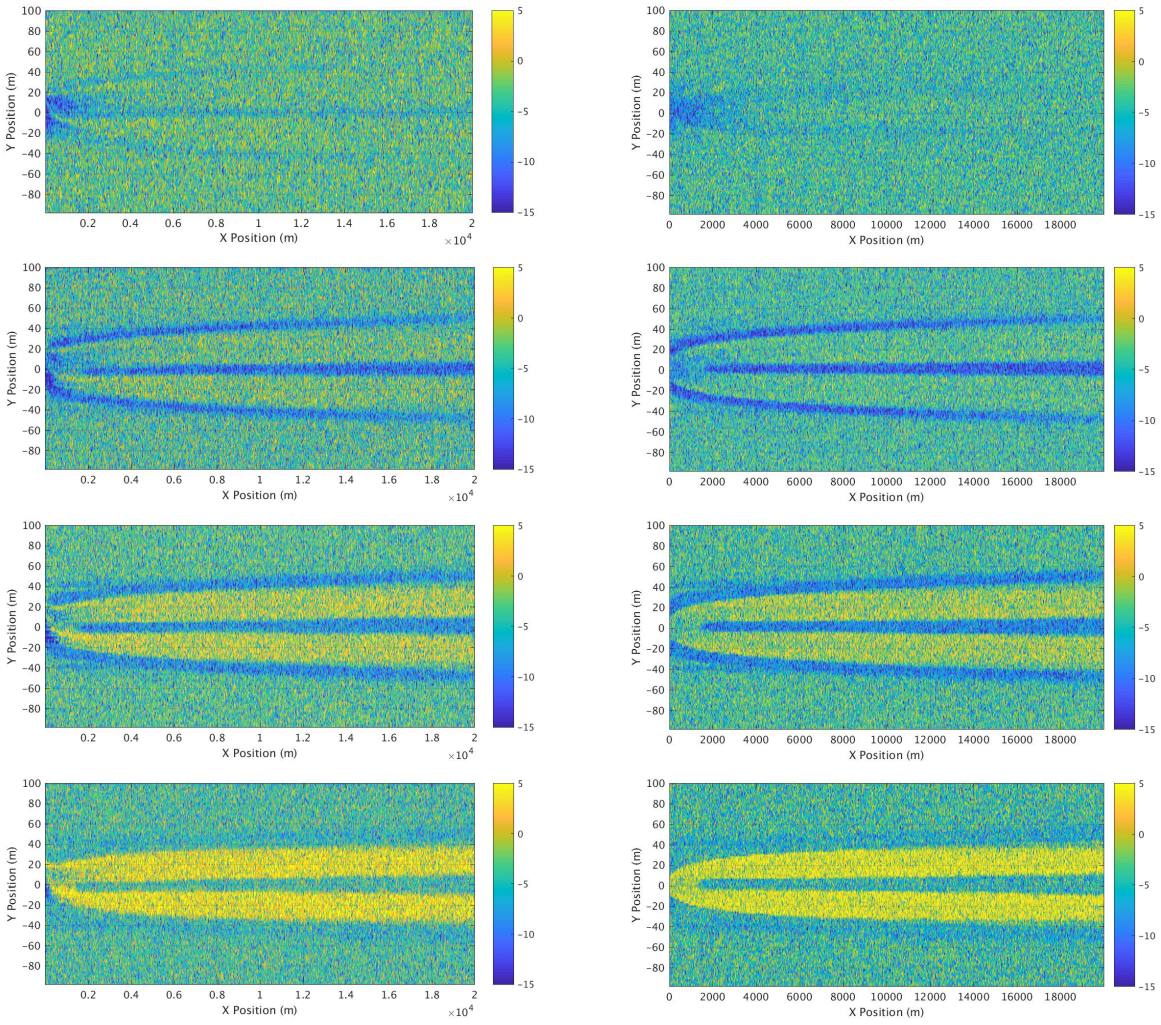

Figure C.12: Simulated SAR images (dB) at L, S, C, and X band with vv polarization at 50 degree incidence with the azimuth along (left) and across (right) the wake for a head seas condition with 1.0m wave amplitude.

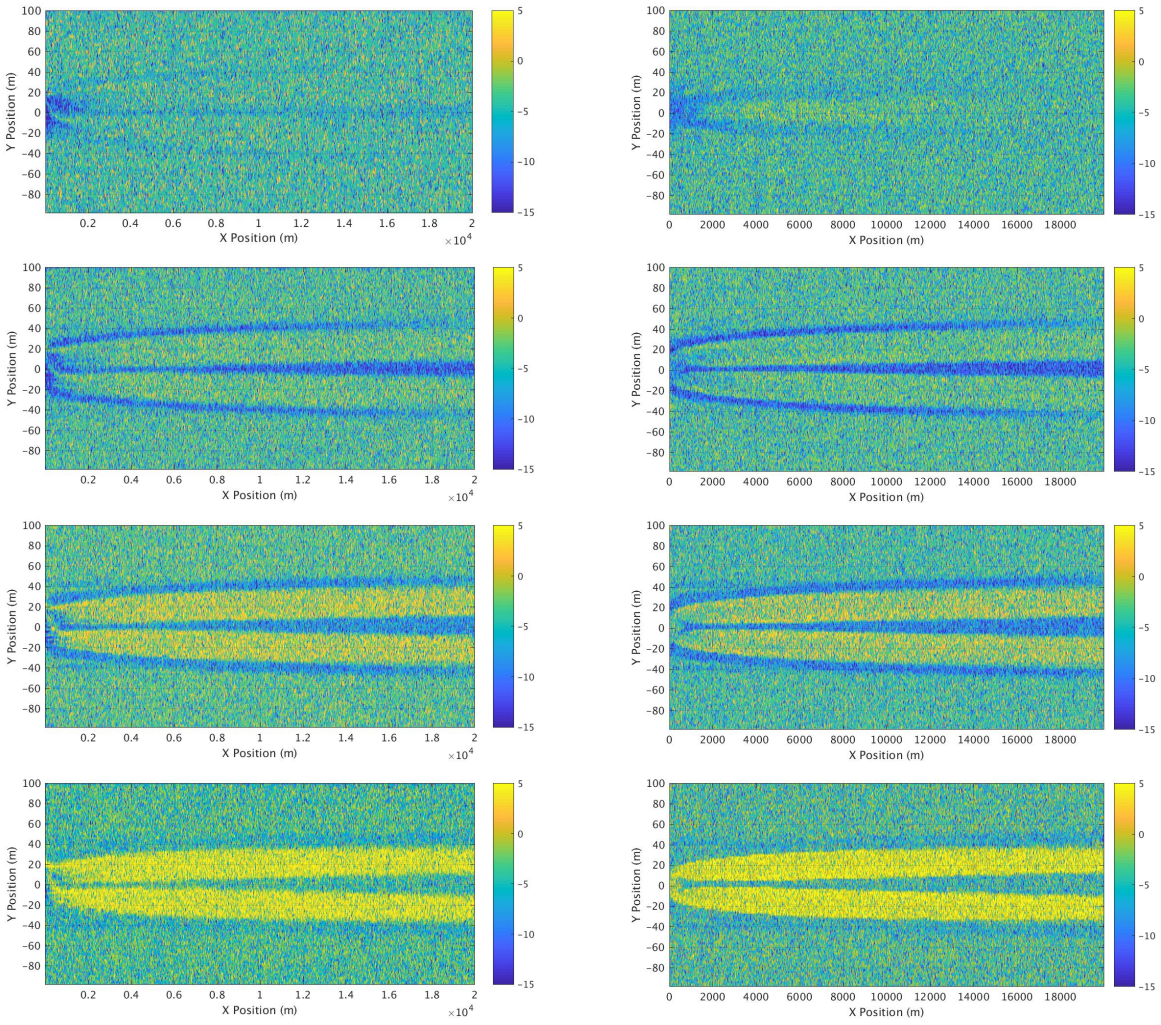

Figure C.13: Simulated SAR images (dB) at L, S, C, and X band with vv polarization at 50 degree incidence with the azimuth along (left) and across (right) the wake for a head seas condition with 1.5m wave amplitude.